

---

# **Long Term Monitoring of Mrk421 from 2005-2008 with the MAGIC Telescope**

**Ching-Cheng Hsu**

---



München 2010



---

# **Long Term Monitoring of Mrk421 from 2005-2008 with the MAGIC Telescope**

**Ching-Cheng Hsu**

---

Dissertation  
an der Fakultät für Physik  
der Ludwig–Maximilians–Universität  
München

vorgelegt von  
Ching-Cheng Hsu

München , Mai 2010

Erstgutachter: Prof. Dr. Christian Kiesling

Zweitgutachter: Prof. Dr. Masahiro Teshima

Tag der mündlichen Dr. Prüfung: August 6, 2010

# Abstract

Active Galactic Nuclei (AGNs) are among the most luminous objects in the universe. At the center of an AGN, there is a SuperMassive Black Hole (SMBH) with a mass above  $10^6 M_\odot$ , which is believed to be the engine of a huge energy output. Blazars are a subclass of AGNs, which usually have bipolar jets, one of which is pointing towards us. Markarian 421 (Mrk421) is one of the bright and nearby established TeV blazars. Its TeV emission was first discovered by the Whipple telescope in 1992 [1], and it became one of the most studied extra-galactic objects in the TeV regime. Mrk421 shows strong variabilities in time and amplitude in different energy regimes.

The Mrk421 data collected so far from many historic multiwavelength observations is not yet sufficient to fully constrain the theoretical models. In particular, it is not yet clear whether the leptonic or hadronic processes play a decisive role inside the jets.

Due to short duty cycles and limited observation time, studies of bright TeV ( $E \geq 100$  GeV) blazars are mostly restricted to flaring episodes or short time period (a few days to weeks) of multiwavelength campaigns. However, to study these objects long time monitoring is needed in order to constrain theoretical jet models. Only unbiased long-term studies are adequate for the determination of flaring states probabilities and for estimating the statistical significance of possible correlations between TeV flaring states and other observables, like X-ray or neutrinos. Besides, regular observations can also provide triggers for multiwavelength ToO observations. This is particularly necessary for identifying and studying orphan TeV flares.

The MAGIC (Major Atmospheric Gamma-ray Imaging Cherenkov) telescope is one of the precise Imaging Air Cherenkov Telescopes (IACT) for VHE  $\gamma$ -ray astronomy. It has a mirror area of about  $236 m^2$  and today it is the largest operating single-dish IACT. It is located on the Canary Island La Palma ( $28^\circ 45' N, 17^\circ 53' W$ ) at an altitude of about 2200 m.

MAGIC has observed Mrk421 since 2004 and then constantly monitored this source from 2006. In this thesis, the Mrk421 data taken from 2005 to 2008 will be presented. The physics results from several times of joint observations will be also discussed.

To further increase the sensitivity of the MAGIC telescope, a second telescope was built. The photosensors, PMTs, with light collectors, Winston Cones, of the second telescope were tested in order to know the performance of the new system. The different characteristics of the PMTs and their performance tests will be also described.

# Zusammenfassung

Aktive Galaktische Kerne (Active Galactic Nuclei: AGNs) gehören zu den lichtstärksten Objekten im Universum. Im Zentrum eines solchen Kerns befindet sich ein supermassives Schwarzes Loch mit einer Masse von mehr als  $10^6 M_{\odot}$ , in dem, wie man annimmt, ungeheure Energiemengen produziert werden. Blazare sind eine Untergruppe der AGNs mit üblicherweise bipolaren Jets, von denen einer in unsere Richtung zeigt. Markarian 421 (Mrk421) ist ein heller, nicht weit von der Erde entfernter und gut bekannter TeV Blazar, dessen Emissionen im TeV-Bereich zuerst vom Whipple-Teleskop im Jahre 1992 [1] entdeckt wurden, und der sich zu einem der meistuntersuchten außergalaktischen TeV-Objekte entwickelte. Mrk 421 weist starke Schwankungen in Zeit und Fluss in unterschiedlichen Energiebereichen auf. Mehrfach wurden in der Vergangenheit Beobachtungen von Mrk421 gleichzeitig in verschiedenen Wellenlängenbereichen durchgeführt. Die dabei gesammelten Daten reichen jedoch für eine exakte Eingrenzung theoretischer Modelle nicht aus. Insbesondere ist unklar, ob es leptonische oder hadronische Prozesse sind, die innerhalb der Jets eine entscheidende Rolle spielen.

Aufgrund der kurzen Zyklen und begrenzter Beobachtungszeiträume beschränken sich Untersuchungen von hellen TeV ( $E \geq 100 \text{ GeV}$ ) Blazaren im wesentlichen auf Strahlungs-aus-brüche oder kurze Zeitabschnitte (einige Tage oder Wochen), in denen Beobachtungen gleichzeitig in verschiedenen Wellenlängenbereichen durchgeführt wurden. Zur Erforschung dieser Objekte und Eingrenzung theoretischer Jet-Modelle sind Langzeitbeobachtungen jedoch unabdingbar. Nur objektive Langzeitstudien dieser Art erlauben es, die Wahrscheinlichkeit von Strahlungs-aus-brüchen zu bestimmen und die statistische Signifikanz möglicher Korrelationen zwischen TeV Strahlungs-aus-brüchen und anderen Beobachtungsgrößen wie Röntgen- oder Neutrino-Fluss abzuschätzen. Regelmäßige Beobachtungen ermöglichen es auch, Trigger für die gleichzeitige Beobachtung eines aktuell in den Fokus tretenden Objekts in mehreren Wellenlängenbereichen zu definieren, was speziell für die Identifikation und Untersuchung von einzelnen Strahlungs-aus-brüchen im TeV-Bereich erforderlich ist.

Das MAGIC (Major Atmospheric Gamma-ray Imaging Cherenkov) Teleskop ist eines der am genauesten abbildenden Luft-Cherenkov-Teleskope für Hochenergie-Gammaastronomie. Mit seiner Spiegelfläche von ca.  $236 \text{ m}^2$  ist es derzeit das größte alleinstehende Teleskop dieser Art. Sein Standort befindet sich in etwa 2200 m Meereshöhe auf der kanarischen Insel La Palma ( $28^{\circ}45'N, 17^{\circ}53'W$ ).

MAGIC hat Mrk421 seit dem Jahre 2004 mehrfach beobachtet und überwacht diese Quelle ständig seit 2006. In der vorliegenden Arbeit werden Mrk421-Daten aus dem Zeitraum 2005 bis 2008 präsentiert. Weiterhin werden die physikalischen Ergebnisse aus einigen gemeinsamen

Beobachtungen diskutiert.

Um die Sensibilität des MAGIC-Teleskops weiter zu verbessern, wurde ein zweites Teleskop errichtet. Die Lichtsensoren, PMTs und Lichtkollektoren (Winston Cones) des zweiten Teleskops wurden getestet, um die Leistungsfähigkeit des neuen Instruments beurteilen zu können. Die unterschiedlichen Merkmale der PMTs und die Überprüfung ihrer Leistung werden ebenfalls hier beschrieben.

# Contents

<b>Abstract</b>	<b>v</b>
<b>Zusammenfassung</b>	<b>vi</b>
<b>Introduction - This Thesis</b>	<b>xxxii</b>
<b>Acknowledgement</b>	<b>xxxiv</b>
<b>1 High Energy Astrophysics with Gamma Rays</b>	<b>1</b>
1.1 Multi-messenger Universe . . . . .	1
1.2 Cosmic Rays . . . . .	2
1.3 Cosmic Accelerators . . . . .	3
1.3.1 Fermi Acceleration Mechanism . . . . .	4
1.4 Very High Energy Photons . . . . .	9
1.5 VHE $\gamma$ Ray Sources . . . . .	12
1.5.1 High Energy $\gamma$ Sky . . . . .	12
1.5.2 High Energy Galactic Sources . . . . .	13
1.5.3 High Energy Extra-galactic Sources . . . . .	18
1.6 Impact and Role of VHE Gamma Ray Astrophysics in Physics . . . . .	19
1.6.1 Fundamental Physics and Cosmology . . . . .	19
1.7 Future Prospects . . . . .	20
1.7.1 Next Generation IACTs: CTA and AGIS . . . . .	20
1.7.2 Multi-messenger Study of the Energetic Universe . . . . .	21
<b>2 Active Galactic Nuclei</b>	<b>22</b>
2.1 Introduction . . . . .	23
2.2 Properties and Classification . . . . .	26
2.2.1 Orientation-based Unified Scenario . . . . .	27
2.3 Blazars: OVV and BL Lacs . . . . .	28
2.3.1 Relativistic Beaming . . . . .	28
2.3.2 Short Time Variability in Photon Flux and Spectrum . . . . .	29
2.3.3 Superluminous Motion . . . . .	29
2.4 VHE $\gamma$ -Ray Emission from Blazars . . . . .	30

2.4.1	Leptonic Models . . . . .	31
2.4.2	Hadronic Models . . . . .	33
2.4.3	Mixed Models . . . . .	34
2.4.4	Other possibilities ? . . . . .	34
2.5	The Impact of VHE $\gamma$ -ray Observation of AGNs on Physics . . . . .	35
2.5.1	Extra-galactic Background Light . . . . .	36
<b>3</b>	<b>Imaging Cherenkov Telescopes</b>	<b>37</b>
3.1	Extensive Air Showers . . . . .	37
3.1.1	Products in Extensive Air Showers . . . . .	39
3.2	Electromagnetic Showers . . . . .	40
3.3	Hadronic Showers . . . . .	41
3.4	Lateral Distribution of the Showers . . . . .	42
3.5	Cherenkov Light . . . . .	43
3.6	Imaging Cherenkov Telescopes . . . . .	47
3.6.1	Introduction . . . . .	47
3.6.2	Imaging Techniques . . . . .	47
<b>4</b>	<b>The MAGIC Telescope</b>	<b>49</b>
4.1	The Unique Features of MAGIC . . . . .	50
4.2	The Data Chain . . . . .	50
4.3	The Telescope Structures and the Drive System . . . . .	51
4.4	The Reflector and the Mirrors . . . . .	52
4.5	Active Mirror Control . . . . .	53
4.6	The Camera . . . . .	54
4.7	Signal Transmission . . . . .	54
4.8	Receiver Board and Trigger . . . . .	55
4.8.1	Receiver Board . . . . .	55
4.8.2	Trigger . . . . .	55
4.9	FADC/MUX-FADC . . . . .	56
4.10	Calibration System . . . . .	58
4.11	Observational Mode . . . . .	58
4.12	MAGIC II . . . . .	60
<b>5</b>	<b>Photodetector Studies for the MAGIC II Telescope</b>	<b>61</b>
5.1	Introduction . . . . .	61
5.2	The Basic Requirements . . . . .	61
5.3	Characteristics and Different Measurements . . . . .	63
5.3.1	Quantum Efficiency . . . . .	63
5.3.2	Single Photoelectron Spectrum . . . . .	67
5.3.3	Afterpulsing . . . . .	69
5.3.4	Aging . . . . .	71
5.3.5	Pulse Shape and Timing Characteristics . . . . .	72

---

5.3.6	Transition Time Jitter . . . . .	73
5.4	Light Guides . . . . .	74
5.4.1	Introduction . . . . .	74
5.4.2	Design . . . . .	76
5.4.3	Measurements . . . . .	76
5.4.4	Results, Summary and Discussion . . . . .	77
5.5	Remarks about Photo-sensors during Moon / Twilight Observations . . . . .	84
<b>6</b>	<b>Standard Analysis Chain for MAGIC Data</b>	<b>85</b>
6.1	MARS Software Package and the Analysis Chain . . . . .	85
6.2	Calibration and Pulse Extraction . . . . .	88
6.2.1	The Pulse Extraction . . . . .	88
6.2.2	F-factor Method . . . . .	88
6.3	The Image Cleaning . . . . .	89
6.4	The Image Parameters . . . . .	90
6.5	The $\gamma$ -Hadron Separation . . . . .	91
6.6	Gamma Signal Extraction and Background Subtraction . . . . .	92
6.6.1	Source Dependent Analysis . . . . .	92
6.6.2	Source Independent Analysis . . . . .	93
6.6.3	Significance and Sensitivity . . . . .	93
6.7	Determination of the Lightcurve and the Spectrum . . . . .	94
6.7.1	The Effective Time . . . . .	94
6.7.2	The Lightcurve . . . . .	94
6.7.3	Determination of the Spectrum . . . . .	95
6.8	ONLINE Analysis . . . . .	96
6.9	Basic MAGIC Performance . . . . .	98
<b>7</b>	<b>Monitoring of Mrk421 with the MAGIC Telescope</b>	<b>99</b>
7.1	Introduction: Physics Motivation for the AGN Monitoring in the TeV Energy Band	99
7.2	Markarian 421 . . . . .	100
7.3	Morphology . . . . .	103
7.4	Mrk421 TeV Observations in the Past 17 Years 1992-2005 . . . . .	104
7.4.1	From Discovery to 1998 . . . . .	104
7.4.2	From 1998-2004 . . . . .	105
7.5	MAGIC Strategies of Long-term Monitoring . . . . .	109
7.6	Fast ONLINE Analysis . . . . .	111
7.7	Mrk421 Data Overview and Strategies Of Data Classification and Selection . . . . .	111
7.8	Moon and Twilight Observation . . . . .	113
7.8.1	Moonlight Conditions . . . . .	114
7.8.2	Twilight Conditions . . . . .	115
7.9	Multiwavelength Study on Blazars and Brief Review of Optical and X-ray Experiments . . . . .	119
7.9.1	Multiwavelength Data . . . . .	119

---

7.10	The Analysis Tool . . . . .	120
7.10.1	Variability . . . . .	120
7.10.2	Temporal Analysis . . . . .	121
7.10.3	The Hardness Ratio . . . . .	122
7.10.4	Excess $\sigma$ -Flux Relations . . . . .	122
7.10.5	Correlation Between Different Wavelengths . . . . .	122
7.10.6	Intra-Night Short Time Variability . . . . .	123
7.10.7	The EBL De-absorption . . . . .	124
7.10.8	SED . . . . .	125
7.11	Mrk421 P0, P1 Data . . . . .	125
7.11.1	Data Samples and Selections from P1 Mrk421 Data. . . . .	125
7.11.2	Analysis Results from the P1 Mrk421 Data. . . . .	126
7.11.3	Multiwavelength Study . . . . .	127
7.11.4	The Spectrum . . . . .	128
<b>8</b>	<b>The Mrk421 from April 2006 to June 2007</b>	<b>134</b>
8.1	Mrk421 P2, P3 Data Summary and Analysis Results . . . . .	134
8.2	Lightcurve from Mrk421. . . . .	136
8.2.1	Variability of the Short Time Scale . . . . .	136
8.3	The Spectrum . . . . .	140
<b>9</b>	<b>Mrk421 data from December 2007 to June 2008</b>	<b>142</b>
9.1	The Data Selection and Quality Check. . . . .	142
9.2	Mrk421 Data Selections and Analysis . . . . .	142
9.2.1	Lightcurve . . . . .	142
9.2.2	Short Time Variability . . . . .	145
9.2.3	Short Time Lightcurve . . . . .	151
9.2.4	Variability . . . . .	151
9.2.5	Variability vs Flux States . . . . .	157
9.2.6	$\sigma$ - Flux Relation . . . . .	157
9.2.7	Further Discussion on Lightcurves . . . . .	160
9.3	Multi-Wavelength Study . . . . .	163
9.3.1	Multiwavelength Correlation. . . . .	163
9.3.2	TeV/X-ray, TeV/Optical Time Lag search. . . . .	164
9.4	June Flare of Mrk421: Multiwavelength Observation. . . . .	165
9.4.1	Observations in VHE $\gamma$ -Rays . . . . .	165
9.5	Spectral Distribution . . . . .	169
9.5.1	Hardness Ratio . . . . .	169
9.5.2	Spectral Study . . . . .	169
9.6	Flare Analysis . . . . .	172
9.6.1	6 February 2008 . . . . .	172
9.6.2	31 March 2008 . . . . .	173
9.6.3	15 January and 11 February 2008 . . . . .	174

---

9.7	The Spectrum Study . . . . .	182
9.7.1	Observed Spectrum Study . . . . .	182
9.7.2	Intrinsic Energy Spectrum . . . . .	182
9.8	SED Modeling . . . . .	187
<b>10</b>	<b>Summary of Long Term Monitoring</b>	<b>189</b>
10.1	Long time Lightcurve . . . . .	189
10.2	Variability . . . . .	191
10.2.1	Short Time Variability . . . . .	194
10.3	Search for Time Lag . . . . .	200
10.4	Multiwavelength Correlation . . . . .	201
10.4.1	X/TeV correlation . . . . .	201
10.4.2	TeV Orphan Flares . . . . .	203
10.4.3	Optical/TeV correlation . . . . .	205
10.4.4	Radio/TeV correlation . . . . .	205
10.5	TeV Spectrum . . . . .	206
10.6	SED Modeling . . . . .	208
10.6.1	The Constraints on the SSC Parameters . . . . .	208
10.6.2	Photons from the External Field . . . . .	211
10.7	Different State Probabilities . . . . .	212
10.8	Comparison with Mrk501 . . . . .	213
10.9	Future Prospects . . . . .	214
<b>Summary and Conclusion</b>		<b>216</b>
<b>A</b>	<b>Crab Analysis</b>	<b>i</b>
A.1	Crab December 2005 to March 2006 . . . . .	i
A.1.1	Results from the Crab Analysis. . . . .	ii
A.2	Crab Results from P2 and P3 . . . . .	vi
A.2.1	Crab Data from December 2006 to January 2007 . . . . .	vi
A.2.2	Crab Data from February 2007 to June 2007 . . . . .	vii
A.2.3	Stability Check . . . . .	viii
A.3	The Data Selection and Quality Check. . . . .	xiii
A.3.1	Crab Data from December 2007 to March 2008 . . . . .	xiii
A.3.2	Moon and Twilight Observations . . . . .	xvi
A.3.3	The results from the Crab Data . . . . .	xvii

# List of Figures

1.1	The cosmic diffuse photon flux from different energy bands. The plot is from [2]	1
1.2	The cosmic ray spectrum from 1 GeV up to higher than $10^{11}$ GeV. The cosmic rays with energies lower than 1 GeV will be mostly blocked by the solar magnetic wind such that they will not enter the solar system. The slope of the power spectrum begins at -2.7 and changes to a steeper spectrum of -3.1 around $3 \times 10^6$ GeV, the so-called knee region. Up to the second knee region, which is around $4 \times 10^8$ GeV, the spectrum becomes softer to -3.3. At the so-called ankle region, the spectrum seems to flatten to a spectral index of about -2.7 again. The vertical axis is set with the unit: $E^2 dN/dE$ . This plot is taken from [3]	2
1.3	The plot depicts Fermi's original idea. Particles are accelerated by collision with magnetic clouds. There are two possibilities. The left plot shows the head-on collision between the particles and the magnetic clouds. The right plot shows the follow-up collisions.	4
1.4	A relativistic particle moving across a strong, sub-relativistic shock from downstream to upstream. In the rest frame of the upstream plasma, the downstream flow is moving at speed $V = 3U/4$ . Furthermore, we could calculate the final energy in the same frame if we knew the scattering angle $\theta_2$ . By equating the initial and final energies, we know how much energy was gained because of the collision.	7
1.5	The so-called Hillas plot for the different possible astrophysical accelerators.	9
1.6	This all-sky map constructed from 3 months of Fermi-LAT observations (4 August to 30 October, 2008) represents a deeper, better-resolved view of the gamma-ray sky than any previous space mission. The photo is taken from [4]	12
1.7	The sky map of the TeV observation. The statistics is until May 2010. In total, there are 98 established sources. The plot is from [5]	13
1.8	The results from the H.E.S.S. 2004 Galactic survey.	14
23		
2.2	The power law spectrum of the synchrotron radiation, which is the sum of the radiation produced by individual electrons as they are moving inside the magnetic field. The turnover at low frequency which we have seen in the AGN spectrum is due to the synchrotron self-absorption effect.	24
2.3	The unified model based on orientation.	27

---

2.4	The explanation of superluminal motion . . . . .	30
2.5	The leptonic model of blazar TeV emission. Blobs of high energy accelerated electrons are moving away from the central black hole and emit synchrotron photons. Relativistic electrons interact with these synchrotron photons via the inverse Compton process producing the synchrotron self-Compton (SSC) peak. The thermal photons from the accretion disk may also interact with electrons in the jet to produce the External Comptonization of Direct disk radiation (ECD) peak. Photons also come from the clouds of gas in the broad line region (BLR) and interact with the blobs of electrons to produce External Comptonization of radiation from the Clouds (ECC) peak. The plot is from [6] . . . . .	33
3.1	The longitudinal development of an extensive air shower. The x-axis is the atmosphere depth expressed as the number of radiation lengths. The y-axis gives the number of electromagnetic particles in the air shower. Sea level is about 28 radiation lengths, 2600 m above sea level is about 20 radiation lengths [?]. The primary particle is photons at 100 TeV. . . . .	38
3.2	Heitler Model of EM showers. In this model, the $\gamma$ -ray initiated showers are simplified as the combination between the $e^+/e^+$ production and bremsstrahlung interactions. . . . .	40
3.3	The longitudinal electron distribution in EAS. . . . .	41
3.4	Conceptual sketch of hadronic showers . . . . .	42
3.5	The Nishimura-Kamata-Greisen (NKG) electron lateral density distribution. The primary particles are proton showers with different energies. . . . .	43
3.6	The Cherenkov spectrum after the absorption in the atmosphere for the gamma ray showers with an incidence angle of zenith and zenith angle of 60 degrees. . . . .	44
3.7	The Cherenkov light lateral distribution, compared with proton shower and gamma shower. The observational level for this simulation is about 2200 m above sea level. . . . .	45
3.8	The Cherenkov light pool on the ground. The small black dots are the Cherenkov photons. The left plot is the from a 300 GeV $\gamma$ shower, the right plot is from a 1 TeV proton shower. . . . .	45
3.9	The Cherenkov photon density with different energies and different primary particles. The photon density is taken within 125 m of the shower core for vertical showers [7]. . . . .	46

---

3.10	The Cherenkov light image on the camera. The orientation of the image depends on the inclination of the shower. The length and the position of the image are determined by the angular difference $\phi_2 - \phi_1$ and the impact distance R. The bottom plot shows that the later distribution of the shower could be seen from the width of the shower image. The 4 points A, B, C, D on the top plot are imaging on the focal plane in the bottom plot. From the plot, we know that the mapping is not linear. With decreasing height, the points are mapped further away. Finally, the image is more compressed inside and dilated on the outside yielding an asymmetric shape along the image axis. Nevertheless, the two symmetric points C and D are off-axis symmetrically from the image axis . . . . .	48
4.1	The first MAGIC telescope. . . . .	49
4.2	The complete data readout chain of MAGIC before the MUX FADC was installed. The figure is from [8] . . . . .	51
4.3	All the CCD cameras in the middle of the reflector of the MAGIC telescope. All of them have different purposes, which are illustrated in the text. The figure is from [9] . . . . .	52
4.4	The left plot shows the measured reflectivity of the mirror in different wavelengths. The right picture shows the backside image of the mirror. The big silver-colored box contains the AMC electronics. The small yellowish box below controls the mirror heating. . . . .	53
4.5	The left picture shows two different sizes of the PMT pixels used in the MAGIC telescope. The right picture shows the PMT pixel module in the camera plane. . . . .	54
4.6	Simulated distributions of the RMS of the arrival time distribution for $\gamma$ , $\mu$ and proton events measured by MAGIC-like but ultra-fast telescopes. From the plot, the RMS value of the arrival time provides a separation power between three different types of events. . . . .	55
4.7	Sketch of the trigger topology in the MAGIC camera. . . . .	56
4.8	Performance comparison between old FADC and new MUX-FADC. The left plot shows the pulse sampling and the right plot depicts the pixel distribution of the integrated noise. . . . .	57
4.9	The different components of the calibration system used in the MAGIC telescope. . . . .	57
4.10	Illustration figure for different observational modes. In the ON-mode, the source is positioned in the center of the camera (red circle). For the WOBBLE observation, the source is placed at $0.4^\circ$ off center (marked as "signal region" in the plot.) The background region in the WOBBLE-mode can be found at the opposite side of the signal region or even any other regions on the $0.4^\circ$ circle. This provides a simultaneous measurement of the background. On average, every 20 minutes, the wobble positions are swapped. More background samples can be taken if the observation time is long enough. This increases the statistics of the background data. The plot is adapted from [10]. . . . .	59
4.11	Sensitivity curve of MAGIC stereo-observation. . . . .	59

5.1	ET company's PMT QE curves with and without a diffuse lacquer coating. . . . .	63
5.2	Hamamatsu Photonics PMT QE curves with and without a diffuse lacquer coating. . . . .	64
5.3	PMT QE curves with and without a diffuse lacquer coating from the two companies. PMTs were operated as photocells. . . . .	66
5.4	PMT coating with a scattering layer outside the tube. The picture is taken from [11].	67
5.5	Example of a SPE of the PMT DW139 from Electron Tubes. The left peak originates pedestal events, the second broad peak the single photoelectron events.	67
5.6	Example of SPE of the PMT DW139 and et10006 from Electron Tubes. . . . .	68
5.7	The afterpulse rate for the Hamamatsu PMT (R7373A-01MOD) serial number XC3351 as a function of thresholds. . . . .	69
5.8	The afterpulse rate for the ET PMT (9116WA) serial number XC3351 as a function of thresholds. . . . .	70
5.9	The afterpulse rate shows strong correlation with photocathode sensitivity from Auger 10-inch Photonics PMT. . . . .	71
5.10	The afterpulse rate as a function of QE for the Hamamatsu PMT (R7373A-01MOD) and Electron Tubes PMTs. The peak value of the QE is shown here. . .	72
5.11	The aging measurement for the Hamamatsu and ET PMTs. . . . .	73
5.12	Single photoelectron pulse from a Hamamatsu PMT. The pulse was measured by a digital oscilloscope of 1.5 GHz of bandwidth and a 5 GSamples/s FADC. . . .	74
5.13	The transit time jitter for single photoelectron pulses from the Hamamatsu PMT. The horizontal axis is the transition time. The transit time spread (TTS) is about 960 psec. Note that TTS becomes shorter for higher amplitude pulses. . . . .	74
5.14	The basic operation principle of the non-imaging optics. . . . .	75
5.15	The basic structure of the Winston cone. . . . .	75
5.16	Compared single photoelectron events of coated and uncoated Hamamatsu PMT xc3346 without coupling with a Winston cone. The shadow region is the angular span or MAGIC reflector. . . . .	78
5.17	Comparison of the two different types of Winston cones with bared PMTs. The plot on the left hand side is the normalization to the uncoated bared PMT at zero degree. The plot on the right side is normalized to the un-coated bared PMT at corresponding angles. . . . .	79
5.18	Comparison of the measured results with simulation prediction. All measured values are normalized to efficiency at zero degree. The two configurations for the Winston cone are hex→hex with an exit window of 19mm (left plot) and 20mm (right plot), respectively. . . . .	81
5.19	Comparison of the measured results with simulation prediction. All measured values are normalized to efficiency at zero degree. The two configurations for the Winston cone are hex→hex with an exit window of 21mm (left plot) and 22mm (right plot), respectively. . . . .	82
5.20	The efficiency curve of the cone with hex to hex (19 mm) and hex (22 mm) configuration. The black curves in both plots are uncoated PMTs, the red curves are coated PMTs. . . . .	82

---

5.21 Comparison of the number of single photoelectron events with the same uncoated PMT (Hamamatsu xl3346) but different cones. All measured values are normalized to bared tubes at zero degree. . . . .	83
6.1 Schematics of the MAGIC analysis chain. The center blue line is the data quality cut. When the $\alpha$ , $\theta^2$ hadronness (h), Energy (E) are calculated in each event, cuts are applied and the sensitivity is optimized. The effective collection area can be derived from final cuts on MC gamma samples. The effective observation time and total number of gamma excess are calculated from the data sample. . . . .	87
6.2 An example of the Camera pattern before (left) and after image cleaning (right). The basic idea is to get rid of the fired pixels which are due to random NSB. . . . .	89
6.3 The Hillas parameters. . . . .	90
6.4 An example of the $\alpha$ -plot. The background events are normalized such that the off-signal region (here, $30^\circ \sim 80^\circ$ ) matches the between ON and OFF data. . . . .	92
6.5 An example of an effective collection area plot. The right figure, The energy density matrix from the RF method. . . . .	95
6.6 An example of the ONLINE analysis output plot. Two different Size cuts are used, $\text{Size} \geq 200 \text{ ph.e.}$ and $\text{Size} \leq 200 \text{ ph.e.}$ The COG and $\phi$ plot give shifters a rough knowledge about the status of the camera inhomogeneity. . . . .	97
6.7 Alpha plot from ONLINE analysis . . . . .	97
6.8 The sensitivity of current gamma ray telescopes and satellites. The plot is from [12]	98
7.1 The SEDs of Mrk421 from radio to TeV band. Mrk421 is a HBL object, in which the two peaks, are located at X-rays and $\gamma$ -rays respectively. Usually, the first peak is well sampled and measured, however, the high energy peak usually has a lot of uncertainties. . . . .	101
7.2 The optical image of Mrk421 and its companion galaxy, 421-5. Image credit: Aimo Sillanpaa, Nordic Optical Telescope. . . . .	102
7.3 The total intensity map of Mrk 421 from radio observation (frequency 5GHz) at three different flux states from March - April 1998. The figures are from [13] . .	103
7.4 The spectrum of Mrk421 observed by the HEGRA telescopes. This was the first time, the spectrum indices changing with different flux states was observed. . . .	104
7.5 Whipple observed the Mrk421 flare in April 2004. The upper panel is the $\gamma$ -ray observation, the lower panel is from the ASM results. The X-ray flare was obviously ahead of TeV flare by one or two days [14]. . . . .	107
7.6 The spectra of Mrk501 during the 1997 flare and Mrk421 during the 2001 flare. The observed spectra are well described by a power law with exponential cut-off. The cut-off energy and the photon index are different for both spectra. The cut-off energy and photon index are $\alpha = 1.92 \pm 0.03_{\text{stat}} \pm 0.2_{\text{sys}}$ , and $\alpha = 2.19 \pm 0.02_{\text{stat}} \pm 0.04_{\text{sys}}$ for Mrk501 and Mrk421, respectively. The dashed curve in the plot results from fixing the cut-off energy $T_{\text{cut}}$ at 6.2TeV as measured from Mrk501. the $\xi^2 = 5.7$ (12 d.o.f.). The plot is adapted from [15]. . . . .	109

---

7.7	MAGIC I sensitivity plot : The integrated TeV flux is from 300 GeV to 30000 GeV. From 1 to 5 minutes, the sensitivity is limited by photon statistics, above 5 minutes, the sensitivity increases with square root of time. . . . .	110
7.8	The data check procedures for the MAGIC dataset . . . . .	111
7.9	The data quality selection procedures. . . . .	112
7.10	Reconstructed integrated flux with different energy thresholds by increasing the SIZE cut. The reconstructed integrated flux cannot be fully recovered by increasing the threshold. The Crab data was taken on 24 February 2007 with an average DT = 29. . . . .	114
7.11	The red region is the trigger region, the pink region is the whole camera. When DT in the inner region (red) is increasing, shower B, which is partially contained in the inner trigger region, will not trigger anymore. . . . .	115
7.12	The plot shows the hadron rate (after spark cut and 100 phe. SIZE cut), inner pixel DC current and DT under moonlight conditions. Note that the hadron rate and DC current are multiplied by a constant factor separately. The DC value changes very little. All the three values are very stable during moonlight observation. . . . .	116
7.13	Hadron Rate vs DT from the early 2007 Crab data. . . . .	117
7.14	The left plot shows the Width distribution of all the events on the camera with the SIZE 400. The right plot shows the SIZE distribution of the events of three different DT nights. . . . .	117
7.15	The DIST distribution of the events under three different background light conditions and three different DTs. The left plot shows the event DIST distribution in the whole Camera with a SIZE cut larger than 400 phe. The right plot shows only the events which are fully contained in the inner camera with the same SIZE cut of 400 phe. These two plots show that if we increase the analysis energy threshold (here 400 phe) and limit the events to only those that are fully contained in the inner camera, the triggered events will have the same DIST distribution irrespective of the light conditions. However, if we consider the full camera, events such as B in Fig. 7.11 will not trigger, and we will have a discrepancy in the DIST distribution. . . . .	118
7.16	Example of a twilight observation. The plot shows DT, hadron rate and DC from consecutive 15 data runs. It is clear that the DC changes dramatically. . . . .	118
7.17	An example of the structure function. . . . .	121
7.18	The plot shows the correlation time searching window between the TeV/X-ray or TeV/Optical observation. . . . .	123
7.19	Compare the two different EBL absorption models. Red dots show the model of Mazin-Raue 2007, blue dots show the Kneiske low model. Assume the source is at z=0.03, where the Mrk421 is located. The x-axis is the $\gamma$ energy in TeV, the y-axis is the surviving probability of the corresponding high energy of $\gamma$ rays. . . . .	124

---

7.20	The hadron rate versus zenith angle from this period of Mrk421 data . The left plot shows the hadron rate before cut. From the plot, a deficit of the hadron rate at low zenith angle can be clearly seen. The bad data are from 27 December 2007. The plot on the right gives the distribution after the cut. . . . .	125
7.21	The daily flux ( $\geq 300\text{GeV}$ ) from Mrk421 in period P0. . . . .	127
7.22	The Mrk421 lightcurve above 350 Gev in period P1. In order to have a complete picture, we display the data from the Whipple very preliminary public results in the same plot. . . . .	128
7.23	The 10 minutes' lightcurve background fit per night from Mrk421 data. 10 minutes' lightcurves were produced per night and the background was fitted with a constant value. Afterwards, bad points which were $5\sigma$ away were excluded and the data points within one night re-fitted. The $\chi^2$ distribution is shown. . . . .	130
7.24	The background and signal $\chi^2$ fit results from December 2005 to March 2006. Most of the fitting signals per night show a smaller $\chi^2$ within 1. . . . .	130
7.25	Mrk421 10 minutes' flux states histogram. The data are from December 2005 to January 2006 after data selection and stability cut. The histogram shows that the TeV observation is completely biased by high flux states. . . . .	131
7.26	The three different wavelength lightcurves from Mrk421 data in this period. . . . .	132
7.27	Mrk421 spectral energy densities for different flux levels. The solid curves are fitted by a simple power law (PL) (upper) and a PL plus exponential cutoff (bottom). The fitted parameters are shown in Table7.8 and Table7.9. . . . .	133
8.1	The hadron rate of Mrk421 data in period P2. Note that only the data within $46^\circ$ are presented here. The left plot shows the hadron rate versus zenith angle before cuts. The plot on the right hand side shows the results after the data quality cut. The red curves on both plots are the best fit for the good data. . . . .	135
8.2	The daily lightcurve above 350 GeV from Mrk421 in periods P2 and P3. . . . .	136
8.3	The daily lightcurve above 350 GeV from Mrk421 in period P2. . . . .	137
8.4	The daily lightcurve from Mrk421 from February 2007 to June 2007 (period P4) . . . . .	137
8.5	The $\chi^2/\text{d.o.f.}$ for background and signal per night for Mrk421 data from December 2006-January 2007. Each point is the data per night and the $\chi^2$ 10 minutes' lightcurves per night are calculated . . . . .	138
8.6	The $\chi^2/\text{d.o.f.}$ for background from Mrk421 data from December 2006 to January 2007 (upper panel) and February 2007 to June 2007 (lower panel). Each entry in the histogram is a 10 minutes' timing bin. . . . .	138
8.7	The $\chi^2/\text{d.o.f.}$ for background and signal per night for Mrk421 data from February 2007 to June 2007. 10 minutes' timing bins per night are used. . . . .	139
8.8	The spectrum of Mrk421 from P2, P3 and P4. . . . .	140
8.9	The correlation of flux level and slope. The figure shows the integral flux at energy $E \geq 300\text{GeV}$ . The spectral index is obtained from a power law fit to the energy spectrum between 150 GeV and 5000 GeV. The correlation shows the spectra's tendency of hardening with an increasing flux level. . . . .	141

---

9.1	The total Mrk421 lightcurve from December 2007 to June 2008 . . . . .	146
9.2	The total Mrk421 lightcurve from December 2007 to June 2008 above 350 GeV with VERITAS data. . . . .	147
9.3	The total Mrk421 lightcurve from December 2007 to June 2008 multiwavelength . . . . .	148
9.4	The Mrk421 P5 data, $\chi^2$ fitting of the background and the signal using 10 minutes timing bins. From the plot, it is clear that there are few nights which show a stable background with controllable $\chi^2/\text{d.o.f}$ but with large $\chi^2/\text{d.o.f}$ in the signals. These nights give a hint of the intra-night variability. . . . .	149
9.5	The total Mrk421 30min lightcurve from December 2007 to June 2008. . . . .	150
9.6	The Mrk421 10min total lightcurve from December 2007 to June 2008. integrated flux above 300 GeV. . . . .	152
9.7	The Mrk421 flux states histogram in P5 data. The upper plot shows linear scale in horizontal axis, the bottom plot shows integrated flux distribution in log scale. Both are fitted with Gaussian. . . . .	153
9.8	The $F_{var}$ and $F_{pp}$ in the daily scale. The plot indicates that most of the nights show very small or even negative $F_{var}$ and $F_{pp}$ in daily scale, except for the nights which show hints of daily variability. . . . .	154
9.9	The $F_{var}$ and $F_{pp}$ in two weeks' scale. Note that the two weeks (14 days) are counted from the first observational day of this period. . . . .	154
9.10	$F_{var}$ and $F_{pp}$ in a monthly (28 days) scale. Note that the 28 days are counted from the first observational day of this period; therefore, the monthly average is not counted as in our daily calendar. . . . .	155
9.11	$F_{var}$ in four different time scales in different periods of data. $F_{var}$ is closer to the value 0.4, once the time scale is longer than one month, the errors are smaller if we consider longer time scales. . . . .	156
9.12	$F_{var}$ and $F_{pp}$ vs average integrated flux (above 300 GeV) in a two weeks, (14 days) scale. Note that the 14 days are counted from the first observational day of this period; therefore, the two weeks average is not necessary counted from Monday. . . . .	157
9.13	$F_{var}$ and $F_{pp}$ versus average integrated flux (above 300 GeV) in a monthly (28 days) scale. Note that the 28 days are counted from the first observational day of this period; therefore, the monthly average is not counted like in our daily calendar. . . . .	158
9.14	The ratio between $F_{var}$ and $F_{pp}$ in two different time scales, daily and monthly (28 days). Note that from the daily scale, $F_{var}$ is the similar to $F_{pp}$ , however, in longer time scale, $F_{var}$ is always larger than $F_{pp}$ , which hints at Mrk421 showing bigger variabilities in the longer time scale during this period. . . . .	158
9.15	The figure shows the $\sigma$ -flux relation in the TeV band using the MAGIC P5 data. Each point represents a measurement over one day. For each daily measurement, we use 30 minutes lightcurves to calculate the mean flux and $\sigma$ . The correlation coefficient between $\sigma$ and average flux is $0.39 + 0.16 - 0.19$ . and the significance is $2\sigma$ away from 0. . . . .	159

9.16	The excess r.m.s. versus average fluxes for the segments of lightcurve of different time durations. The data and plots are from AGN PKS2155 from H.E.S.S. observation [16]. The plot on the left-hand side has 20 minutes duration. The sampling rate is 1 minutes. The plot on the right-hand side shows the duration of 80 minutes and sampling rate of every 4 minutes. . . . .	160
9.17	Left: The structure function of the ASM data from Mrk421. Right: The structure function of the TeV data from Mrk421. . . . .	161
9.18	The structure function of the ASCA data from three bright blazars: Mrk501, PKS2155-304, Mrk421. All the data are from ASCA monitoring. Mrk501, PKS2155-304 were observed continuously for 10 days in 2000. Mrk421 was observed for 7 days in 1998. . . . .	162
9.19	The correlation coefficient. against different time lags. The plot shows the results of auto-correlated function. The inputs are two identical Mrk421 30 minutes lightcurves from P5 data. We selected the data points with more than 10 data pairs after the time delay. Thus, after the selection cut, there is a neutrino data point between 10-day to 20-day delays. The time resolution for the correlation scan is 6 hours. . . . .	163
9.20	Left : The correlation between ASM X-ray flux and TeV $\gamma$ flux with different time lags. The X-ray data are from ASM dwell based data. The time searching window is 6 hours every step. Right : The significance between ASM X-ray flux and TeV $\gamma$ flux correlations with different time lags. The X-ray data are from ASM dwell based data. The time searching window is 6 hours every step. . . . .	164
9.21	The joint lightcurve of MAGIC and VERITAS in June 2008. The combined lightcurve shows that Mrk421 was about 1 C.U. around MJD 54618 and then within 4-5 days, the flux went up to about 4 C.U. around MJD 54622. Afterwards, the flux started to decrease. It is unfortunate that AGILE did not observe during this period. . . . .	165
9.22	Left plot: Mrk421 June flare MAGIC daily lightcurves. The integrated flux is above 300 GeV. Right plot: X-ray and TeV flux diagram. The marker from 1 to 5 represents the time evolution of the source flux in this plane. The X-ray and TeV flux show a high correlation coefficient of $r = 0.75+0.18-0.49$ . . . . .	166
9.23	Time evolution of the Mrk421 June flare on the so-called (F,h) plane. Each point of the plot is the daily averaged lightcurve. Note that the time evolution of Mrk421 on the June flare is very likely following the counterwise rotation in the plane. . . . .	167
9.24	The SED of Mrk421 calculated by combining the data from GASP-WEBT, Swift/UVOT, RXTE/ASM,XRT, SuperAGILE, BAT,GRID and VERITAS data in the first period and the second period. Both of them could be fitted well with one zone SSC models [17]. . . . .	168
9.25	The hardness ratio calculated from three lightcurves with different threshold energies. The red points are the ratio between a daily integrated flux above 350 GeV and 200GeV. The black points are the a daily integrated flux above 300 GeV and 200 GeV. . . . .	169

---

9.26	The hardness ratio of three different threshold energies versus different daily average flux. The left figure is the ratio between a daily integrated flux above 350 GeV and 200 GeV in C.U.. The right figure is the ratio between daily integrated flux above 300 GeV and 200 GeV, also both in C.U. A few nights show big error bars simply because of the short observation time. . . . .	170
9.27	The probability of spectra fitted with a simple power law (PL) and a simple power law with an exponential cut-off (PL+CutOff). The left panel shows the spectra before EBL de-absorption and the right panel shows the spectra after EBL de-absorption. few nights spectra show much better fitting with PL+CutOff. . . . .	171
9.28	The fitted photon index of the spectra versus the integrated flux ( $\geq 300\text{GeV}$ ) before and after EBL de-absorption and subsequent fitting with a simple power law. . . . .	171
9.29	Mrk421 High Flux days in P5. . . . .	175
9.30	Flare fit in the night of 6 February. The lightcurve is above 400 GeV. The red curve shows the fitting with two flares, the black curve shows the fitting with only one giant flare. . . . .	176
9.31	The hardness ratio of 2 different energy thresholds in the night of 6 February. . . . .	176
9.32	Left: The hardness ratio versus flux level in the 10 minutes timing bin in the night of 6 February. Right: The hardness versus flux level using 10 minutes timing bin on 31 March. The flux is above 200 GeV. From the plot, the hardness of the spectrum is almost constant throughout the night. . . . .	177
9.33	The 8 min lightcurve for Mrk421 on 31 March 2008. The lightcurves are above 200 GeV, 300GeV and 400 GeV. . . . .	178
9.34	Lightcurve of 31 March fitted with different flare models. The upper one is fitted with a giant big flare. The bottom plot is fitted with two consecutive flares with different rising and falling times. . . . .	179
9.35	The flare analysis for Mrk421 on 31 March. The lightcurve is above 400 GeV. . . . .	180
9.36	The upper two panels are the lightcurves of Mrk421 and the background control plot above 300 GeV on 15 January. The bottom two panels are the lightcurves and the background control plot above 300GeV on 11 February. . . . .	181
9.37	The spectra of Mrk421 at the two high flux nights with 7 other different flux states. The upper panel, the differential spectra are fitted with a pure power law, PL. In the lower panel, they are fitted with a power law plus exponential cutoff, PL+Cutoff. Note that the spectra here are without EBL de-absorption. . . . .	185
9.38	The spectrum of Mrk421 at two high flux nights with 7 other different flux states. In the upper panel, the differential spectra are fitted with a pure power law, PL. In the lower panel, they are fitted with a power law plus exponential cutoff (PL+Cutoff). Note that the spectra already contain the EBL de-absorption. . . . .	186
10.1	The MAGIC daily lightcurve of Mrk421 from 2005 to 2008. The threshold energy is above 300 GeV. . . . .	189

---

10.2 The Mrk421 daily lightcurves from 2005 to 2008 in different energy bands. The upper one : Daily integrated flux above 350 GeV. The black points are from the Whipple ONLINE analysis and the blue points are from MAGIC. The middle: Daily average of ASM sum band data. The bottom: The KVA R band daily lightcurve. Note that the observations of the KVA telescope were almost overlapping with MAGIC. . . . .	190
10.3 The daily variability $F_{var}$ from 2005 to 2008, using 10 minutes flux bins. . . . .	193
10.4 The monthly and bi-monthly variability $F_{var}$ from 2005 to 2008, using 10 minutes flux bins. . . . .	197
10.5 The monthly and bi-monthly variability $F_{var}$ versus monthly and bi-monthly average integrated flux from 2005 to 2008, using 10 minutes flux bins. . . . .	198
10.6 The bi-weekly and bi-monthly ratio of the values $F_{var}$ and $F_{pp}$ . If the timescale is longer, the ratio between these two values becomes larger. The emission is more red-noise like. . . . .	198
10.7 The values of the ratio $r = F_{var}/F_{pp}$ in 4 different timescales, daily, weekly, monthly and bi-monthly. The value $r$ in each timescale is derived from being fitted with a Gaussian distribution and $\sigma$ is considered to be the error. If the timescale is longer, the ratio between these two values becomes close to 2, meaning it is more red-noise like. . . . .	199
10.8 The X-ray (ASM) and TeV observations (MAGIC) correlations, from 2006 to 2008 data. In order to know how big the significance is, we randomize the pairs of X-ray/TeV observations and then calculate the Pearson's correlation coefficient. The randomized pairs have a significance distribution peak at zero, which is expected. The significance number 0.75 could be derived from the distribution and the number is about $8\sigma$ effects. . . . .	202
10.9 The X-ray TeV correlation with an estimation of statistical errors. Most of the points are within $2\sigma$ , which means that they have good correlations. Note that it is not easy to estimate the systematics errors of this correlation calculation, because the time tolerance is 6 hours. . . . .	203
10.10 The optical R-band (KVA) and TeV observations (MAGIC) correlations, from 2006 to 2008 data. Different colors of the markers show data pairs in different time periods. The Pearson's correlation coefficient is about $0.02 \pm 0.14$ . In order to know how big the significance is, we randomize the pairs of optical/TeV observations and then calculate the Pearson's correlation coefficient. The randomized pairs have a significance distribution peak at zero, which is expected. The significance can be estimated from the distribution, and the probability to obtain such number is about 10%, which is completely randomized. . . . .	204
10.11 The Mrk421 spectrum in different states using different instruments. . . . .	206

10.12 The inverse Compton peak of the Mrk421 spectrum from historical results. The peak energy $E_p$ is calculated according to the text. Right plot: Relation between the flux state at 1 TeV (determined from a power law fitting of the spectra between 700 GeV and 4 TeV) and the fitted photon index. A correlation between the flux and photon index can be seen. Note that in the plot, we added MAGIC crab points and also other Whipple measurements inside. . . . .	207
10.13 The $(\log B, \log \delta)$ plane. The calculation is based on the multiwavelength observations assuming different time variation scales $t_{var}$ . A, B, C, and D are estimated by the conditions in Eq.10.5, Eq.10.6, Eq.10.7 (Eq.10.8) and Eq.10.9, respectively. The region marked by S is the allowed region. . . . .	208
10.14 The $(\log B, \log \delta)$ plane. The calculation is based on the multiwavelength observations assuming two different time variation scales $t_{var}$ , 1 day and 1 hour. A, B, C, and D are estimated by the conditions in Eq.10.5, Eq.10.6, Eq.10.7 (Eq.10.8) and Eq.10.9, respectively. The region marked by S is the allowed region. . . . .	209
10.15 The TeV state probability. These two plots are fitted by the exponential formula described in the text. Note that the fitting starts from appr. 1 C.U. . . . .	212
10.16 The TeV state probability. The distribution is fitted with a simple power law. Note that the fitting starts from appr. 1 C.U. . . . .	213
A.1 The plot shows the hadron rate against $zd$ from per Crab data run. The red line is fitted with the formula $R = R_0 * (\cos\theta)^{0.85}$ . The SIZE cut with 100 ph.e. was applied. . . . .	ii
A.2 The plot shows the Crab lightcurve from December 2005 to April 2006. Only the data taken in Wobble mode and with low zenith angles ( $\leq 30^\circ$ ) are shown here. . . . .	iii
A.3 The plot shows the re-fitting results after excluding the bad points from the first fitting. $\chi^2$ per degree of freedom both on the background and signal from three Crab nights in the P1 period are shown. . . . .	iv
A.4 The SED of the $\gamma$ -ray emission from the Crab Nebula. The lower energy part ( $\leq 10$ GeV) is from EGRET. At energies above 400 GeV, all measurements are fitted quite well with a simple power law. The dashed curve is a model predicted by [18]. . . . .	iv
A.5 The figures show the Crab spectrum from period P1. Two days of Crab data are shown. The results are superimposed with the MAGIC published spectrum. . . . .	v
A.6 The plots show the hadron rate of individual runs as a function of zenith angle after the SIZE cut 200 ph.e.. Left and right pictures are before and after the cut, respectively. The red line is the curve with the formula $R = R_0 * \cos(\theta)^{0.85}$ . The data are from September 2006 to January 2007, i.e. period P3. . . . .	vii
A.7 The daily lightcurve of the Crab above 300 GeV in period P3. . . . .	viii
A.8 The figure shows the $\chi^2$ values for background and signal light curves of period P3 Crab data, assuming constant fluxes in both cases. The $\chi^2$ is calculated after binning data in 10 minutes' bins. The $\chi^2/d.o.f$ are the results from excluding the bad points (background fluctuates more than $5\sigma$ away from the average) and subsequent refitting. . . . .	ix

---

A.9	The figure shows the gamma ray flux distribution of Crab for every 10 minutes-bin. Data were taken from September 2006 to January 2007 in period P3. Bad data showing large deviations in the background event rate are excluded. . . . .	ix
A.10	The Crab spectrum from P4 data. Spectra of three different days are superimposed with the MAGIC published spectrum. . . . .	x
A.11	The plots show the Crab data from February 2007 to June 2007 (period P4), hadron rate vs zd per data run before and after the hadron rate cut. The red line is based on the formula $R = R_0 * \cos(\theta)^{0.85}$ . . . . .	xi
A.12	The plot shows the daily lightcurve of Crab data from February 2007 to June 2007. . . . .	xi
A.13	The Crab data from February 2007 to June 2007 (period P4). The $\chi^2/\text{d.o.f.}$ distribution of the signal and background. . . . .	xii
A.14	The Crab spectrum from P3 data. Crab spectra from three different days are superimposed with the MAGIC published one. . . . .	xii
A.15	Crab dark night data (zenith angle less than 28 degrees). The left figure shows the hadron rate as a function of cloudiness. The right figure shows the gamma ray reconstructed integral flux above 300GeV as a function of cloudiness. Both hadron rate and integrated flux decrease with higher cloudiness. We decided to cut out the data with a cloudiness larger than 25. . . . .	xiii
A.16	Crab data taken from December 2007 to January 2008. Only the Crab data taken during dark nights are shown. The zenith angle is up to 45 degrees. Depending on the SIZE cut (energy threshold), the hadron rate changes with different powers of zenith angle. The larger the SIZE cut, the larger the power of the cosine dependent. . . . .	xv
A.17	From December 2007 to January 2008, the hadron rate of the Crab dark night data for different zenith angles up to 45 degrees. The hadron rate could be formulated with $R=R_0 * \cos^{p_0}(\theta)$ , the power $p_0$ depends on different SIZE cuts (energy threshold). The fitting parameters $p_0$ are shown in Table A.6 . . . . .	xix
A.18	The left plot: Crab moon night data from October 2007 to March 2008. Note that the upper MAGIC line is from the Crab data in period P5, which has been analyzed in this thesis. The lower MAGIC line is from the MAGIC published Crab paper. The right plot: From December 2007 to March 2008 Crab twilight observation for lower zenith angles ( $\leq 28\text{deg}$ ). The expected Crab integrated flux is given by measurements from two different groups. Note that the upper MAGIC line is from the Crab data in the period P5, which I has been analyzed in this thesis. The lower MAGIC line is from the MAGIC published Crab paper. . . . .	xx
A.19	The upper panel: Crab dark night data from December 2007 to March 2008: The black line is the fitted flux from the observed data. Crab fluxes from two independent groups are presented. Note all the data shown here are after the selection cuts. The bottom panel: Crab dark night daily flux from December 2007 to March 2008. The mean flux above 300 GeV is about $1.44 \times 10^{10} \text{ cm}^{-2}\text{s}^{-1}$ , with small RMS $1.15 \times 10^{11} \text{ cm}^{-2}\text{s}^{-1}$ for 21 data sets in total. The RMS value is less than 10% of the mean value. . . . .	xxi

A.20 Histograms of Crab flux in P5, with 5 minutes (the upper) and 10 minutes (the bottom) timing bins are shown. . . . .	xxii
A.21 The scatter plot of the $\chi^2$ distributions of the background and the signal lightcurves using 5 minutes timing bins. . . . .	xxiii

# List of Tables

1.1	Extra-galactic TeV $\gamma$ sources until May 2010. . . . .	17
2.1	Wide range spectrum of AGNs could be explained by the emission from different components. . . . .	26
2.2	The table shows the unification model of AGNs adapted from Urry and Padovani (1995) [19]. QSO: Qusi-Stellar-Object. NLRG: Narrow Line Radio Galaxy. BLRG: Broad Line Radio Galaxy. FSRQ: Flat Spectrum Radio Quasar. SSRQ: Step Spectrum Radio Quasar. FR: Fanaroff-Riley . . . . .	28
3.1	The list of currently operated IACTs with two selected older generation IACTs, HEGRA and CAT. The table is adapted from [20] . . . . .	48
5.1	Transmission as a function of wavelength $\lambda$ for many different glasses used as PMT input windows. The cut-off wavelength is the wavelength where the light transmittance is decreasing to only 10% of the coming value. . . . .	65
5.2	Different configurations of Winston cones designed by MPI. The cutting angle is calculated by the formula: $\theta = \sin^{-1}(\frac{a'}{a})$ . Since the entrance window could be hexagonal, the size of their radius is estimated by the radius of the inner circle and the outer circle. . . . .	77
5.3	The fitting parameters for different configurations of the Winston cone. . . . .	80
5.4	Results of different configurations of Winston cones: Count the single photo-electron events. . . . .	83
5.5	The efficiency of different configurations of Winston cones after integrating the area of the reflector at different angles. . . . .	84
7.1	Several historical multiwavelength observations of Mrk421. Observations which at least include one IACT are listed. . . . .	106
7.2	High state triggers due to MAGIC ONLINE analysis . . . . .	109
7.3	Major Hardware and software changes of the MAGIC Telescope from 2004-2008	111
7.4	Classifies the Mrk421 Data taken in 2004-2008 into 6 different periods. Note that Mrk421 is visible from October to next June at the La Palma Site. . . . .	113
7.5	Summary of the different instruments from different energy bands whose data were used in this thesis. . . . .	120

---

7.6	Mrk421 observed by MAGIC Telescope from December 2005 to January 2006, period P1. . . . .	126
7.7	Mrk421 observed by the MAGIC Telescope and ASM from December 2005 to January 2006 (i.e.:P1). The variability and point to point variability of the measurements are listed. Note that for calculating $F_{var}$ and $F_{pp}$ , a 10 minutes lightcurve is used instead of a daily lightcurve. Therefore, each data point has equal observation of about 10 minutes. . . . .	128
7.8	The fitting parameters for the spectrum of Mrk421 data in P1. All the spectra are fitted with a pure power law $dF/dE = f_0 \cdot (E/E_0)^\alpha$ with $E_0 = 300$ GeV. The normalization factor $f_0$ is given in units of $10^{-9} \text{ cm}^{-2} \text{s}^{-1}$ . . . . .	129
7.9	The fitting parameters for the spectrum of Mrk421 data in P1. All the spectra are fitted with a simple power law plus exponential cutoff. $dF/dE = f_0 \cdot (E/E_0)^\alpha e^{E/E_c}$ with $E_0 = 300$ GeV. The normalization factor $f_0$ is given in units of $10^{-9} \text{ cm}^{-2} \text{s}^{-1}$ . $E_c$ is the cutoff energy. . . . .	129
8.1	The Mrk421 data which were taken from April 2006 to January 2007, (periods P2 and P3), i.e. just before installation of the MUX FADCs. . . . .	135
8.2	The spectrum fitting parameters of Mrk421 data in P2, P3 and P4. All the spectra are fitted with a pure power law $dF/dE = f_0 \cdot (E/E_0)^\alpha$ with $E_0 = 300$ GeV. The normalization factor $f_0$ is given in units of $10^{-9} \text{ cm}^{-2} \text{s}^{-1}$ . . . . .	141
9.1	Mrk421 data used in the final analysis, from December 2007 to January 2008. The data shown here are already after the data selection and quality cuts. . . . .	143
9.2	Mrk421 Data used in the final analysis, from February 2008 to June 2008. The data shown here are those after data selection and quality cuts. . . . .	144
9.3	The data from the nights which showed $2\sigma$ away from constant flux values. The $\chi^2$ fitting using an integrated flux above 300GeV 10 minutes lightcurve. These nights may give hints about intra-night variability. . . . .	145
9.4	Mrk421 data taken from December 2007 to June 2008. The data are calculated by using 10 minutes lightcurves. . . . .	151
9.5	Results on the fitting parameters in the night of 6 February 2008. The first row assumes that there was only one big flare in the plot. The second and third rows assume there were two flares in that particular night but with different rising and falling times. . . . .	173
9.6	Results of the fitting parameters in the night of 31 March 2008. The first row assumes that there was only one big flare. The second and third rows assume that there were two flares in that particular night but with different rising and falling times. . . . .	174
9.7	The spectra fitting for 9 different flux levels in period P5, using a pure power law. The fitting function has the formula : $dF/dE = f_0 (E/r)^\alpha$ . $r$ is chosen to be 0.3 TeV. $f_0$ has the unit $10^{-8} \text{ cm}^{-2} \text{s}^{-1} \text{TeV}^{-1}$ . Note that these spectra are the measured ones, i.e. before EBL de-absorption. . . . .	182

9.8	The spectra fitting for 9 different flux states in this period, using a power law plus exponential cutoff. The formula is $dF/dE = f_0 (E/r)^\alpha \exp(-E/E_\alpha)$ . r is chosen to be fixed at 0.3 TeV. $f_0$ has the unit $10^{-8} \text{ cm}^{-2} \text{s}^{-1} \text{TeV}^{-1}$ . Note that this spectrum is the observed one, i.e. without EBL de-absorption. . . . .	183
9.9	The spectrum fitting for several different flux nights in this period, using a power law. The formula is $dF/dE = f_0 (E/r)^\alpha$ . Note that this spectrum is after EBL de-absorption. The EBL de-absorption is adapted from Raue and Mazin 2007. . . . .	184
9.10	The spectrum fitting for 9 different flux states in this period, using a power law plus exponential cutoff. The formula reads $dF/dE = f_0 (E/r)^\alpha \exp(-E/E_\alpha)$ . Note that these spectra already contain the EBL de-absorption. . . . .	184
9.11	The simultaneous data sets of MAGIC and Swift-XRT observations in P5 [21]. In total, there were 8 nights, 145 minutes of overlapping time slots. . . . .	187
9.12	The fitted spectra (without de-absorption) of the 8 overlapping days' observations. The spectra are all fitted with power law with variable power indexes, where power index $\alpha = a + b * \log_{10}(E/r)$ . The table is from [21]. . . . .	187
9.13	SED fit with a one zone SSC model in 8 nights of simultaneous observation performed by MAGIC and Swift-XRT in P5 [21]. The $\gamma_{min}$ , $\gamma_{max}$ and $\gamma_b$ are minimum, maximum and break energies of the electron spectrum. $n_1$ and $n_2$ are the two slopes of the electron energy spectrum. K is the electron density. B is the magnetic field, R is the size of the emission region and $\delta$ is the Doppler factor. This table is from [21]. . . . .	188
10.1	Different AGNs show different variabilities in different time scales. . . . .	192
A.1	Crab data observed by the MAGIC Telescope from December 2005 to April 2006. Only Wobble data were selected. All the data have zenith angles lower than 30deg. . . . .	i
A.2	The Crab Spectrum observed by different IACT groups. The data are from DESY, multi-messenger webpage [22]. . . . .	iii
A.3	The Crab data taken from September 2006 to January 2007. Here, only the data with zenith angles of less than 46° are counted. . . . .	vi
A.4	Crab data taken in period P4 (February 2007 to March 2007). We selected eight days' data with low zenith angles ( $\leq 46^\circ$ ) and excluded the data which did not pass the quality check. In the end, 11.7 hours of good data were left. . . . .	x
A.5	Crab data in P5 which were used in the final analysis after all quality cuts. . . . .	xiv
A.6	The hadron rate vs different zenith angles. With a higher SIZE cut, the fitting slope changes. The data were taken during December 2007 and January 2008. . . . .	xv
A.7	P5 Crab data taken under the moon conditions. . . . .	xvii
A.8	Crab Data from twilight conditions within this period. . . . .	xvii

A.9	Crab data was taken from December 2007 to January 2008. The $F_{var}$ variability and $F_{pp}$ are calculated. The negative value of $F_{var}$ shows that the average intrinsic variability is much smaller than the measurement errors. The results are expected since Crab is a steady source. The $F_{pp}$ is calculated by using the daily timing bins. . . . .	xviii
-----	---	-------

# Introduction - This Thesis

Compared with optical astrophysics, whose foundations can be traced back to prehistoric times, the field of high energy astrophysics is a relatively new field of science, dealing with extreme and violent astrophysical objects and conditions. Not even one single celestial object is hot and stable enough to thermally emit very high energy (VHE)  $\geq 100\text{GeV}$  photons. High energy radiations must be produced non-thermally. The high energy phenomena were discovered with the development of instrumental techniques. From the first discovery of a brightest X-ray source, Sco X-1 by the X-ray rocket in 1962, within only thirty years, the ROSAT satellite dramatically increased the number of discovered sources up to 150,000 at 0.1-2.5 keV. Very soon, right after ROSAT, the Compton Gamma Ray Observatory (CGRO) opened a new  $\gamma$ -ray window stretching our vision capability up to 30 GeV. Furthermore, in the past 20 years, ground-based Imaging Atmosphere Cherenkov Telescopes (IACTs) have imaged the sky at TeV energies with unprecedented spatial and temporal clarity.

It is known that our Earth is constantly bombarded by continuous flux of high energy particles from outer space. Their compositions mainly consist of positively charged nuclei and a few electrons, positrons, photons and a still unknown flux of neutrinos. Although these tiny particles have been known since the beginning of the 20th century, their origins and sources still remain puzzles and have not yet been unambiguously identified. The irregularly distributed interstellar magnetic fields are one of the major difficulties, as they destroy the direction information of the arriving charged particles. Only neutral particles give direct information about their origin. Therefore, in order to study the sources and acceleration of these charged cosmic rays, one has to observe our universe with neutral high energy particles, for example VHE  $\gamma$ -rays.

Up to now, VHE  $\gamma$ -ray emissions from active galactic nuclei (AGN), supernova remnants, pulsar wind nebulae, X-ray binaries and star burst galaxies have been found. A particularly interesting object for a cosmic ray acceleration site are the active galactic nuclei (AGN). At the center of an AGN, there is a super massive black hole of above  $10^6 M_\odot$ , which is believed to be the engine of a huge energy output. Blazars are a subclass of AGNs, which usually have bipolar jets, one of which is pointing towards us. So far, about 30 AGNs have been recognized as TeV  $\gamma$ -ray emitters or sources, and 27 among them are blazars.

Markarian 421 (Mrk421) is the first established extra-galactic TeV source, and it is a blazar with a companion elliptical satellite galaxy. It is well known for its variabilities in different time scales and energy bands. In addition, it is one of the most studied TeV blazars. Several multiwavelength campaigns have been organized for observing it since it was first discovered as a TeV emitter. However, the currently existing data are still not enough for distinguishing

between different Very High Energy (VHE) radiation emission models.

MAGIC, compared with other ground-based IACTs like CANGAROO, H.E.S.S and VERITAS, explores the northern very high energy sky, but with a lower energy threshold of 60 GeV and up to about 30 TeV. Since operation started in 2004, it has successfully detected TeV  $\gamma$ -rays from Mrk421. There was a simultaneous observation with the H.E.S.S. collaboration on this particular source at the end of 2004, which helped cross calibration between two instruments and covered an unprecedented wider energy spectrum in the VHE regime. Starting from 2006, Mrk421 has been selected to be a regularly monitored bright blazars in the MAGIC monitoring program. The planned observation schedule is 40 observational slots evenly distributed in one MAGIC observation cycle. Each time slot is about 30 minutes. Self-triggered MAGIC or externally triggered extended observations outside MAGIC are possible if it is in high flux state.

In this thesis, I want to determine the relatively long-term behavior of this particular source and also to constrain the emission models from its short time variability. The final goal is to obtain a better understanding of the AGN jets. It is important to have regular, long-time and unbiased high quality TeV monitoring data with very good sensitivity at a very short time (few minutes) scale. High quality multiwavelength data will help the modeling as well. The spectral modeling of the multiwavelength data helps to identify the physical process at the source. This thesis describes the detailed study on long term observations with the MAGIC telescope on this famous extra-galactic TeV  $\gamma$  source, Markarian 421, using the data from 2005 to 2008. The contents is organized as follows:

- In chapter 1, I will give a brief introduction on the current status of VHE  $\gamma$ -ray astrophysics. Up-to-date discovered TeV  $\gamma$ -ray sources, different source categories/types are reviewed and the relation between cosmic ray and TeV  $\gamma$ -ray is discussed. Special interest will be paid to understanding the Fermi particle acceleration mechanisms in the astrophysics objects.
- In Chapter 2, Active Galactic Nuclei (AGN), a class of extra-galactic TeV emitters, which is also the main topic of this thesis, are discussed. BL Lac objects are a subclass of AGNs and are of particular interest. I will discuss different models which explain multiwavelength non-thermal emissions from radio to TeV regimes. Special emphasis is given to the description of the favored model - the Synchrotron Self-Compton (SSC) model. Several important characteristics of AGN in VHE  $\gamma$ -ray emissions, such as short time variability, and cross wavebands correlations will be outlined and possible explanation under the SSC framework will be given.
- Chapter 3 describes the detection principle of Imaging Air shower Cherenkov Telescopes, (IACT). The development of Extended Air Showers (EAS) in the Earth atmosphere and the consequent emission of the Cherenkov light will be explained.
- In Chapter 4, the main hardware components of the MAGIC telescope will be described with the main focus on the imaging pixel camera. This camera is equipped with high QE pixels and an ultra fast FADC readout system. A few special and unique hardware features will be discussed.

- In chapter 5, I will discuss the photonsensors for the second MAGIC telescope (M-II) and their performances. I will explain how the different characteristics of these photonsensors will eventually affect the performance of our telescopes.
- Chapter 6 gives an overview of the standard analysis chain for MAGIC data and the necessary analysis tools for this thesis work. I will describe how important physics quantities are derived and calculated, such as effective area and energy spectrum.
- In Chapter 7, the main target source of this thesis work, Markarian 421 (Mrk421) is introduced. I will give a brief review on several important historic observations and what we have learned about this source in the TeV- $\gamma$  ray domain in the past 17 years. Subsequently, the results from analyzing the MAGIC Mrk421 data taken in 2005 will be presented. In addition, several analysis tools will be introduced such as multiwavelength correlations, variability strength... etc.
- Chapter 8 deals with the Mrk421 data obtained from 2006 to 2007. Data selection rules will be outlined in relation to the data taken under various conditions. The method of systematically searching for a short time TeV variability will be introduced.
- Mrk421 was intensively observed by MAGIC from the end of 2007 to June 2008 because of repeated high intensity flaring activity. A spectral and temporal analysis of around 45 observation nights was performed. Two nights with high fluxes are particularly emphasized. Thanks to the high sensitivity of the MAGIC telescope, one night shows a hint of intra-night variability (INV), and the doubling time is down to 20 minutes. The spectral evolution in this observation period was clearly seen. Due to the intensive and long observation time, those high quality data gives us the possibility to use temporal analysis in the TeV domain. The flux variability in different time scales from one day to a few months was derived.
- The final chapter summarizes all results from the previous chapters. Long term lightcurves and spectra from 2005 to 2008 are discussed. A long term correlation study on TeV emissions and multiwavelength data is presented. Possible explanations of the correlations are discussed in different TeV  $\gamma$ -ray emission models. The physics constraints on short time variabilities are also discussed. From the three years of high statistics data, the probability distribution of different TeV flux states is derived.
- The concluding short chapter comments on all the observational facts from Mrk421 MAGIC data taken from 2005 to 2008. Several key results of this thesis are summarized. Together with 17 years of historical observations from different experiments, I draw the conclusion that the TeV gamma ray emission from Mrk421 is dominated by the inverse Compton component due to  $e^-/e^+$  high energy particles in the jet instead of high energy protons dominant in jets.

# Acknowledgement

First and foremost, I would like to thank my thesis advisors, Prof. Dr. C. Kieseling and Prof. Dr. M. Teshima, for accepting me as a PhD student in the Max-Planck-Institut (MPI) für Physik working in the MAGIC collaboration. Thanks for their patience and helping me to grow into a much better scientist during my PhD career. I profited very much from this exciting and blooming field of astrophysics. In addition, I would like to express my gratitude towards Dr. R. Mirzoyan and Dr. E. Lorenz for many inspired discussions on photonsensors, physics and, like Asian wise elder men, sharing their invaluable experiences.

I have greatly enjoyed working in the MPI MAGIC group (both current and former members): Thanks to everybody for many discussions, book-readings, lunches, BBQ and gossip time. I want to thank to P. Majumdar, R.M. Wagner, D. Mazin, D. Paneque, E. Carmona, M. Hayashida, T. Schweizer, T. Saito, J. Sitarek, B. Steinke, D. B. Tridon, D. Britzger, M. Shayduk, P. Colin, N. Otte, T. Jogler, H. Bartko, H. Miyamoto, R. Orito M. Fuchs. and M. Garczarczyk. Special thanks to P. Majumdar, R.M. Wagner, J. Sitarek and D. Mazin for discussing about the analysis and AGN physics. Of course, thanks also to D. Paneque and M. Hayashida for their conveying of legendary "shaking" PMT-coating techniques.

Many thanks to MPI electronics and workshop members: O. Reimann, J. Hose, D. Fink and T. Engelhardt. J. Hose and D. Fink helped me a lot on the photonsensor measurements.

I would like to thank all the members of the MAGIC collaboration who have shared many happy times with me and all the VHE  $\gamma$  colleagues from other groups. The communications with F. Tavecchio, W. Bednarek and A. Stamerra are greatly acknowledged. Moreover, I will never forget the friendship with M. Errando, G. Bonnoli. A. Moralejo, N. Tonello, R. Zanin, E. Bernardini and K. Satalecka. Specially thanks to R. Zanin and A. Moralejo for their nice work on MAGIC ONLINE analysis and G. Bonnoli for providing Mrk421 2008 MWL campaign SED data. Last but not least, it was a pleasure to work with K. Satalecka on the AGN monitoring program; thanks also to E. Bernardini for providing me the chance to work in DESY Zeuthen for three months.

I would like to express my deeply appreciations and tribute to F. Goebel who was the PI of the MAGIC AGN monitoring program. He followed my thesis work since I joined MAGIC. His valuable insights on physics and passion of life have created a good example and always encouraged young people inside the collaboration.

I shared a lot of joy with the people in MPI Chinese group. Our weekly discussions on many different fields of physics and political issues about "China" and "Taiwan" made life more interesting. I will always remember our happy times.

This thesis would not have been finalized without S. Rodriguez Schneider. I would like to show my great gratitude to her. Her patience and really professional physics English corrections speeded up the thesis progress and sharpened the whole thesis contents.

With all my heart, I would like to thank my parents for their endless encouragement and support of my scientific career. I can imagine that my late beloved father would be happy if he could have seen the completion of this thesis. I am indebted to my lovely wife Min-Li Wang, who always supported me during this period. Her countless encouragement is the greatest power engine to push me further. This thesis is dedicated to her.

# Chapter 1

## High Energy Astrophysics with Gamma Rays

### 1.1 Multi-messenger Universe

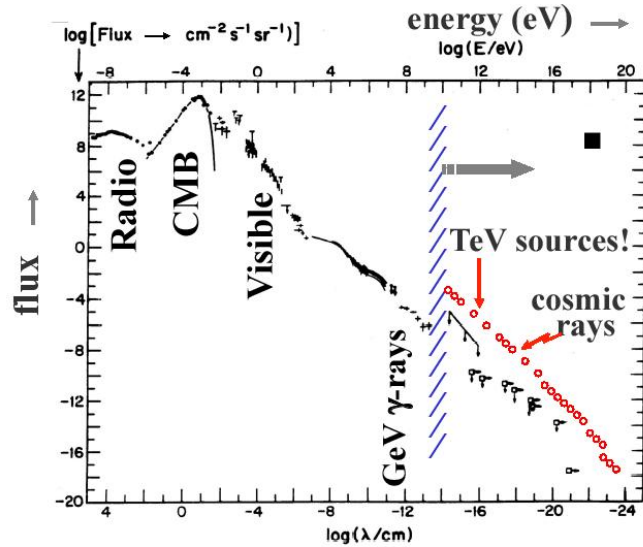


Figure 1.1: The cosmic diffuse photon flux from different energy bands. The plot is from [2]

The sky presents itself in various appearances through different cosmic messengers, such as photons, neutrinos, cosmic rays (proton, nuclei, electron) and gravitational waves. Among these messengers, photons are so far the most studied ones. In the whole photon spectrum,  $\gamma$ -rays possess the highest energy, having the strongest ability to penetrate normal materials. Due to the absorption of  $\gamma$ -rays in the atmosphere, the development of  $\gamma$ -ray astrophysics is relatively late compared to that of longer wavelengths. In 1960s, scientists finally developed the capability

to detect  $\gamma$  emissions from the sky. Gamma rays and Very High Energy (VHE) gamma rays ( $\geq 30\text{GeV}$ ) carry information about high energy phenomena in the Universe, for instance, Supernovae, Pulsars, Active Galactic Nuclei (AGNs) and Gamma Ray Bursts (GRBs). They could be produced as secondary particles at sources, via, interaction of cosmic rays and high energy electrons with ambient gas and a photon fields. On the other hand,  $\gamma$ -ray productions may also be concerned with more fundamental processes in the Universe, such as dark matter annihilation and decay. GeV gamma rays are usually measured by space-borne detectors. However, VHE gamma rays can be measured by ground-based Imaging Atmospheric Cherenkov Telescopes (IACTs). The main topic of this thesis is to study of VHE gamma rays coming from AGNs using IACT techniques.

## 1.2 Cosmic Rays

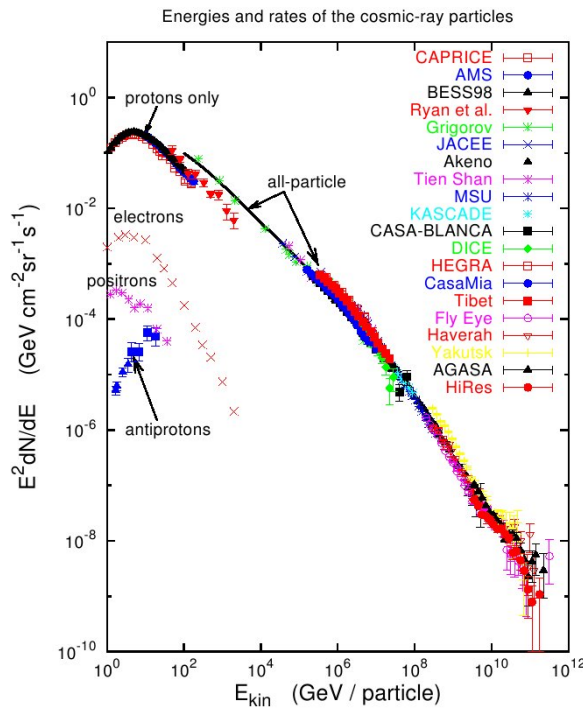


Figure 1.2: The cosmic ray spectrum from 1 GeV up to higher than  $10^{11}$  GeV. The cosmic rays with energies lower than 1 GeV will be mostly blocked by the solar magnetic wind such that they will not enter the solar system. The slope of the power spectrum begins at -2.7 and changes to a steeper spectrum of -3.1 around  $3 \times 10^6$  GeV, the so-called knee region. Up to the second knee region, which is around  $4 \times 10^8$  GeV, the spectrum becomes softer to -3.3. At the so-called ankle region, the spectrum seems to flatten to a spectral index of about -2.7 again. The vertical axis is set with the unit:  $E^2 dN/dE$ . This plot is taken from [3]

Scientists have observed the ionization of the air in early 1900 after the discovery of radioactivity by Henri Becquerel in 1896. At the beginning, people thought the ionization was due to the radiation isotopes on the ground. Later, in 1912, Victor Hess, based on previous studies, found that high energy radiations are actually coming from outer space. Fig. 1.2 shows the current measured cosmic ray energy spectrum. Note the unit on the vertical axis is multiplied by  $E^2$ . The cosmic ray flux drops sharply at higher energies. The very low energy cosmic rays ( $\leq 1$  GeV) are blocked by the solar wind. Energies with slightly higher values ( $\geq 1$  GeV but  $\leq 15$  GeV) are modulated by the solar magnetic field. Due to the solar activities of 22 years, the flux of GeV cosmic rays which we measured is also correlated with cycles of solar activity. The cosmic ray spectrum has an index of about 2.7 at an energy up to  $3 \times 10^{15}$  eV, then it becomes steeper with a slope of 3.1. This transition region is called the knee. A second knee is sometimes mentioned, around  $4 \times 10^{17}$  eV, where the spectrum tends to become even steeper at higher energies with a spectral index of -3.3. If we go to even higher energies, we will reach the so-called ankle region. The spectrum becomes flatter again with a spectral index of about -2.7. The "ankle" could be seen as part of a "dip" in the spectrum between  $10^{18}$  and  $10^{19}$  eV. The flux of the cosmic rays goes from 1 particle/ $m^2/\text{sec}$  at  $10^{11}$  eV, to 1 particle/ $m^2/\text{year}$  at  $10^{16}$  eV, to 1 particle/ $km^2/\text{yr}$  at  $10^{19}$  eV.

Concerning the chemical composition, the energies below  $10^{14}$  eV are well known because they are measured directly. They are believed to be generated by the supernova shock waves. However, the composition around the knee is still not completely known.

The knee region could be understood by the cutoff of the galactic proton spectrum due to the leakage of protons from the galaxy. This cutoff energy will be higher for heavier nuclei because of their higher charge Z and smaller rigidity pc/Z in the magnetized galaxy. However, the knee could also be explained by the different maximum energies of the supernova shock fronts accelerations on different nuclei [23]. Concerning the second knee, it is always related to the ankle. Historically, the ankle was interpreted as the transition from a rapidly falling galactic iron dominated component to a flatter spectrum of extra-galactic components. But it could also be explained as that the extra-galactic protons with the dip due to  $e^+$  and  $e^-$  creation in the integration with CMB and produce  $e^-$  and  $e^+$  pairs [24]. The general feature of the non-thermal spectrum of the cosmic rays indicates that the acceleration results from stochastic processes in the presence of the magnetic fields.

## 1.3 Cosmic Accelerators

A general question in cosmic ray physics is how and where these charged particles are accelerated. Are they accelerated on a large scale or just at discrete point sources ? This open question is listed as one the "Eleven Science Questions for the New Century" [25]. So far, not a single source, neither galactic nor extra-galactic, has been clearly proved to be the cosmic accelerator. Nevertheless, we know that at least, the proved origin/sources of cosmic rays must explain the following observed issues [26].

- A power law energy spectrum for particles of all types.

- The acceleration of cosmic rays to very high energies,  $E \sim 10^{20}$  eV.
- The acceleration mechanism should produce chemical abundances for the cosmic rays which are similar to the cosmic abundances of the elements.

One of the most successful models so far was originally developed by Fermi in 1949 [27]. The idea was that the particles are accelerated by colliding with clouds in the interstellar medium stochastically. In the original version of Fermi's theory, charged particles are reflected by the magnetic mirrors due to the magnetic field strength changes when moving along a field line. The charged particles will be bounced back in the high field strength region. In the next section, I will explain how the Fermi acceleration mechanism works.

### 1.3.1 Fermi Acceleration Mechanism

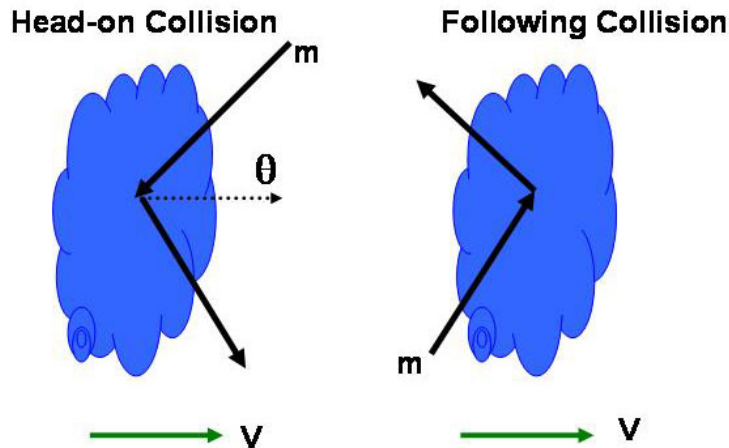


Figure 1.3: The plot depicts Fermi's original idea. Particles are accelerated by collision with magnetic clouds. There are two possibilities. The left plot shows the head-on collision between the particles and the magnetic clouds. The right plot shows the follow-up collisions.

The basic idea of the Fermi acceleration mechanism is transferring the kinetic energy of the magnetized plasma to individual charged particles. Particles are gaining energy by reflections in magnetic mirrors, which usually have irregularities in the magnetic fields. Fermi shows: (i) The particles on average could finally gain the energy in these reflections. (ii) If the particles remain in the acceleration region for a long but finite time, a power law spectrum will be produced. The reason is presented below. If we assume that the cloud/irregularities are infinitely massive and they move along in x-direction with velocity  $V$ . The center of the mass is on the cloud. The energy of the particle in the center of mass frame is

$$E' = \gamma(E + Vpcos\theta) \quad (1.1)$$

the momentum  $p$  along the horizontal direction is  $p_x$ . From the Fig. 1.3 is  $p'_x = p' \cos\theta = \gamma(p \cos\theta + V E/c^2)$ . Since the energy is conserved and the momentum along the horizontal direction is reversed after the collision  $p'_{before} = p'_{after}$  and  $E'_{before} = E'_{after}$  in the cloud frame. If we transform it back to the observer's frame,

$$E'' = \gamma(E' + V p') \quad (1.2)$$

In addition, we know  $p_x/E = v \cos\theta/c^2$ , where  $v$  is the particle's velocity. Thus the energy of the particles becomes:

$$E'' = \gamma^2 E [1 + (2V v \cos\theta)/c^2 + V/c^2] \quad (1.3)$$

The net energy gain is :

$$E'' - E = (2V v \cos\theta)/c^2 + 2(V/c)^2 \quad (1.4)$$

Since the particles may come from every direction, we have to average in different angles. Note that the probability of the collision must be proportional to the relative velocity of the approach of the particle and the cloud, which is  $1 + V \cos\theta/c$ . The range of  $\theta$  is from 0 to  $\pi$ . We take the average of  $\theta$  in equation 1.4. The term with  $\cos\theta$  will be

$$\langle 2V v \cos\theta/c^2 \rangle \sim \left(\frac{2V}{c}\right) \left[ \frac{\int_{-1}^1 x(1 + Vx/c) dx}{\int_{-1}^1 (1 + Vx/c) dx} \right] = \frac{2}{3} \left(\frac{V}{c}\right)^2 \quad (1.5)$$

$$(1.6)$$

where  $x = \cos\theta$ . The gain in energy from Eq. 1.4 after averaging the angle  $\theta$  is

$$\langle E'' - E \rangle \sim \frac{8}{3} \left(\frac{V}{c}\right)^2 \quad (1.7)$$

This result was first derived by Fermi. The net energy gain is positive and it is second order in  $V/c$ . Because the gain in energy is proportional to  $(V/c)^2$ , we call it the second order Fermi acceleration mechanism.

If we consider the diffusion equation and assume that the accelerated particle remains in the accelerated region for a characteristic time  $\tau$ . The diffusion-loss equation is written like,

$$\frac{dN}{dt} = D \nabla^2 N + \frac{\partial}{\partial E} \left[ -\frac{dE}{dt} N \right] - \frac{N}{\tau} + Q \quad (1.8)$$

Here, we look for a steady (the left term is 0), no diffuse (the first term on the right is 0), no source (the last term on the right is 0) solution. Then the power law spectrum could be derived. There are two realistic and important issues concerning Fermi's second order acceleration:

- The typical velocities of the clouds (ISM) are  $V/c \sim 10^{-4}$ . Consequently, the energy gain is a very small number.

- The mean free path between the particles and ISM is long and about 1 pc, which means only one collision per year at the speed of the light.

Hence, Fermi's original idea is not very efficient in the real case. Some modifications are necessary.

The problem of the energy gain term being second order in the Eq. 1.7 is that the collision is not always head-on as depicted in the Fig. 1.3. Therefore, in order to have a net energy gain with the first order, we need to construct a special geometry such that the head-on collisions are always favored. The astrophysical shock waves serve our purpose. Shock waves are ubiquitous in astrophysical plasma. Their speed is super-sonic. The sound waves cannot transmit the information about the disturbance fast enough to the plasma which is ahead of the shock. Let us consider a simple 1 D planar shock wave, propagating with velocity  $U$  through a stationary plasma. Ahead of the shock ("upstream"), the plasma is at rest. The "downstream" region swept up by the shock is moving supersonically. In the rest frame of the shock, the upstream moves toward the shock with the velocity  $v_1 = |U|$ , pressure  $p_1$ , temperature  $T_1$  and mass density  $\rho_1$ , see Fig. 1.4. The downstream moves away from the shock with velocity  $v_2$  and pressure  $p_2$ , temperature  $T_2$  and mass density  $\rho_2$ , while across the discontinuity of the shock, mass, momentum and energy must be conserved. Thus, the following formula could be satisfied:

$$r = \frac{\rho_2}{\rho_1} = \frac{v_1}{v_2} = \frac{(\gamma + 1)}{(\gamma - 1) + 2/M_1^2} \quad (1.9)$$

where  $M_1 = \frac{v_1}{s_1}$  is the Mach number and  $s_1$  is the sound velocity,  $r = \frac{\rho_2}{\rho_1}$  is the compression ratio.  $\gamma$  is adiabatic index.

The so-called first order of the Fermi acceleration mechanism means that the particles gain their energy as a result of the repeated scattering across a shock front. For a strong shock, the  $\gamma = 5/3$ , from Eq. 1.9,  $r = 4$ . Thus we have  $v_2 = 1/4v_1$  and  $v_1 = |U|$  in the rest frame of the shock front. Consider a fast particle in the upstream region, the particle will scatter and spatial diffusion will bring it to the shock region. While the particle crosses the shock, it will undergo head-on collisions. In the frame of the downstream flow, the upstream flow is advancing at a speed of  $\frac{3}{4}U$ . So when the particle crosses the shock again, it will have a different energy gain. The energy gain per complete cycle of shock crossing depends on the collision angle  $\theta$ , which is the angle between the particle momentum and the normal vector of the shock front. We assume a relativistic particle moving across a strong, sub-relativistic shock from downstream to upstream. I denote the rest-frame of the downstream and upstream flows with "+" and "-" respectively. In the rest-frame of the upstream flow (where the shock is moving at speed  $U$  and the downstream flow is moving at speed  $V = \frac{3}{4}U$ ), the particle's initial energy while entering is

$$\epsilon_i^- = \epsilon_i^+(1 + \frac{V}{c} \cos\theta_1) \quad (1.10)$$

The particle then collides with the scattering center in the upstream flow and re-crosses the shock at an angle  $\theta_2$ . Its final energy in the rest-frame of the upstream flow is

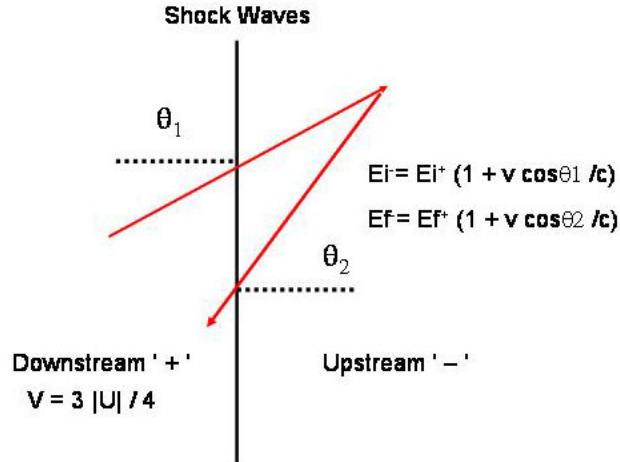


Figure 1.4: A relativistic particle moving across a strong, sub-relativistic shock from downstream to upstream. In the rest frame of the upstream plasma, the downstream flow is moving at speed  $V = 3|U|/4$ . Furthermore, we could calculate the final energy in the same frame if we knew the scattering angle  $\theta_2$ . By equating the initial and final energies, we know how much energy was gained because of the collision.

$$\epsilon_f^- = \epsilon_i^+(1 + \frac{V}{c} \cos\theta_2) \quad (1.11)$$

Because the scattering is elastic,  $\epsilon_f^- = \epsilon_i^-$ , then

$$\frac{\epsilon_f^+}{\epsilon_i^+} = \frac{1 + (V/c)\cos\theta_1}{1 + (V/c)\cos\theta_2} \quad (1.12)$$

In consequence,

$$\frac{\Delta\epsilon_f^+}{\epsilon_i^+} = \frac{V}{c}(\cos\theta_1 - \cos\theta_2) \quad (1.13)$$

Subsequently, the average energy gain per cycle must be calculated. Following the calculation in Fermi's original idea, the probability of the particle crossing the shock at an angle between  $\theta$  and  $\theta + d\theta$  is  $P(\theta) \propto \cos\theta \sin\theta d\theta$ . We integrate the  $\theta$  from 0 to  $\pi/2$  for the head-on collision over a complete cycle. Then Eq. 1.13 will be:

$$\frac{\langle \Delta\epsilon \rangle}{\epsilon_i^+} = \frac{2V}{c} \int_0^{\pi/2} \cos^2\theta \sin\theta d\theta = \frac{2}{3} \frac{V}{c} \quad (1.14)$$

The particle's velocity is randomized without any energy loss by scattering in the downstream region and it then recrosses the shock again and gains energy by another  $\frac{2}{3}(V/c)$ . In consequence, making one round trip across the shock and back again the energy gain is, on average,

$$\frac{\langle \Delta\epsilon \rangle}{\epsilon_i^+} = \frac{4V}{3c} \quad (1.15)$$

Therefore, the average energy gain is 1st order in  $V/c$ . This mechanism is also called the first order of Fermi acceleration mechanism. Sometimes, it is also referred to as diffusive shock acceleration

Although the diffusive shock acceleration seems to be an efficient and natural particle acceleration mechanism, there is another possible acceleration mechanism which is moving particles inside an electromagnetic field. However, the static electric field cannot be sustained in most of the astrophysical conditions due to ionized plasma having a very high electric conductivity.

The attainable maximum energy of accelerated particles can be estimated with the following equation:

$$E_{max} = \gamma mc^2 = \int ZeEdl \sim \beta c ZeBL \quad (1.16)$$

where  $L$  is the geometric size of the acceleration site and  $\beta c$  is the shock velocity. The equation states that the gyro-radius of the particles being accelerated must be fully contained within the acceleration region. The formula does not take into account the energy loss. In reality, there are energy losses in the acceleration sites, like synchrotron radiation or photopion production (eg.  $p\gamma \rightarrow \pi^+n$ ). The maximum energy is determined by the balance between the acceleration and the energy loss.

### Summary and Comment on Cosmic Accelerators

Fermi acceleration well explains the experimental data. For example, we have observed the clear evidence of Fermi acceleration in the heliosphere. The ISEE satellite has observed an acceleration of  $\sim 10\text{-}100$  keV protons by shock in the solar wind [26].

From Eq. 1.16, we know that the  $E_{max}$  depends on the magnetic field, geometric size of the acceleration sites and the time duration in which particles are able to interact with plasma. The Hillas diagram in Fig. 1.5, presents possible astrophysical sources of UHE particles on the plane "B versus L", where in the region, particle gyro-radius  $r_g \leq \beta L$  defines the allowed range for sources with the acceleration parameter  $\beta$ .  $\beta$  is defined as a respective velocity parameter for the different acceleration mechanisms. For example, particle acceleration at relativistic shock can be characterized with  $\beta \sim 1$ . Usually,  $\beta$  is smaller or equal to 1. This means the size of the site should always be larger than the particle gyro-radius [28]. Traditional objects are placed on the diagram including AGNs, clusters of galaxies, pulsars. With recent new models, GRB shocks, magnetars, and relativistic pulsar winds are added. In these astrophysical systems, shock wave acceleration is not the only way to accelerate particles. The rapid rotation of small, highly magnetized objects generates strong fields which may accelerate particles to extremely high energies.

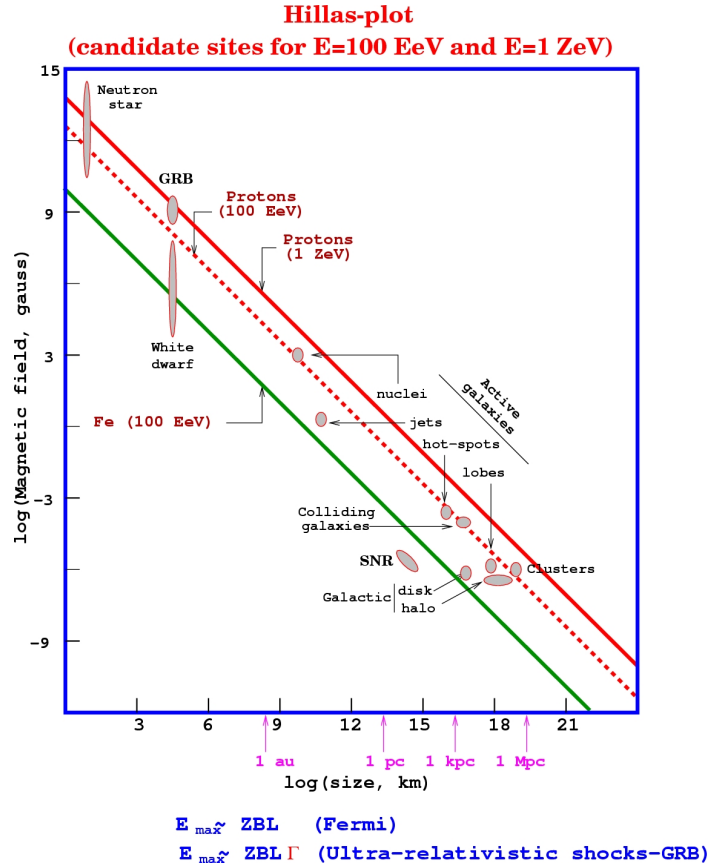


Figure 1.5: The so-called Hillas plot for the different possible astrophysical accelerators.

One of the striking news which was released by the Auger collaboration at the end of 2007 is the discovery of their recorded 27 highest energy events (with Energy  $\geq 5.7 \times 10^{19}$  eV) which are correlated with nearby ( $z \leq 0.017$ ) AGNs. Twenty out of twenty-seven events are within  $3.1^\circ$  from one AGN. While for isotropic arrival distribution, one expects only 5 coincidence events. Five of the non-correlating events come from less than  $12^\circ$  galactic latitude, which can be understood as larger deflections in the galactic magnetic field. It is very surprising that there is no event coming from the direction of the Virgo cluster, which includes a large number of powerful galaxies, such as M87. The correlation between UHECRs and AGNs is impressive, however, the statistics is still limited. We can also interpret the arrival direction distribution of UHECRs observed by Auger correlating with the matter density distribution by the nearby Universe, for example like [29] [30] [31].

## 1.4 Very High Energy Photons

By Wien's law, it can be easily proved that the average energy of the photon from a thermal radiation source at temperature  $T$  is about  $2.3 \times 10^{-10} (T/K)$  MeV. In order to have photons with

maximum energy of 1 GeV, thermal bodies with a temperature of  $\sim 10^{13}$  K are necessary. This temperature cannot be found in any steady astrophysical objects, but only in explosive events such as supernovae or the big bang. Thus, typical astrophysical HE  $\gamma$ -ray spectra are continuum and have a non-thermal rather than a thermal origin.

There are several major mechanisms which can produce high energy photons.

- **Synchrotron radiation:** A relativistic particle moving in the magnetic field could be described by its "pitch angle"  $\theta$ . This is the angle between the particle trajectory and the direction of the magnetic field. According to the Lorentz law, the particle will rotate on the plane perpendicular to the field with the gyration frequency  $\nu_g = eB/2\pi m$ . The radiated energy comes from the velocity component perpendicular to the field. The resulting synchrotron photon spectrum peaks at frequency

$$\nu_c = \frac{3}{2} \gamma^2 \cdot \frac{eB}{2\pi m \sin \theta} \quad (1.17)$$

The synchrotron radiation spectrum of an electron was first given by Ginzburg and Syrovatski in 1964. A high energy cosmic electrons in a typical interstellar magnetic field will radiate synchrotron photons at

$$E_{h\nu} \sim 0.05 \cdot \left( \frac{E}{(TeV)} \right)^2 \cdot \frac{B}{(3\mu G)} (eV) \quad (1.18)$$

Thus, higher magnetic fields and energies shift the peak of the photon energy to a higher value.

Synchrotron radiation is limited by the following condition:

$$\frac{E_e}{m_e c^2} \frac{B}{B_{cr}} \ll 1 \quad (1.19)$$

where the  $B_{cr}$  is  $4.4 \times 10^{13}$  G.

- **Curvature radiation:** When the magnetic field is particularly strong, curvature radiation may occur. Since the synchrotron radiation is so effective, a particle within an intense magnetic field will dissipate the component of its momentum perpendicular to the line of the magnetic field and follow with a uniform motion along the line. In many astrophysical conditions, such as close by regions of pulsars and black holes, the magnetic lines are not straight, but curved. In such case, the particle follows a curved line and it also radiates. This is the curvature radiation.
- **Bremsstrahlung:** When a relativistic charged particle, like an electron, is accelerated in the electrostatic field of a nucleus or other charged particles, it will emit bremsstrahlung radiation. The spectrum remains flat up to roughly the electron kinetic energy. It drops sharply towards zero, which means effectively all the kinetic energy of the electrons is transferred to bremsstrahlung photons.

- Inverse Compton Scattering: When a high energy photon impinges on a charged particle, it transfers its momentum to the charge particle. This is the so-called Compton effect. The inverse process, Inverse Compton effect (IC), also exists. Energetic particles transfer momentum to low energy photons and endow them with a larger momentum and energy. If we assume that the energetic electron energy is  $\epsilon$  and the coming photon energy is  $\omega_0$ . The angle-averaged total cross-section of IC depends only on the product of the energies of  $\epsilon$  and  $\omega_0$ . If the incoming photon energy is much smaller than the rest mass energy of the electron (ie:  $\kappa_0 \ll 1$ ), Compton scattering behaves as Thomson scattering, and the cross section is

$$\sigma_{IC} \sim \sigma_T (1 - 2\kappa_0) \quad (1.20)$$

However, the cross section of the IC must be computed by QED, when the incoming photon energy is closer to the electron rest mass energy. If this is the case, the cross section is described by a well known formula called Klein-Nishina formula. The total cross section could be described as follows:

$$\sigma_{IC} = \frac{3\sigma_T}{8\kappa_0} \left[ \left(1 - \frac{2}{\kappa_0} - \frac{2}{\kappa_0^2}\right) \ln(1 + 2\kappa_0) + \frac{1}{2} + \frac{4}{\kappa_0} - \frac{1}{2(1 + 2\kappa_0)^2} \right] \quad (1.21)$$

- Photo-meson production: The interaction of a highly relativistic proton with a photon can produce pions if the energy of the photons in the frame of the proton exceeds the threshold energy  $E_{th}=134.7\text{MeV}$ , which is the  $\pi^0$  mass. This is the same process which degrades the energy of the extra-galactic ultra-high energy cosmic rays to less than  $10^{20}$  eV originating at distances larger than 100 Mpc, the so-called Greisen-Zatsepin-Kuz'min (GZK) cut-off. The produced  $\pi^0$  will decay to 2  $\gamma$ s immediately due to the short life time.
- $\pi^0$  decay from proton-proton interactions: The dominated  $\pi$  producing channels in hadronic interactions are proton proton interactions. The following process is there:

$$p + p \rightarrow p + p + \pi^0 + \pi^\pm \quad (1.22)$$

$\pi^0$  has a very short life time which is about  $10^{-15}\text{s}$ . We know that the electron-positron pairs are also created in the pp interactions because of the  $\mu$  decay from the  $\pi$ . These pairs can finally again generate  $\gamma$ -rays through relativistic Bremsstrahlung, IC or synchrotron processes depending on the environments.

- Annihilation : Annihilation of pairs of particles and antiparticles could also produce  $\gamma$ -rays. The simple case is the electron positron annihilation. The energy of produced two photons are 0.511 MeV in the rest frame. Another possibility is the  $\pi^0$  decay from the proton-antiproton annihilation. The basic reaction chain is:  $p + \bar{p} \rightarrow \eta \pi$  and then  $\pi^0 \rightarrow 2\gamma$ .

Only a limited fraction of the universe is visible in  $\gamma$ -ray. Far distance VHE  $\gamma$ -rays will not be seen because of their absorption by the extra-galactic photon background. This implies that

all the objects beyond our Galaxy are not visible in PeV  $\gamma$ -rays and about 10 Mpc for 100 EeV  $\gamma$ -rays. In other words, by reducing the energy threshold of the detectors down to 100 GeV, we can approach cosmological distances up to redshift  $z \sim 1$ . Though TeV  $\gamma$ -rays could not be a direct probe of cosmological epochs, studying of the HE photons is still highly motivated.

## 1.5 VHE $\gamma$ Ray Sources

### 1.5.1 High Energy $\gamma$ Sky

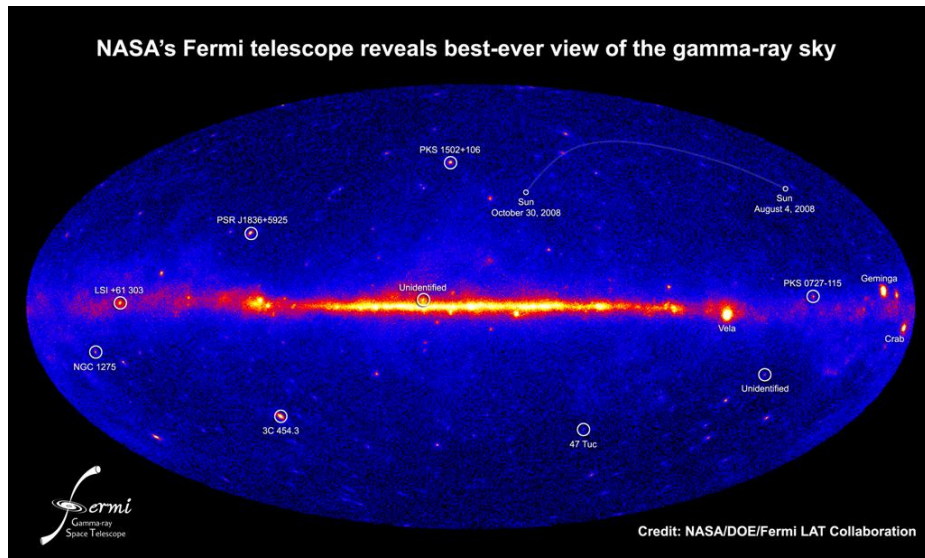
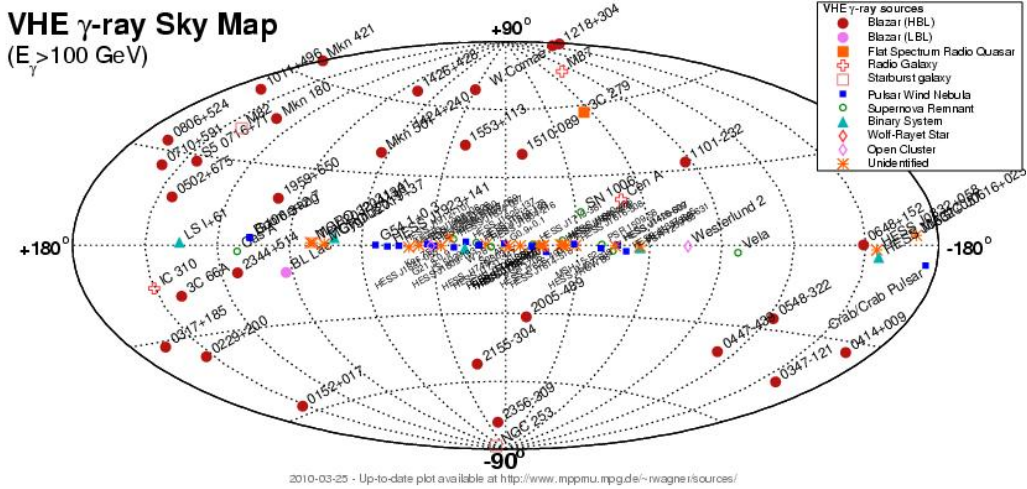


Figure 1.6: This all-sky map constructed from 3 months of Fermi-LAT observations (4 August to 30 October, 2008) represents a deeper, better-resolved view of the gamma-ray sky than any previous space mission. The photo is taken from [4]

In the last decade of the last century, scientists obtained the first complete all-sky survey in  $\gamma$ -ray ranging from 1 MeV to more than 1 GeV. The surveys were mostly performed by the telescopes COMPTEL (Compton Telescope 1-30 MeV) and EGRET (Energetic Gamma-Ray Experiment Telescope 100 MeV - 10 GeV), which were on board NASA's Compton Gamma-Ray Observatory (CGRO). Later, there was a galactic plane survey at TeV range since 2004, performed by the H.E.S.S. collaboration.

The first COMPTEL source catalog includes 32 persistent sources at  $\geq 3\sigma$  level [32]. The persistent sources of continuum emission belong to three different types of objects. They are (i) Spin-down pulsars, (ii) Stellar Black-Hole candidates, and (iii) AGNs, mostly blazars. Totally, 9 sources remain unidentified. At slightly higher energies, the detection of cosmic  $\gamma$  radiation becomes easier and the detectors have better angular and energy resolutions. The EGRET surveys eventually results in the third EGRET Catalog [33], which consists of 271 sources detected above



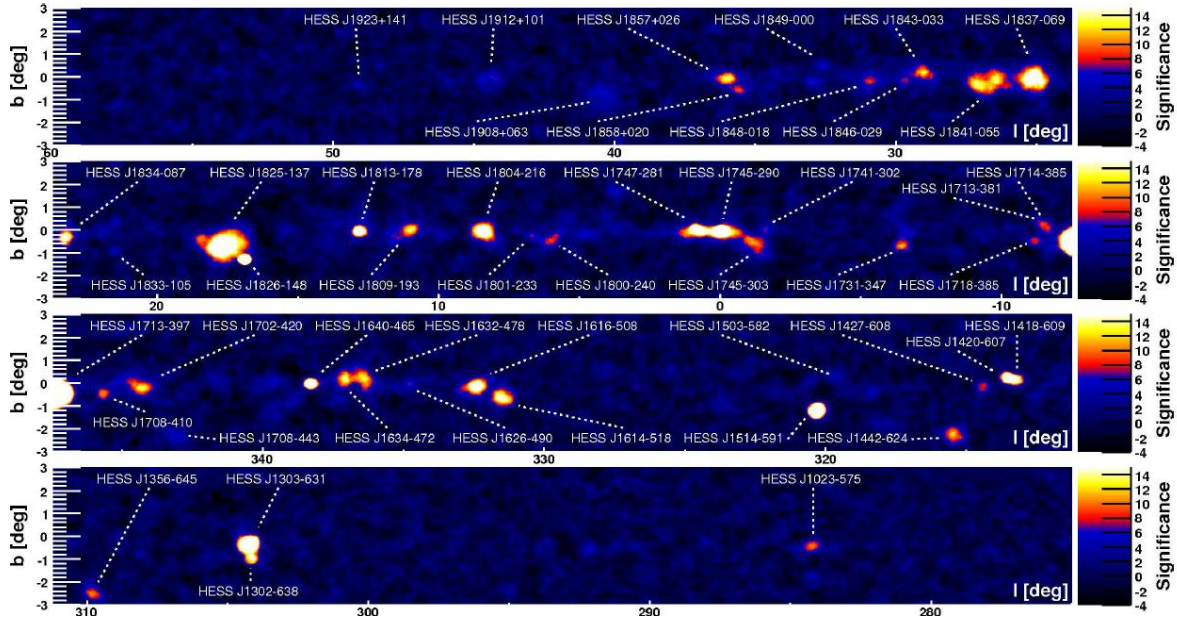


Figure 1.8: The results from the H.E.S.S. 2004 Galactic survey.

in other wavelengths has been found. Moreover, H.E.S.S observations of the central region of our Galaxy revealed a diffuse TeV  $\gamma$ -ray emission component which is apparently dominated by contributions from giant molecular clouds (GMCs). It serves as a cosmic ray beam dump for interactions of relativistic particles from nearby active cosmic accelerators. This new discovered source could be new type of sources besides the three known and established ones.

### Pulsars and Their Wind Nebulae

Most information from pulsars is derived from their timing properties. For measuring their period  $P$  and the period derivative  $\dot{P}$ , we know that they are rapidly-rotating neutron stars with a strong dipole magnetic field. The high energy  $\gamma$ -ray emission could come from three different regions in the pulsar system, namely (a) the pulsar magnetosphere, (b) the unshocked ultra-relativistic wind which carries almost the entire rotational energy of the pulsar, and (c) in the pulsar wind nebula: the result of termination of the pulsar wind which can accelerate particles. According to theory, the energy spectra and the structure of the lightcurve in the region from several GeV to 30 GeV carry the crucial information about the location of the  $\gamma$ -ray production region in the pulsar magnetosphere. So far, EGRET has discovered 6 pulsars, the new launched FERMI has discovered about 30 pulsars during the first 3 months' survey. Due to the pair production in the strong magnetic field, no TeV emission is expected from the pulsar magnetosphere. Thus, it is not surprising that the observation of the pulsed TeV  $\gamma$  from the pulsars mostly resulted in only upper limits. Just one year ago, the MAGIC collaboration discovered VHE pulsations from the Crab pulsar at energies around 25 GeV, which is considered to be a great achievement in this field.

A Pulsar Wind Nebula (also known as "plerion", PWN) is a nebula powered by the relativistic wind of an energetic pulsar. PWN are often found inside the shells of the supernova remnants in their very early stage of life. The Crab nebula is one of the best examples. PWN becomes so far the most populated category of TeV emitters. The production of the TeV  $\gamma$ -rays is due to the termination of the wind which leads to the acceleration of electrons' energies up to 10 TeV or even higher. Afterwards, many  $\gamma$ -rays are produced due to inverse Compton scattering on different diffuse radiation fields. The CMB forms a universal population of seed photons which guarantee TeV  $\gamma$ -ray emission from any powerful accelerator of multi-TeV electrons and from PWN. An important and remarkable feature of all observed PWNs is the fact that the extended sources are offset from the pulsar location, i.e. the gravitational centers of TeV emission do not coincide with the positions of the parent pulsar position. The same happens in X-ray images. This tells us two things:

- The observed offset of pulsar, X-ray and TeV images could be due to the propagation of the reverse shock created at the termination of the pulsar wind in a highly inhomogeneous medium.
- The similarity in morphologies of PWN in X-ray and TeV  $\gamma$  bands supports that both emission components are due to the radiation of the same population of multi-TeV electrons by the synchrotron and inverse Compton scattering.

## Supernova Remnants

Supernova Remnants (SNRs) have for a long time been conjectured as candidates for the acceleration of the bulk of the galactic cosmic ray protons and nuclei. The diffusive shock will accelerate the particles up to certain high energies. We know that the shock acceleration has a limited characteristic time. Therefore, the maximum energy which the particles could be accelerated to is limited. The hard energy spectrum of the protons extending to multi-TeV range should lead to VHE  $\gamma$ -rays from hadronic origin. So far all young SNRs are sources of non-thermal radiation. They have X-ray radiations from the synchrotron radiation from the very hot electrons ( $\geq 10$  TeV). Those synchrotron radiation could be boosted to high energy  $\gamma$ -rays by inverse Compton scattering (IC). Therefore there are two emission processes responsible for the TeV radiation. In SNRs, the gamma ray radiations from the hadronic origin will be expected to have been significantly contaminated by the IC components. Thus the important issue in  $\gamma$ -ray studies in SNRs is not only detecting TeV signals, but also provide spatially resolved measurements and morphological studies which are correlated with other multi-wavelength data. This will allow the identification and extraction of the hadronic components. One good example is the source IC443 which was discovered independently by MAGIC and VERITAS. The centroid of the emission is consistent in two different measurements. However, this position is not coincident with the X-ray PWN within the same remnant nor with the SNR shell. The challenges of this field is to establish a detailed study of the brighter sources and identify the nature of the accelerated and radiating particles.

## Binary Systems

In principle, X-ray binaries are thermal sources which can transform the gravitational energy of accreted materials into X-ray emission. However, non-thermal radiation due to particle acceleration, is possible as well. The position of the high energy emission could be the termination of the pulsar wind or through the internal shocks inside the jet which are in the vicinity of the black hole. If the above conjectures are true, then TeV  $\gamma$ -rays could be produced because of the collision with dense target photons and materials around the companion star. Currently, three very promising  $\gamma$ -ray binaries have been established. The first one is PSR B1259-63/SS2883, a 3.4 year period binary of a pulsar in an eccentric orbit around a Be-star. The remaining two are much closer binaries. So far, the mass and the nature of the compact objects are not very well known. One of them is the LS5039, discovered during the H.E.S.S. galactic plane survey. The TeV emission from this source shows a periodicity of about 3.9 days, which corresponds to the orbital period of the binary system. The last one is LSI+61, discovered by the MAGIC collaboration in 2006, which also shows a periodicity of 26 days. Since the nature of the compact object is not precisely known in the last two systems, it is not so clear whether the emission is due to relativistic outflow from the neutron stars inside the system or accretion on the compact object (either black hole or neutron star) which may introduce jets inside the system.

## Unidentified Sources

It is quite surprising that some of the galactic TeV  $\gamma$ -ray sources have no clear counterpart at the other wavelengths. One of the main reasons is that many of these sources are widely extended and their morphology differs significantly from the other wavelengths. There are two categories of unidentified TeV sources:

- Sources have TeV emissions but no other strong association with other wavelengths.
- MILAGRO sources: The MILAGRO collaboration has discovered three sources. MGRO J2031+41, MGRO J2019+37 and MGRO J1908+06. Those sources have fluxes approaching Crab nebula above 20 TeV. MGRO J2019+37 has been confirmed by the Tibet telescope. Another source, MGRO J1908+06, was discovered by a non-IACT instrument (MILARGRO) and later confirmed by an IACT (H.E.S.S.). There are dozens of physics explanations about these sources. One possible explanation is that they originate in the collisions of cosmic rays with molecular clouds, with little emission at the other wavelengths. The problem for this scenario is that the acceleration sites for these cosmic rays are unknown. Of course, there are also exotic explanations which propose TeV emission from those unidentified sources are due to the annihilation of the dark matter in localized clumps.

Source Name	Discover Year	Group	class	z	ref
Cen A	2009	HESS		0.00183	[34]
M87	2003	HEGRA	LINER	0.00436	[35]
Mrk421	1992	Whipple	HBL	0.031	[1]
Mrk501	1996	Whipple	HBL	0.034	[36]
1ES2344+514	1998	Whipple	HBL	0.044	[37]
Mrk180	2006	MAGIC	HBL	0.045	[38]
1ES1959+650	2002	TA	HBL	0.048	[39]
PKS0548-322	2006	HESS	HBL	0.067	[40]
BL lac	2006	MAGIC	LBL	0.069	[41]
PKS2005-489	2005	HESS	HBL	0.071	[42]
RGB J0152+017	2008	HESS	HBL	0.080	[43]
W Comae	2008	VERITAS	IBL	0.102	[44]
PKS2155-304	1999	Durham	HBL	0.117	[45]
RGB J0710+591	2009	VERITAS	?	0.125	[46]
H1426+428	2002	Whipple	HBL	0.129	[47]
1ES0806+524	2008	VERITAS	HBL	0.138	[48]
1ES0229+200	2007	HESS	HBL	0.140	[49]
H2356-309	2005	HESS	HBL	0.165	[50]
1ES1218+304	2005	MAGIC	HBL	0.182	[51]
1ES1101-232	2005	HESS	HBL	0.186	[50]
1ES0347-121	2007	HESS	HBL	0.188	[52]
1ES1011+496	2007	MAGIC	HBL	0.212	[53]
PG1553+113	2005	HESS	HBL	0.3-0.4	[54] [55]
3C66A	1998	Crimea	IBL	0.444	[56]
MAGIC J0223+430	1998	Crimea	IBL	0.444	[57]
3C279	2007	MAGIC	FSRQ	0.536	[58]
S50716+714	2008	MAGIC	HBL	?	[59]
PKS 1424+240	2009	VERITAS	IBL	?	[60]
NGC 253	2009	HESS	Starburst	0.0008	[61]
M82	2009	VERITAS	Starburst	0.0007	
VER J0521+211	2009	VERITAS	Blazar	?	[62]
RBS 0413	2009	VERITAS	HBL	0.19	[63]
1ES 0414+009	2009	HESS/Fermi-Lat	HBL	0.287	[64]
1ES 0502+675	2009	VERITAS	HBL	0.341	[65]
PKS 0447-439	2009	HESS	BL Lac	0.2	[66]
PKS 1510-089	2010	HESS	Broad-line Quasar	0.36	
RGB 0648+152	2010	VERITAS/Fermi-Lat		?	[67]
IC 310	2010	Neronov et al.	Head-tail Radio	0.019	[68]

Table 1.1: Extra-galactic TeV  $\gamma$  sources until May 2010.

### 1.5.3 High Energy Extra-galactic Sources

#### Active Galactic Nuclei

Active galactic nuclei (AGNs) are thought to host a very active accreting supermassive black holes which drive relativistic jets into their surrounding environments. In the 1990s, EGRET has found that the 100MeV sky was dominated by blazars. Those EGRET AGNs all had flat spectra above 10 GeV, which was auspicious for TeV astronomy. Nevertheless, the early observations of those selected EGRET sources by ground-based observers showed disappointing results [69]. It became apparent that AGNs were important TeV sources after the discovery of Markarian 421 (Mrk421). Among many different types of AGNs, Blazars are AGNs with jets aligned very closely (normally  $\leq 10^\circ$ ) with the line of sight of the observer. They show rapid variability in different time windows and different energy bands. The spectral energy distribution of blazars is double peaked at the optical/X-ray domain and the GeV/TeV domain. The most common explanation for these two bump components are synchrotron and inverse Compton radiation by high energy electrons within a region (a blob) with bulk relativistic motion along the jets. The first component usually is quite well-measured, however, the origin of the second component is still debated. The high energy component could be due to accelerated hadrons via several different radiation processes. The "hadronic" origin explanation is relevant for UHE cosmic ray physics because AGNs are proposed as one of the possible acceleration sites for UHE particles. The TeV emission from blazars not only tell us that the particles (electron and/or protons) are accelerated to very high energies, but also provides the strongest evidence that the non-thermal radiation is produced in a relativistic outflow (jet) with a Doppler factor of  $\delta \geq 10$ . The beaming effect dramatically reduces the intrinsic luminosity of the object and allows a larger size of the  $\gamma$  ray emitter. Up to now, there are 27 established extra-galactic TeV emitters. 24 of them are blazars. Several of them were already in the EGRET third catalog, such as 3c66A, MRK421, PKS2155-304 and BL Lacertae. The fact that many EGRET-detected AGNs are not seen at TeV regime is important. The lack of the TeV detections for these AGNs may imply cutoffs in the acceleration mechanism or absorption by the soft photons either locally inside the sources or in the intergalactic space. The physics of TeV emission from the AGNs will be explained more profoundly in the next chapter.

#### Potential Extra-galactic Sources

- Starburst galaxies have higher supernova explosion rates. There are accelerated electrons or protons up to TeV or PeV, TeV  $\gamma$ -rays are produced by particles bombarding the copious targets like ambient gas and radiations. Two objects of this type have been recently observed and proved to be VHE gamma sources, NGC253 and M82. [61]. There are also ultra-luminous infrared galaxies (ULIRG) or even hyper-luminous infrared galaxies (HLIRG), which emit at least 90% of their light in the infrared. Their total luminosities are about  $10^{11-12}$  times of solar luminosities in infrared. Many of them are starburst galaxies, and some contain an AGN in the center as well. Arp 220 is the closest representative of these objects. 15 hours of observations by the MAGIC telescope in 2005 gave an upper limit of TeV emission from this source. The predicted flux of the TeV  $\gamma$  emission from

this object depends much on many unknown parameters, such as the overall non-thermal luminosity, the internal absorption of the TeV photons and so on. Hence, the detection of significant  $\gamma$  ray signals will provide more informations on these objects.

- **Clusters of Galaxies:** Clusters of galaxies are the biggest gravitational bound systems in the Universe. The prediction of the TeV  $\gamma$  ray emission is based on the interactions of accelerated protons with the ambient gas. In the case of  $\gamma$  rays produced by the interactions of multi-TeV electrons with the CMB, the unknown strength of the inter-cluster magnetic fields makes the flux prediction suffer huge uncertainties. So far, two such sources have been observed, one is the Perseus cluster and the other one is M13. They have been observed by H.E.S.S. and MAGIC, respectively. So far, only upper limits have been derived.
- **Gamma Ray Bursts:** The origins of Gamma-ray bursts have been a mystery. The high energy component of the  $\gamma$  photons was seen by EGRET, but not yet seen in the TeV regime. Some of the GRB models predict significant emission of TeV  $\gamma$  rays and VHE neutrinos as well. The spectra have a peak at photon energy around a few 100 KeV and the spectra are nonthermal. From EGRET data, it is clear that the spectra could extend to at least several GeV. The nonthermal spectra imply that a significant fraction of the explosion energy is transferred to another form of energy then dissipated and converted to nonthermal radiations. The current most popular model is the "fireball" model, which explains the GRBs as the core-collapse of massive stars or coalescence of two compact objects. Since GRBs are transient sources, the  $\gamma$ -ray flashes usually last very little time. To respond faster is the most critical issue for smaller FOV instruments, such as IACTs. MAGIC has been designed with a light-weight concept with the special aim of GRB observations. The slew speed for MAGIC is about  $\sim 10^\circ/\text{s}$ . The heavier built instruments, like H.E.S.S. and VERITAS, have slew rates of about  $\sim 2^\circ/\text{s}$  and  $\sim 1^\circ/\text{s}$ , respectively. From this point of view, wide FOV instruments like MILAGRO and Tibet AS $\gamma$  have clear advantages for this study. However, large portions of the GRBs are located in large  $z$ ; the EBL absorption will attenuate the VHE  $\gamma$  from the GRBs.

## 1.6 Impact and Role of VHE Gamma Ray Astrophysics in Physics

### 1.6.1 Fundamental Physics and Cosmology

Detection of very high energy (VHE)  $\gamma$ -rays from the Universe could be a probe not only for the sources but also cosmology or even more fundamental physics:

- **Dark matter and exotic particles search:** Evidence of the existence of dark matter comes from the astrophysical observations. VHE  $\gamma$ -rays could also be produced by dark matters or exotic particles, though with current IACTs, it is very hard to identify these exotic signals. Nevertheless, in some particular sources like dwarf galaxies, huge amounts of

dark matter are believed to be exist. These sources have a high potential for detecting the DM signal.

- The precise measurement of the spectrum cut-off of the TeV AGNs at different red-shift  $z$  provides the history of cosmological evolution. The VHE  $\gamma$ -rays are attenuated by Extra-galactic Background Light (EBL) and the column density of the EBL depends on the red-shift and the evolution of the universe.
- The  $e^+e^-$  pairs which are products of  $\gamma\gamma$  interactions will initiate cascades. We believe that a weak cosmological primordial magnetic field exists in the intergalactic space. If this magnetic field is small enough ( $\leq 10^{-11}$  G), the  $e^+e^-$  pairs will not be deflected very much. The direction of the up-scattered photons will not be deviated too much either and may produce a gamma ray halo around the sources. Actually, the whole universe could be considered as a scene of continuous creation of electromagnetic cascades. The superpositions of contributions of  $\gamma$ -rays from these cascades may constitute a fraction of the diffuse cosmic  $\gamma$ -ray background.

## 1.7 Future Prospects

### 1.7.1 Next Generation IACTs: CTA and AGIS

Currently, designing and developing next generation IACTs are being heavily discussed. There are several different working directions: (i) Low energy threshold: A reduction in energy threshold of conventional IACTs would increase the overlap with GeV instruments, such as FERMI, and would extend the  $\gamma$ -ray horizon allowing the detection of more distant extra-galactic sources and GRBs. (ii) High sensitivity: Current IACTs have limitation on duty cycle. Limited observation time makes people hesitate to observe weaker sources. With high sensitivity instruments, the detection of weaker sources within shorter periods of time becomes feasible. Moreover, transient phenomena, such as AGN flares, GRBs, need sensitive instruments for being caught. (iii) Large field of view instruments or arrays of telescopes covering the all sky area: Conventional imaging IACTs are narrow field instruments for which observations must be guided by some other source of information (such as  $\gamma$ -rays and X-rays satellites.). For variable sources, like AGNs and GRBs, a trigger from a wide-field instrument is required and the time to slew a large telescope may well exceed the most interesting timescale. Therefore, to achieve sensitivity to the shortest AGN flares, to provide continuous converging of the rapidly varying emission, to provide spectral cutoffs for a large samples of AGNs, and to catch short and long duration GRBs during their development, a local or global network of IACTs with good sensitivity to  $E \geq 30$ GeV events is required. The current generation of space-based gamma-ray detectors (AGILE and FERMI) will provide all-sky coverage and good sensitivity both on point sources and diffuse emission at energies above 100 MeV. Above 50 GeV, the next generation IACTs, CTA (Cherenkov Telescope Array) and AGIS (Advanced Gamma-ray Imaging System) will provide the high point source sensitivity and huge effective areas (more than  $10^4$  times of the satellite experiments) required to study the shortest variability time-scales and to provide time-resolved

spectra from 50 GeV up to 50 TeV. CTA and AGIS have been proposed to be the next generation imaging Cherenkov telescope systems. The design goal is not only restricted to pure astrophysical observations, but also allows significant contributions to the field of particle physics and cosmology. The next generation of IACTs is proposed to have a factor of ten improvement in sensitivity in the current energy domain of about 100 GeV to a few tens TeV and an extension of the energy range well below 100 GeV and to above 100 TeV. With a future better angular, energy resolution, wider sky and energy coverage, we expect striking and fruitful results from the next generation of IACTs.

### 1.7.2 Multi-messenger Study of the Energetic Universe

Detection of radiations from the traditional EM bands has been well practiced in the last thirty years. Physicists gained a lot of results from multi-wavelength observations. The best example is the understanding of the SED (Spectral Energy Distribution) of variable AGNs. Closer cooperation with telescopes in other wavelengths, such as Fermi, MAXI (Monitoring of All-sky X-ray Image), will help us to better understand the physics of the sources. Especially with closest in energy i.e.: GeV photons, observation of IACTs with AGILE and Fermi together, spans six orders of magnitude in energy (0.1 GeV~100 TeV) for probing particle accelerators, which allows us to apply the most rigorous tests of the theoretical models. In the recent twenty years, with the progresses of instrumentation and technologies, neutrinos from extra-solar systems have been detected. UHE cosmic ray physics has achieved great results as well. In fact, evidence of the correlation of the arrival direction of the UHE cosmic rays with AGNs was really impressive and exciting. These findings give more hints to search for cosmic Zevatrons. The epoch of "Multi-messenger" astrophysics is coming. The use of different messenger particles such as neutrinos (IceCube, ANTARES, KM3NJET), GeV to TeV  $\gamma$ -rays (satellite and ground-based  $\gamma$  detectors) and UHE cosmic rays (AUGER) are necessary for understanding the origin of the highest energy radiations in the Universe. TeV  $\gamma$ -rays play a key role as they provide an important link between low energy photons and the highest energy cosmic rays. Furthermore, they are sensitive to radiations of leptonic and hadronic origin, thus holding a key to understand the energy budget in different types of cosmic accelerators.

# Chapter 2

## Active Galactic Nuclei

Galaxies are collections of stars and gases. In a small percentage of them, violent and highly non-thermal activities are observed. These activities were thought to be driven by their energetic nuclei. These active galaxies are called Active Galaxies and the central engines are called Active Galactic Nuclei (AGN). The study of AGNs started in 1943, while Seyfert first detected nuclear emission lines in the core of several galaxies. There were two special features in Seyfert galaxies which were observed at the very beginning and people realized that they were completely different from normal galaxies. The first feature is its brighter nucleus outshining the whole galaxy and the light output from the nucleus varying from time to time. The second one is a Seyfert galaxy contains strong emission lines and a continuum which looks like nonthermal emission. Several years later, the major breakthrough was achieved when the quasars (quasi-stellar objects) were discovered through their radio emissions. Their very high red shifts imply that they are the most luminous objects ever known. The nearest quasars have subsequently been found to be embedded in galaxies and hence were considered to be an extreme examples of Seyfert galaxies.

The huge amount of energy output from AGN introduces people's originalities and creativity. There were dozens of conjectures which tried to explain their energy suppliers, the very central engines. In 1964, Salpeter and Zeldovich [70] [71] proposed that the QSO energy production originate from accretion onto a super massive black hole. From a simple calculation, we know that for the materials gradually spiraling to the innermost stable orbit of a non-rotating black hole at  $r = 6GM/c^2$ , the energy released per unit mass would be  $0.057c^2$ , enough to provide the energy of a luminous QSO from a reasonable mass. Until now, the super massive black hole model is still the most popular model to explain the central engine of AGNs.

This chapter is organized as follows: First, AGN phenomenology will be outlined in general and the key components of AGNs will be discussed. Then, I will describe the unified model of AGNs, which explains the observed different AGN phenomena by different observational orientations. Subsequently, I focus on one of the specific types of AGNs, the so-called blazars. I will explain some general characteristics observed in this particular type of objects. Finally, I will consider why we are interested in studying VHE emissions from AGNs, and what are the impacts of this study on the astrophysics and cosmology.

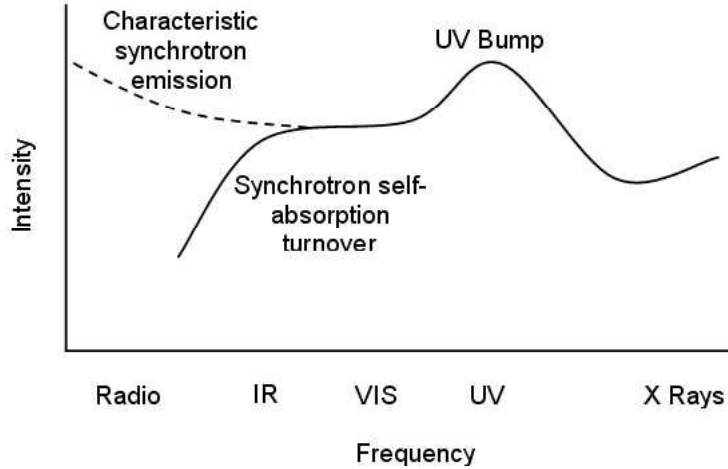


Figure 2.1: A typical sketch of the continuum spectrum observed from many different types of AGNs. The plot is about the intensity vs frequency<sup>1</sup>

## 2.1 Introduction

Different AGNs have different emission spectra. Unfortunately, most of them are quite complicated. However, there are many general common features. Fig. 2.1 is a generic schematic of the radiation continuum for a typical AGN. One of the notable features is the emission energy range crossing one decade of frequencies from radio to X-ray. The spectrum is totally different from the thermal (blackbody) spectrum of a star. A power law  $F_\nu \propto \nu^{-\alpha}$  could be used to describe the monochromatic energy flux,  $F_\nu$ . The shape and the polarization of the visible to UV range indicates that it can be decoupled into two different contributions. One is from thermal sources with low polarization and the other one is the non-thermal component with significant polarization. As we will see later, the thermal component is missing in objects known as blazars. The low frequency part could be described by a simple power law. It is a signature of the synchrotron radiation. The synchrotron spectrum of individual electrons could be described as a power law. Note that the spectrum does not continue to rise without limit as the frequency decreases. At transition frequency, the spectrum turns over and varies as  $\nu^{2.5}$ . The reason is that the electrons becomes opaque to their own synchrotron radiation at that energy range, which is called synchrotron self-absorption. People believe that the wide range of emission continuum should originate from different components of AGNs instead of only one certain place. Some key components of AGNs are introduced below:

- The Super Massive Black Holes (SMBHs): SMBHs are believed to power not only the central engine of AGNs but also most of the other galaxies, like our Milky Way. Until recently, people have found that the SMBH mass is related to the evolution in high red shift

<sup>1</sup>The figure is adapted from: <http://www.jeffstanger.net/Astronomy/>

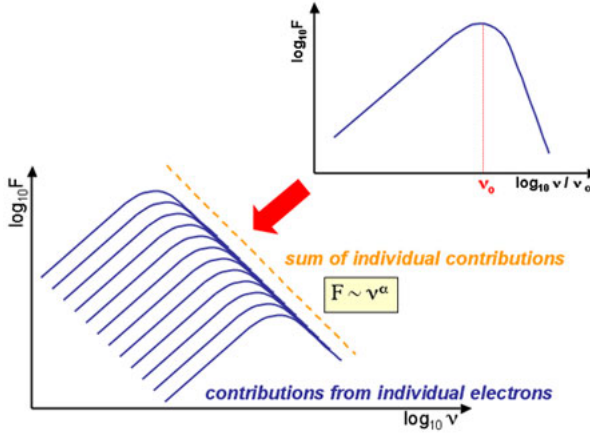


Figure 2.2: The power law spectrum of the synchrotron radiation, which is the sum of the radiation produced by individual electrons as they are moving inside the magnetic field. The turnover at low frequency which we have seen in the AGN spectrum is due to the synchrotron self-absorption effect.

quasars and the evolution of early galaxies. SMBHs are the most massive BHs, usually from  $10^6 - 10^9 M_\odot$ , with a physical size of about 0.001 - 10 AU. Usually, the size of a BH is considered to be that of the event horizon, since the light or the particles can not escape within the event horizon. The basic parameters of BHs can be expressed by using their gravitational radius  $r_g$  and Schwarzschild radius  $r_s$

$$r_g = \frac{GM}{c^2} \quad r_s = 2r_g \quad (2.1)$$

The typical quasar luminosity  $\sim 10^{46} \text{ ergs}^{-1}$  is more than a hundred times of the luminosity of our Milky Ways. We know that the luminosity,  $L$ , of any spherically symmetric object which is in equilibrium, must be lower than the Eddington luminosity. Eddington luminosity is the luminosity when the gravitational force  $f_g$  is equal to the radiation force  $f_{rad}$ . It is  $L_{Ed} \sim 1.5 \times 10^{38} \frac{M}{M_\odot} \text{ ergs}^{-1}$ . If we put the quasar luminosity  $1.5 \times 10^{46} \text{ ergs}^{-1}$  into the formula, we will find the mass of the quasar should be larger than

$$M = \frac{L}{1.5 \times 10^{46} \text{ ergs}^{-1}} M_\odot = 10^8 M_\odot \quad (2.2)$$

There is a huge amount of mass dwelling inside a very small volume which is about a few AU. This is enough to support the idea that the SMBHs are the most probable candidates for powering AGNs.

- The Central Accretion Disk: The AGN accretion disk is formed naturally by in-falling gas that sinks into the central plane while retaining most of its angular momentum. If the

disk is thick and dense enough, it can provide the necessary conditions for transferring angular momentum out and allow the gases to infall into the central black hole. Generally speaking, the disk is an object of high column density gas at  $10 - 100 r_g$  which can be exposed to part of the centrally produced continuum emission. This region can result in emission and/or absorption lines, depending on the geometry. The disk itself has been proved to be emitting the optical, UV radiation and part of the X-ray emission in SED. Possible models which are considered in literature include that the disk is illuminated by a central point source with X-rays which are produced and scattered by an extended corona. The geometry and the famous  $\alpha$  parameters (a parameter describing the effective increase of the viscosity due to the turbulent eddies within the disk) are usually unknown. Therefore the ionization conditions are usually difficult to tell.

The accretion disk is related to the huge amount of luminosity output. From studies of the galactic binary systems, we know that the energy released by binary systems could originate mainly from the mass accretion on the surface of the compact object, either a neutron star or a white dwarf. Simply dropping matter straight down to a black hole is not efficient because there is no surface for the mass to strike. If the matter spirals in toward a black hole through an accretion disk, a substantial fraction of the rest energy can be released. The accretion luminosity which is generated by a mass accretion rate  $\dot{M}$  through the disk can be written as

$$L_{disk} = \eta \dot{M} c^2 \quad (2.3)$$

where  $\eta$  is the efficiency of the process, usually the value is  $0.05 \leq \eta \leq 0.45$ . The rapid rotating BH (Kerr BH) with an accretion disk is an extremely efficient system to produce large amounts of energy.

- **Jets and Radio Lobes:** Jets in active galaxies emit over a wide range of energies from the radio to  $\gamma$ -ray. Synchrotron and inverse-Compton-scattering are the two main physics processes within the jets. The radio lobes are produced by charged particles ejected from the central nucleus of the AGN at relativistic speeds. These particles are accelerated away from the nucleus in two opposite directions powered by the energy of accretion and/or by the extraction of rotational kinetic energy from the black hole (the Blandford-Znajek mechanism) [72].

The jet must be the electrically neutral. However, it is not clear if the components inside the jets are leptonic  $e^+/e^-$  dominated or hadronic  $e^-/\text{ions}$  dominated plasma. In the former case, the jets are less massive, therefore particles are easier to be accelerated. It is known that the jets are highly collimated. The reason is that the disk's magnetic field is coupled ("frozen in") to the flow of charged particles. The resulting magnetic torques may remove angular momentum from the disk, which would allow the accretion material to move inward through the disk. The motion of the charged particles and the magnetic fields within the lobes of radio-loud objects contain a huge amount of energy.

- **The Broad Line Region:** About a light-year's distance from the central source, there are clouds or filaments of dense gas swirling around with velocities of about a few thousands

Region	Continuum Features of AGN
Dusty Ring	Thermal emission-IR bump
Accretion Disk	unpolarized thermal emission
-	big blue bump
Hot Corona	Compton reflection
Base of Jets	Inverse Compton Scattering
-	Soft X-ray excess
Jets	Inverse Compton Scattering, synchrotron radiation
Relativistic accretion disk	Broad $FeK_{\alpha}$ emission line

Table 2.1: Wide range spectrum of AGNs could be explained by the emission from different components.

of kilometers per second. These clouds are ionized and heated by UV and X-ray photons from the very central source. Fluorescent emission from these clouds produce the broad emission features seen in the spectra of quasars and Seyfert 1 galaxies.

- Molecular Torus: Outside the broad-emission line region, there is a doughnut-shaped region of molecular gas and dust. They are heated by the non-thermal radiations from the central source, emitting infrared light. Besides, this layer of dust could optically hide the central black hole.
- The Narrow Line Region: The region has a lower column density ( $\sim 10^{20-21} \text{ cm}^{-2}$ ) and low density clouds ( $\sim 10^4 \text{ cm}^{-3}$ ). The ionization condition of the gas in this region is similar to the region BLR, but the velocity is lower, about few hundreds of km/s, because of the larger distance from the center. The physics condition in this region is different from the BLR, despite the very similar level of ionization. For instances, the observed spectrum of this component includes intense forbidden lines, because of the low densities. Low densities of the environments prevent the meta-stable state electrons from colliding with other electrons before emitting forbidden photons.

## 2.2 Properties and Classification

Classification sometimes is one of the best ways to understand unknown phenomena when they have diverse properties. There are several challenges in classifying AGNs e.g.:

- The diversity of different classification methods in different wavelengths. As mentioned before, the diverse classification methods in different wavelengths sometimes makes things more complicated. For example, the quasar classification is based on optical morphology, whereas the Seyfert 1 galaxies is based mainly on the optical spectroscopic. It is hard to draw a dividing line in luminosity between quasars and Seyfert 1 galaxies.

- Variability with time evolution: Since the time we have been able to accurately measure brightness of AGNs has been just 100 years, this is, compared to estimated typical lifetimes of AGNs ( $10^7$  -  $10^8$  years), only a short period. Therefore, it is possible that the properties of AGNs may change later. In reality, we have known that some AGNs change their spectral in the time scales of years.
- Classification may change: Due to the improvement of the detectors and developments of new techniques, new observational evidence comes. The classification may change. This happens in particular with the presence of broad emission lines in the optical spectra, like BLRG/NLRG.

### 2.2.1 Orientation-based Unified Scenario

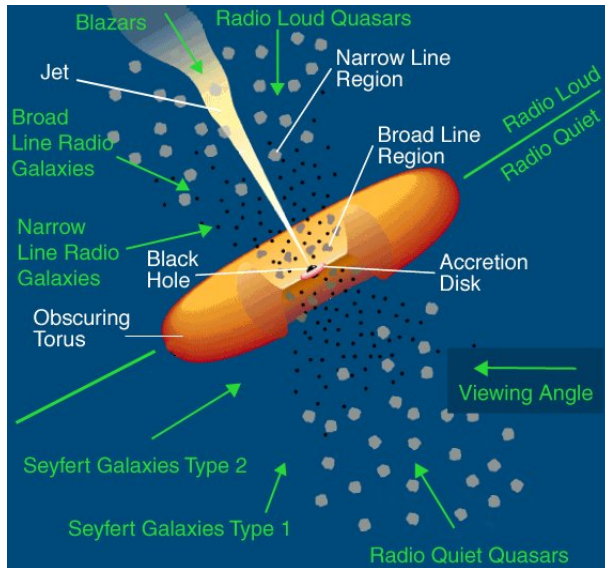


Figure 2.3: The unified model based on orientation.

The basic idea of the orientation-based classification is that we believe all the different types of AGNs belong to the same parent population of AGNs with similar intrinsic properties. The differences are due to the orientation and anisotropy effects. It is important for astronomers to investigate the observed parameters which are orientation-dependent and those which are not. Table 2.2 adapted from Urry and Padovani (1995) [19] shows the simple classification of AGNs according to two parameters: "radio-loudness" and "optical emission line properties". The distinctions in the horizontal direction are due to the viewing effect, the cause of distinction in the vertical direction, i.e.: radio-loud or radio-quiet, is still unknown. Fig. 2.3 shows the orientation-based ideas which was originally proposed in 1995.

<sup>1</sup>The title of the thesis: Long-term X-ray Variability of Active Galactic Nuclei and X-ray Binaries.

Radio loudness	Optical emission line properties		
Radio-quiet (85-90%)	Type 2 (narrow lines) Seyfert 2	Type 1 (broad lines) Seyfert 1 QSO	
Radio-loud (10-15%)	NLRG (FR I, FR II)	BLRG SSRQ FSRQ	Blazars BL Lac, FSRQ
Decreasing jet angle to line of the sight. →			

Table 2.2: The table shows the unification model of AGNs adapted from Urry and Padovani (1995) [19]. QSO: Qusi-Stellar-Object. NLRG: Narrow Line Radio Galaxy. BLRG: Broad Line Radio Galaxy. FSRQ: Flat Spectrum Radio Quasar. SSRQ: Step Spectrum Radio Quasar. FR: Fanaroff-Riley

## 2.3 Blazars: OVV and BL Lacs

Blazars are members of AGNs with a relativistic jet that is pointing in the general direction of the Earth. This accounts for the rapid variability and compact features of both types of blazars. In addition, many blazars have apparent superluminal features. It can be divided into two subclasses: highly variable quasars, sometimes called Optically Violent Variable (OVV) quasars, and BL Lacertae objects. The generally accepted picture is that OVV quasars are intrinsically powerful radio galaxies, having stronger broad emission lines and tending to have higher red shift. While BL Lac objects are intrinsically weak radio galaxies, BL Lacs are characterized by a rapid and large amplitude flux variability and significant optical polarization. They have spectra dominated by a featureless non-thermal continuum. In both cases, the host galaxies are usually giant ellipses.

### 2.3.1 Relativistic Beaming

The observed emission from a Blazar is strongly enhanced by relativistic effects in the jet. The bulks of the plasma inside the jet have a speed of up to 99.97% of the speed of light (the  $\gamma$ -factor is about several tens). The relativistic bulk emits photons mostly through synchrotron radiations. The beaming effect could be shortly summarized into three different effects. (i) Relativistic aberration (beaming), (ii) time dilation, and (iii) blue(red) shift. The first effect is understood by the following picture: Photons emitted by an object moving close to light speed will appear to be emitted in a cone around the direction of the motion. The opening angle of the cone depends on the velocity. Thus, if we look along the objects moving direction, the source appears brighter. Quantitatively, aberration accounts for a change in luminosity of  $D^2$ , where  $D$  is usually called the Doppler factor:

$$D = \frac{1}{\Gamma(1 - \beta \cos\theta)} \quad (2.4)$$

where  $\Gamma = \frac{1}{\sqrt{1-\beta^2}}$ , is called the Lorentz factor, and  $\beta = \frac{v}{c}$ . The time dilation is the special relativity effect. The time duration becomes shorter along the moving direction of the bulk, thus

the number of photons per unit time received by the observer along the moving direction is larger. This contributes a change in observed luminosity by a factor  $D$ . The last effect is blue-shifting. This is similar to the Doppler effect, changing the observed luminosity. The rapid variability of these objects in brightness and in polarization could be explained by relativistic jets. The apparent luminosity  $L_{app} \sim 10^{45}$  erg/s during the strong flares of Mrk421 or Mrk501 will be enhanced because the radiations produced by a source move with a big Doppler factor,  $L_{in} \sim D^{-4} L_{app}$ . Relativistic beaming effects can strongly alter the appearance of a distant galaxy. Also note that the jet on the other side, which is moving away from the Earth at relativistic speeds, is affected differently. The observed luminosity from this counter-jet is redshift and less luminous.

### 2.3.2 Short Time Variability in Photon Flux and Spectrum

The emission of blazars is intrinsically highly variable in all time scales and energies. The different scales of variability have been observed in different wavelength bands. Usually the flux at a shorter observed wavelength varies with larger amplitudes. Moreover, the flux variations at different wavelengths are almost simultaneous, but in some cases, time lags of a few days between optical and UV [73], UV and X-ray and X-ray and TeV emissions have been found. The observed TeV variability could be very rapid and big. The shortest doubling time reported so far is about a few minutes of Mrk501 [74], PKS2155 [75] and about 15-20 minutes for Mrk421 [76]. This can be explained by the beaming effect (with a high Doppler factor) and a quite small emission region. From the causality argument, the emission region could be estimated with  $R \leq ct_{flare} \delta/(1+z)$ , because the information traveling inside the sources could not be faster than the speed of light. At present, there is no strong indication that short time variability happens preferentially during specific states of average intensity.

There are many theories which try to explain the short time variabilities of blazars. Tanihata et al. 2003 [77] and Guetta et. al. 2004 [78] associated the blazar flares with the shocks inside the jet with the apparent variability time scale strongly compressed because of the bulk relativistic motion of the jet materials. Short time variability will be discussed in more detail in Chapter 10.

### 2.3.3 Superluminous Motion

There is no spectral line in the blazar emitted spectrum, which means that the speed of the jet materials could not be measured directly from the Doppler shifting of the emission lines. However, physicists believe that the energy power of AGNs mainly comes from the accretion of the matter into the black hole and the kinetic energy of the black hole rotation. The most compelling evidence involves the radio observations of materials ejected from the cores of AGNs with the so-called superluminal motion [79].

Suppose a source is traveling with a velocity  $v$ , with an inclined angle  $\theta$  measured from the line of sight. A photon is emitted along the line of sight at time  $t = 0$  when the source is at a distance  $d$  from the Earth. At a time  $t = t_1$  later, another photon is emitted where the distance to the Earth is  $d - vt_1\cos\theta$ . Photon A reaches Earth at time  $t_2$ , where  $t_2 = \frac{d}{c}$ . Photon B arrives at Earth at time  $t_3$ .

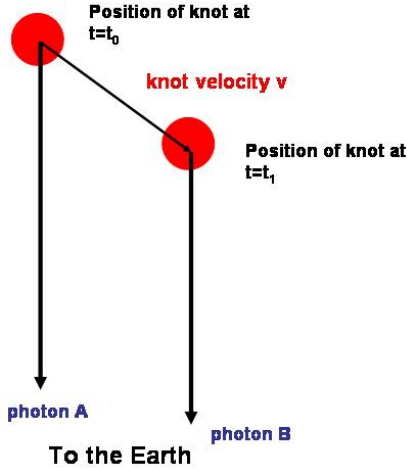


Figure 2.4: The explanation of superluminal motion

$$t_3 = t_1 + \frac{d - vt_1 \cos\theta}{c}, \quad (2.5)$$

The time on Earth between the reception of the two photons A and B is  $\delta t = t_3 - t_2$ . For the observers, the transverse velocity measured on Earth is then

$$v_{app} = \frac{v \sin\theta}{1 - v \cos(\theta)/c} \quad (2.6)$$

$v_{app}$  becomes the largest value of  $v/\sqrt{1 - (v/c)^2}$ , when  $\cos\theta = v/c$ . If  $\gamma (1/\sqrt{1 - (v/c)^2}) \gg 1$ , the apparent velocity becomes about  $\gamma$  times of the light velocity.

$$\gamma_{min} = \frac{1}{\sin\theta_{min}} \quad (2.7)$$

## 2.4 VHE $\gamma$ -Ray Emission from Blazars

Only few EGRET blazars have been detected at TeV energies. They are Mrk501, PKS2155-304 and 3C279. It seems that there is a GeV-TeV anti-correlation. Actually, this anti-correlation agrees with expectations [80]. The strong EGRET blazars are located at large distances, therefore the TeV  $\gamma$ -rays emitted by these blazars suffer intergalactic absorption due to extragalactic IR background. In addition, the significantly higher density of infrared and optical photons in quasars not only produce effective  $\gamma$ -ray production through IC, but also limit the maximum energy of the accelerated electrons due to the same process. In consequence, a strong shift of both

synchrotron and IC peaks in the SED of powerful blazars towards lower frequencies is expected. Of currently established 27 TeV  $\gamma$  AGNs, 24 are blazars. The dramatically enhanced fluxes of the Doppler-boosted radiation, resulting from the orientation of the jets towards the observers, make these objects a good laboratory for studying the AGN jet physics. The emissions from blazars at longer wavelengths, such as radio and optical, are due to synchrotron radiation. Emission in the high energy band such as  $\gamma$  is widely believed to be IC scattering of low energy photons up to TeV energy. However, the so-called proton-induced cascades or other hadronic scenarios cannot be ruled out at present. In the next section, I will discuss the blazar  $\gamma$ -ray emission models.

### 2.4.1 Leptonic Models

#### The SSC Model

The most favorite and successful model of blazars TeV emissions is the so-called SSC (Synchrotron-Self Compton) model. It assumes that both the X-ray and the TeV emissions originated in the relativistic jets due to the synchrotron radiation and IC scattering of the same population of high energy electrons. In the simplest case, the one zone homogeneous SSC model, assumes that the seed photons for the IC scattering are the synchrotron photons in the same emission region within the jet. The emission region has a characteristic size  $R$ , moving at the relativistic speed  $\beta = v/c$ , with an angle  $\theta$  to the observer's line of sight. In the co-moving frame of the source, the distributions of hot electrons and photons are isotropic and homogeneous. The observed SED of TeV-emitting blazars is characterized by two broad peaks, as mentioned. Below and above both peaks, the spectrum could be described with the power law indices  $\alpha_1$  and  $\alpha_2$ , respectively, where usually  $\alpha_1 \leq 1$  and  $\alpha_2 \geq 1$ . The left sides of both peaks normally have identical power indexes. However, the spectrum on the right hand side of the peak (the highest energy regime) is still poorly known and can be also affected by intergalactic absorption.

To fulfill the observed curved spectral shape, we require the relativistic electron spectrum to steepen with increasing energy. This behavior is normally attributed to a broken power law [81] with indexes  $n_1 \leq 3$  and  $n_2 \geq 3$  below and up the break energy  $\gamma_b m_e c^2$  [81]. With the above assumptions, there are seven parameters which in total can fully describe the models. They are the magnetic field intensity  $B$ , the size of the emission region  $R$ , the Doppler factor  $\delta$ , the slopes  $n_1$  and  $n_2$  of the electron spectrum, the Lorentz factor of the electrons at the break energy  $\gamma_b$ , and the electron density parameter  $K$  [82]. The peak synchrotron power is emitted by electrons with a break energy of  $E_b$ . The maximum energy  $\gamma_{max}$  is not very crucial here if  $\gamma_{max} \gg \gamma_b$  and  $\gamma_{min} \leq 100$ .

From the multiwavelength data, there are at least 6 observables which can be derived from observations. They are

- the photon index of the synchrotron radiation before the break:  $\alpha_1$
- the photon index of the synchrotron radiation after the break:  $\alpha_2$
- the frequency of the synchrotron at the peak:  $\nu_s$
- the frequency of IC peak:  $\nu_c$

- the total measured energy flux of the synchrotron component:  $L_s$
- the total measured energy flux of the IC component:  $L_c$

The above mentioned observables are ideally the result of a fitting procedure on simultaneous multiwavelength data. Usually, the best sampled region is from optical to X-ray, thus  $\alpha_1$ ,  $\alpha_2$ ,  $\nu_s$  and  $L_s(\nu_s)$  are better determined. Sometimes additional observables can be found. One example is the minimum timescale of variation,  $t_{var}$ . From  $t_{var}$ , we can derive the upper limit of the size of emission region R, if we assume a certain value of the Doppler factor. Occasionally, the constraints in the parameter-space for the given maximum size  $R_{max} = t_{var}c\delta_j$  are expressed in terms of two parameters on the (logB.  $\log\delta_j$ ) plane. Other, stronger, constraints could be provided for example by the optical depth of  $\gamma$ - $\gamma$  interaction, or by the observed time lags between soft and hard photons, or by the consistency value of  $\gamma_b$ . These extra information could be checked for physical consistency of the one zone homogeneous SSC model. The (logB.  $\log\delta_j$ ) plane analysis will be discussed in Chapter 10.

### EIC Model

In some cases, the SSC model cannot satisfactorily explain the observed SED. For instance, the number of seed photons from the synchrotron radiation of high energy electrons does not sufficiently explain the huge amount of luminosity of the observed IC peak. Therefore, one may think of adding more seed photons. A possible additional source of the seed photons are ambient infrared or optical photons, cosmic microwave background, or thermal radiation photons. The thermal photons may come from the accretion disk or scattered photons from surrounding clouds. All these sources are outside the jet, therefore we often call this model External Inverse Compton (EIC) model.

### Summary of the Leptonic Model

From current observations, the SSC model can well explain most of the VHE  $\gamma$ -ray emission from blazars, e.g. the observed correlation between X-ray and VHE  $\gamma$ -ray flux levels during the big flares of VHE  $\gamma$ -ray emissions. The leptonic models have two attractive features. The first one: The required TeV electrons in the jet can be explained through the relatively better understood shock acceleration mechanism. The second one: Both the synchrotron and IC radiation channels operate at very high efficiency. This is true because the IC cooling time of the electrons is  $t_{IC} \propto E_e^{-1}$ , and in the mean time, the IC boosts the ambient photon energy, which is  $\propto E_e$ . Therefore the characteristic time of the  $\gamma$ -ray emission decreases with energy as  $\propto E_\gamma^{-1/2}$ . This will explain why we see different variability timescales for different wavelengths. The relatively low energy electrons responsible for the lower energy radiation (such as GeV, MeV, optical/UV photons..) cannot respond promptly to the changes of the physical conditions in the source. Thus, the VHE emissions give a prompt response from the sources.

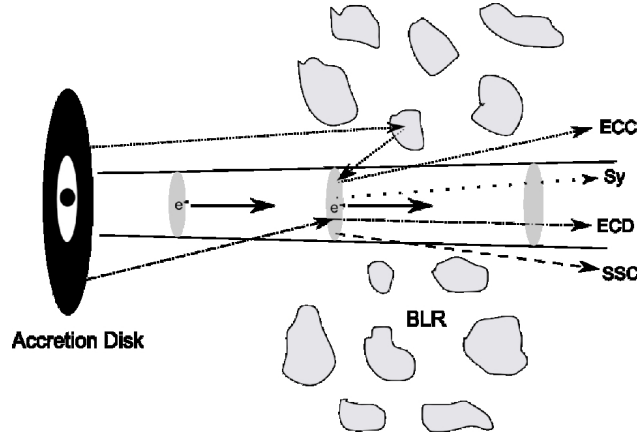


Figure 2.5: The leptonic model of blazar TeV emission. Blobs of high energy accelerated electrons are moving away from the central black hole and emit synchrotron photons. Relativistic electrons interact with these synchrotron photons via the inverse Compton process producing the synchrotron self-Compton (SSC) peak. The thermal photons from the accretion disk may also interact with electrons in the jet to produce the External Comptonization of Direct disk radiation (ECD) peak. Photons also come from the clouds of gas in the broad line region (BLR) and interact with the blobs of electrons to produce External Comptonization of radiation from the Clouds (ECC) peak. The plot is from [6]

## 2.4.2 Hadronic Models

The hadronic models assume that there are high energy protons accelerated together with the electrons inside the jet. They explain the observed  $\gamma$ -ray emission as being initiated by accelerated protons interacting with ambient matter [83], photon fields [84], magnetic fields (pure proton synchrotron model) [85], or both magnetic and photon fields [86].

In these models, protons need to be accelerated to very high energies ( $\geq 10^{18}$  eV), otherwise, they cannot provide sufficient  $\gamma$ -rays inside the jets. Particularly in the proton synchrotron and proton-radiation interaction models, protons have to be accelerated to close to  $10^{20}$  eV. Moreover, in order to make the proton synchrotron radiation become an effective mechanism of  $\gamma$ -ray production, we need a strong magnetic field close to 100G inside the jet.

Although, we do not know how those protons are accelerated up to such high energies, we do see particles with such high energies in ultra-high energy cosmic rays. We believe that AGNs are one of the possible acceleration sites for such energetic particles. The low energy peak of the SED in this scenario is explained by the synchrotron radiation of the co-accelerated electrons, since the proton synchrotron radiation will not be as efficient as electrons. Unless the magnetic field inside the proton jet is higher than SSC jets, it is very difficult to explain the low energy peak only from protons. Investigations show that if the proton acceleration takes place at a very high rate, for a typical Doppler factor  $\delta \geq 10$ , the proton synchrotron radiation would extend well into the TeV regime. Also, this process allows very hard intrinsic  $\gamma$ -ray spectra, giving a reasonable explanation for the stable spectral shape of TeV emission as observed during the strong flare of

Mrk501 in 1997, and it predicts significant spectral steepening in low states [85].

The problem for the hadronic models is how to explain the correlation variability of the X-ray and TeV observations. In the proton synchrotron model, the synchrotron peak at X-ray is explained by the counter components of UHE protons in the jets, i.e. electrons. Synchrotron photons are generated by the electrons but at different places from the TeV photons production region by protons. The reason is that in the high magnetic field region where TeV photons are produced, the electron synchrotron loss is very fast, the time is much shorter than the dynamical time. This results in a flat synchrotron spectrum from optical/UV to MeV/GeV, which is not fitted to the observed data.

However, there is another possibility of the synchrotron radiations coming from secondary electrons produced by the interactions of the primary TeV  $\gamma$ -rays with the ambient low frequency radiation. With this scenario, we expect tight correlations between X-ray and TeV photons, because these secondary electrons are immediately cooled down in the strong magnetic field. Nevertheless, more complicated correlations can not be excluded, if the magnetic field outside the blob drops significantly.

### 2.4.3 Mixed Models

In some cases, the TeV flare of a blazar can not find any X-ray counterpart. This is the so-called "orphan TeV flares". Genuine orphan TeV flares would not be easily understood either by SSC or hadronic models. It is interesting that the orphan flare may be understood in a hybrid scenario where protons are present in the jet but not necessarily the dominating component compared to lepton components [87]. In this case, the TeV orphan flare is associated with and follows a pair of simultaneous X-ray and TeV flares that originate in the standard SSC process. The synchrotron photons (here X-ray) are then reflected due to some external clouds and return to the jet. The return photons will interact with the protons inside the jet to produce pions and thus the following "orphan" TeV flaring originates from the  $\pi_0$  decay. This model has shown to work for the "orphan" TeV flare observed in 1ES1959+650 [87].

### 2.4.4 Other possibilities ?

At the beginning of 2009, the H.E.S.S. collaboration made a new discovery: the detection of the VHE gamma rays from the Cen A region. The Cen A is classified as a FR I galaxy and has jets which are  $40^\circ$  away from our line of sights. The spectrum extrapolated from the EGRET spectrum about GeV to VHE energies regimes which H.E.S.S. measured is roughly matched. There are several models which predict VHE emission from Cen A or even more generally the radio galaxies. The first model proposed the VHE emission region to be located in the immediate vicinity of a super massive black hole. [88] and [89] proposed the particle acceleration was taking place in the magnetosphere of the sub-Eddington accretion super massive black hole. This model was successfully applied to M87. One characteristic of this model is that the luminosity of the IC emission is proportional to the mass of the black hole, i.e.  $L_{IC} \propto M_{BH}$ . Because we already know (from gas kinematics measurements) that the mass of the central black hole in Cen A is around  $10^8 M_\odot$ , which is about 30 times less than M87, the IC emission luminosity is also

about 30 times less from Cen A in this model. Another explanation is proposed by Lenain et al. 2008 [90]. He explains the VHE emission of Cen A with a multi-blob SSC model.

One possibility and maybe the most interesting explanation is that the VHE emission is due to extended emission. When  $\gamma$ -rays are produced in the immediate vicinity of the nucleus, they are absorbed by the starlight in the host galaxy. The created  $e^\pm$  pairs could interact with starlight by inverse Compton scattering. This process will create isotropic halos and the angular size of the halo is about 4 arcmin in diameter, depending on the local magnetic field. [91] predicts that VHE emission of Cen A is a steady flux with a photon index of  $\propto 2.6$  at the TeV energy regime. This model explains the H.E.S.S data quite well. This scenario could be resolved by the future project CTA with better angular resolution.

## 2.5 The Impact of VHE $\gamma$ -ray Observation of AGNs on Physics

The blind survey of the Galactic plane performed by the H.E.S.S. collaboration has revealed interesting and previously unknown populations of the VHE  $\gamma$  sources. Unfortunately, a survey with a similar sensitivity of the extra-galactic sky has to wait until wide field of view Cherenkov telescopes or arrays of telescopes are available. Some of the big questions about the blazars are [92]:

- Is a simple one-zone SSC model sufficient to explain all (multi-wavelength) data ?
- Where does the acceleration of particles actually take place ?
- What is the dominant acceleration mechanism in blazars and what is the composition of the jet ? Are jets mainly electron/hadron or electron/positron ?
- How are the jets formed and collimated ?
- Are jets merely accretion powered or can jets gain the energy from the central black hole ?
- How strong is the beaming effect ? From the above section, we know that the opening angle of the beam depends on the Lorentz factor  $\Gamma$ . If the  $\Gamma$  is big, the opening angle gets narrower. In consequence, a high beaming factor can lead to a dramatically increased number of blazars that are not pointing in our direction.
- Can particles be accelerated to TeV energies without a jet ?
- Is there any internal absorption due to photon-photon scattering with pair production ? If the answer is yes, how big is the effect ?
- How strong is the absorption on the extra-galactic background light (EBL) ?

TeV observations have provided and will give useful inputs:

- The central engine: The limit on the black hole mass derived from TeV observations due to time variability appears to be inconsistent with the current study on black-hole/bulge relation.

- The kinematics inside the jets: A lower limit on the Lorentz factor of the emitting fluid can be derived from the requirement that the pair production opacity at TeV energies is small enough to allow the TeV photons to escape into infinity. The size of the emission region could also put another constraints. Thus, we could derive a limit on the Doppler factor of the TeV emission zone independent of its location. The Doppler factor  $D$  has been calculated for each flare. In some extreme cases, values from 30 to 100 were found.
- Where is the location of the TeV emission zone ?

### 2.5.1 Extra-galactic Background Light

TeV  $\gamma$ -rays from distant sources are absorbed by a huge amount of infrared photons due to the photon-photon interaction. The effect will result in the existence of a "Gamma Ray Horizon (GRH)", which limits the visibility of observing the very high energy  $\gamma$  rays coming from very far distances in the universe. The distance of the horizon depends on the number density of the diffuse background photons in the corresponding relevant energy range. In the energy range which can be studied effectively by ground-based  $\gamma$ -ray telescopes (from 50 GeV to 50 TeV), the most relevant EBL component is the ultraviolet (UV) to infrared (IR) contribution. Though EBL could be "directly" measured with different methods through different wavelengths [93], these methods suffer from a lot of uncertainties due to subtracting the uncertain foreground objects, such as zodiacal light. Thus the "indirect" probe by TeV  $\gamma$  telescopes could provide an effective method for measuring the EBL.

# Chapter 3

## Imaging Cherenkov Telescopes

High energy particles and electromagnetic (EM) radiations usually cannot be detected directly. They are normally detected through their interactions with matters. High energy particles or high energy EM radiations coming from extraterrestrial space, will be visible from ground-based detectors only with sufficiently high energies, the rest will be inevitably interacting with the materials inside and then be absorbed by our atmosphere. The interactions of particles and photons with matters are different. The detecting method depends on the characteristics of the primary particles (such as the energy and the species), the target materials (such as the compositions and the density). In this chapter, I will first focus on the high energy particle interactions inside the atmosphere and the idea of extensive air showers (EAS). Subsequently, I will discuss the Cherenkov radiation phenomenon and the Imaging Atmospheric Cherenkov Telescope (IACT) techniques.

### 3.1 Extensive Air Showers

Photons interact with materials with photoelectric effect, Compton scattering and pair productions. Generally speaking, photons are either absorbed (photoelectric effect, pair production) or scattered (Compton effect). The interaction processes are totally statistical. Therefore, the range of a gamma ray is generally quite difficult to define.

In case of photons with energies above 3 MeV, pair production becomes the major effect. Electrons and positrons are created in the Coulomb field of a nucleus. The radiation length is defined as a thickness of material where the electrons lose their energy due to the bremsstrahlung and reduce their energy to 1/e of its original value. The mean free path for high energy photons is 9/7 of radiation length. It is convenient to use the unit of radiation length to describe photon and electron interactions in the material.

Our atmosphere, unlike the usual calorimeters in the lab which are constant in density, has exponential structures of density from top to bottom. The density profile of our atmosphere may also change with the seasons or the weathers. In the first approximation, it could be described as a density profile  $\rho_{atm} \sim \rho_0 e^{-h/h_0}$ , where the constant  $\rho_0 \sim 1.225 \text{ kg/m}^3$  and  $h_0$  is 8.4 km. It is useful to apply a parameter, the slant depth X, which defines the actual amount of air traversed

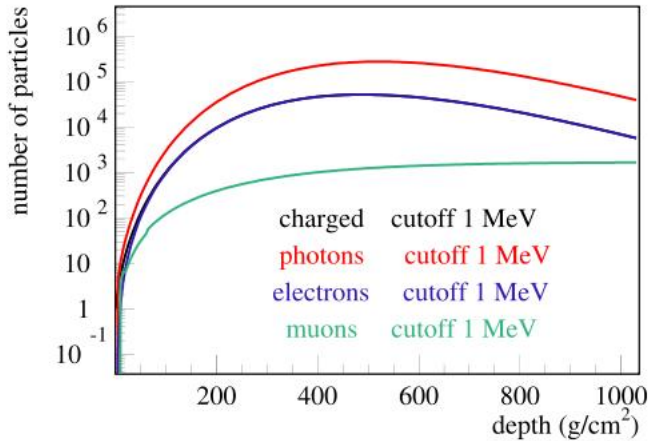


Figure 3.1: The longitudinal development of an extensive air shower. The x-axis is the atmosphere depth expressed as the number of radiation lengths. The y-axis gives the number of electromagnetic particles in the air shower. Sea level is about 28 radiation lengths, 2600 m above sea level is about 20 radiation lengths [?]. The primary particle is photons at 100 TeV.

by the extensive air showers. While a gamma ray produces an electron-positron pair,  $e^\pm$  produce a new generation of gamma rays through bremsstrahlung. The whole process produces cascades of particle showers with increasing numbers of electrons, positrons and photons. Fig. 3.1 shows the number of cascade particles as a function of the atmospheric depth. The whole phenomenon is called electromagnetic cascade or electromagnetic shower. The electromagnetic showers and hadronic showers (these will be described later) occur in the Earth atmosphere; they are called Extensive Air Showers (EAS).

Because of ionization energy loss and existing threshold energy for pair production, the numbers of secondary particles will not increase infinitely during the shower development. In reality, the average energy of these secondary electrons and positrons drops down to the point where the ionization energy loss per radiation length becomes higher than electron, positron energies. The shower development begins to fall off as fewer electrons have sufficient energy to produce secondaries. Since these charged particles are relativistic and faster than the speed of light in the medium, Cherenkov light will be produced. There are more abundant cosmic rays rather than high energy gamma rays bombarding the Earth. Those cosmic rays are mainly composed of protons or charged nuclei. If the energy of the incident particles is high enough, these particles produce hadronic secondary particles via interactions with nuclei in the atmosphere. The secondary particles consist of many mesons and baryons. They may, in turn, interact and produce or decay into further secondary particles in the atmosphere. This phenomenon is called hadronic shower / hadronic cascade. The multiplicity slowly increases with the energy.

### 3.1.1 Products in Extensive Air Showers

There are several different interaction processes happening in the EAS. In principle, the products of each process could be used for indirect detection of the incident primary particles, some of which are mentioned below:

#### Charged Particles

Shower particles can be detected on the ground, either by scintillators or particle counters. Normally, we can measure electrons, photons and muons. Because the rate of very high energy air showers is very low, particle detectors are usually deployed in wider areas with relatively large spacing in between such that we can detect the showers more efficiently. Experiments like AGASA, AUGER and KASKADE are that type of experiments. This technique works well for shower energies larger than 100 TeV.

#### Cherenkov Radiations

The relativistic particles in EAS produce Cherenkov light. The reflective index of the atmosphere near the ground is 1.0003. If the particles have gamma factors larger than about 40, they can emit Cherenkov light. I will discuss this phenomenon more deeply in section 3.5.

#### Fluorescence Light

When shower particles pass through the atmosphere, they may excite atmospheric nitrogen molecules. These molecules will be in de-excited states and emit light isotropically in the near UV regime. This phenomenon will become more important, if the primary particles have very high energies, say 1 EeV. The fluorescence light gives important information about the shower developments. The typical fluorescence light emission is within 10 to 50 ns after excitation, which is longer than Cherenkov light emission. Experiments like HiRes, AUGER and TA have fluorescence light detectors which are in operation along with other surface detectors.

#### Radio Emission

Charged particles inside the showers, mostly electrons and positrons, are deflected slightly because of the Earth's magnetic field. When these particles change directions, they emit synchrotron radiation. This radiation is visible as a bright flash on the sky for several nanoseconds at frequencies of up to a few hundred MHz. Experiments like LOPES, having 30 dipole antennas, are operated together with air shower surface arrays to see such kind of signals. Future projects like LOFAR, aim to build an interferometric arrays of radio telescopes in Europe to look for such radio signals.

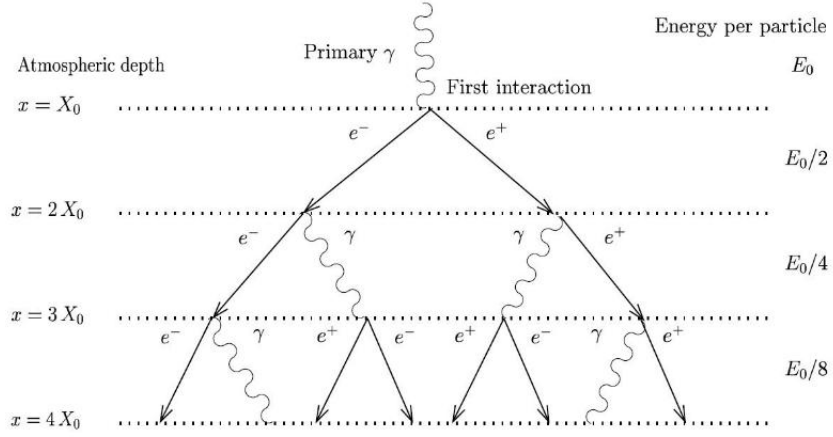


Figure 3.2: Heitler Model of EM showers. In this model, the  $\gamma$ -ray initiated showers are simplified as the combination between the  $e^+e^-$  production and bremsstrahlung interactions.

## 3.2 Electromagnetic Showers

The EM shower has been mentioned in Section 3.1. The cascade processes could be described with a simplified model. Fig. 3.2 shows a toy model developed by Heitler. Electron and positron roughly share half of the initial energy of the gamma. After a certain distance  $nX_0$  (n radiation length),  $2^n$  particles will be created. Each has an average energy of  $E_0/2^n$ , where  $E_0$  is the energy of the primary particle. Once the energy of each particle is lower than  $E_c$ , which is called critical energy, the multiplication process will stop and the whole cascade will have the maximum number of particles. Below  $E_c$ , the major energy loss of the electrons is due to ionization rather than to bremsstrahlung. Note that the energy loss of an electron due to bremsstrahlung is proportional to its original energy.

$$\frac{-dE_e}{dx} = \frac{E_e}{X_0} \quad (3.1)$$

$$(3.2)$$

$X_0$  is commonly called radiation length. The value is  $37.2\text{g}/\text{cm}^2$  in the air. For photon pair creation, the mean free path is given by  $\frac{9}{7}X_0$ . The two values are quite comparable. The longitudinal shower development of EM cascades depends on the critical energy of the materials. In Rossi and Greisen's classical calculation, they considered only bremsstrahlung and pair production neglecting the Compton effect and photon-nucleus interactions. The total number of electrons above the critical energy  $E_c$  in the shower can be approximated by

$$N_e(t) = \frac{0.31}{\sqrt{\ln(E_0/E_c)}} \cdot \exp(t(1 - 1.5\ln s)) \quad (3.3)$$

where

$$s = \frac{3t}{t + 2\ln(E_0/E_c)} \quad (3.4)$$

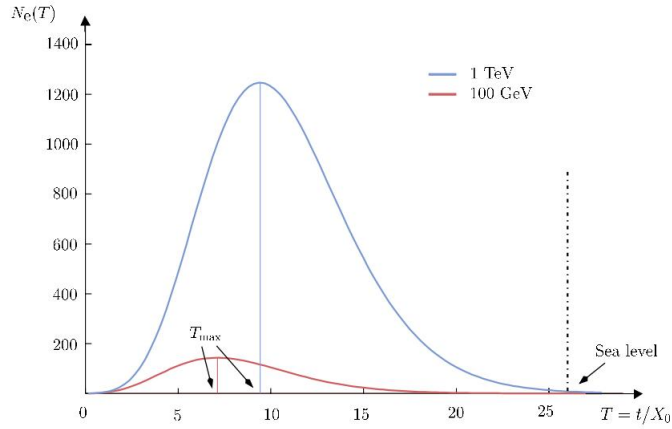


Figure 3.3: The longitudinal electron distribution in EAS.

$$t = X/X_0 \quad (3.5)$$

where  $s$  is called the "age" of the shower. When  $s \leq 1$ , it means that a shower is developing. When  $s = 1$ , the shower is at its maximum. If  $s \geq 1$ , this means the shower is decaying.  $t$  is the atmospheric depth. The longitudinal electron distribution from Equation 3.3 is shown in Fig. 3.3. The plot shows that the higher the energy of the primary, the deeper the air shower penetrates into the air. From the second equation, we can see the shower maximum ( $s=1$ ) happens at  $t_{max} = \ln(E_0/E_c)$ , which depends on the energy of the primary photons. The energy window of the MAGIC telescope ranges from 60 GeV to 30 TeV. From the same figure, we know that these showers develop their maximum well above the telescope level. The critical energies and radiation lengths of electrons vary in different materials. They depend on the material atomic number  $Z$ . The larger  $Z$ , the lower the critical energy and the shorter the radiation length. For example, the electron critical energies and radiation lengths in the water and in the air are quite comparable.

### 3.3 Hadronic Showers

Hadronic showers are initiated by cosmic ray protons and nuclei. Hadronic particles mostly participate in hadronic interactions which are governed by QCD. They are different from interactions initiated by electrons and photons which are governed by QED (see Fig. 3.4). However, since  $\pi^0$  are always produced in hadronic showers, and then decay into two  $\gamma$ s, the hadronic showers could be considered as being many sub-electromagnetic showers combined with a hadronic core.

The production of secondary particles in a hadron cascade is caused by an inelastic hadronic process. Charged and neutral pions are produced, but also with lower multiplicities kaons, nucleons and other hadrons. The particle multiplicity per interaction varies only slightly with energy. About 1/3 of the neutral pions are produced. They are subject to large fluctuations which are determined by the first inelastic interaction. Compared with electromagnetic showers, whose

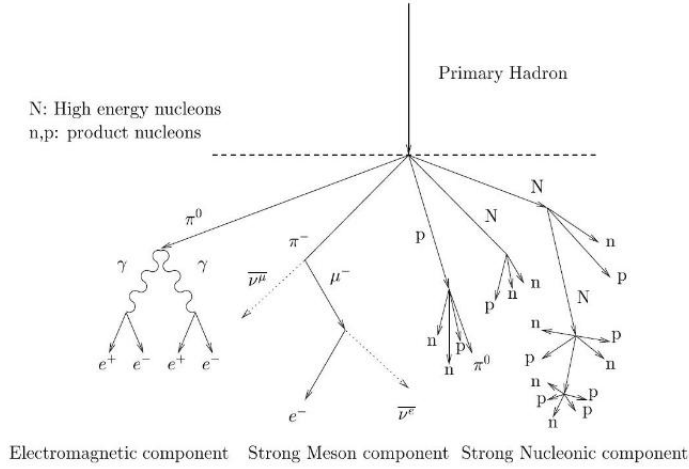


Figure 3.4: Conceptual sketch of hadronic showers

energy may be completely deposited inside the atmosphere, a portion of the energy of hadronic showers is simply "missing" because of several reasons. The first one is that neutrinos will be generated in EAS. The second one is that the energies of penetrating muons produced in hadronic showers can not be fully absorbed in the atmosphere. Consequently, the total hadron shower signals with the same energy are normally smaller than photon/electron shower signals. Around 1 TeV energy, the energy deposit of hadronic showers in the atmosphere is about 1/3 times smaller than the same energy of electromagnetic showers.

### 3.4 Lateral Distribution of the Showers

The multiple Coulomb scattering (described by the theory of Moliere) of the secondary electrons inside the showers results in a lateral spread of the showers. In the case of electromagnetic showers, the lateral distribution scale could be estimated by a quantity known as Moliere radius  $R_{mol}$  and is given by :

$$R_{mol} = x_{mol}/\rho, \quad x_{mol} = X_0 E_s / E_c \quad (3.6)$$

where  $E_s$  is the average scattering energy of electrons in the path of one radiation length material, which is  $m_e c^2 (4\pi/\alpha)^{1/2} \sim 21.2 \text{ MeV}$ . At sea level,  $R_{mol} \sim 80 \text{ m}$  at the position of the shower maximum of 1 TeV photon ( $\sim 10 \text{ km}$  above sea level), the value becomes about 200m. The Moliere radius is the radius of a cylinder containing roughly 90% of the secondary particles produced in a cascade. The lateral distribution in three dimensions is approximated by numerical solutions which are known as the Nishimura-Kamata-Greisen (NKG) function, given in Fig. 3.5. We have known that the air shower experiments can only sample the shower front with arrays of small detectors. The total number of particles in a shower therefore has to be obtained by fitting the individual densities sampled at each detector to NKG lateral distribution. The electron density in lateral distribution is shown in Fig. 3.5.

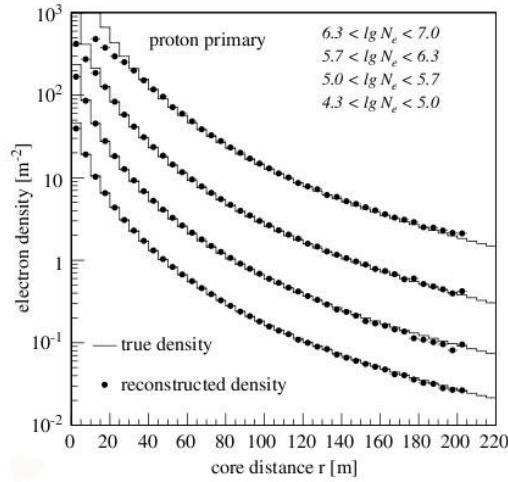


Figure 3.5: The Nishimura-Kamata-Greisen (NKG) electron lateral density distribution. The primary particles are proton showers with different energies.

Another important issue is the muon component. The muons which are detected at sea level reflect the shower development in the atmosphere. Those muons originate from pion decay. The lateral distribution of the muons has a spread of about 300m on the ground (Greisen's empirical formula) and it is wider than for electrons.

## 3.5 Cherenkov Light

Cherenkov light is produced when a particle moves through a medium with a velocity larger than the light velocity in the same medium. For a particle with velocities  $\beta_c$  in a medium with an index of refraction  $n$ , the angle  $\theta_c$  of Cherenkov radiation, relative to the particle's direction is:

$$\cos\theta_c = \frac{1}{n\beta} \quad (3.7)$$

Since in the atmosphere the index of refraction  $n$  changes with height (because of the temperature, density...etc), the Cherenkov angle  $\theta_c$  changes with the height as well. At STP the  $\theta_{max} = 1.3$  degrees. The threshold velocity required to produce Cherenkov emissions  $\beta_t$  is  $1/n$ . Thus the threshold energy for the emission of the Cherenkov light could be roughly estimated:

$$E_{min} = \frac{0.511}{\sqrt{2\delta}} \quad (MeV) \quad (3.8)$$

where

$$\delta = 1 - n, \quad \delta \propto \exp(-H/H_s) \quad (3.9)$$

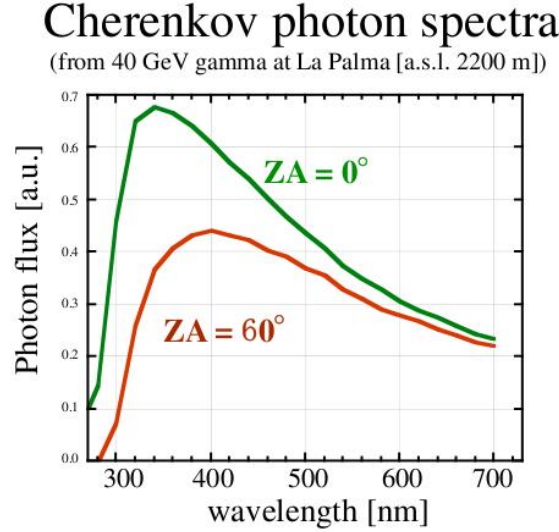


Figure 3.6: The Cherenkov spectrum after the absorption in the atmosphere for the gamma ray showers with an incidence angle of zenith and zenith angle of 60 degrees.

H is the altitude. From the above, we know that the threshold energy changes with the height as well. For example, at sea level, the threshold energy is 21 MeV, however at 8 km above sea level, the value increases to 35 MeV.

Normally, Cherenkov radiator materials are dispersive. Assume  $w$  is the photon's frequency, and  $k = 2\pi/\lambda$  is the wavenumber. The photons propagate at the group velocity  $v_g = dw/dk$ . In a non-dispersive medium, this simplifies to  $v_g = c/n$ . The number of photons produced per unit length of a particle with a charge Ze and per unit energy interval of the photons is

$$\frac{dN_p}{dl} = 4\pi\alpha(1 - (\frac{E_{min}}{E})^2) \int \frac{\delta}{\lambda^2} d\lambda \quad (\text{photons/meter}) \quad (3.10)$$

From the above we know that photons with longer wavelengths are suppressed because of the  $1/\lambda^2$  factor. In Fig. 3.6, a typical Cherenkov light spectrum from a 50 GeV gamma ray shower is shown. Cherenkov photons are absorbed by Rayleigh and Mie scattering once they have been produced inside the atmosphere. Those two effects will distort the pure Cherenkov spectrum, especially in the shorter wavelengths, photons are attenuated heavier. In consequence, compared with vertical showers, inclined showers are more "reddish" because of the longer path and heavier attenuation of the shorter wavelength photons in the atmosphere. A clear atmosphere has good transmittivity down to 290 nanometers. Below 290 nm, the ozone absorption starts.

The Cherenkov photon lateral distribution is useful and generally employed for energy estimations. The lateral distribution is affected by longitudinal shower developments, such as the shower maximum point. The intensity of the Cherenkov light is a function of the atmospheric depth X.

$$I \propto (1 - \frac{c^2}{n^2 \nu^2}) \propto X \quad (3.11)$$

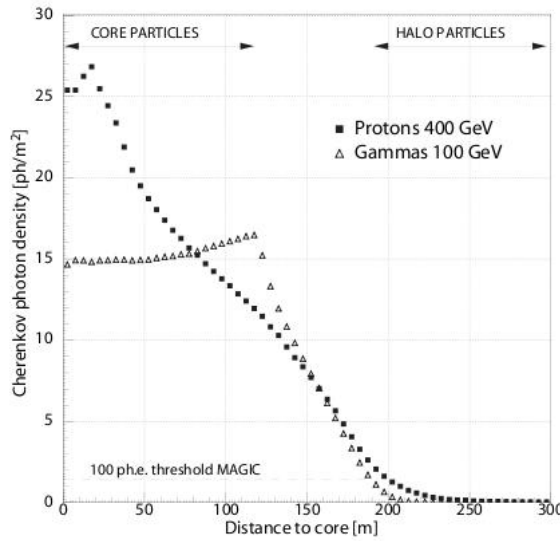


Figure 3.7: The Cherenkov light lateral distribution, compared with proton shower and gamma shower. The observational level for this simulation is about 2200 m above sea level.

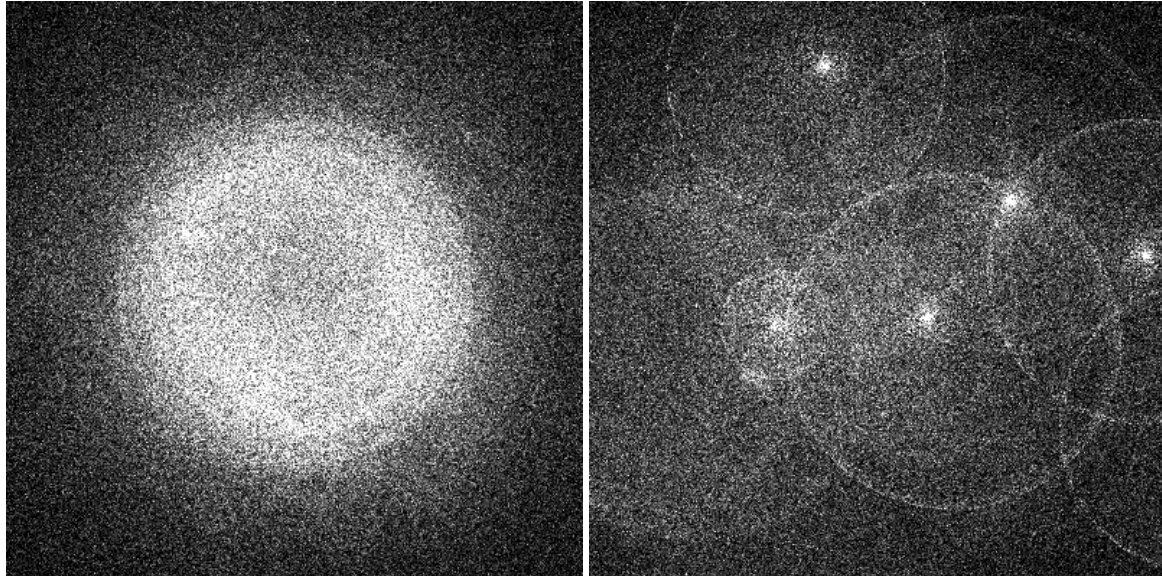


Figure 3.8: The Cherenkov light pool on the ground. The small black dots are the Cherenkov photons. The left plot is from a 300 GeV  $\gamma$  shower, the right plot is from a 1 TeV proton shower.

The maximum of the Cherenkov light emission is reached while the shower dies out. All relativistic secondary particles inside the shower produce Cherenkov photons with a cone along the shower axis and form a "donut ring" on the ground. These rings overlap producing the so-called Cherenkov light pool. The orientation of the ring depends on the incident angle of the shower and the size of the ring depends on the altitude of the detection level and the height of the shower maximum, see Fig. 3.8<sup>1</sup>. In Fig. 3.7, the Cherenkov light density inside the light pool is almost proportional to the energy of the primary particle. The photon density inside the light pool as a function of the energy of the primary particle is given for different particle types in Fig. 3.9. For  $\gamma$ -rays, an almost constant fraction of the primary energy is converted into Cherenkov photons. Thus, a measurement of the Cherenkov photon density is a good probe of the energy of the primary VHE  $\gamma$ -ray.

The Cherenkov light from electromagnetic and hadronic showers looks different. Hadronic showers look more messy because they produce many subshowers. Those differences of Cherenkov light patterns will give us hints for discriminating between hadronic and electromagnetic showers. However, the differences will become smaller if the energy is lower.

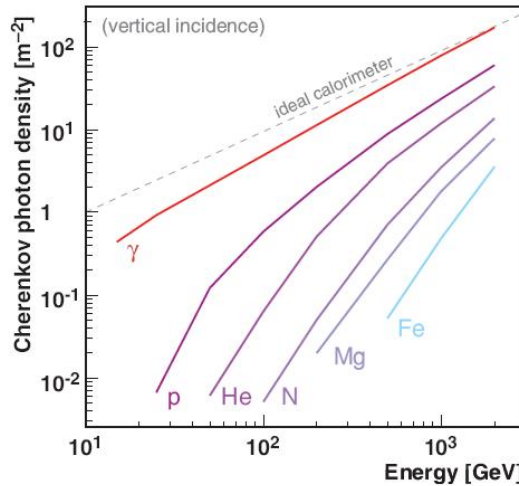


Figure 3.9: The Cherenkov photon density with different energies and different primary particles. The photon density is taken within 125 m of the shower core for vertical showers [7].

Another useful information is the timing information from the Cherenkov light fronts. The Cherenkov light pulse shape is related to the shower's longitudinal development. The typical time duration of the Cherenkov pulses produced by a gamma air shower is around 3 ns within the light pool which is about 120 m. For the hadronic showers, the time spread is wider.

If two particles are close enough, smaller than 1 wavelength of their radiation, the electromagnetic fields from these particles may add coherently such that the Cherenkov radiation is affected. The radiation from an  $e^+ e^-$  pair at close separation is suppressed compared to two independent leptons. Coherent radio Cherenkov radiation from electromagnetic showers is large

<sup>1</sup>These figures are taken from the website: <http://www.mpi-hd.mpg.de/hfm/CosmicRay/ChLight/ChLat.html>.

and significant. It has been used to study VHE cosmic ray air showers and search for  $\nu_e$  induced showers.

## 3.6 Imaging Cherenkov Telescopes

### 3.6.1 Introduction

Our Earth's atmosphere can be considered as a very deep electromagnetic calorimeter with approximately 30 radiation lengths of material (above sea level). Normally, the VHE shower maximum is about 10 km above sea level.

A typical IACT has a light collection mirror with a size of  $100\text{-}250\text{ m}^2$ , relatively small compared to the area of the lightpool of  $5 \times 10^4\text{ m}^2$ . As a result, the intrinsic fluctuations in the shower development as well as limited sampling with the ground-based detectors constitute a fundamental limit to the energy resolution. IACTs could provide good energy resolutions up to 15% - 20%.

### 3.6.2 Imaging Techniques

The Cherenkov telescopes map the Cherenkov photons using mirrors onto a camera which is located in the focal plane. Parallel light rays with equal opening angles towards the optical axis are imaged onto the same point in the camera. The basic mapping principle could be explained by Fig. 3.10. The shower light distribution on the camera plane could be seen from the same figure. The shower image on the camera is not a perfect ellipse. With decreasing height, the points are mapped further away. As a result, the image is asymmetric along the longitudinal direction.

Hillas [94] first introduced the diagonal form of the matrix of the second moments of the shower images to parametrize the shower images. The sets of parameters are called "Hillas parameters", and they have become the standard analysis method in gamma ray astronomy. The details of those parameters will be discussed in Chapter 6.

The success of this technique results in the ability to reject a huge amount of the cosmic-ray background based on the shape of the images. The use of the multiple IACTs in stereo observation helps to increase the sensitivity and resolution because of the better shower sampling and better background rejection. The muon rings could be useful for the telescope energy calibration.

The current existing Cherenkov telescopes and telescope arrays are summarized in Table 3.6.2 [20]. Recently, the MAGIC collaboration has finished the construction of the second telescope with the aim of using stereoscopic techniques to improve the sensitivity and reduce the energy threshold. The H.E.S.S. collaboration is constructing its second phase and plans to build a  $600\text{ m}^2$  telescope at the center of the existing array, with the goal of achieving sensitivity in the unexplored  $\leq 50\text{ GeV}$  region. The IACT technique has been proved to be a useful tool for exploring the high energy universe.

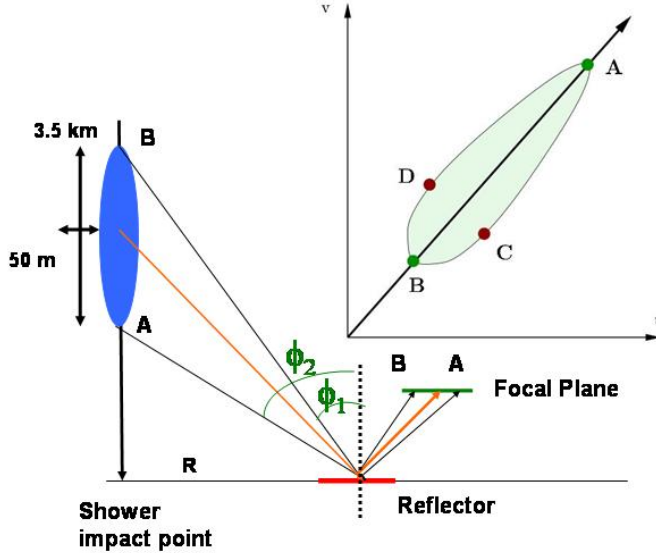


Figure 3.10: The Cherenkov light image on the camera. The orientation of the image depends on the inclination of the shower. The length and the position of the image are determined by the angular difference  $\phi_2 - \phi_1$  and the impact distance  $R$ . The bottom plot shows that the later distribution of the shower could be seen from the width of the shower image. The 4 points A, B, C, D on the top plot are imaging on the focal plane in the bottom plot. From the plot, we know that the mapping is not linear. With decreasing height, the points are mapped further away. Finally, the image is more compressed inside and dilated on the outside yielding an asymmetric shape along the image axis. Nevertheless, the two symmetric points C and D are off-axis symmetrically from the image axis, because the EM showers are on average symmetric along the shower axis

Instrument	Altitude (m)	Tels	Tel. Area ( $m^2$ )	Total A.	Pixels	FOV	$E_{th}$ (TeV)
H.E.S.S.	1800	4	107	428	960	5	0.1
VERITAS	1275	4	106	424	499	3.5	0.1
MAGIC	2225	1	236	236	574	3.5	0.06
CANGAROO-III	160	3	57.3	172	427	4	0.3
Whipple	2300	1	75	75	379	2.3	0.3
Shalon	3338	1	11.2	11.2	144	8	0.8
TACTIC	1300	1	9.5	9.5	349	3.4	1.2
HEGRA	2200	5	8.5	43	271	4.3	0.5
CAT	1650	1	17.8	17.8	600	4.8	0.25

Table 3.1: The list of currently operated IACTs with two selected older generation IACTs, HEGRA and CAT. The table is adapted from [20]

# Chapter 4

## The MAGIC Telescope

The lower energy threshold together with an improved energy resolution of ground-based Cherenkov telescopes have been the most important breakthrough of gamma ray astrophysics in the GeV -TeV regime. Lowering the energy threshold of ground-based Cherenkov telescopes for the first time makes it possible to cross-calibrate with space-based GeV detectors. The MAGIC telescope (Major Atmosphere Gamma-ray Imaging Cherenkov telescope ) in Fig. 4.1 was designed and built for this purpose. MAGIC covers the unexplored energy regime from 30 to 300 GeV with high sensitivity. This energy regime is important and had not been explored neither by satellite nor by IACTs before 2003, when MAGIC was completed.



Figure 4.1: The first MAGIC telescope.

This energy region is significant particularly for probing the physics of pulsars, far distance GRBs and AGNs. The design study of MAGIC was finished in 1998, the production and construction phase started in 2001. After a commissioning phase, which commenced in mid-2003, scientific observations have been carried out since September 2004. The MAGIC telescope is located on the Canary Island of La Palma. (28°45'N,17°53'W) at the Observatorio del Roque de los Muchachos (ORM), the same observational site as the HEGRA telescopes. The altitude is about

2200 m above sea level. This area has one of the best astronomical conditions in the northern hemisphere. In this chapter, several key hardware components of the MAGIC telescope will be introduced. I will outline their uniqueness and contributions to AGN monitoring and why they are essential in dedicated programs.

## 4.1 The Unique Features of MAGIC

There are several advanced, unique features and techniques adapted in the MAGIC telescope.

- The largest single dish light collection area: MAGIC has a 17 m diameter reflector with a focal length of 17 m. The total reflection area is about  $236 \text{ m}^2$ . It is so far the largest single-dish IACT in the world. The big collection area aims at detecting low energy showers thus lower the energy threshold.
- The mirror supporting structure is made of a space frame structure with the carbon fiber tubes, in order to promptly respond to a GRB trigger. Light weight is a crucial issue and is essential in the MAGIC design.
- The water-proof aluminum mirrors: The surface of all aluminum mirrors is stronger than that of the glass mirrors.
- The active mirror control (AMC): The segmented mirrors are easy to control and to optically re-focus by AMC.
- The high quantum efficiency camera: The PMT pixel-based MAGIC camera will be presented in more detail in the next chapter.
- Optic fiber analogue signal transmission with VCSEL. MAGIC transfers analogue signals with optic fiber cables and VCSELs. This design reduces the weight of the camera and the inertial mass of the telescope in rotation. The signals from PMTs are converted into optical signals and sent to the counting house without attenuation /degradation of the signals via optic fiber cables, and then converted again to electric ones at the counting house before digitization.
- MUX-FADC with a high sampling rate of 2 GHz Samples/sec. The high sampling rate makes the pulse reconstruction more precise. It helps the  $\gamma$ /hadron separation and thus lowers the energy threshold.

## 4.2 The Data Chain

The data readout chain is configured like in Fig. 4.2. The PMT signals are converted into optical ones, sent from the Camera to the counting house. Then the pulses are digitized by the FADC there. The data are stored in the Ring Buffer. Once an event has been triggered, the FIFO will read out the triggered events from the Ring Buffer.

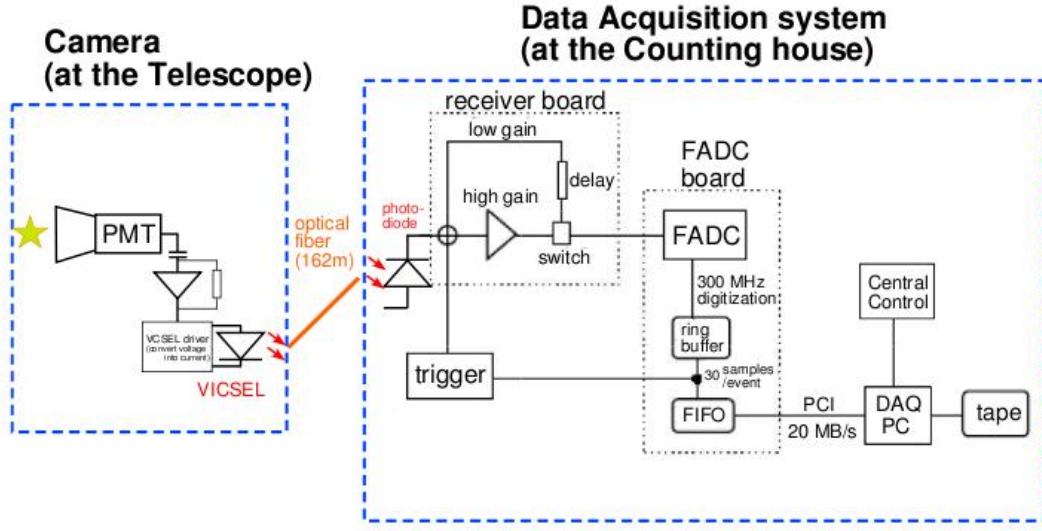


Figure 4.2: The complete data readout chain of MAGIC before the MUX FADC was installed. The figure is from [8]

### 4.3 The Telescope Structures and the Drive System

The whole MAGIC Telescope has been constructed with a space frame structure with carbon fiber tubes. The total weight of the telescope is about 65 tons. It is an alt-azimuth mount on a circular rail. Unlike in equatorial mount systems, a balance of the azimuthal axis can be achieved without additional counterweights. While tracking the stellar objects, the telescope has to move in azimuth and elevation directions. The azimuth axis is equipped with two 11kW motors, while the elevation axis has a single motor of the same power. The angular position of the telescope is measured by three 14-bit shaft encoders.

With its light structure, MAGIC can reach a high slew rate  $\leq 40$  sec for fast response to astrophysical transient objects such as GRBs. This feature has made MAGIC quite unique because it is the only IACT in the world which is able to respond fast to transient objects. The tracking precision is better than 1.5 arc minutes, which corresponds to a quarter (1/4) of the pixel diameter of the MAGIC camera. With these configurations, the telescope pointing accuracy is  $0.02^\circ$ . The pointing of the telescope is calibrated by taking pictures of bright stars at different azimuth and zenith angles using a CCD camera called T-point camera, see Fig. 4.3. The deviations of the observed position of the stars from their expected positions are considered to be errors of the tracking system. The star field monitoring provides us a lot of information, like the sky brightness, and thus implies the weather conditions in the atmosphere. Due to the gravitational force, deformation of the mechanical system is inevitable with time. To ensure reliable pointing and tracking accuracy, this effect has to be monitored and corrected. The corrections are done by the so-called "pointing model" or "bending model" which parametrizes the deviations. Thus, the position of the telescope is constantly monitored by using another CCD camera mounted on the reflector frame, the so-called star guider camera. The position of the PMT camera is recognized

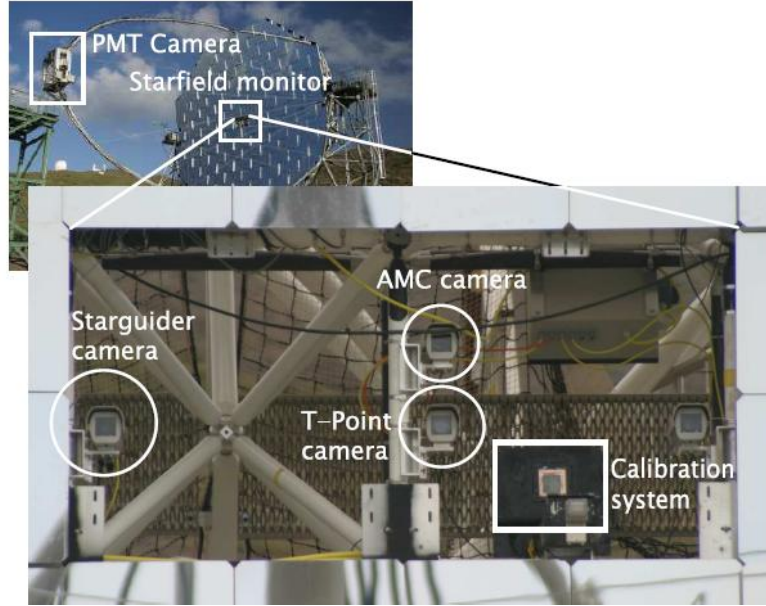


Figure 4.3: All the CCD cameras in the middle of the reflector of the MAGIC telescope. All of them have different purposes, which are illustrated in the text. The figure is from [9]

by the star guider camera using 6 red LEDs mounted on the border of the PMT camera.

## 4.4 The Reflector and the Mirrors

The whole reflector has a parabolic shape with a focal length equal to its diameter, which is 17 m. The F value is equal to 1, which is completely different from conventional optical telescopes and also other IACTs, which mostly follow the so-called Davis Cotten design. The parabolic shape is isochronous conserving time information of the Cherenkov photons. This is particularly important for big dish reflectors. Although the parabolic reflector distorts the image if the photons are not coming along the optical axis, such distortion will not cause a serious problem with the limited FOV of 3.5 degrees. The entire reflector is composed of 956 spherical mirrors, each of them  $50\text{cm} \times 50\text{cm}$  in size. The lightweight, diamond-turned mirrors have a reflectivity of about 80% in the wavelength range of 350 - 650 nm, see Fig. 4.4. Those mirrors are equipped with internal heating wires for disposing of ice and dew.

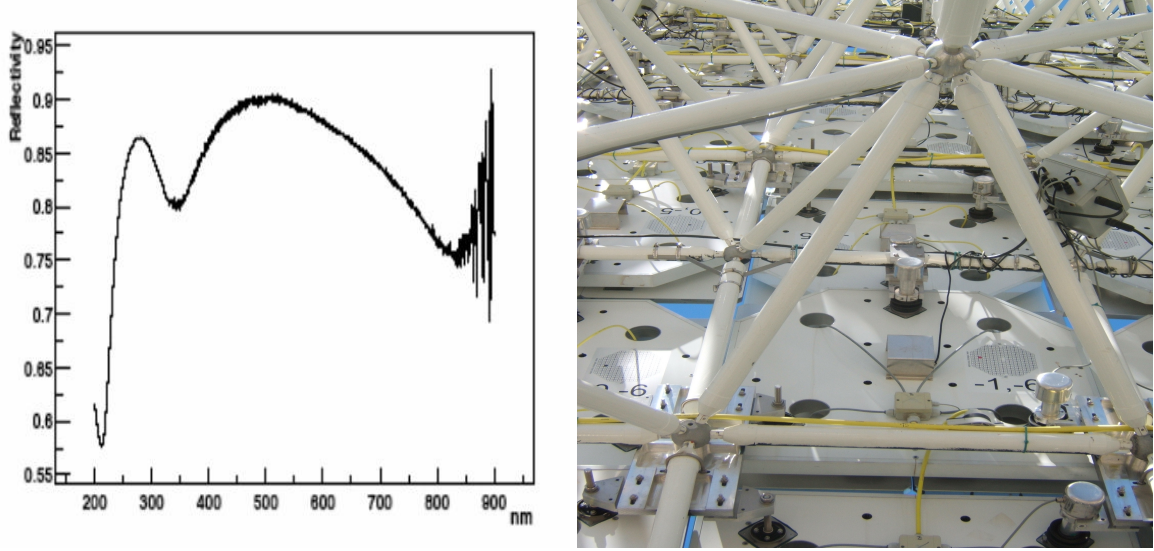


Figure 4.4: The left plot shows the measured reflectivity of the mirror in different wavelengths. The right picture shows the backside image of the mirror. The big silver-colored box contains the AMC electronics. The small yellowish box below controls the mirror heating.

## 4.5 Active Mirror Control

The reflecting surface of the telescope is supported by a lightweight carbon fiber space frame. The system is designed with the cutting-edge technique of the active mirror control system. The electronics control box is behind the mirror mounting, see Fig. 4.4. The active mirror control is an advanced design which has been used in optical astronomy. Each of the mirror supports is equipped with two motors and one laser pointer. The laser shoots a spot on the closed camera system; in addition, there is a CCD camera which is necessary for calibration of the focusing. This CCD camera can determine the laser spot with respect to some references which are defined in respect to several LEDs mounted on the cover of the PMT camera. The same alignment can be achieved by looking at the stars. The CCD camera can identify the reflected star light from each panel. The AMC can adjust the position of the panels such that the spot is focused in the center of the PMT camera. The corresponding positions of the panels are stored as a function of the zenith angle in a so-called look-up tables (LUTs). During data taking, LUTs adjusting and laser focusing is realized. Further details can be found in [95].



Figure 4.5: The left picture shows two different sizes of the PMT pixels used in the MAGIC telescope. The right picture shows the PMT pixel module in the camera plane.

## 4.6 The Camera

The camera is one of the key components of an IACT. The Cherenkov photons reflected from the mirrors will be collected by camera pixels and form images. Since the Cherenkov light pulses are normally short (within 3 ns), we need a fast response device. Photomultipliers are considered to be good candidates. The MAGIC camera is composed of 576 pixels of hemispherical PMTs which were coated with a special lacquer that increases the quantum efficiency by up to 15-20% between 350 - 470 nm [11]. Each pixel is coupled with a dedicated hexagonal light collector which maximizes the double-crossing probability of photons at large incident angles. The inner part of the camera, which is the trigger region, is equipped with 396 1" ET 9116A PMTs. The outer region is filled with 180 1.5"ET 9117A PMTs, see Fig. 4.5. In the outer part of the camera, the light spots are spread over an area of  $\sim 0.2^\circ$  diameter due to coma aberrations of the reflector. Thus, the usage of the bigger pixels in the outer region is reasonable and, in addition, saves cost. More information about the pixels will be presented in the next chapter.

## 4.7 Signal Transmission

At the base of a PMT, the signal is AC coupled to an ultra-fast preamplifier with a gain of about 6. After the preamp, the signals are converted into light by using fast current driver amplifiers coupled to vertical cavity surface emitting laser diodes (VCSELs). The analog optical signal is transmitted from the camera to the counting house by optical fibers which are approximately 162 m long. The optical signals preserve the original characteristics of the electronics signals, like the pulse width and pulse amplitude. All the characteristics of the optical transmission system have been studied in detail in [11].

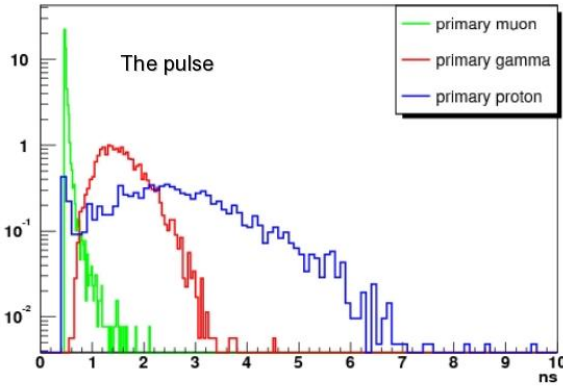


Figure 4.6: Simulated distributions of the RMS of the arrival time distribution for  $\gamma$ ,  $\mu$  and proton events measured by MAGIC-like but ultra-fast telescopes. From the plot, the RMS value of the arrival time provides a separation power between three different types of events.

## 4.8 Receiver Board and Trigger

### 4.8.1 Receiver Board

The optical signals are received and converted back to electrical ones again by fast GaAs PIN diodes on the receiver board. The electronic signals are split into two. One part of the signal is sent to the trigger branch and the other part is sent to the FADC system, see Fig. 4.2. There are discriminators with high gain, low gain amplifiers on top of the board. After the MUX-FADC was installed in February of 2007, the high and low gain splitter is not necessary anymore.

### 4.8.2 Trigger

The MAGIC trigger decision is defined by three different levels. In current operation, only the first two are used.

- Level-0: Very basic discriminating of each pixel. After extraction the signals and charge integration from FADCs, the total amount of charges is digitized and converted into FADC counts. For each pixel, a constant fraction discriminator (CFD) will select only the pulses which pass through the trigger level. The threshold can be easily adjusted by software for different NSB levels, or FOVs, or trigger algorithms (such as SUM Trigger). The discriminator level is decided in order to keep individual pixel rates between 100 and 400 kHz. For MAGIC, the level-0 trigger is restricted to the inner camera only. The total angular span is about 1 degree.
- Level-1: To search for next neighboring coincidence. We know that electromagnetic showers are more compact than hadronic ones. Moreover, the hadronic showers are more messy. Close-neighboring coincidence is used for discriminating the hadronic and EM showers.

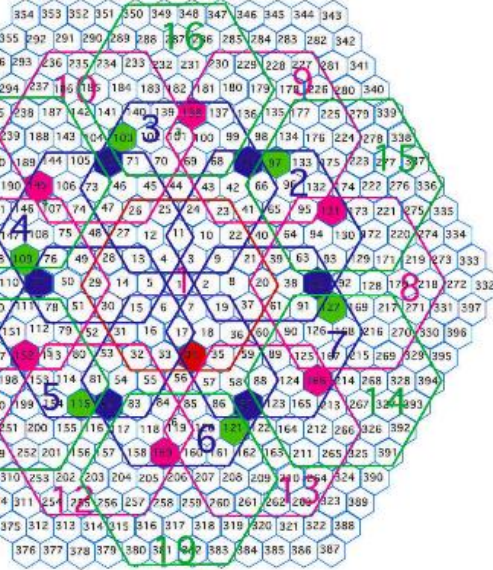


Figure 4.7: Sketch of the trigger topology in the MAGIC camera.

The camera is divided into 19 overlapping cells and with 36 pixels each. Fig. 4.7 shows the level-1 trigger topology. Level-1 gives a trigger signal if for at least one of the cells a logical condition is fulfilled.

- Level-2: Higher level trigger depending on the topology of the trigger pattern.

An individual pixel rate monitoring system is used to prevent high trigger rates which might be caused by the bright stars in the pixels. The whole system is adjusted such that the data are typically taken at a rate of 250 Hz.

## 4.9 FADC/MUX-FADC

Once the trigger has arrived, the FADC system will continuously digitize and write 30 slices into the buffer. The dead time is about 2-3 %. Under normal conditions, events are recorded at a rate of  $\sim 250$  Hz. Nevertheless, the maximum tolerable rate had been about 600 Hz before the MUX-FADC was installed in February 2007. The night sky background level at the MAGIC site is about 130 MHz. MAGIC was using 8-bit, 300 MHz FADCs for each pixel. In order to measure the Cherenkov pulse structure, the typical 2.5 ns FWHM signals are artificially stretched to 6 ns. The stretched pulse shape is unfortunately smears out the differences among pulse shapes induced by  $\gamma$ -ray, cosmic rays (mainly proton) and NSB photons. Furthermore, to provide a dynamical range of  $\sim 1000$ , a two gain charge extraction is implemented. The signal is amplified by a factor of 10 and then digitized. If the high-gain signal exceeds 250 FADC counts, a GaAs switch is activated and the delayed ( $\sim 55$  ns) low gain will be digitized. If the high-gain signal does not exceed that threshold, the recorded information is derived from the high-gain branch.

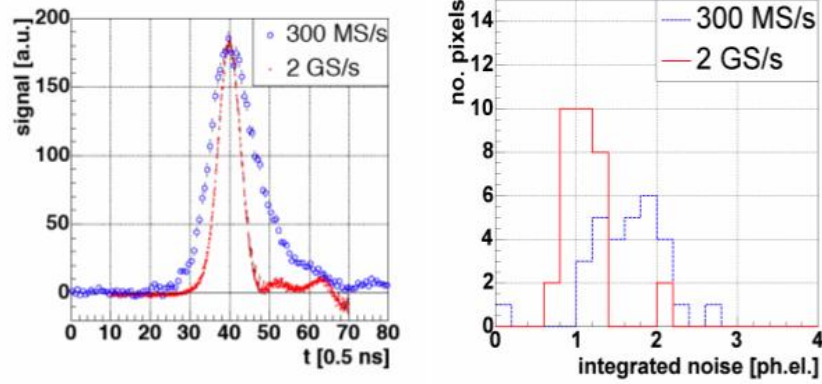


Figure 4.8: Performance comparison between old FADC and new MUX-FADC. The left plot shows the pulse sampling and the right plot depicts the pixel distribution of the integrated noise.

Therefore the recorded signal is either full of 30 slices of high-gain or 15 high-gain slices followed by 15 low-gain slices. If the FADC does not record the low-gain signal, the 15 late slices of the high-gain signal should not contain any information from a signal and thus could be used as an estimation of the pedestals.

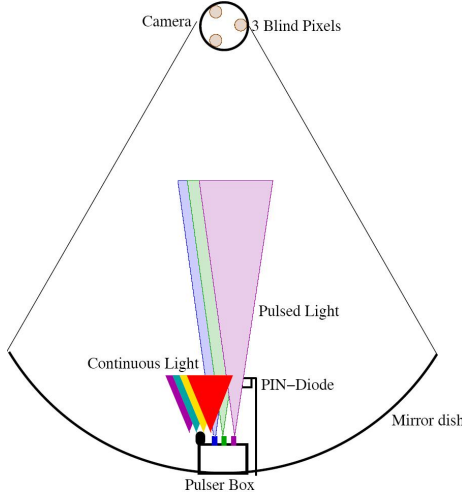


Figure 4.9: The different components of the calibration system used in the MAGIC telescope.

After February 2007, a Fiber-Optic signal multiplex system which uses a 10-bit, 2GSamples/s FADCs to digitize 16 read-out channels consecutively has been installed [96]. The analog signals from each of the 16 pixels are delayed by using optical fibers and digitized sequentially with the single channel of Ultra fast FADCs. This multiplexed (MUX) FADCs read-out reduces the costs by about 85 % compared to using FADCs for each readout channel. A comparison of the pulse sampling between old FADCs and the new MUX-FADCs is shown in Fig. 4.8. The total integrated time window is about 40 ns. If we dispose of the first and the last 5 ns switching noise, the effective time window is about 30 ns. The integrated noise is lower for MUX-FADCs than

for the old FADCs, see Fig. 4.8. A DAQ rate up to 100 MBytes/s corresponding to a trigger rate of 1 kHz has been achieved. The upgrade of the FADCs not only improves the rejection of the NSB photons, but also the  $\gamma$ /hadron separation. In Fig. 4.6,  $\gamma$ -ray, proton induced showers and muons have different distributions of the RMS value of the arrival times. The timing information is expected to improve the separation of  $\gamma$ -ray events from background events. Including a new analysis techniques using timing information from the air showers, the sensitivity moved up by 40 %.

## 4.10 Calibration System

The whole electronic chain of the MAGIC Telescope is calibrated. The main purpose is to obtain the conversion factors and absolute signal timing information. An optical calibration system has been installed [97]. It is composed of several differently colored ultra-fast LEDs with three wavelengths, namely 370 nm, 460 nm and 520 nm. These LEDs can illuminate the camera with different color of light pulses at different intensities. (from 5 to 700 phe. for each inner pixel). The whole system is illustrated in Fig. 4.9. By using this calibration system, the whole dynamical range of the camera is accessible. The pulsed light is used to achieve a relative calibration of the data chain using the F-factor method (will be described in the next chapter). The PIN diode and three blinded pixels are used for absolute calibration of the camera. The calibration events are recorded in dedicated calibration runs and interleaved calibration events during the regular data taking procedures. As a result, the gain variation of the whole data chain (e.g. from PMTs or VCSELs) can be monitored during the data taking.

## 4.11 Observational Mode

During observation, the data-taking sequence is performed in two different modes. In general, an observation sequence consists of a pedestal run, a calibration run and a number of data runs. The pedestal runs contain 1000 randomly triggered events. These events contain the signal baseline and its fluctuations are given by NSBs as well as noise in the readout chain. The calibration runs contain events triggered by the calibration system while synchronously uniformly illuminating the PMT camera by a flash LED or DC light source. These events are used to calculate an initial set of the calibration constants. Data runs contain events that triggered the telescope while tracking a particular sky position. Those runs contain interleaved calibration events at a rate of 50 Hz, which are used for a continuous re-calibration. Part of the events which do not contain any shower image are used to update the pedestal information. In addition to the data run, a number of subsystem monitoring files are produced by the telescope subsystems, for instance, the camera control system, the star field monitor and the central control system. These useful additional system information will be merged with the event data offline. At a certain point in the analysis (which will be described in the next chapter), they are then synchronized to each individual event.

Generally speaking, the MAGIC data was taken in one of the following observation modes.

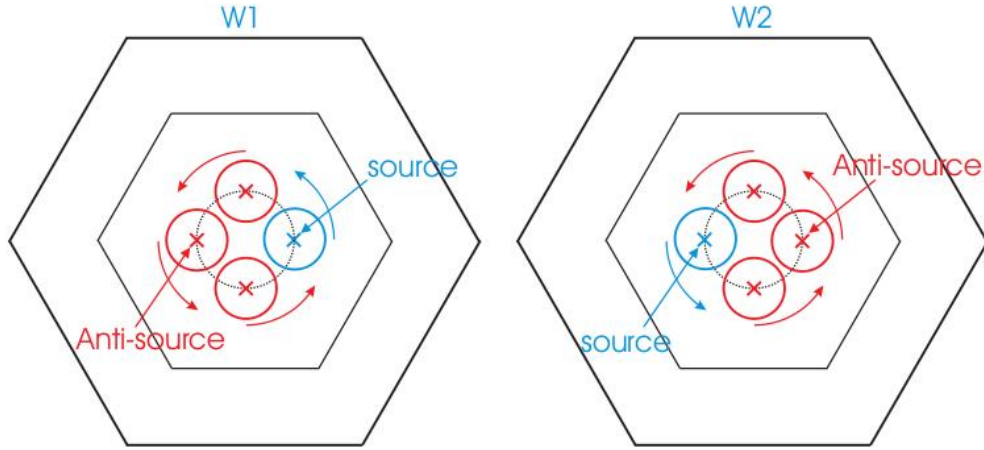


Figure 4.10: Illustration figure for different observational modes. In the ON-mode, the source is positioned in the center of the camera (red circle). For the WOBBLE observation, the source is placed at  $0.4^\circ$  off center (marked as "signal region" in the plot.) The background region in the WOBBLE-mode can be found at the opposite side of the signal region or even any other regions on the  $0.4^\circ$  circle. This provides a simultaneous measurement of the background. On average, every 20 minutes, the wobble positions are swapped. More background samples can be taken if the observation time is long enough. This increases the statistics of the background data. The plot is adapted from [10].

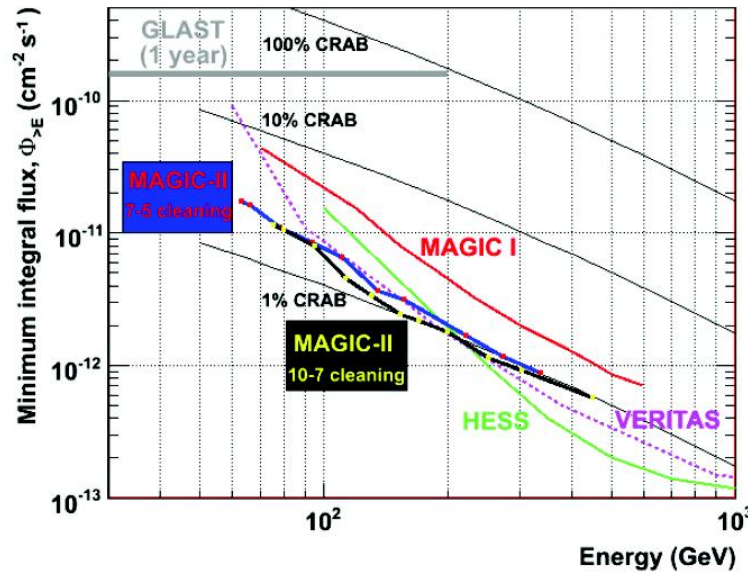


Figure 4.11: Sensitivity curve of MAGIC stereo-observation.

- ON/OFF mode : In this observation mode, ON and OFF observations are complemented by equal amounts of time. During the ON mode, the observed source position is tracked in such a way that the center of the camera is pointing to the source. While in the OFF mode observation, the telescope tracks a position in the sky where no  $\gamma$ -ray source is expected to be. In the ideal case, the OFF region of the sky should have the same background light and atmospheric conditions as the corresponding ON position. The swapping time is about 15-20 min between ON and OFF observations. The time should not be too long because the atmospheric conditions may change. Since the source is located in the center, thus this observation mode is more sensitive and suitable for measuring weak sources. The main problem is that the background and signal region may mismatch because they are taken at different times and the atmospheric conditions change.
- Wobble mode : In the Wobble observation mode, simultaneous recording of the ON and OFF data at different places in the camera is possible. The source position is located at a fixed distance of the camera center. The position which is at the opposite side of the source position is called "anti-source position". It can be used to determine the background. Sometimes, in order to get better statistics, two more background regions are defined at the same distance from the camera center, but  $\pm 90^\circ$  displaced from the source position. In order to reduce the systematics because of the chosen source position in the camera (in case if the camera is not homogeneous), the source and the background positions are regularly swapped in every wobble observation. Since the source is located at offset of the camera center, the acceptance of the trigger area is reduced for higher energy showers. If the data was taken only with one wobble position, the background determination has additional uncertainties because the camera inhomogeneity may destroy the background and data sample. Thus the swapping of the two positions helps to reduce the systematic effects. Moreover, the inhomogeneity of the camera will be smeared out due to frequent swapping between different wobble positions.

## 4.12 MAGIC II

The MAGIC Collaboration has built a second telescope at 85m distance from MAGIC I on the the island of La Palma. With advanced photon detectors and readout electronics, MAGIC-II, the two telescope systems, will have a reduced analysis threshold. The overall sensitivity in stereoscopic/coincidence operation mode is expected to increase by a factor of 2-3. The expected sensitivity curve is shown in Fig. 4.11. In order to reduce the energy threshold, the overall light collection efficiency for the Cherenkov photons has to increase. Therefore the camera of the second telescope will be equipped with optimized Winston cones and photon detectors with the highest possible quantum efficiency (QE) up to 33%. The testing characteristics of these photon sensors will be discussed in the following chapter.

# Chapter 5

## Photodetector Studies for the MAGIC II Telescope

### 5.1 Introduction

The exploration of the high energy cosmic radiation is realized through increasingly complex experiments covering a wide energy range from underground detectors, ground-based detectors, satellites and space observatories. The photodetectors are a basic and crucial part for nearly all the experiments in astroparticle physics. Especially, observing high energy cosmic radiations, such as gamma rays, cosmic rays and neutrinos all use the techniques based on measuring Cherenkov or fluorescence light induced by particle showers in different materials. Efficient photodetectors are required and needed.

The sensitivity of the IACTs relies on the light detection efficiency of the photodetectors. Basically, the higher the detection efficiency of the photodetectors, the better the sensitivity and the lower the energy threshold of the telescope. The Cherenkov light intensity is weak, thus it is necessary to work with photodetectors in photoelectron counting mode. In addition, Cherenkov light pulses are short down to a few ns, and the response time of the photodetector is crucial. For all the above reasons, photomultipliers (PMTs) are so far the most reasonable, best suited and most stable devices. They have been used in high energy physics experiments for quite a long time and the technologies of production and development are mature.

For further lowering the energy threshold and improving the sensitivity of the system, the new telescope was designed and built. It is using higher sensitivity PMTs. Various measurements of different characteristics of these PMTs, such as a single photoelectron spectrum (SPE), afterpulse rate, timing characteristics, aging and photoelectron detections were performed. All the results from the measurements will be presented in this Chapter.

### 5.2 The Basic Requirements

The main purpose of IACTs is detecting high energy photons. Many ideas concerning the detector design could be learned from the high energy physics devices. However, there are

specific requirements for IACTs, which have to be taken into account, which are summarized below:

- Better response in specific wavelengths: Intrinsic Cherenkov radiation starts from the UV regime and its intensities decrease with  $1/\lambda^2$ . At longer wavelengths, Cherenkov light intensity decreases sharply and at the same time, the intensity of the NSB increases. Part of the photons will be absorbed by the ozone layer, the Rayleigh scattering ( $\propto 1/\lambda^4$ ) and the Mie scattering in the atmosphere. After convolution and integrating all the factors, the effective Cherenkov photon spectrum arriving at the telescope is suppressed in the shorter wavelengths. Fig. ?? shows an example of a Cherenkov photon spectrum generated by a 300 GeV  $\gamma$  shower with an incident angle of 30°. The best choice for the photodetectors is the ones whose response windows happens to match with the effective Cherenkov spectrum.
- High quantum efficiency(QE) and photon detection efficiency(PDE): Higher QE and PDE increase the detection efficiency even for low energy showers. On the other hand, a more efficient detector will detect more NSBs as well but the gain is like  $S/\sqrt{B}$ . The NSB level at the MAGIC site is about 1 photoelectron (ph.e.) per 10 ns, the 30% gain in NSB ph.e. collection will not be an issue. In addition, the future stereo observation mode may help to reject random NSB triggers.
- Low gain (from  $2 \times 10^4 \sim 5 \times 10^4$ ): Since MAGIC observes also during moon and twilight time, it is important to slow down the aging effect of each pixel. Operating at lower gain degrades the ability to detect single photoelectrons because of noise limitations. For the second telescope, we look for tubes which have a single photoelectron peak about 5 sigma away from the pedestal peak.
- One-inch in diameter and hemispherical shape photocathodes: The size of the required PMTs depends on the field of view, the angular resolution, parabolic or Davis cotton design, ... etc. The second telescope is designed to have a f value equal to one and the angular resolution is 0.1 degree. In order to fulfill the requirement, one-inch pixel is desirable.
- Hemispherical shape: hemispherical PMTs have the following advantages:
  - Increasing the probability of photons crossing two times the photocathode (double crossing), thus increasing the light collection efficiency.
  - Smaller time jitter: Light arriving at the edge travels almost the same distance to the first dynode as the light arriving at the center.
  - Better mechanical mounting with light collector, such as Winston cones.
- Six-dynode structure for better timing characteristics: The multiplication process of the dynodes is one of the main origins of the time jitter. Fewer dynodes decrease the value of the time jitter.

- Low afterpulsing rate: It has been understood that lowering the triggering threshold is limited in part by the afterpulsing rate induced by single photoelectron pulses due to the NSBs. While MAGIC is operated under a high NSB level, for instance, moon or twilight conditions, the ample background light will certainly increase the probability of afterpulsing inside the tubes. The probability of an accidental coincidence trigger by several pixels will unfortunately increase. At a certain point, the telescope may be in danger of triggering on afterpulses. Thus tubes with a low afterpulsing rate are really necessary.
- Fast and short pulses: Cherenkov pulses are normally short. The tubes should have shorter response times such that the time information from the Cherenkov photons won't be lost.

Considering all the above requirements, we were searching intensively in the current markets. Finally we decided to test tubes produced by the companies **Electron Tubes** and **Hamamatsu Photonics**, respectively, for comparison.

## 5.3 Characteristics and Different Measurements

### 5.3.1 Quantum Efficiency

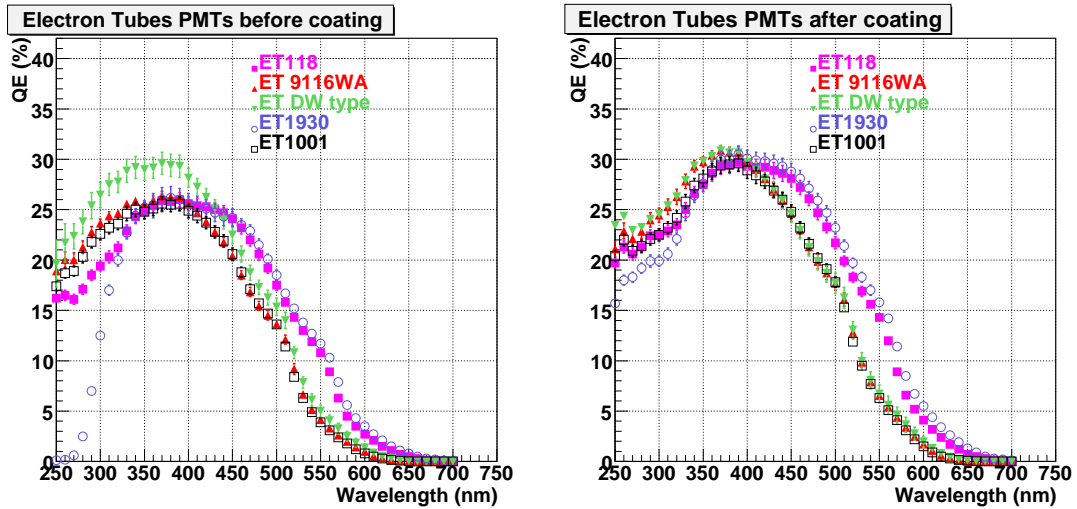


Figure 5.1: ET company's PMT QE curves with and without a diffuse lacquer coating.

PMTs are photo-electric devices which convert photons into electric signals. Electrons are generated in a photocathode by the photoelectric effect. A photocathode is the main part of the PMTs. There are a number of different ways to express the sensitivity of a photocathode. One of them is the Quantum Efficiency " $QE(\lambda)$ ". Normally, the QE of a bialkali photocathode has a peak around 370 nm, which decreases steadily down to zero around 650 nm. At shorter wavelengths,

the sensitivity drops to zero at around 200 nm due to the absorption of the glass window. In order to eliminate the effect of multiplication in the measurement of Q.E., we connected all the dynodes with the anode such that when the photoelectrons were generated, all of them would be collected and the produced current could be measured. In this operation mode, the tube was operated like a photocell. The whole photocathode was fully illuminated and the photocathode current measured with a Keithley picoampere-meter. Later, we compared the current with the calibrated Hamamatsu pin-photodiode. We applied a potential difference of 200V between the photocathode and the first dynode. In total, about 30 PMTs from Hamamatsu (R7373A-01MOD) and Electron Tubes (ET9116WA, ET9116B and DW) were measured.

Tungsten and Deuterium lamps were used for the light source. The light intensity was measured by a  $10 \times 10 \text{ mm}^2$  calibrated Hamamatsu pin photodiode (S6337-01) every one minute within five hours and degradation was found to be less than 0.01%. Also, no short variability down to one minute was seen. With a spectrometer, light of different wavelengths was selected. Inside the spectrometer, there is a rotating plate with 6 different optical filters which select the light with specific wavelength ranges to pass through. The whole spectrometer is attached to a custom-made black box with a small hole for the source of the light to pass through. Inside, the measured PMT is mounted on an optics set. The high voltage for the tubes is powered by a Electron Tubes power supply. The calibrated Hamamatsu pin photodiode had been calibrated to a precision of 2 %. A labview program was written to control the rotating plate in the spectrometer and read out the anode current from the picoampere-meter.

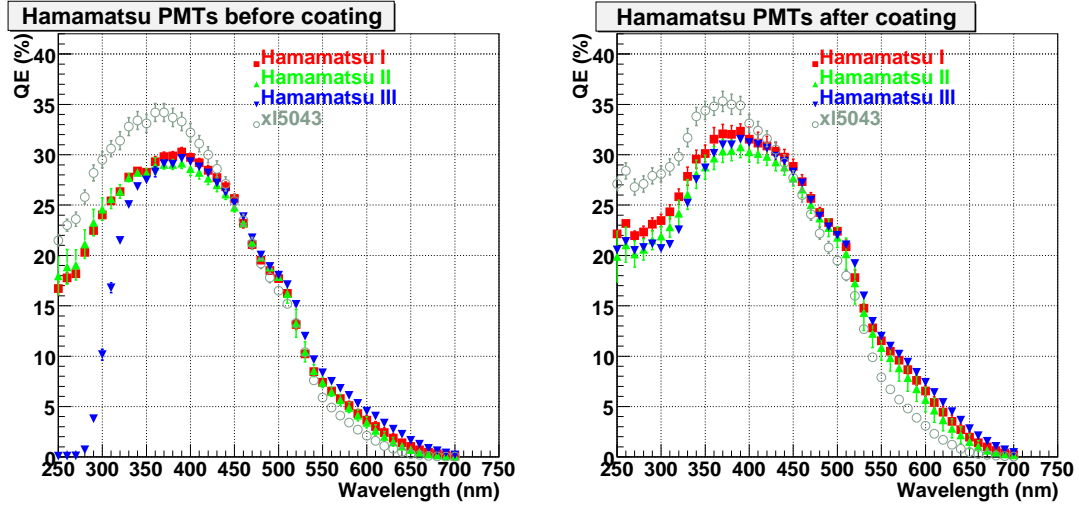


Figure 5.2: Hamamatsu Photonics PMT QE curves with and without a diffuse lacquer coating.

It is known that in MAGIC-I, we increased the QE by applying a special milky coating to the hemispherical PMTs from Electron Tubes (ET9116B) [98]. That coating, consisting of Paraloid B72 (an acrylic base material for lacquers) with a small admixture of a 1.4 p-Terphenyl (PTP) wavelength shifter (WLS), dissolved in Dichloromethane ( $\text{CH}_2\text{Cl}_2$ ), boosted the QE by about

Type of window	Cut off wavelength (nm)	$n_{ref}$
lime glass	300	1.54 (400nm)
borosilicate	270	1.5 (400nm)
UV-glass	190	1.49 (400nm)
fused silica	160	1.47 (400nm), 1.50(250nm)

Table 5.1: Transmission as a function of wavelength  $\lambda$  for many different glasses used as PMT input windows. The cut-off wavelength is the wavelength where the light transmittance is decreasing to only 10% of the coming value.

15% [11]. Using the same technique, we coated these new tubes, hoping also for a sizeable QE boost. The results before coating and after coating for different tubes from the two companies are shown in Fig. 5.1 and Fig. 5.2. In Fig. 5.1, the QE has a cut-off in the shorter wavelength region for the tube ET1930. This is due to the limited spectral response of the window glass of the tube. In Table 5.1, we will see the cut-off wavelengths of different types of PMT window glasses. Unlike to UV glass, in the borosilicate glass, most of the UV light will be absorbed. In the longer wavelength, the cut-off is because of the limited sensitivity of the photocathode.

From Fig. 5.1, it is obvious that there are two different types of PMTs from ET, which show different behaviors in QE. Their QE peaks occur at different wavelengths. One is at around 350 nm - 370 nm with the QE decreasing sooner at longer wavelengths, the other at 370 nm - 420 nm with the QE decreasing slower at longer wavelengths. The former is a K-Cs photocathode, the later is a Rb-Cs photocathode. There is also one tube from Hamamatsu Photonics which stands quite different from the others (zl5004).

When comparing the  $QE(\lambda)$  of a coated Hamamatsu PMT with an uncoated one, we obtained only a 10% improvement with quite large variations from unit to unit. This value is lower than the gain from the coated ET tubes which are used for the MAGIC-I camera. The reason can be explained as follows. We found that the photocathode reflectivity for Hamamatsu tubes is less than that of Electron Tubes. More light is reflected from Electron Tubes tube photocathodes. The reflected light will have a chance to be reflected back to photocathode because of the coating layers outside the glass windows. However, Hamamatsu PMTs have more transparent photocathodes such that more light is passing through the cathodes, less light is reflected back to the coating layer. Therefore, when we compare the bared tubes (without coating), Hamamatsu tubes are better simply because of their higher transparency and the higher quantity of light passing through the cathode. However, when applying a coating of a milky layer outside, the reflected light from Electron Tubes photocathodes have a better chance now to be reflected back to the photocathode. However, for Hamamatsu tubes, the reflected light is considerably less. Thus, the gain of QE after coating is less for Hamamatsu tubes than the tubes from Electron Tubes.

## Coating

The reason why we apply a coating of a milky layer on top of the PMTs enhance in the QE is explained in [11]. Here I summarize the effects of the coating layers:

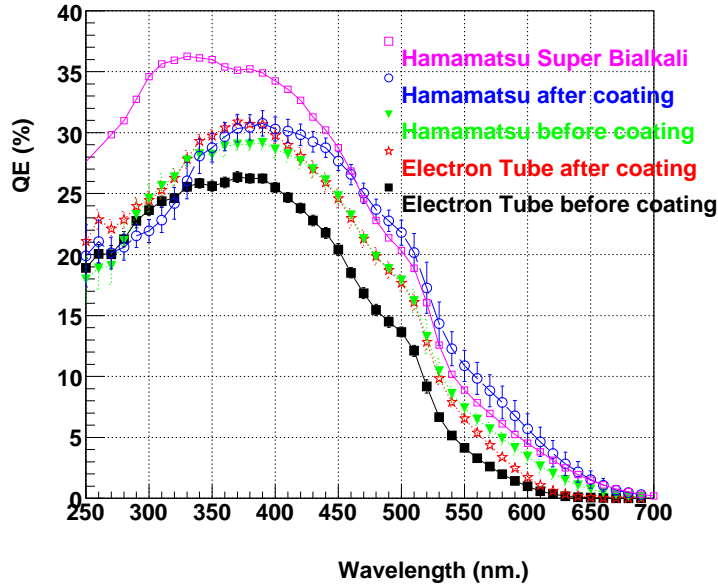


Figure 5.3: PMT QE curves with and without a diffuse lacquer coating from the two companies. PMTs were operated as photocells.

- Due to the wavelength shifter PTP, light with shorter wavelength will be absorbed and re-emit with a longer wavelength, which is more efficiently converted to photoelectrons at the photocathode.
- Due to the localized non-uniformity of the coating layer, the photons will be scattered many times inside the layer (the so-called diffuse reflections). This effect is like trapping the light inside the layer, which increases the probability of the light going through the glass and interacting with the cathode. Without the coating layer, the light which is reflected by the PMT window glass, will never have the chance to re-enter.
- Some photons will be deflected with larger incident angles such that they will pass the photocathode twice because of the hemispherical shape of the tube, see Fig. 5.4.

These three effects make the QE enhancement possible.

Fig. 5.3 shows overall PMT QE from Hamamatsu and Electron Tubes. Since less enhancement (about 10%) is expected for Hamamatsu coated PMTs, and since the custom-made coating introduce additional systematics, we decided not to apply the coating until this variation is understood better. Fig. 5.3 shows the comparison of the  $QE(\lambda)$  curves for six dynode, bialkali cathodes, 1" PMTs from Hamamatsu(R7373A-01MOD) and Electron Tubes (ET9116WA) tubes.

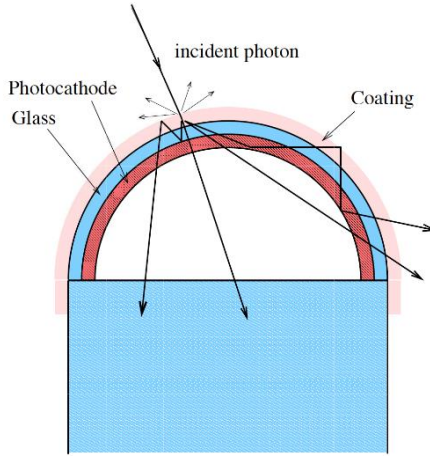


Figure 5.4: PMT coating with a scattering layer outside the tube. The picture is taken from [11].

### 5.3.2 Single Photoelectron Spectrum

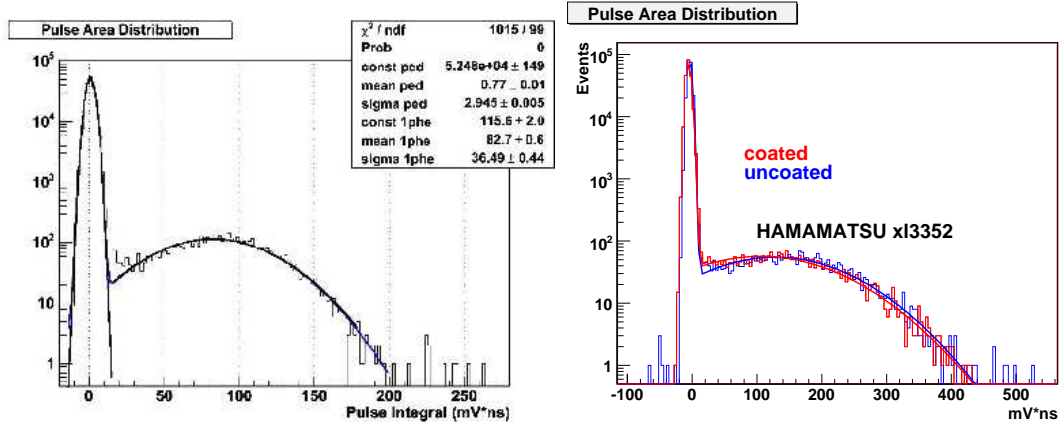


Figure 5.5: Example of a SPE of the PMT DW139 from Electron Tubes. The left peak originates pedestal events, the second broad peak the single photoelectron events.

The Cherenkov light flashes from 30-150 GeV air showers are very weak, typically between 300 and 1500 photons with the detection of the MAGIC telescope. Using classical PMTs, this results will be around 40 to 200 photoelectrons spreading over a few pixels. Therefore, the PMTs must be able to detect single photoelectrons well visible above the electronic noise. However, because of the nature of the secondary dynode emission processes from the dynodes, the signals from single photoelectrons usually show very large fluctuations.

The single photoelectron spectrum (SPE) is a pulse area distribution of the single photoelectron (some people use the pulse amplitude instead). Fig. 5.5 shows an example of SPE

distribution. The following information can be derived from the SPE plot.

- The mean pulse area depends on the secondary emission efficiency. If the efficiency is free of fluctuation, all the pulses would have the same pulse areas.
- The peak-to-valley (P/V) ratio could be calculated. We rejected PMTs which have a P/V value below 1.2 for the second telescope.
- The energy resolution. The resolution depends on the ratio between the width and the mean of the single photoelectron peak. If the value is small, the resolution is good due to the peak being narrower and higher.

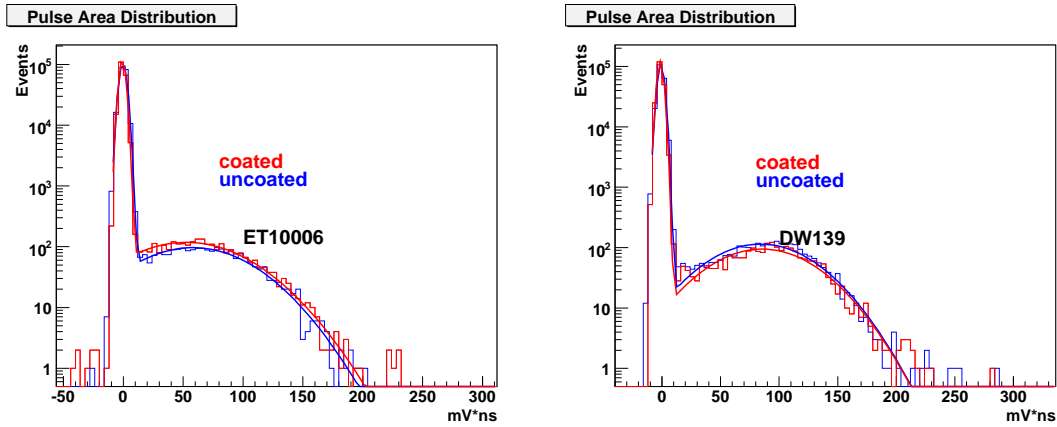


Figure 5.6: Example of SPE of the PMT DW139 and et10006 from Electron Tubes.

We illuminated the PMTs with ultra-short light pulses of 80 psec from a semiconductor laser operating with a wavelength of 405 nm. The laser light intensity was dimmed down to produce mostly a single photon per pulse. We kept the average probability for producing a single photoelectron below 5% such that the admixture of 2 photoelectrons events in the SPE peak was less than 2.5% of single photons. The laser also triggered an FADC to record the PMT pulses. Examples of our results of the single photoelectron spectrum are shown in Fig. 5.6. Note that there is always a small portion of small pulses due to imperfect secondary emission or imperfect light focusing. The amount of such events could be calculated from subtracting the pedestals.

### The F-factor

The F-factor is also called excess noise factor. While operating PMTs, the amplification process (the secondary-emission from the dynodes) does not follow simple Poisson statistics. Therefore the number of initial photoelectrons cannot be calculated from the spread in measured values. The amplification process introduces a widening of the spread in the distribution. The "widening" factor is called the excess noise factor.

$$F = (\sigma_{output})/(\sigma_{input})$$

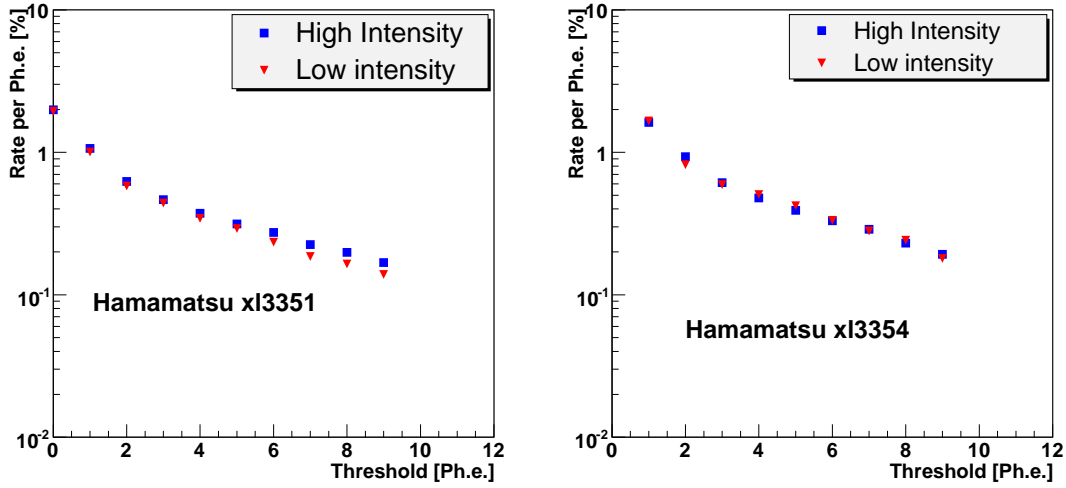


Figure 5.7: The afterpulse rate for the Hamamatsu PMT (R7373A-01MOD) serial number XC3351 as a function of thresholds.

The F-factor is a good index for the PMT quality check. However it is very tricky to directly measure it in the lab. One of the common methods is to calculate it from the single photoelectron spectrum. The most tricky part is to count the single photoelectron events, especially those which are closer to the pedestal region. The ambiguity between them and null events make the single photoelectron counting difficult. Thus the uncertainties of a derived F-factor are usually large.

### 5.3.3 Afterpulsing

Afterpulses are pulses which appear after the true main pulses. There are two main origins:

- Ionization of residual gases: There are residual gases left inside the tube after evacuation or adsorbed by materials of the tube's own structure, or helium that has migrated through the PMT glass (in the old days). Their time delay depends on the dimension of the tubes and the point where the gas atoms/molecules are ionized.
- Ionization of residual molecules adsorbed on the dynodes: Due to the imperfect sealing or evacuation of the tubes, there are molecules (such as water) inside the PMTs and adsorbed particularly by the Cs layers covering the dynode material by VanderWaals forces on the dynodes. While electrons are bombarding the dynodes, those molecules will be ionized by energetic electrons. Since the voltage of the dynodes is relatively higher than that of the photocathode, the positive ions will fly back and bombard the photocathode. Additional electrons will be produced and the following multiplication process will be the same as with normal photoelectrons do. The delay time for these afterpulses depends on the dimension of the tubes, the flying velocity of the ions and the voltage between the first dynode and the photocathode. Normally, afterpulses which are produced by this origin

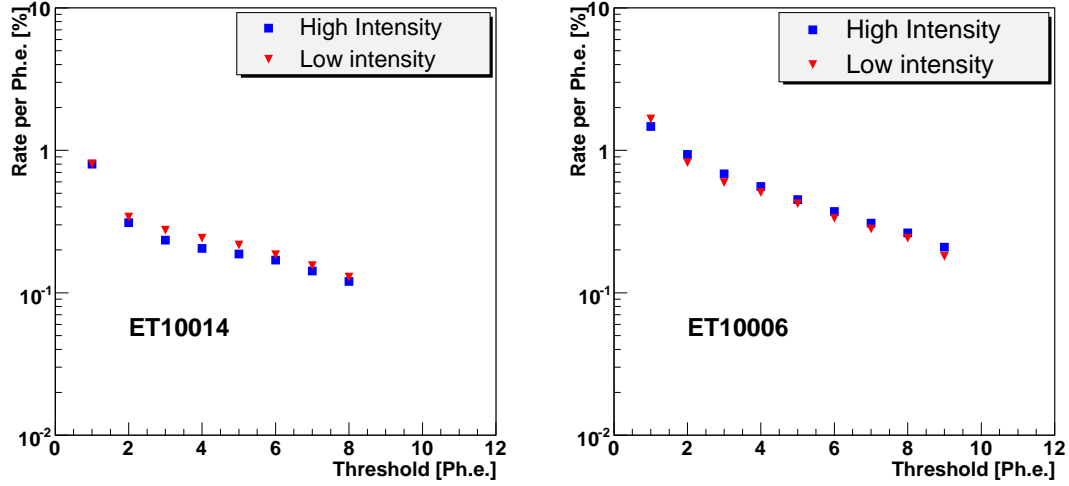


Figure 5.8: The afterpulse rate for the ET PMT (9116WA) serial number XC3351 as a function of thresholds.

could be reduced when the tubes have been used for a certain period of time. The residual molecules will become fewer when the tube has been used many times. On the other hand, for the new tubes, the most common method to wash-out the resting molecules is to use the high flux of photons at the very beginning to "wash-out and clean" the dynodes before operation.

We used a pulsed laser (wavelength 405 nm) as a light source and as a trigger for the FADC readout system. Afterpulses were searched for in a  $2 \mu$  sec timing window between the two consecutive main triggered main pulses. We applied different thresholds and counted the number of afterpulses. Finally we normalized this number to the total number of photoelectrons in the main pulses. To check if the results depended on the intensity of the laser pulse, we measured the afterpulse rate with two different light intensities. In Fig. 5.7 and Fig. 5.8, the normalized afterpulse rate of the Hamamatsu PMTs with different selection thresholds with two different light intensities is presented. The measured PMTs had an afterpulse rate of about 0.2 % to 0.8 % in the case of a threshold of 4-5 photoelectrons.

### Afterpulse Rate and QE

Since the bombarding effect of the ions on the cathodes is purely kinematic, the probabilities of heavy ions kicking out electrons from the photocathode should not depend on the sensitivity of the cathode. However, as shown in Fig. 5.9, the Auger collaboration found a positive correlation between the sensitivity (Corning Blue values) of the cathode and the afterpulsing rate from their 10-inch Photonis PMTs. Nevertheless, at the MPI in Munich, we tested six one-inch tubes from ET and Hamamatsu and did not find similar behavior, see Fig. 5.10. Why there is a correlation between QE and the afterpulse rate is not very clear. It may depend on the different materials of

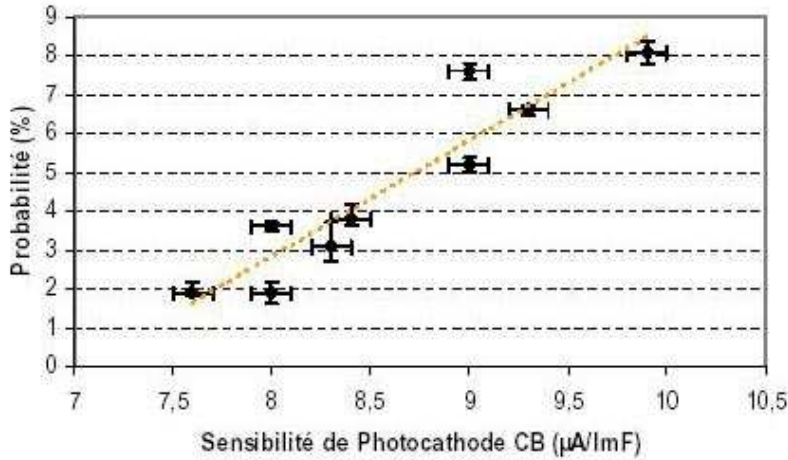


Figure 5.9: The afterpulse rate shows strong correlation with photocathode sensitivity from Auger 10-inch Photonics PMT.

the cathodes of different tubes from different companies. Or it may depend on the dimensions of the tubes. Further investigation is necessary and indispensable.

### 5.3.4 Aging

Exposing the PMTs to a sizable light intensity over a period of time will decrease the gain. It drops because of fatigue of the last dynode. The damage is a function of the dynode material, the gain, and the dynode area. This effect is called "aging". The speed of the aging process could be quantified by a value, the lifetime. The lifetime of the PMT is defined as the time when the gain of the PMT drops to  $1/e$ . For IACTs, the PMTs are constantly exposed to the NSB during observation. For example, in MAGIC, the PMTs are exposed to at least 0.7 GHz photons (dark area of the night sky outside the galactic plane). During moon or twilight the value could be several times higher. Consequently, huge amounts of photoelectrons and secondary electrons bombard the dynodes at the same time. This speeds up the aging process. Usually, the aging process takes a few years. In order to accelerate the measurements in the lab, all tested PMTs were illuminated by high intensity light. We tuned four different PMT gains such that they had the same initial anode current of  $150 \mu A$ . The measurements were taken over a period of one week (10150 minutes in total.) We tested four PMTs from the two companies mentioned. A pin photodiode was used to monitor the light flux. The result is shown in Fig. 5.11. From the degradation we estimated a lifetime of at least 50 - 60 years, assuming that the NSB at La Palma induces an anode current of  $1 \mu A$  and a 10% duty cycle per 24 hours.

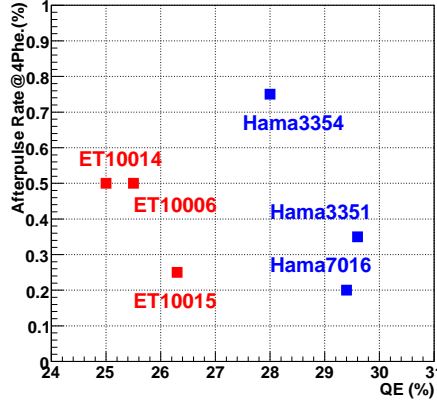


Figure 5.10: The afterpulse rate as a function of QE for the Hamamatsu PMT (R7373A-01MOD) and Electron Tubes PMTs. The peak value of the QE is shown here.

### 5.3.5 Pulse Shape and Timing Characteristics

#### Response Pulse Width, $t_w$

The timing characteristics of photodetectors are quite important for IACTs, since the Cherenkov light flashes are always quite short. The response pulse width is determined by the anode current pulse width  $t_{w,a}$  (which is what we measure) and the pulse width of the incoming light pulse  $t_{w,l}$ . Normally, we would like to use an incoming light pulse as short as possible such that the measured anode light pulse width will be closer to the real response pulse width. Their relationship could be described as:  $t_w = \sqrt{t_{w,a}^2 - t_{w,l}^2}$ . The rise and decay time of a pulse are defined as the time required for the anode current to increase from 10% to 90% of its total value. The response pulse width depends on the incoming light level and its minimum is reached when the light level enters the single photoelectron regime. In order to specify the timing resolution, we measured the half maximum (FWHM) of the anode current pulse delivered in response to a very short and narrow laser light pulse of about 80 psec pulse duration. The PMT pulse width depends on the light illumination level. We amplified the single ph.e. signal with a 2GHz bandwidth amplifier (gain 100) and recorded the signal with a fast digital oscilloscope (1.5 GHz in bandwidth, 5 GSamples/s). The single photoelectron pulses of both tested PMT models had a rise time of approximately 600 to 800 psec and a fall time of 700 to 1000 psec. The pulse width (FWHM) was around 1.5 nsec. Fig. 5.12 shows an oscilloscope recording of a single photoelectron pulse in one Hamamatsu PMT.

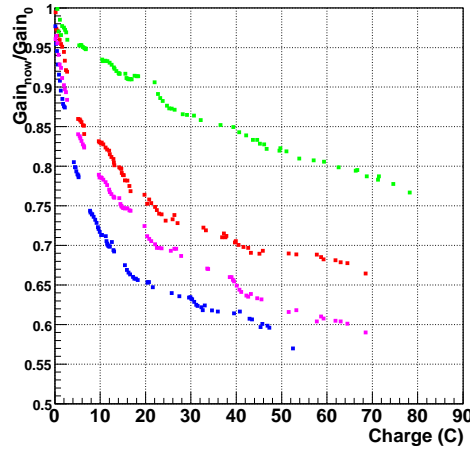


Figure 5.11: The aging measurement for the Hamamatsu and ET PMTs.

### 5.3.6 Transition Time Jitter

The time interval between the arrival of a light pulse at the photocathode and that of the corresponding current pulse at the anode is called the transition time. The transition time spread manifests itself by a broadening of the pulse distribution when superposing many single electron signals. We believe that the main reason for the spread originates from the different flight path lengths of photoelectrons in the PMT front-end structure between the cathode and first dynode. Thus, the voltage applied between the first dynode and the photocathode,  $V_{C-D1}$ , can affect the value of the jitter. For example, a lower  $V_{C-D1}$  will increase the jitter. However,  $V_{C-D1}$  cannot be very high as well, because, the afterpulses rate increases. From our measurements, we found a jitter of 960 psec for the Hamamatsu PMT operated at a gain of  $1.15 * 10^5$  under the single photoelectron level, see example in Fig. 5.13. We also found that by lowering the gain by 30%, the time jitter becomes only slightly wider. In addition, if we increase the light level, the time jitter decreases as the square root of  $1/N$ , where  $N$  is the number of photoelectrons.

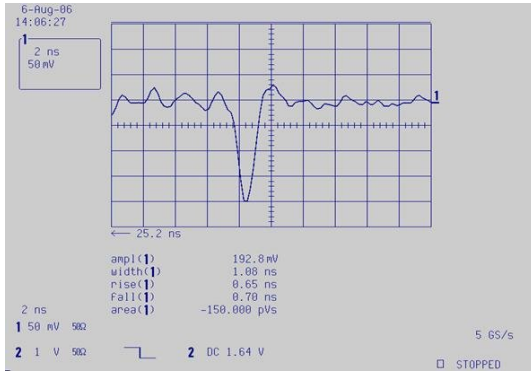


Figure 5.12: Single photoelectron pulse from a Hamamatsu PMT. The pulse was measured by a digital oscilloscope of 1.5 GHz of bandwidth and a 5 GSamples/s FADC.

## 5.4 Light Guides

### 5.4.1 Introduction

There is a permanent search for collecting as much light as possible by employing cheaper and easier methods. Non-imaging optics is such a field while we care only about light collection instead of the images. So far, many applications have become available, e.g. the solar panel, which collects the maximum of sunlight during a sunny day.

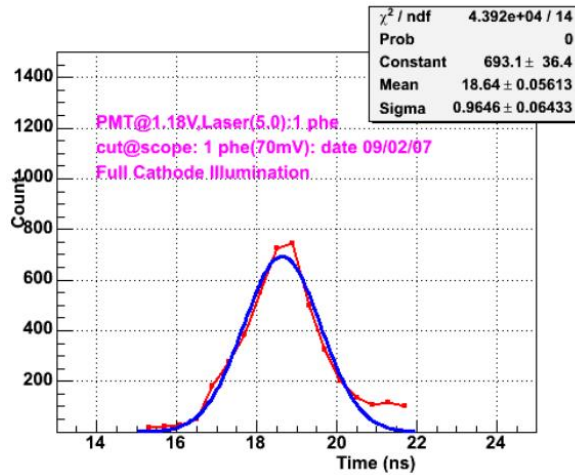


Figure 5.13: The transit time jitter for single photoelectron pulses from the Hamamatsu PMT. The horizontal axis is the transition time. The transit time spread (TTS) is about 960 psec. Note that TTS becomes shorter for higher amplitude pulses.

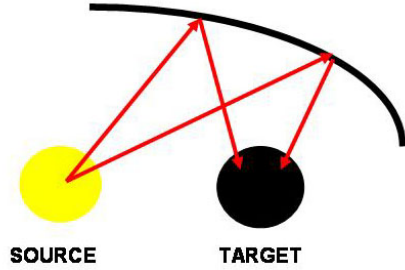


Figure 5.14: The basic operation principle of the non-imaging optics.

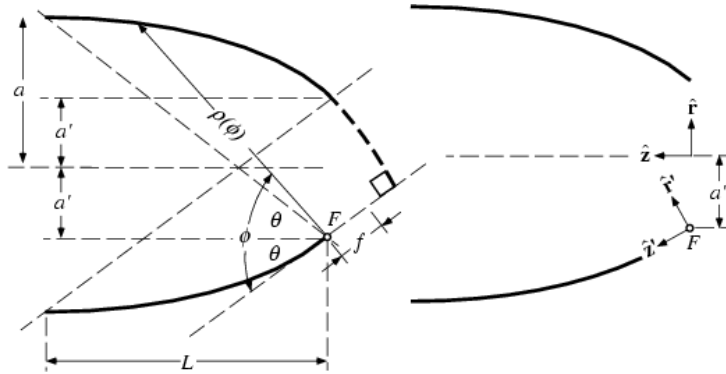


Figure 5.15: The basic structure of the Winston cone.

The basic principle of non-imaging optics to collect light is demonstrated in Fig. 5.14. Geometric optics methods are used to collect light.

A Winston cone is an off-axis parabola design to maximize the collection of incoming light within a defined field of view [99]. Fig. 5.15 shows the scheme of a Winston cone.  $F$  is the focus of the parabola, and  $f$  is its focal length. The length of the cone is  $L$ . The diagram on the right shows the origins and orientations of the focus-centered and symmetry axis-centered coordinate systems. Winston cones are non-imaging light concentrators designed to funnel all wavelengths passing through the entrance aperture out through the exit aperture. They maximize the collection of incoming light by allowing off-axis rays to make multiple bounces before passing out through the exit aperture. However, they also reject a certain amount of off-axis light which have a too large angle of incidence, thus they act like, for example stray light outside the mirror area. There are many advantages to couple PMT pixels with Winston cones. The most important points are:

- To reject large angle NSB photons. By choosing the proper entrance window of the cones, the pixels could only accept the photons which are reflected from the mirrors.
- To focus the light on the sensitive regions of the photon sensors. Usually the entrance

windows of the photon sensors are not homogeneous. Especially the side edge of the sensors will not be as sensitive as the center. By choosing the proper size of the cones, we increase the number of photons reaching the sensitive region of the sensors.

- Winston cones minimize the dead space between the pixels.

### 5.4.2 Design

There are several important parameters which should be taken into account while designing Winston cones.

- The size of the entrance and exit windows, and the length of the Winston cone. These parameters decide the opening angle of the cone.
- The geometry of the exit and entrance windows.
- Method of coupling the exit window with the photon sensors.
- The reflectivity of the reflective surface of the cone at different wavelength (in practice we lined the cones by aluminized Mylar foil).

In order to know the performance of different configurations, simulations with different configurations of the cones were performed. MAGIC II Winston cones have a few unique design features:

- The exit window of the cone is hexagonal.
- The coupling of the Winston cone with the PMT is well adopted.
- The foil inside the cone is specially designed such that the reflectivity fulfills our requirements in specific wavelengths.

### 5.4.3 Measurements

The optimal configuration of the Winston cone is the one which can collect the largest number of incoming photons, so the relative light collection efficiency of different configurations coupled with the photon sensors needs to be measured. The idea was the following: the cones were coupled with PMTs, then a very dim laser light illuminating the whole system was used. At last, the number of single photoelectron events was counted. In order to have a good background control, we took pedestal measurements before each data run. We were using the PICO laser, with a wavelength 405 nm and a pulse width of 80 psec. Instead of a rotating the light source, we mounted the PMT together with the Winston cone on a rotating machine such that the light could arrive with different incident angles. The rotation direction could be counter-clockwise or clockwise. The measurements were done in symmetrical positions.

We tested several different configurations of the cones. The configurations are listed in Table 5.2. The size of the entrance window was fixed to 30 mm such that the dead space in front of

Entrance d1 [mm]		Exit d2 [mm]	Cover PMT Area	Cutting angle(min, max)
Hexagonal to Circular				
30	19		$\pm 48.4^\circ$	$28.36^\circ, 39.3^\circ$
30	20		$\pm 51.94^\circ$	$30^\circ, 41.8^\circ$
30	21		$\pm 55.94^\circ$	$31.67^\circ, 44.5^\circ$
Hexagonal to Hexagonal				
30	19		$\pm 48.4^\circ$	$28.36^\circ, 39.3^\circ$
30	20		$\pm 51.94^\circ$	$30^\circ, 41.8^\circ$
30	21		$\pm 55.94^\circ$	$31.67^\circ, 44.5^\circ$
30	22		$\pm 60.0^\circ$	$33.37^\circ, 47.16^\circ$

Table 5.2: Different configurations of Winston cones designed by MPI. The cutting angle is calculated by the formula:  $\theta = \sin^{-1}(\frac{a'}{a})$ . Since the entrance window could be hexagonal, the size of their radius is estimated by the radius of the inner circle and the outer circle.

the camera was minimized. In order to know the coating effects, for each configuration, we measured the same PMT with and without coating and then compared the single photoelectron events with each other. Note that for the Hexagonal→Hexagonal type, the inner surface is a parabolic shape. However, for the Hexagonal→Circular type (the traditional one), the inner surface is cut with flat surfaces.

#### 5.4.4 Results, Summary and Discussion

The final number of signal photoelectron events depends very much on the following factors:

- The wavelength of the incoming light.
- The optical properties of the PMT surface: Either glass or chemical coating materials.
- The covered area of the PMTs.

All the important factors could be summarized into one formula:

$$n_{final} = n_{source} * F_{cone} * \epsilon_{cone\_PMT} * F_{PMT}$$

$n_{source}$  is the number of photons coming from the light sources.  $F_{cone}$  is a function concerning the Winston cone, which could be further written as

$$F_{cone} = n_{cone} * \epsilon_{cone}(\theta) * \epsilon_{foil}(\theta, \lambda)$$

Note that,  $n_{cone}$  is the number of photons which enter the cone; the number could be geometry dependent. If our light beam is bigger than the entrance window, part of the photons will be

blocked because of the geometric effect.  $\epsilon_{cone}$  is the efficiency of the cone. It is a step function about the incident angle of the light.

$$\epsilon_{cone}(\theta) = 1. \quad for \quad \theta_{inc} < \theta_{cut-off} \quad \epsilon_{cone}(\theta) = 0. \quad for \quad \theta_{inc} > \theta_{cut-off}$$

$\epsilon_{foil}(\theta, \lambda)$  is the reflectivity efficiency of the wrapped foil, which depends on the incident angle and wavelength of the photons. Some photons will be reflected a few times because of the smaller exit window compared with the entrance one.

$\epsilon_{cone\_PMT}$  is the coupling efficiency between the cone and the tube. The maximum value is 100%.  $F_{PMT}$  is a function concerning the tube. It could be written as

$$F_{PMT} = \epsilon_{coating}(\theta, \lambda) * QE_{PMT}(\lambda) * \epsilon_{light\_collection}(\theta, \lambda, r)$$

$\epsilon_{coating}(\lambda)$  is the coating efficiency. The manual coating procedure brings many uncertainties; the efficiency may deviate from this time to the next.  $QE_{PMT}(\lambda)$  is the QE of the PMT.  $\epsilon_{light\_collection}(\lambda, r)$  is more complicated; it is a function of wavelength, a photoelectron generated position and a function of wavelength. Note that all the above parameters above should be independent of PMT gains. The  $\epsilon_{light\_collection}(\theta, \lambda, r)$  depends on the voltage between the photocathode and first dynode. Once the voltage is fixed, the value of  $\epsilon_{light\_collection}(\theta, \lambda, r)$  should not vary much.

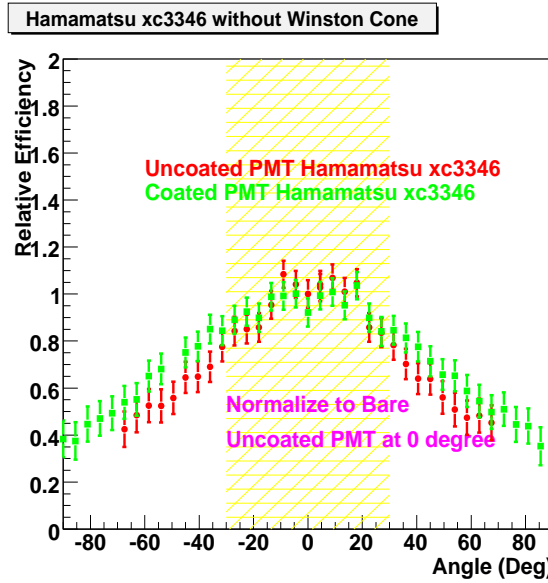


Figure 5.16: Compared single photoelectron events of coated and uncoated Hamamatsu PMT xc3346 without coupling with a Winston cone. The shadow region is the angular span or MAGIC reflector.

Fig. 5.16 shows numbers of the single photoelectron events for coated and uncoated PMTs, respectively. The number of events is normalized to the number of the uncoated one in the 0

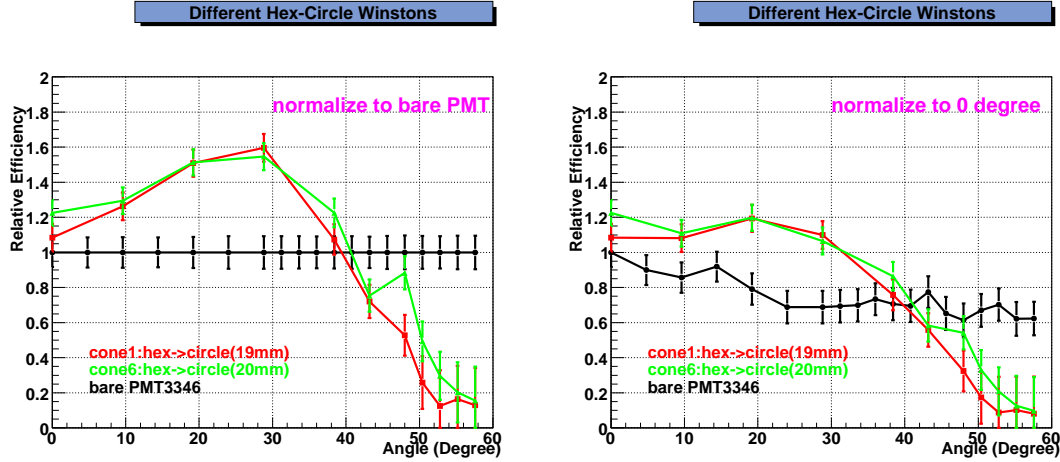


Figure 5.17: Comparison of the two different types of Winston cones with bared PMTs. The plot on the left hand side is the normalization to the uncoated bared PMT at zero degree. The plot on the right side is normalized to the un-coated bared PMT at corresponding angles.

degree. Both measurements are taken without the light cones. The results show that within smaller angles, uncoated and coated PMTs provide comparable results. On the other hand, at larger angles, coated tubes perform better.

The measured results were also compared with simulation results, see Fig. 5.18 and Fig. 5.19.

We have found that the curves obtained could be fitted approximately by an mathematical function:

$$\begin{aligned} F_1(x) &= P_0 * ((e^{(P_1*(-x-P_2))} - P_3)/(e^{(P_1*(-x-P_2))} + P_3)) \\ F_2(x) &= P'_0 * ((\exp^{(P'_1*(x-P'_2))} - P'_3)/(\exp^{(P'_1*(x-P'_2))} + P'_3)) \end{aligned}$$

The complete efficiency curve could be fitted by a function  $F(x)$ , which is a linear combination of  $F_1(x)$  and  $F_2(x)$ . The parameter  $P_3$  is related to the width of the curve.  $P_0$  concerns the height of the curve which is the efficiency. The value  $P_2$  is about the dropping point of the curve after the plateau region. It is an important parameter because of its relation to the cut-off angle of the cone.

The final results are shown in Fig. 5.20. Note that every data point is normalized relatively to the bared PMT with zero degree of incident laser light. The fitting parameters are shown in the Table 5.3.

In Fig. 5.21, we can see the relative single photoelectron efficiency with the Hamamatsu tube xc3346 coupled with different types of Winston cones. We measured by rotating the tube from -60 degree to +60 degree to check if the results were symmetrical. From the plot, the "hex→circle" type shows a lower efficiency but a wider cut-off angle. The hex→hex type shows a higher efficiency but a sharper cut-off at smaller angles. The different efficiencies could be

Config	$P_0$	$P_1$	$P_2$	$P_3$	$P'_0$	$P'_1$	$P'_2$	$P'_3$	$\chi^2/\text{ndf}$
Coated 19 mm	$-0.89 \pm 0.11$	$0.37 \pm 0.06$	$27.23 \pm 1.7$	20	$-0.76 \pm 0.11$	$0.36 \pm 0.05$	$26.21 \pm 0.95$	20	33.91/12
Uncoated 19 mm	$-0.88 \pm 0.05$	$0.47 \pm 0.06$	$29.13 \pm 0.74$	20	$-0.93 \pm 0.06$	$0.4 \pm 0.05$	$28.32 \pm 0.77$	20	18.18/15
Coated 20 mm	$-1. \pm 0.05$	$0.30 \pm 0.02$	$27. \pm 1.8$	20	$-0.96 \pm 0.048$	$0.254 \pm 0.016$	$27.31 \pm 0.35$	20	38.47/21
Uncoated 20 mm	$-0.98 \pm 0.05$	$0.38 \pm 0.06$	$30.3 \pm 0.4$	20	$-0.99 \pm 0.03$	$0.42 \pm 0.05$	$31.32 \pm 0.47$	20	20.8/15
Coated 22 mm	$-0.94 \pm 0.08$	$0.15 \pm 0.02$	$26.4 \pm 2.4$	20	$-0.81 \pm 0.08$	$0.21 \pm 0.03$	$27.22 \pm 1.5$	20	20.9/15
Uncoated 22 mm	$-0.63 \pm 0.16$	$0.44 \pm 0.11$	$41.34 \pm 1.3$	20	$-1.06 \pm 0.17$	$0.23 \pm 0.03$	$35 \pm 1.3$	20	32.2/19

Table 5.3: The fitting parameters for different configurations of the Winston cone.

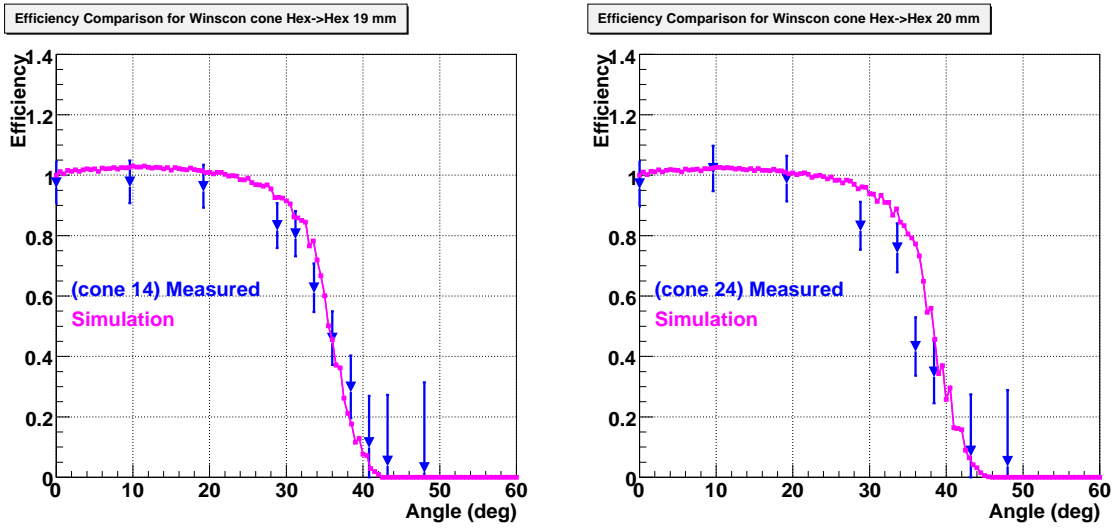


Figure 5.18: Comparison of the measured results with simulation prediction. All measured values are normalized to efficiency at zero degree. The two configurations for the Winston cone are hex→hex with an exit window of 19mm (left plot) and 20mm (right plot), respectively.

explained as follows. Though the light cone can focus the light on more sensitive regions of the photodetector, under the condition that the size of the entrance window is fixed, the exit window could not be too small. The reason is that the cut off angle is determined by the ratio between the two and should not be too small. On the other hand, the size of the exit window could not be too big either, as it would then cover too much of the photodetector's insensitive region. In other words, the size of the exit window must be optimized for obtaining the maximum efficiency. In addition, we have to take into account the reflector effect. The reflector area per solid angle is not the same in all cases. So while calculating the total efficiency, we have to convolute all the curves in Fig. 5.21 with the reflector area in corresponding angular bins. The results are summarized in Table. 5.5. The table shows the total efficiency after integration of the efficiency curve of the Winston cone with the reflector area at different span angles. The calculation shows that the integrated efficiency for the hex→circle type is a 13 % smaller than for the hex→hex type. For the 4 different types of the Hex→Hex, the difference is not big, i.e. within 5%.

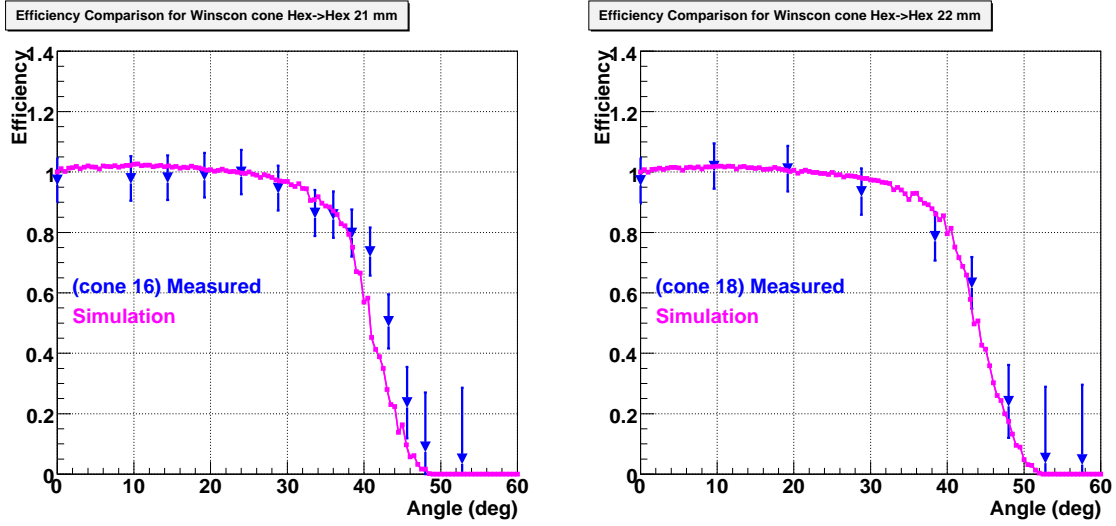


Figure 5.19: Comparison of the measured results with simulation prediction. All measured values are normalized to efficiency at zero degree. The two configurations for the Winston cone are hex→hex with an exit window of 21mm (left plot) and 22mm (right plot), respectively.

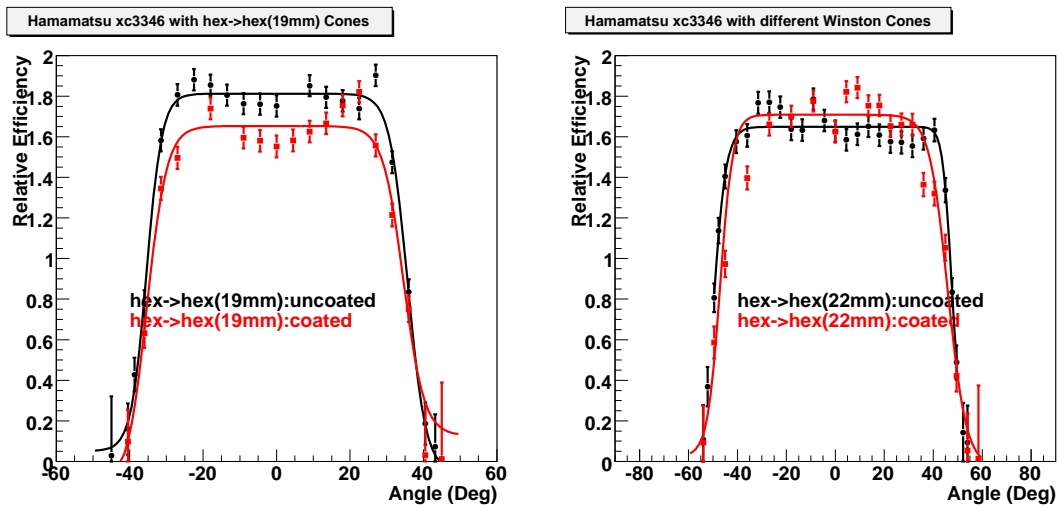


Figure 5.20: The efficiency curve of the cone with hex to hex (19 mm) and hex (22 mm) configuration. The black curves in both plots are uncoated PMTs, the red curves are coated PMTs.

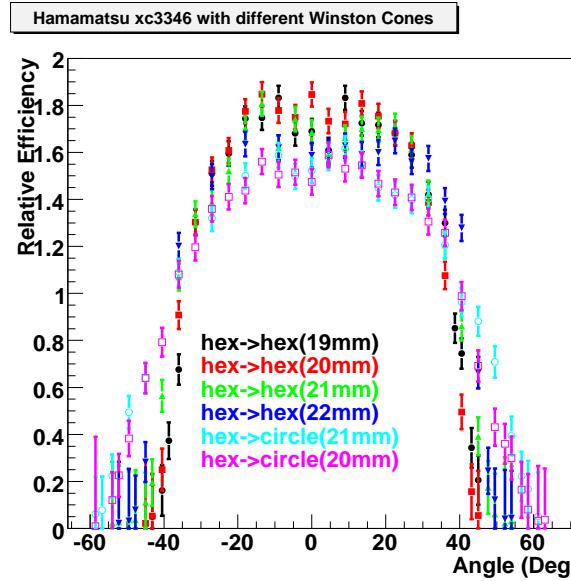


Figure 5.21: Comparison of the number of single photoelectron events with the same uncoated PMT (Hamamatsu xl3346) but different cones. All measured values are normalized to bared tubes at zero degree.

Entrance d1 [mm]	Exit d2 [mm]	Cover PMT Area	Cutting angle(min, max)
Hexagonal to Circular			
30	19	$\pm 48.4^\circ$	$28.36^\circ, 39.3^\circ$
30	20	$\pm 51.94^\circ$	$30.0^\circ, 41.81^\circ$
30	21	$\pm 55.94^\circ$	$31.67^\circ, 44.43^\circ$
Hexagonal to Hexagonal			
30	19	$\pm 48.4^\circ$	$28.36^\circ, 39.3^\circ$
30	20	$\pm 51.94^\circ$	$30.0^\circ, 41.81^\circ$
30	21	$\pm 55.94^\circ$	$31.67^\circ, 44.43^\circ$
30	22	$\pm 60.0^\circ$	$33.37^\circ, 47.16^\circ$

Table 5.4: Results of different configurations of Winston cones: Count the single photoelectron events.

## 5.5 Remarks about Photo-sensors during Moon / Twilight Observations

The Night Sky Background originates from different sources [100]. The value is site-dependent, and even time-dependent (e.g. the seasons). A study about the NSB at the La Palma site [101] is available. The rate of the NSB at the MAGIC camera amounts to about 130 MHz per pixel. On average, within 10 ns, we have 1.7 photoelectrons per pixel from NSB. However, this number is obtained from measurements taken during dark moonless nights. If we restrict IACTs operations to the dark moonless night only, the duty cycle is about 10%, which is about 900 hours per year. Developers of the first IACTs, like WHIPPLE, have identified this problem and tried to improve the situation at that time. The solution was to observe during the small moon phase. The problem was that the NSB level during such period may be still several times higher than in dark nights. In the old times, PMTs were covered by a density filter which decreased the light level during moon observations. However, the filters also decrease the Cherenkov light intensity, therefore the price to be paid was the increase of the energy threshold [102]. In MAGIC, we tune our telescope hardware such that moon observation is feasible.

- The nominal gain is tuned to be so low that the aging effect will be small.
- The observational target is kept 90 degrees away from the moon. The purpose is to avoid the moon-light shining directly into the camera or being reflected from the mirror to the camera.
- The discriminator threshold is increased such that the trigger rate will not be too high.

Config.	Exit d (mm)	Efficiency
Hex→Hex	19	$38.71 \pm 0.62$
	20	$39.178 \pm 0.62$
	21	$38.06 \pm 0.63$
	22	$37.65 \pm 0.63$
Hex→Circle	21	$34.46 \pm 0.638$
	20	$34.13 \pm 0.64$

Table 5.5: The efficiency of different configurations of Winston cones after integrating the area of the reflector at different angles.

# Chapter 6

## Standard Analysis Chain for MAGIC Data

The EAS initiated by cosmic charged particles are more abundant than cosmic  $\gamma$ -rays. Therefore, the main issue in the analysis is to define a method for separating them. In addition, the goals of the analysis is to derive useful physics quantities from the primary  $\gamma$  rays, such as their directions, energies and arrival times.

This chapter is structured as follows. First, I will give a short general overview of the MAGIC standard analysis software MARS (MAGIC Analysis and Reconstruction Software) [103] and the entire analysis chain. Then I will proceed from lower-level to higher level data analysis concerning the signal extraction, event reconstruction, image cleaning, and  $\gamma$ /hadron separation. Subsequently, important physics quantities such as lightcurves and energy spectra will be introduced. The contribution of this thesis about the MAGIC ONLINE analysis will also be presented. In the final section, the performance of the MAGIC telescope will be described.

### 6.1 MARS Software Package and the Analysis Chain

The MAGIC software package MARS has been developed and continuously upgraded since 2004. Its application ranges from very low level data processing like reading DAQ raw data to higher level data analysis like calculating the lightcurves and source spectra. The whole package is mostly written in C++ and based on the CERN ROOT framework <sup>1</sup>. The fast ONLINE analysis which reads DAQ raw files, has a quick calibrations and it estimates the flux level of the sources. It will be described in section 6.8.

The entire basic standard analysis scheme can be seen from Fig. 6.1. The overall procedure is divided into several key steps:

- Program "callisto": It calibrates DAQ raw data from each pixel. The main purpose is to convert FADC counts into the numbers of photoelectrons from each pixel while taking into account the different conditions of each pixel. Moreover, signal timing information is also converted.

---

<sup>1</sup><http://root.cern.ch/drupal/>

- Program "star": Removes pixels which are contaminated by any kind of noise. The idea is to have really pure shower images on the camera, not noise. Subsequently, Hillas parameters will be calculated based on these surviving pixels.
- Program "osteria": Tries to separate  $\gamma$  and hadron showers by Random Forest learning process [104]. In addition, the energy estimation matrices will be produced by training a sub-samples of Monte-Carlo  $\gamma$  events.
- Program "melibea": Applies the  $\gamma$ /hadron separation and energy estimation matrices on the other sub-samples of Monte-Carlo  $\gamma$  events.
- Program "fluxlc": The effective observation time is determined by observational data. Multi-parameter cuts are applied both on observational data and Monte-Carlo  $\gamma$  events. The cuts are decided by optimizing the sensitivity on Crab data. Once the cuts are applied, the number of excess events and the effective area are calculated. The lightcurves and the spectra are determined in the bins of estimated energy.
- Program "unfolding": The energy spectrum is unfolded taking into account the energy resolution of MAGIC and other analysis effects, like different hadronic samples for Random Forest training. Finally, the energy spectrum is binned in "true" energy instead of "estimated" energy.

The analysis relies very much on Monte-Carlo (MC) simulated  $\gamma$ -ray events. The MC samples are used for calculating the effective areas, which, in turn, is needed for calculating the source energy spectrum and the lightcurve. However, for representing the background hadrons, MAGIC data with no  $\gamma$ -ray signal in the analysis region are used instead of using MC hadron samples. In the case of Wobble observation mode, background data are extracted from the same field of view but different regions of the camera. In the case of the ON/OFF observation, additional OFF-mode data taken is necessary to represent the background.

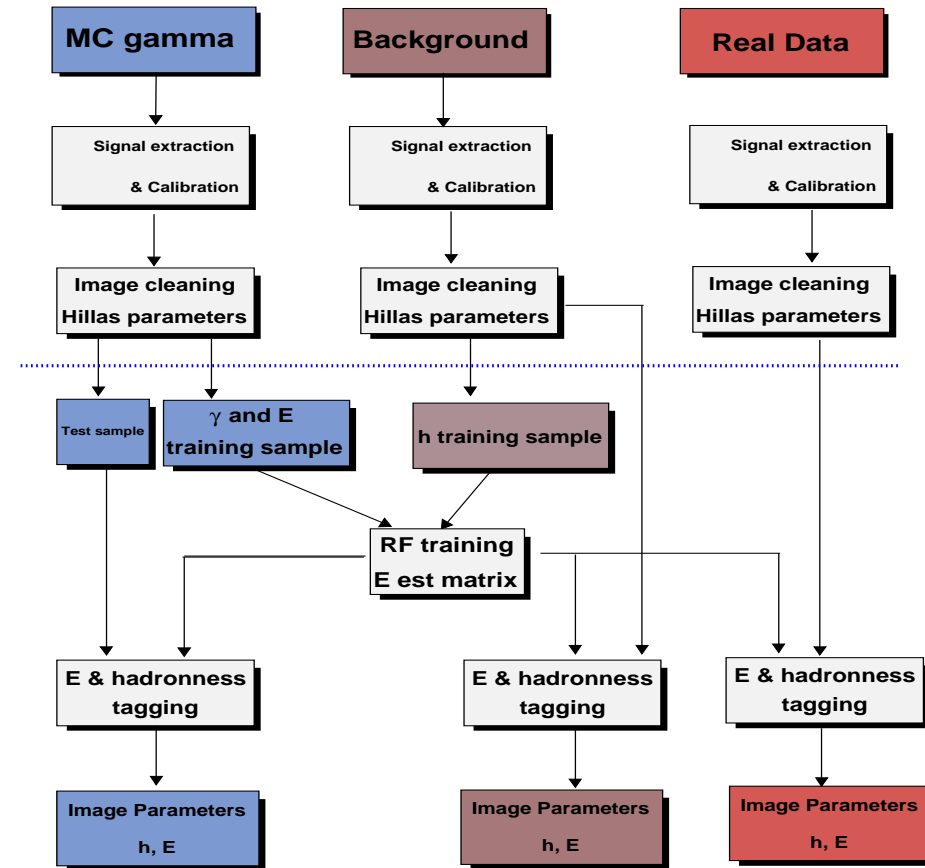


Figure 6.1: Schematics of the MAGIC analysis chain. The center blue line is the data quality cut. When the  $\alpha, \theta^2$  hadronness (h), Energy (E) are calculated in each event, cuts are applied and the sensitivity is optimized. The effective collection area can be derived from final cuts on MC gamma samples. The effective observation time and total number of gamma excess are calculated from the data sample.

## 6.2 Calibration and Pulse Extraction

### 6.2.1 The Pulse Extraction

Once the triggered events are digitized, the calibration software extracts the signals from the FADC slices and converts the information into numbers of photoelectrons. Several different signal extraction methods are used. Among them, the Digital filter method [96] proved to be the most suitable one.

- Fix Window: The extractor adds the complete FADC slice contents of a fixed range of consecutive FADCs slices. Since the window is always fixed, it is important to have a larger timing window such that the complete pulse is included and even when the electronic timing jitters are present. Thanks to AC-coupling of the entire read-out chain, the extracted signals have no bias, even when the pedestal is fluctuating.
- The sliding window: As mentioned before, the electronic jitters could be a problem for the fix window method. The sliding window method is used to avoid this problem. The arrival time of the signal is weighted by the amplitude of the FADC slices. It is necessary to properly choose the width of the sliding window.
- Cubic Spline with Sliding window: The pulse shape is fitted by a cubic spline algorithm [105]. It searches for the position of the spline maximum.
- Digital Filter: The method was introduced by Bartko in 2005 [106]. It fits the signal to a standard pulse form by three assumptions. (1) The normalized signal shape is independent of the signal amplitude and arrival time. (2) The noise and the signals are completely independent. (3) The noise correlation matrix has to be constant.

Detailed information about the Digital Filter method can be found in [106].

### 6.2.2 F-factor Method

The conversion factor (which describes the relation between the number of photoelectrons and FADC counts) of each pixel is calculated according to the calibration runs. The F-factor method [107] is used for this purpose. The method is described briefly as follows. Assume the number of the generated ph.e per calibration event is a Poisson distribution, i.e if the distribution of the ph.e has a mean of  $N$ , then the fluctuation is  $\sqrt{N}$ . Moreover, assume the measured quantity in FADC counts after the pedestal subtraction is  $Q$ , the mean is  $\bar{Q}$ , and the RMS is  $\sigma$ . Then, the measured fluctuation  $\sigma$  will be wider than a pure Poissonian  $\sqrt{N}$ . This is due to the multiplication process inside the PMT. The "wider" factors is called F-factor and it varies in different tubes. It can be calculated by:

$$F = \frac{\sigma}{\bar{Q}} / \frac{\sqrt{N}}{N} \quad (6.1)$$

For the MAGIC-I telescope, the averaged F-factor is approximately  $1.15 \sim 1.2$ . The F value could be derived from measurements in the lab.  $\sigma$  and  $\bar{Q}$  are calculated from the calibration events. Thus, the conversion factor C could be calculated by:

$$C = \frac{N}{\bar{Q}} = F^2 \frac{\bar{Q}}{\sigma^2} \quad (6.2)$$

As described in Chapter 04, during the data taking, interlaced calibration light flashes are fired with 50 Hz. The purpose is to update the conversion factor calculations.

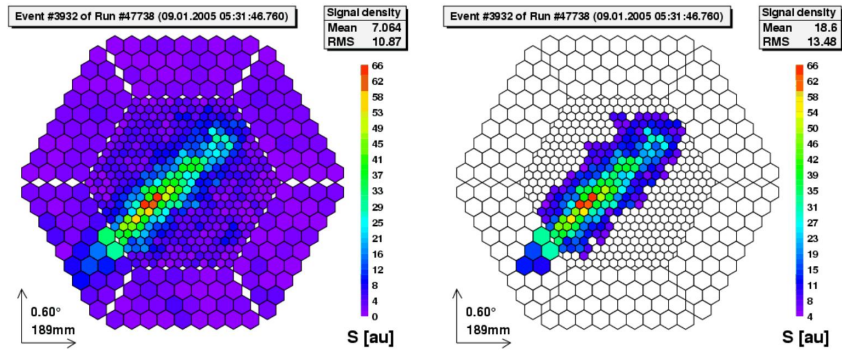


Figure 6.2: An example of the Camera pattern before (left) and after image cleaning (right). The basic idea is to get rid of the fired pixels which are due to random NSB.

## 6.3 The Image Cleaning

The calibrated data contain three important information: (i) The number of ph.e in each pixel (ii) The relative arrival time of the measured signals in FADC slices. (iii) The RMS of the NSB fluctuations per pixel. In order to separate the shower-triggered pixels from NSB-triggered ones, image cleaning is applied. The standard image cleaning for MAGIC, the criteria to keep or reject a given pixel from an event, is relying on the charge inside. It is therefore called "absolute" image cleaning. The criteria are the core pixel,  $Q_{core} \geq 10$  ph.e, and one boundary  $Q_{boundary} \geq 5$  ph.e. In addition, at least one neighboring pixel must fulfill this condition as well. Within one event, we can have several isolated groups of core pixels. Then the boundary pixels are determined if they have at least one connected core pixel and at least 5 ph.e. The number of the boundary rings is usually set to 1. This means that the pixels which are neither core nor boundary ones in the first boundary ring are removed from the event. An example of the event image before and after the image cleaning is shown in Fig. 6.2. After image cleaning, the left image can be used for further analysis.

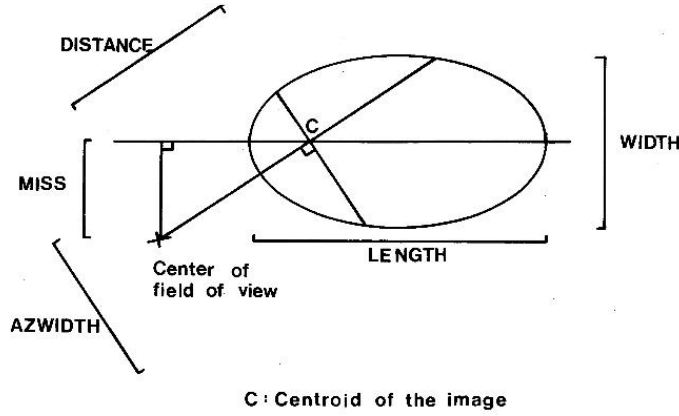


Figure 6.3: The Hillas parameters.

## 6.4 The Image Parameters

After the image cleaning, the image remaining on the camera should represent the light distribution from the EAS. The shower images are then parametrized by the moments of the distribution in the camera, the so-called Hillas parameters. In Fig. 6.3, several image parameters are shown. Each parameter has its own physics implications.

- Size : The total charge contained in the cleaned image. This parameter is roughly proportional to the energy of the primary  $\gamma$ -ray, if the impact point is within the light pool.
- Length : This is the RMS value along the image major axis and the second moment of the image. The length implies the EAS longitudinal development.
- Width : Another second moment of the image. It is the RMS value along the image minor axis. The width distribution implies the EAS lateral development.
- CoG : The center of gravity of the image. It is the position in the camera plane weighted by the mean signal.
- Conc(n) : Concentration parameters. Conc(n) is defined as the ratio between the light contained in the first few  $n$  pixels with the strongest signal and the total light contained in the image.
- Dist : The angular distance between the COG of the image and the expected source position in the camera. The Dist parameter can only be calculated if the source position is known. The Dist is related to the impact parameter of the EAS. Therefore it is very important for energy estimation.
- Leakage: Defined as the fraction of the light contained in the image pixels in the outermost ring of the camera. For images with  $\text{Leakage} \geq 10\%$ , the major part of the image is outside

the camera and will therefore not be recorded. Since the shower image is truncated, the energy estimation is not reliable.

- Alpha: This is the angle of the orientation of the shower image according to the line connecting COG and the source position. Alpha can only be calculated if the source position is known. For  $\gamma$  showers, since the source location in the camera is known, the value of Alpha is expected to be small. However, cosmic ray showers are isotropically distributed, a flat distribution of the alpha parameter is expected. Thus, Alpha is one of the most powerful parameters to reject the cosmic ray background.
- $\theta^2$  :  $\theta$  is the angular distance between the real source position and the estimated source position. The estimated source position in MAGIC is calculated with the DISP method [108], which has been optimized for MAGIC  $\gamma$  ray showers. It includes all above Hillas parameters, except Dist and Conc. Note that there is degeneracy in the DISP calculation. There are two solutions along the shower major axis. The shower image is not totally symmetrical in the longitudinal direction. With one more additional information, which is M3Long, we can tell which solution is the most probable one.
- M3Long: The third moment along the ellipse major axis, which indicates the shower direction.

## 6.5 The $\gamma$ -Hadron Separation

Most of the IACT triggered events are cosmic rays, not  $\gamma$  rays. Even for strong VHE  $\gamma$  ray emitters, such as the Crab Nebula, the ratio between  $\gamma$  showers and cosmic showers in the camera is about 1:2000 above 200 GeV. Hence, an effective hadron suppression is necessary. MAGIC is using the Random Forest (RF) method. This method uses training samples to find a set of classification trees in the parameter space of input images. The training samples for the  $\gamma$ -rays are generated from MC; the training samples for the hadron showers are from the real data. The final outcome from the decision tree is called "Hadronness", which means the level of the "likeness" of hadrons. If it is 1, this means that the event most probably is of hadron origin. If it is 0, it is most likely that the event has a  $\gamma$ -ray origin. More information about the RF method can be found in the dedicated paper [104]. The input parameters for RF are image Hillas parameters. Different sets of parameters are used in source dependent or source independent analysis. For instance, if the Alpha-approach is adopted, meaning signals are extracted from the Alpha distribution, the following parameters are used for RF training: Width, Length, Dist, Conc, M3Long and Size. For the  $\theta^2$  approach, the source dependent parameters cannot be used in RF (for example, Dist and Alpha). For MUX FADC data, additional information from the photon arrival time is used to discriminate  $\gamma$ s and hadrons. These important time parameters can be defined as follows:

- Time Gradient: The pixel information is projected along the major axis of the image such that the problem is reduced to one dimension. Finally, a graph of the arrival time is built

and fitted with a linear function  $y = m \cdot x + q$ . The coefficient  $m$  is the time gradient of the image.

- Time RMS: It measures the arrival time spread of the Cherenkov photons in the pixels after image cleaning.

A more detailed explanation about the time image cleaning parameters can be found in [109].

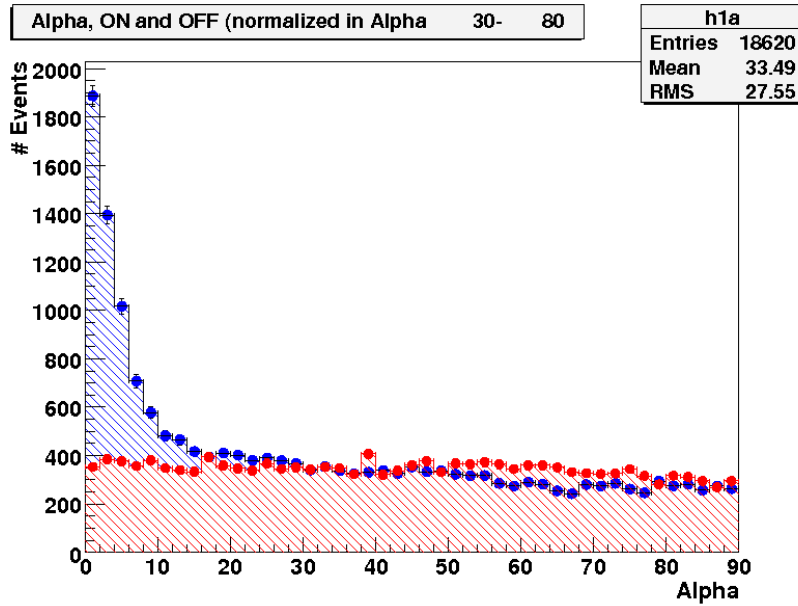


Figure 6.4: An example of the  $\alpha$ -plot. The background events are normalized such that the off-signal region (here,  $30^\circ \sim 80^\circ$ ) matches the between ON and OFF data.

## 6.6 Gamma Signal Extraction and Background Subtraction

### 6.6.1 Source Dependent Analysis

The possible  $\gamma$ -ray events have smaller Alpha values. A typical Alpha plot is shown in Fig. 6.4. In the plot, a Size cut of 200 ph.e. and a hadronness cut at 0.15 have been applied. The events with image parameters calculated with respect to the source position are shown by red color. The background distribution is calculated from the Alpha values with respect to a position on the opposite side of the camera with respect to the source position. One has to be careful that both the ON and OFF Alpha plots are highly correlated because they contain the same events. In order to avoid an unwanted contribution from the  $\gamma$  events in the OFF samples, an additional cut has been applied, which is the anti-Alpha cut. The events with  $\text{Alpha}_{on} \leq \alpha_0$  are excluded from the OFF samples. On the other hand, the events with  $\text{Alpha}_{off} \leq \alpha_0$  are excluded from the ON

samples. This cut can ensure that the Alpha distribution of ON and OFF events are statistically independent in  $\text{Alpha} \leq \alpha_0$  distributions.

### 6.6.2 Source Independent Analysis

In some cases, the source position is not known a priori (like dark matter or EGRET unidentified sources analysis) or the source is not point-like (like Galactic extended sources). For these cases, the Hillas parameters which are calculated based on the source position cannot be used. Therefore, the ALPHA analysis will not be valid anymore. Analysis methods which can reconstruct individual photons arrival directions are quite essential in these cases. For this purpose, the "DISP" method is used. The source position is assumed to be situated on the major axis of the Hillas ellipse, at a certain distance  $|\text{DISP}|$  away from the center of gravity of the image. So there are two parameters which need to be calculated from the shower images. One is the distance  $|\text{DISP}|$ , the other one is the direction of the source position, the so called the head-tail information. The value of the DISP is related to the structures of the telescope. The idea of DISP was first presented by [110]. The basic idea is that the showers which are closer to the telescope rather have a round shape, whereas those which are a bit further away have a more elliptical one. The Cherenkov photons from the beginning of the shower development create a narrower shower image with a higher photon density, the so-called "head". On the other hand, photons from the shower tail are more fussy and gives a wider image. Consequently, the shower image will not be symmetrical. This phenomenon has been explained in Chapter 3.

### 6.6.3 Significance and Sensitivity

The significance of the signal can be calculated by assuming that  $\text{Alpha}/\theta^2$  are Poissonian distribution. For example, if we receive a signal with a significance  $1.64 \sigma$ , this means that with a probability of  $(100\% - 90\%) = 10\%$ , the observed signals are coming from the background fluctuations. Usually the significance is calculated by formula 17 in Li and Ma [111].

$$S = \sqrt{2} \left( N_{on} \ln \left[ \frac{1 + \alpha}{\alpha} \left( \frac{N_{on}}{N_{on} + N_{off}} \right) \right] + N_{off} \ln \left[ (1 + \alpha) \left( \frac{N_{off}}{N_{on} + N_{off}} \right) \right] \right)^{1/2} \quad (6.3)$$

$N_{on}$  and  $N_{off}$  are the numbers of the ON and OFF events in the signal region, respectively. The  $\alpha = t_{on}/t_{off}$  is the ratio between the effective ON and Off time. It could be written as  $\alpha = N_{bg}/N_{off}$ , since usually the trigger is dominated by the background. If we have a smaller  $\alpha$  and fix the number  $N_{on}$  and  $N_{bg}$ , we obtain a better significance  $S$ . A smaller value of  $\alpha$  implies a higher statistics and better understanding on the Off region. If the observation is in Wobble mode, and we use the Alpha approach,  $\alpha$  is equal to 1.

The sensitivity of the telescope is usually determined by hardware and analysis. The increase of sensitivity means being able to detect sources within a shorter time. Usually, we employ the Gaussian approximation instead of Eq. 6.3. The sensitivity of the analysis can be formulated as

$$S_{sens} = \frac{N_{ex}}{\sqrt{N_{bg}}} \cdot \sqrt{\frac{t}{T}} \quad (6.4)$$

$N_{ex}$  is the number of excess events,  $N_{ex} = N_{on} - N_{bg}$ .  $T$  is the observation time, and  $t$  is the normalization time. Note that the major difference between Eq. 6.3 and Eq. 6.4 is that Eq. 6.4 does not take into account the fluctuations of background events. For example, an experiment with a poor background estimation may overestimate the sensitivity compared with an experiment with better background estimation. The current MAGIC-I sensitivity is about  $2.21 \pm 0.05 \pm 0.02\%$  of the Crab flux [112].

## 6.7 Determination of the Lightcurve and the Spectrum

### 6.7.1 The Effective Time

The effective observation time is not simply the time of the last event minus the time of the first event. The reason is very simple; there could be a hole in time during the observation. In addition, the dead time of the detector has to be taken into account. If there are  $N$  events during an observation  $T_{obs}$ , the event rate is  $R_{rate}$ , the effective observation time  $T_{eff}$  is defined as :

$$T_{eff} = N/R_{rate} \quad (6.5)$$

The event rate is estimated by fitting the distribution of the time differences of the consecutive events by an exponential function:

$$dn/dt = n_0 * R_{rate} * e^{-R_{rate}t} \quad (6.6)$$

### 6.7.2 The Lightcurve

Once the number of excess events is obtained, the differential flux level can be estimated as follows,

$$dF = \frac{dN_\gamma}{dEdA_{eff}dT_{eff}} \quad (6.7)$$

Flux is defined as the number of photons per unit time, per unit area and per unit energy. Since the thresholds of different experiments are quite diverse, it is easier to see the integrated effect. We can integrate the flux above a certain energy threshold  $E_0$ .

$$dF_{E>E_0} = \int_{E_0}^{\infty} dE \frac{dN_\gamma}{dEdA_{eff}dT_{eff}} \quad (6.8)$$

$$(6.9)$$

Lightcurves are a series of integrated fluxes in certain time bins. What concerns is the effective area. Since it changes with time, it is estimated from Monte-Carlo samples for each time

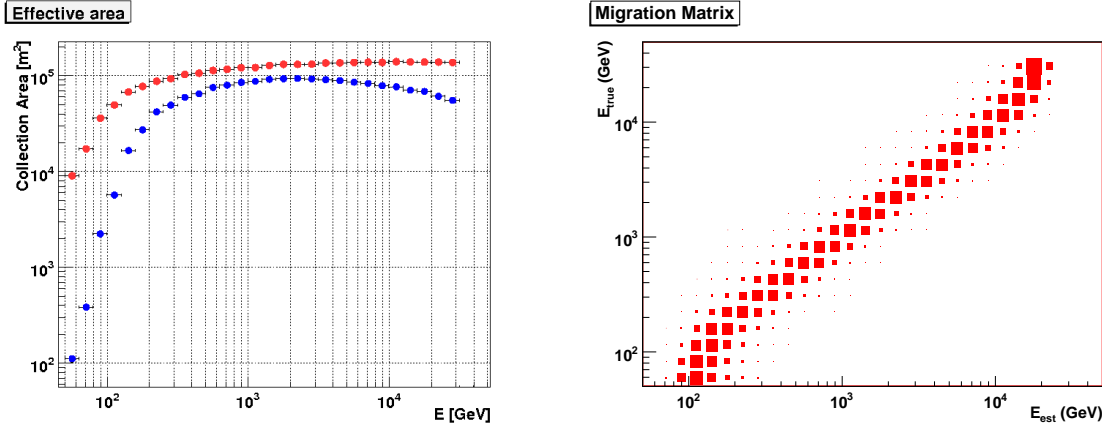


Figure 6.5: An example of an effective collection area plot. The right figure, The energy density matrix from the RF method.

bin with the corresponding zenith angle. Normally, the effective collective area is rising sharply close to the energy threshold, see Fig. 6.5. Therefore,  $E_0$  in Eq. 6.9 should be chosen very carefully. Usually choosing the plateau region is the safest way to proceed, since in this region the collection area is not sensitive to the little differences between reconstructed energy and true energy.

### 6.7.3 Determination of the Spectrum

The event energy is estimated by using the Random Forest technique. Pure MC  $\gamma$  samples which are used for  $\gamma$ /hadron separation are also used for energy training.<sup>2</sup> The input of the training parameters for the energy training are the same as for the  $\gamma$ /hadron separation.

The MC training sample is divided into many different energy bins. The probability density function for each event in each energy bin is calculated. Such probabilities are then used as weights to assign the energy of the events. The derived matrix of the energy estimation is applied to an independent MC  $\gamma$  samples. The actual migration from the true energy into the estimated energy is called migration matrix. Fig. 6.5 shows an example of the matrix.

The spectrum depends a lot on the energy estimation of the events. If the energy resolution is poor, the derived spectrum has many systematic errors. The final spectra are determined in bins of estimated energy. The estimated energy of a  $\gamma$  event is derived from image parameters. Due to finite energy resolution and the bias of the energy estimation, distributions in estimated energy have to be converted into distributions in the true energy. This is what "unfolding" does.

Accurate measurements of the VHE spectrum are important for AGN physics. First, the shape of the high energy spectrum is a key input parameter in the AGN emission models, particularly as it relates to the MeV-GeV measurements by EGRET. Second, how the spectrum varies with

<sup>2</sup>Occasionally, the same samples are used for energy estimation. It has been found that the energy estimated this way only slightly disagrees with the estimation from different samples, i.e. approximately 10 % only.

flux level, compared with longer wavelength observations, provides further emission model tests. Third, the spectral features, such as breaks or cutoffs, can indicate changes in the primary particle distributions.

## 6.8 ONLINE Analysis

The ONLINE Analysis (OA) is a program based on MARS which performs a rough estimation of the source flux level during data-taking. The need of OA is strongly motivative:

- To catch fast transient sources, like AGN flares. OA could be used either as a "self-trigger" tool for extended observation inside MAGIC or as an "external-trigger" tool for other IACTs like VERITAS and HESS.
- OA could give shifters a very preliminary analysis result of the taken data. OA provides plots which can help the shifters on site to monitor the quality of the observations, e.g. the camera inhomogeneities and the conversion factor (the relative gain) of each pixel and the source activities.

Several features of the ONLINE analysis will be introduced below:

- Signal reconstruction: Search for the slices in the range 16 - 64 instead of the full range. The reason is to avoid the switching noise. For pedestal calculation, one moves 25 slices away from the peak and measures the average baseline of the 10 FADC slices around that position.
- Calibration: For the relative calibration, we loop over the first 300 interleaved calibration events and extract the correction factor in each event. For absolute calibration, we fix the conversion factor to 0.018 ph.e. per FADC count. Note that if the gain of the telescope changes, this value should be adjusted.
- Image cleaning: A rough image cleaning is applied. We try to keep all the pixels with at least 8 ph.e and a neighbor with at least 8 ph.e.. In addition, Hillas parameters are calculated.
- Spark cut is applied. Center of Gravity (COG), camera  $\phi$  plot, and conversion factor plot are shown. Those plots are good for shifters to check the status of the telescope during data taking. An example of the plots are shown in Fig. 6.6.
- Alpha plot: The search for a possible signal from a certain source is performed through a alpha plot. The  $\alpha$  plot is calculated for three different zenith angle ranges:  $\leq 30^\circ$ ;  $30^\circ \sim 43^\circ$  and  $\geq 43^\circ$ . A pre-trained RF matrix is used. The matrix is produced by training with low zenith angle hadrons and MCs with a PSF of 12 mm. The re-determined cuts are : (1) Size  $\geq 200$  ph.e. (2) hadronness  $\leq 0.1$  (3)  $\alpha \leq 8^\circ$ . The gamma rate per minute and Li&Ma significance are calculated.

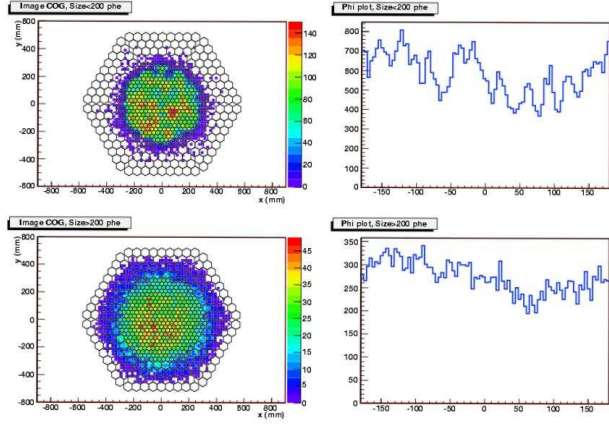


Figure 6.6: An example of the ONLINE analysis output plot. Two different Size cuts are used,  $\text{Size} \geq 200 \text{ phe}$ . and  $\text{Size} \leq 200 \text{ phe}$ . The COG and  $\phi$  plot give shifters a rough knowledge about the status of the camera inhomogeneity.

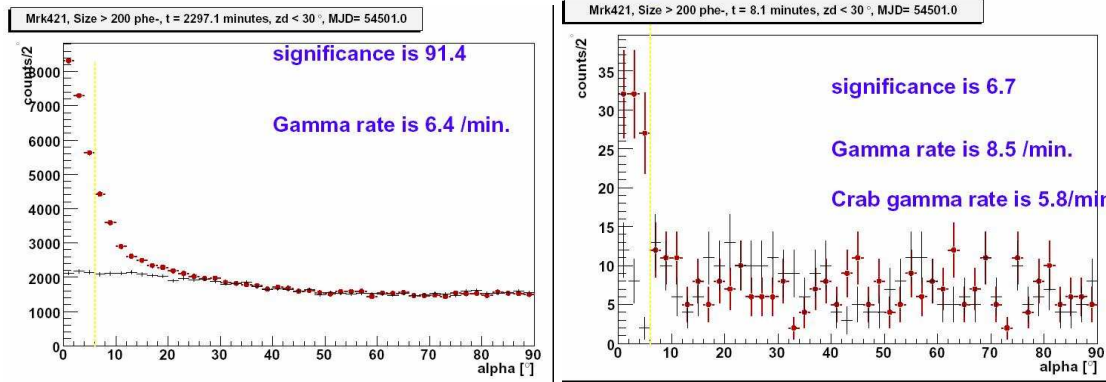


Figure 6.7: Alpha plot from ONLINE analysis

- Lightcurve: The daily average lightcurve is shown immediately after the observation. Additionally, the observational flux within the recent three months (90 days) will also be shown. The flux level is estimated by comparing the rate of  $\gamma$ -rays per unit time between Crab and the observed source.

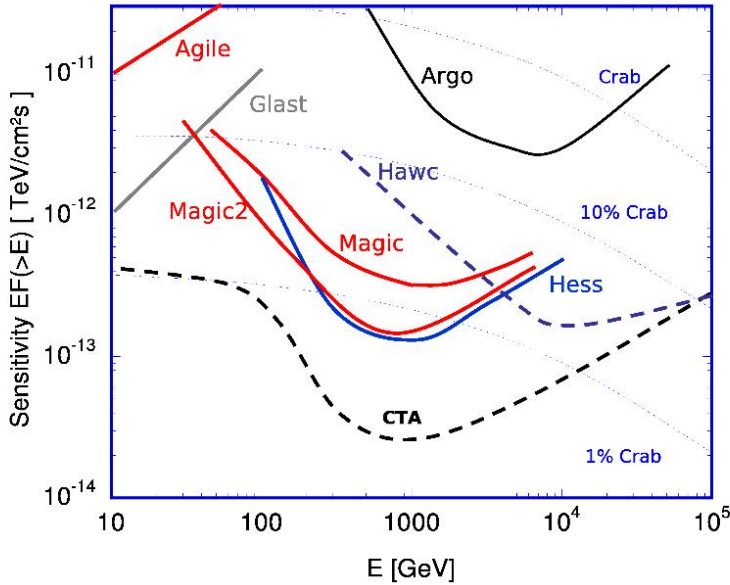


Figure 6.8: The sensitivity of current gamma ray telescopes and satellites. The plot is from [12]

## 6.9 Basic MAGIC Performance

In order to have no bias on selecting all the cuts and "massage" the real dataset while doing analysis, people analyze Crab data first to see if their analysis method is verified. Afterward, the significance on Crab data is optimized by adjusting different cuts in multi-dimensional parameter spaces. Once the cuts are fixed, the same set of cuts are applied on the real data. The VHE  $\gamma$ -ray emission from the Crab Nebula was first discovered by the Whipple collaboration in 1989 [113], and those gamma radiations are believed to be produced by the pulsar wind nebula which is about 0.1 pc away from the central powerful pulsar. The flux is stable from 80 GeV up to 80 TeV [114] [115]. Since the Crab nebula constantly emits VHE  $\gamma$  rays, the so-called standard source, the data from Crab can be used as a calibration tool. The sensitivity in the VHE  $\gamma$ -ray community, has a common definition, which is the lowest flux level at which a telescope can detect  $5\sigma$  within 50 hours. The MAGIC sensitivity is shown in the plot in Fig. 6.8. After the FADC was installed, the MAGIC sensitivity improved to 1.8% of Crab,  $5\sigma$  and 50 hours of observations [112].

# Chapter 7

## Monitoring of Mrk421 with the MAGIC Telescope

The blazar Markarian (Mrk) 421 is one of the most-studied extra-galactic objects in the VHE  $\gamma$ -ray domain. It is the first extragalactic object discovered in TeV regime. During the past almost 20 years, several times of high states (the so-called flares) in X-ray and TeV bands were observed. Also, intensive multi-wavelength campaigns were carried out many times on this source. Numerous of fruitful physics results have been published which will be discussed later. This chapter is organized as follows: A description of the physics motivations of the AGN monitoring program will be followed by a very brief historical review on the observations of Mrk421, particularly in the TeV band. Subsequently, MAGIC strategies of Mrk421 monitoring will be introduced, as well as several analysis tools and formulas which will be used in our further analysis. In the last section, analysis results on MAGIC Mrk421 data from 2004 to 2005 will be presented.

### 7.1 Introduction: Physics Motivation for the AGN Monitoring in the TeV Energy Band

A few possible blazar high energy emission mechanisms have been discussed in Chapter 2. TeV blazars show short time variability in TeV band and are usually correlated with X-ray. The sensitivity of the current generation of IACTs is high enough for detecting flux variability down to a few minutes while the sources are at high states. The observation of short time variabilities and flares are crucial, because short time variability constrains the size of the emission region. However, with the small field of view and tight observation schedule of IACTs, catching short time variabilities and flares seems to depend on luck. In old times, people relied much on X-ray triggers because of the strong correlation between X-ray and TeV emissions. Even so, TeV flares without a X-ray counterpart have been detected and proved to be important identifiers for the modeling. Therefore, to work with "self-trigger" mode is necessary for IACTs. Based on this purpose, constant monitoring of selected interesting sources is highly motivated. Nevertheless, it was argued that the scaling of the black hole properties is proportional to the

black hole mass, in particular the stellar mass black hole (like in X-ray binaries systems in our galaxy) and very massive black holes like AGNs. Thus the question is "Why should we put so much efforts on monitoring far distant AGNs, especially when we can get better sampling of Galactic stellar-mass black holes ?" Particularly, all the time scales are scaled with BH mass, a year in the life of a quasar corresponds to a second of the X-ray binaries. Although the scaling rule sometimes works, the difference between the X-ray binaries and AGNs is argued, like by R. Blandford [116]. For example, the former does not show ultra-relativistic jets or prominent broad emission lines. Moreover, the environments outside the systems are completely different from each other. However, comparing between different mass scales black holes and testing the scale parameters is still important for revealing the interacting processes between black holes and surrounding environments, such as their accretion disks. The constant monitoring of AGNs also provides solutions for such purpose. In the following I briefly summarize the physics motivations for TeV long term monitoring of AGNs.

- Understand the temporal high energy emission behaviors.
- Catch orphan flares or variabilities without any counterpart.
- Get a better sampling for different states in order to find the basic intrinsic differences between states.
- Search periodicity. We can expect two different mechanisms to produce periodic/quasi-periodic emissions. One is due to the emission process, the other one is due to the modulation of the external factors such as rotation blobs on the disk. For instances, the long-term periodicity in the lightcurve of blazars could be introduced by underlying physical processes such as the existence of supermassive binary black holes, or the oscillations of the accretion disk [117].

## 7.2 Markarian 421

Markarian 421 (RA:  $11h04m27.4s$ , Dec:  $38^\circ12'34''$ ) is a well-known BL Lacertae object and the first detected extragalactic TeV  $\gamma$ -ray source. Its red shift is 0.03, which is about 360 M light years away. When it was first discovered, its spectroscopic shows large optical polarization and variability (e.g. Ulrich et al. 1975 [118]). In addition, the weak absorption lines from its elliptical host galaxy is a featureless spectrum. In 1975, Mrk421 was for the first time associated with the radio source B2 1101+38. The same year, Ulrich et al [118], showed that Mrk421 had non-thermal optical emission, variable polarization, and a low ratio of infrared-to-total nuclear luminosity. Those radio emissions are suspected to come from synchrotron radiation. In addition, highly concentrated optical nuclei, and featureless continuum spectra, have been found. Ulrich concluded in his paper that the source Mrk421 is a normal elliptical galaxy with a central non-thermal nucleus, which is quite similar to the source BL Lacertae (BL Lac). It is known that BL Lac later became the prototype for this class of objects. Ulrich at that time also determined the red-shift of Mrk421 from three stellar absorption lines. Later, other measurements confirmed

the result  $z = 0.03$ . Today, this value is still valid. It is one of the closest blazars to the Earth. In 1976, Ricketts et. al.(1976) [119] had discovered a highly variable soft X-ray components from Mrk421 with the Arial V satellite. This was the first time a BL Lac object was associated with an X-ray source. The X-ray emission from Mrk421 was quite different from other discovered galactic X-ray sources (e.g.: Cygnus X-1) at that time, the intensity varying from one order of magnitude over different time periods from one day to a few tens of days. Mrk421 is one of the AGNs detected by the Energetic Gamma Ray Experiment Telescope (EGRET) [120], an instrument working in the 30 MeV-30 GeV energy range of the Compton gamma ray observatory (CGRO) [121]. The imaging Compton telescope (COMPTEL) also detected Mrk421 in the 10-30 MeV range at a  $3.2\sigma$  level (Collmar et al. 1999) [122]. In 1992, the first detection of TeV emission from Mrk421 was achieved by the Whipple telescope. Since that time, Mrk421 has constantly been monitored by the Whipple telescope and a series of further discoveries were realised. Concerning the history of TeV observation of Mrk421, a full discussion will be presented in the next section.

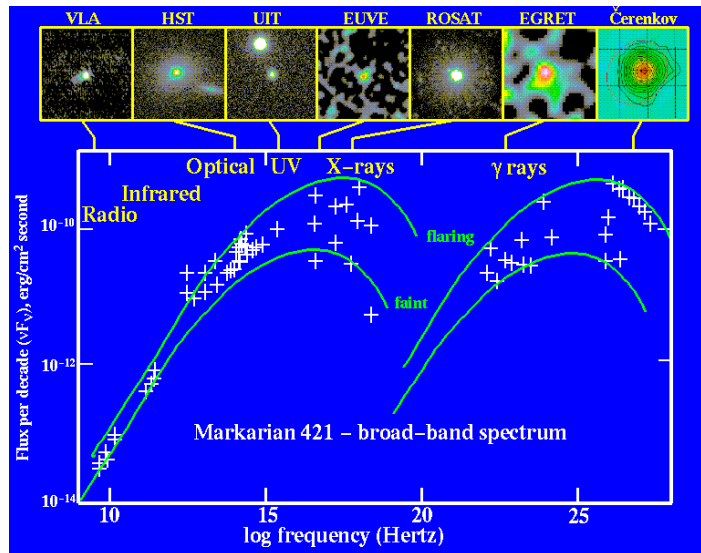


Figure 7.1: The SEDs of Mrk421 from radio to TeV band. Mrk421 is a HBL object, in which the two peaks, are located at X-rays and  $\gamma$ -rays respectively. Usually, the first peak is well sampled and measured, however, the high energy peak usually has a lot of uncertainties.

Fig. 7.1 shows the SED of Mrk421. It ranges from radio to TeV observations. The first peak, the synchrotron peak, is clearly located in X-ray. However, the second peak is usually not directly measured; it shows the location between the energies probed by EGRET and by the TeV IACTs. From the plot, approximately equal power seems to be generated in each of the two humps of the SEDs.

Some observational features of Mrk421 in different energy bands are listed below:

- In radio : Radio observation has a much better angular resolution compared to that of TeV IACTs. Imaging the radio emission from blazar jets with radio telescopes, such as VLBI,

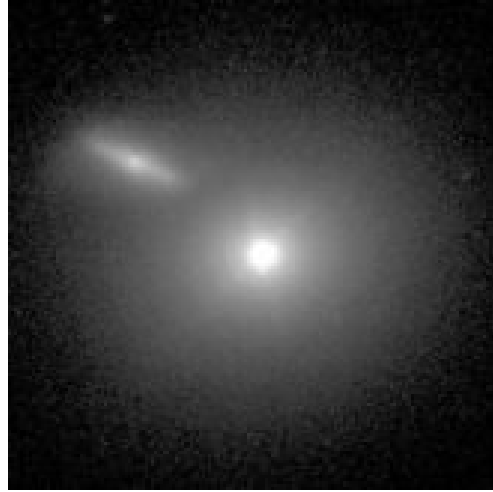


Figure 7.2: The optical image of Mrk421 and its companion galaxy, 421-5. Image credit: Aimo Sillanpaa, Nordic Optical Telescope.

provides us a unique opportunity to study the evolution of the shocks up to parsec scales or even larger. [123] showed only subluminal apparent motions of about  $0.3 c$  in the jet of Mrk421 at a distance of about 1 pc from the radio core. This observation suggests that the bulk Lorentz factor at the parsec-scale radio jets is only moderately relativistic. It turns out to be a common property of other TeV blazars, such as Mrk501 [124]. More implications about the Mrk421 jet from radio observation will be discussed later.

- In near infrared : Results from near-IR J band monitoring have been reported [125]. It was found that Mrk 421 showed significant Intra-Day Variability (IDV) and short term variability in this energy band as well. A maximum variation about 0.89 mag was reported. Flaring activity, with typical brightness variations of  $\sim 0.4$ , were also seen [125].
- In optical : The magnitude varies from 11.6 to more than 16. There is a companion galaxy, merely 13" away to the north-east, see Fig. 7.2. This galaxy is interacting with Mrk421. Observations show two features. One is that non-periodic and fast violent variations in the intensity are on the time scales of hours to days. The other one is that there seems to be periodicity with a possible period of  $23.1 \pm 1.1$  years [126]. Thus, the binary black hole model is proposed to explain the periodicity of the optical light curve. Liu et al. [126] compiled these data from 22 publications to assemble a long-term light curve dating back to 1900. In their study, the B band data was used since in the B band more data was available. They found that in the past decade the brightness of Mrk421 varied from 11.6 to 16 and their lightcurve analysis revealed that Mrk 421 undergoes non-periodic rapid variations on time scales of hours to days. However, it is surprising that they have also found the periodic behavior occurring at  $23.1 \pm 1.1$  years, with another possible periods of  $15.3 \pm 0.7$  years in their studies. Even though, the results does not show strong significance. More data are necessary to prove this claim. The companion galaxy Mrk421-5, has a bright,

compact nucleus that may be an early-type spiral galaxy. Gorham et. al [127] suggest that Mrk 421-5 contains a Seyfert-like nucleus, but does not have any detectable emission lines according to ground-based studies. It is thought that the companion is within the potential well of Mrk 421 and may be sweeping through its stellar halo.

- In UV : Mrk421 has a strong emission in UV, suggesting a nonthermal origin. Mrk421 was discovered on the basis of its strong UV continuum and unusual blue spectrum (Markarian and Lipovetskii, 1972) [128].
- In X-ray : As I have described, a highly variable soft X-ray (2-18keV) counterpart to Mrk421 was discovered by the Aerial V satellite. In 1984, Mrk421 was discovered in the 2-6 keV band with the HEAO-1 sattelite [129] and was classified as a BL Lac object in 1989 [130].
- In Particles : No ultra-high energy cosmic ray or neutrino has been detected yet.

### 7.3 Morphology

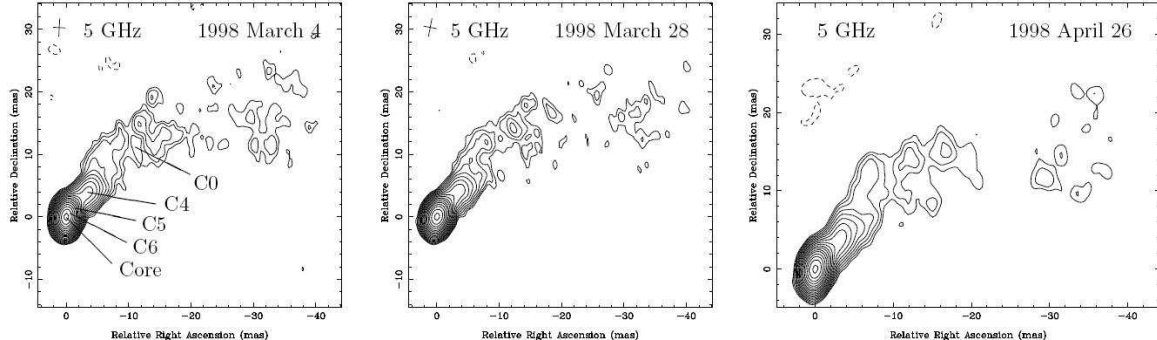


Figure 7.3: The total intensity map of Mrk 421 from radio observation (frequency 5GHz) at three different flux states from March - April 1998. The figures are from [13]

The angular resolution of the current generation of IACTs is about 3-6 arcmin, all the extragalactic AGNs are considered as point sources. However, with the higher angular resolution of radio telescopes, like the Very Large Array (VLA) from NRAO, the substructures could be resolved [13]. In the center of the figure, there is an unresolved core surrounded by a diffuse halo [131]. The halo has an angular extent of about 3 arcmin, corresponding to of a physical size of 70 - 100 kpc. The radio images observed with Very Long Baseline Interferometry (VLBI) at three close-spaced epochs one month apart in March-April 1998 is shown in Fig. 7.3. In the same time, Mrk421 was monitored by TeV instruments. Details will be described later. This size is much larger than its optical/IR extent, which is about  $0.5^\circ$  [132]. VLBI is a group of radio telescopes which provides powerful angular resolutions based on very long baselines. In

many radio-loud AGN sources, shocks in jets become visible as superluminal moving "blobs" or "components" on VLBI images and can sometimes be traced for several years following the flare events. VLBI has observed a single jet extending from the very central core.

## 7.4 Mrk421 TeV Observations in the Past 17 Years 1992-2005

### 7.4.1 From Discovery to 1998

Since the first discovery of TeV emission from Mrk421 by the Whipple collaboration in 1992, Mrk421 had been intensively studied by all different telescopes in different energy bands, including several coordinated multiwavelength campaigns. The first discovery by Whipple in 1992 had a statistical significance of  $6.3\sigma$  based on 7.5 h of observations. The quoted flux about  $\phi(E \geq 0.5\text{TeV}) = 1.5 \times 10^{-11} \text{ photons cm}^{-2}\text{s}^{-1}$ , which is about 30 % of the Crab flux. An independent detection of Mrk421 was achieved by the HEGRA CT1 and CT2 telescopes [133]. Based on the data taken in 1994-1995, HEGRA observed a  $\gamma$ -ray signal at  $5.8\sigma$  and the flux was about 50 % of the Crab. HEGRA also reported a measured spectrum from Mrk421 similar to the Crab Nebula. The Whipple Observatory has regularly monitored Mrk421 since its first detection. Between 1992 and 1994, the source was observed in each observing period, the  $\gamma$ -ray fluxes were always considerably variable [134]. In May 1994, a flare was observed when the TeV  $\gamma$  flux increased by 10 times within a few days [69].

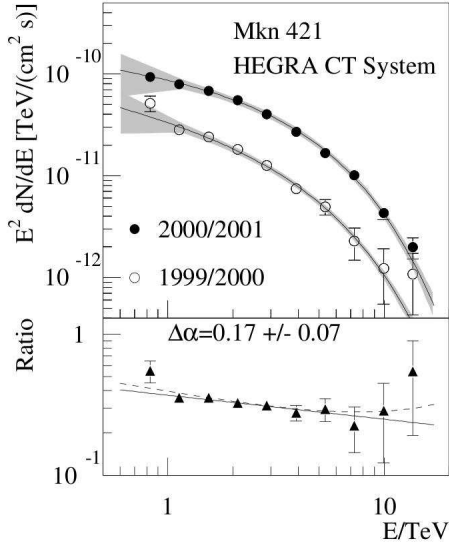


Figure 7.4: The spectrum of Mrk421 observed by the HEGRA telescopes. This was the first time, the spectrum indices changing with different flux states was observed.

The highest TeV flux of this flare (15 May 1995) occurred one day before the major X-ray flare detected by the Advanced Satellite for Cosmology and Astrophysics (ASCA) instrument.

A following analysis of multiwavelength observation results showed that the most significant energy output during the flare occurred in the X-ray and TeV  $\gamma$  bands. However, only a relatively small increase in the GeV  $\gamma$ -ray flux was seen by EGRET during the time of the flare. One of the most important results from this multiwavelength campaign was that the first evidence of a correlated variability between VHE  $\gamma$ -rays and the other lower energy bands was observed. In 1995 and 1996, a few multiwavelength observations were successfully performed and an even more remarkable variability in the TeV band was observed [135]. A flare was seen and the doubling time was a bit less than one day. These facts gave scientists two important information. One was that the region for the TeV emission is limited, the other one was that the TeV variability maybe even shorter than one day. The multiwavelength campaign in April and May 1995, shows two important features in Fig.37 in [135]. The first one is that there seems to be certain degree of correlations between several different energy bands, which strengthens the results in 1994. The second one is that the maximum variability occurs in the X-ray and TeV bands. It is worth noting that the MeV/GeV gamma ray flux was at a level below the sensitivity threshold of EGRET. In addition, the radio flux at 14.5 GHz from Mrk421 showed no significant changes. In 1996, the Whipple telescope reported historically dramatic flares from Mrk421 [76]. In the first flare, the  $\gamma$  rate increased to about 40 times higher than the baseline ( $\geq 350$  GeV) within a doubling time of about  $\sim 1.5$  hour. In the second flare, the gamma rate increased to 15 times that of the baseline ( $\geq 350$  GeV) with a doubling time of only 15 minutes. These remarkable short times and large intensity increases in the TeV  $\gamma$  flux were almost one to two orders of magnitude bigger than those typically seen in the EGRET observations of AGN at MeV/GeV band. These short time variabilities imply that the TeV emission region must be relatively small. In the meantime, air shower arrays have searched for  $E \geq 10$  TeV  $\gamma$  emission from Mrk421. However, none of them claimed discovery. Until the big flare in 2001,  $\gamma$ -rays above 10 TeV from Mrk421 were claimed to be detected [136].

In 1998, R.A. Ong in his review paper [137], draws the following important points regarding Mrk421 observations until that time.

- A simple power law fit cannot represent the spectrum which is observed from Mrk421. During the flare periods, Mrk421 is emitting significantly greater power at TeV.
- There is a large variability seen in the TeV regime of Mrk421, but it is not seen in MeV/GeV energies.
- The upper limits around 10 TeV from the air shower array measurements generally lie below a simple power law extrapolation from TeV data, giving hints of a cut-off energy above 10 TeV.

### 7.4.2 From 1998-2004

In September 1998, the envisaged five-telescope system from HEGRA was completed after refurbishment of CT2 with new hardware and software. In 1999, both Whipple and HEGRA published their Mrk421 observation papers. The spectrum of Mrk421 measured by Whipple

Time	Participants	Main Achievements	Ref
1998	BeppoSAX, Whipple	Established the first hour-scale correlations between X-rays and TeV in a blazar	[140]
1998 April	ASCA,CAT, HEGRA	confirm sub-hour scale correlation.	[141]
2000 Feb,May	HEGRA,RXTE	No curvature on the spectrum Time average spectral index $2.94 \pm 0.6_{stat}$	[142]
2003 Feb, 2004 Feb	Whipple, RXTE	Multi-zone SSC is better fitted. Orphan flare ?	[14]
2005,2006	Whipple, RXTE, WEBT	$F_{var}/F_{pp} \sim 2$	[143]

Table 7.1: Several historical multiwavelength observations of Mrk421. Observations which at least include one IACT are listed.

during the high state was [138]

$$\frac{dN}{dE}(250GeV - 10TeV) \propto E^{-2.54 \pm 0.03_{stat} \pm 0.1_{sys}} \quad (7.1)$$

However, HEGRA had measured the Mrk421 spectrum during the lower flux (about 0.5 Crab Unit) [139].

$$\frac{dN}{dE}(500GeV - 7TeV) \propto E^{-3.09 \pm 0.07_{stat} \pm 0.1_{sys}} \quad (7.2)$$

Though, they measured the spectrum during the different flux states of Mrk421, the important conclusion at that moment was that both HEGRA and Whipple measured "no" spectral variability with different flux levels.

HEGRA observed Mrk421 in February and May 2000 [142]. They found flux variabilities, however, the time averaged spectrum index was more or less the same as in the previously published paper,  $2.94 \pm 0.06_{stat}$ . In 2001, another big flare from Mrk421 was observed. Whipple [144] [145] and HEGRA [146] presented their results on spectral variability with the different flux levels, see Fig. 7.4. The change of the spectral index during different flux level implies that the IC peak shifts while the flux changes. During the 2001 high flare state, Whipple and HEGRA also derived a spectrum up to 15 TeV with an exponential cutoff which had never been seen before in the case of Mrk421, but had already been shown in Mrk501 in its 1997 high state [147]. The formula is described as  $dN/dE = KE^\gamma \exp(-E/E_0)$ . For the Mrk501 flare in 1997 and the Mrk421 flare in 2001, there are different combinations of  $(\gamma, E_0)$ . For Mrk421,  $\gamma = 2.23 \pm 0.04$  and  $E_0 = 4 \pm 0.4$  TeV [148], for Mrk501,  $\gamma = 1.92 \pm 0.03$  and  $E_0 = 6.2 \pm 0.4$  TeV [147]. Fossati et al. 2007 [149] produced very detailed studies on 2001 flare data. The unprecedented details of correlations between variations in the X-ray and TeV bands supports the same electron distribution in the same physical region. They are responsible for the emission in both energy bands. However, their detailed findings also pose a serious challenge to the current TeV photon emission model [149]. In April 2004, variations of approximately one order of magnitude in TeV

flux were observed both in X-ray and TeV bands. The X-ray synchrotron peak shifts to above 2 keV during high states [150]. In a high flux night (April 18th, 2004), intra-night variability was detected with a decay time of shorter than 1 hour. The time averaged energy spectrum is curved and is well described by a power-law with an exponential cutoff at  $E_{cut} \sim 2$  TeV, and an average integral flux above 3 Crab flux units. Significant variations of the spectral shape were detected with a spectral hardening when the flux increased. H.E.S.S. reported a Mrk421 energy spectrum which had a clear roll-over at high energies (above  $\sim 5$  TeV) and was best fitted by a power law with an exponential cutoff. STACEE also reported the data from January to April 2004. Their data are well fitted by a single power law form from 100 GeV to 1.5 TeV [151]. MAGIC observed Mrk421 from November 2004 to April 2005 [152]. During the whole observation period, the Mrk421  $\gamma$ -ray flux varied from 0.5 - 2 Crab units (above 200 GeV). Although the flux variation happened on a day-by-day basis, no short time variability (Intra-Night Variability) was found. A clear correlation between X-ray and TeV fluxes was seen, but no significant correlations between TeV and optical data [152]. An interesting coordinated observations of Mrk421 by H.E.S.S. and MAGIC was performed during the night of 18 December, 2004. The result shows a good agreement between the energy spectrum as measured by MAGIC and H.E.S.S., where the spectral data could be fitted by a single power law form across two orders of magnitude of energies [153]. In addition, this coordinated campaign gave IACTs an opportunity to cross-calibrate the telescopes using variable sources.

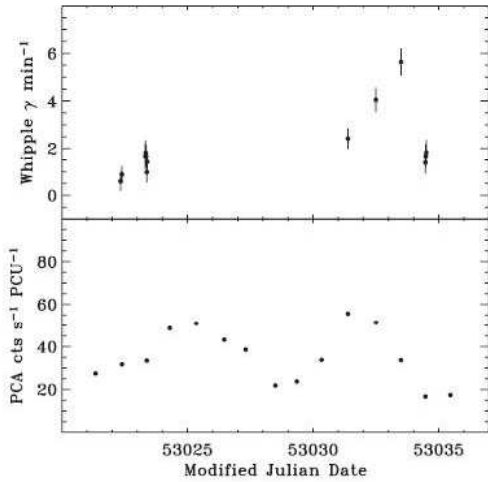


Figure 7.5: Whipple observed the Mrk421 flare in April 2004. The upper panel is the  $\gamma$ -ray observation, the lower panel is from the ASM results. The X-ray flare was obviously ahead of TeV flare by one or two days [14].

Another important result from this period is reported by the Whipple group. They observed Mrk421 over the period 2003-2004. The source was observed simultaneously by Whipple and RXTE during each clear night within the Whipple observation windows. At the same time, supporting observations were carried out by using radio and optical telescopes to provide the data for a SED study. Among their results, the presence of TeV flares that have no coincident

counterparts at longer wavelengths is of particular interests. Whipple found as well that the TeV flux reached its peak a few days before the X-ray flux did during a giant flare in 2004 [14]. Their SED could not just be explained by a simple one zone SSC model, but fit better with multiple zones [14]. From Fig. 7.5, we clearly see the X-ray flare was ahead of TeV flare. It is hard to tell if this TeV flare really was similar to the reported "orphan" flare in 1ES1959+650 or not. If this really was an orphan flare, it could be explained by a hybrid model in which both electrons and protons are presented in the jet. On the other hand, if the preceding X-ray flare turns out to be the counterpart, the TeV 1-2 day lag then the X-ray emission could not be explained by current emission models. The orphan flare and hybrid model will be discussed in Chapter 10.

Since September 2005, the Whipple 10m VHE Gamma-ray telescope has been operated primarily as a blazar monitor. There are five established northern hemisphere blazars which were chosen to be monitored routinely each night when they were visible. Mrk421 is one of them. In Whipple's recent articles [143], their the multiwavelength results from November 2005 and June 2006 were presented. The authors calculated the fractional RMS variability amplitude  $F_{var}$  and the point to point fractional RMS variability amplitude  $F_{pp}$  for each waveband and found that the  $F_{var}$  increased with higher frequency wavebands<sup>1</sup>. Furthermore, in general, the value of  $F_{var}$  in one day binning ranges between 15 % and 33 % [143]. This value is comparable with Whipple's results from 2003-2004 [14]. In Giebels et al. (2007) [154], the authors found evidence for a power law behavior of  $F_{var}$  over four decades of energy of Mrk421 on MJD 51991-51992. However, in [143], no such relation was found. Whether a power law behavior of  $F_{var}$  is a general feature or just a particular case, still remains to be proved. For the SED study, a big Doppler factor of  $\sim 90$  and a magnetic field of  $\sim 0.1$  Gauss is derived. The large Doppler factor results in some inconsistencies in the shock acceleration parameters, namely a very hard electron spectrum ( $\sim E^{-1.5}$ ).

The flares are produced by shocks inside the jet [77] [78] with an apparent variability time which is strongly compressed because of the bulk relativistic motion of the jet. From the one zone homogeneous SSC model, the variability of Mrk421 requires a high relativistic Doppler factor in order to reproduce the observed energy spectrum and variability. For instance, Maraschi et. al. [140] modeled the emission from Mrk421 in April 1998 with a  $\delta = 20$ . Krawczynski et al. in 2001 [142] and Konopelko et al. in 2003 [155] found that the emission during 2000 is best fitted with  $\delta \sim 50$ . We will discuss these SSC parameters in later chapters when we discuss about the MAGIC results. A short TeV observational history of Mrk421 until 2005 was briefly reviewed in this section. From 2005, the so-called third generation of IACTs, H.E.S.S., MAGIC and VERITAS have been ONLINE and delivered more sensitive and reliable results.

---

<sup>1</sup> $F_{var}$  and  $F_{pp}$  will be explained later in this chapter.

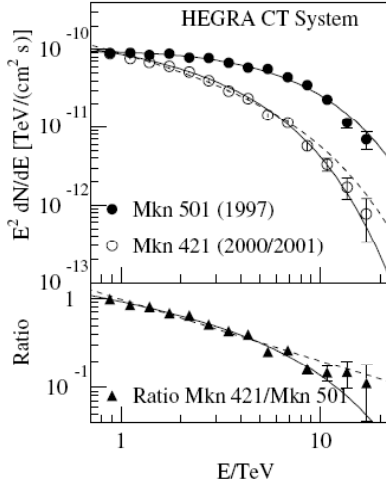


Figure 7.6: The spectra of Mrk501 during the 1997 flare and Mrk421 during the 2001 flare. The observed spectra are well described by a power law with exponential cut-off. The cut-off energy and the photon index are different for both spectra. The cut-off energy and photon index are  $\alpha = 1.92 \pm 0.03_{stat} \pm 0.2_{sys}$ , and  $\alpha = 2.19 \pm 0.02_{stat} \pm 0.04_{sys}$  for Mrk501 and Mrk421, respectively. The dashed curve in the plot results from fixing the cut-off energy  $T_{cut}$  at 6.2TeV as measured from Mrk501. the  $\chi^2 = 5.7$ (12 d.o.f.). The plot is adapted from [15].

## 7.5 MAGIC Strategies of Long-term Monitoring

Based on highly motivating physics reasons, from December 2006, MAGIC has continuously observed Mrk421 every 3 or 4 days in each observational period, i.e. 30 minutes in each time slot. Besides Mrk421, a few other established TeV blazars are, at times, being constantly monitored. In the following, basic strategies of the MAGIC AGN monitoring program are listed.

- Use observation time under moonlight and twilight.
- The monitoring program can trigger MAGIC itself or other IACTs or even neutrino telescopes, if the sources are in high states. See later explanation.

Source	Date
M87	08 January
Mrk421	04, 06, 12 February
	31 March, 04 April, 04 May
	04, 08 June

Table 7.2: High state triggers due to MAGIC ONLINE analysis

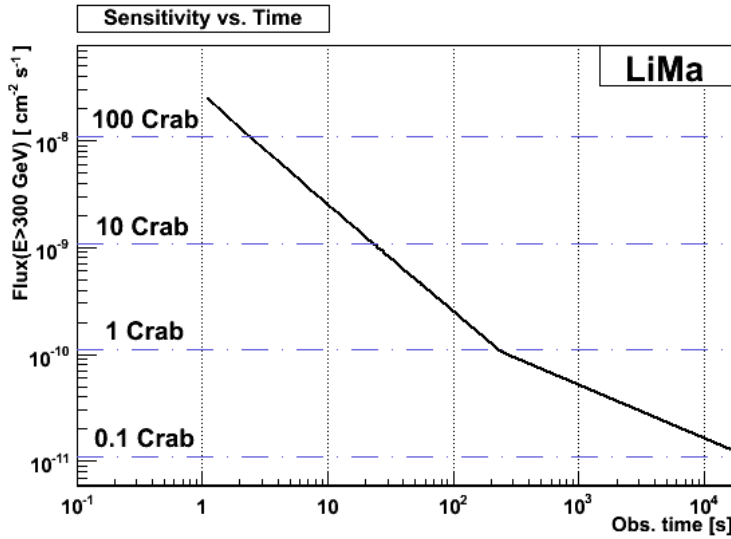


Figure 7.7: MAGIC I sensitivity plot : The integrated TeV flux is from 300 GeV to 30000 GeV. From 1 to 5 minutes, the sensitivity is limited by photon statistics, above 5 minutes, the sensitivity increases with square root of time.

- Observe just 20-30 mins per night because of the good sensitivity of MAGIC. From Fig. 7.7, within the first 20 mins, the sensitivity of the MAGIC telescope could reach up to 20% of the Crab flux  $\geq 300\text{GeV}$ .
- Fast ONLINE analysis: ONLINE analysis has been mentioned in Chapter 6. Shifters on-site can know immediately the activities of the monitored source.
- Extended observation with MAGIC is possible if the flux state is higher than 2.0 Crab Unit(C.U.) above 200 GeV: Once the flux level is higher than two Crab ( $\geq 200\text{ GeV}$ ), continuous observation with MAGIC starts. The time for extended observation depends on the zenith angle, weather conditions, the source's behavior and other conditions (such as simultaneous observation with other telescopes or satellites).
- Possible alert among MAGIC, HESS and VERITAS in case of finding high states of sources. Simultaneous or consecutive observations of the same source with other IACTs such as HESS and VERITAS are useful and practical. They increases the sampling of the high states taking into account the time difference between individual sites. A wider energy range is covered in the spectrum because of the observational zenith angle difference between individual sites. In addition, cross calibrations between different telescopes are also possible by watching the same source simultaneously.

Date	Major changes
2004 - April 2006	Siegen FADCs
April 2006 - Jan. 2007	Siegen FADCs+Splitters
Feb. 2007 - Sep. 2007	MUX FADCs 80 slices
Sep. 2007 - now	MUX FADCs 50 slices
Oct. 2007	MUX FADCs SUM trigger installation
May 2008	Data format changes

Table 7.3: Major Hardware and software changes of the MAGIC Telescope from 2004-2008

## 7.6 Fast ONLINE Analysis

The ONLINE analysis was mentioned in Chapter 6. Table 7.5 lists the successful high states triggers due to AGN flares released by the MAGIC fast ONLINE analysis. The fast ONLINE analysis not only increases the chances to catch TeV flares or even orphan flares, but also gives operators a hint of the source states during observation.

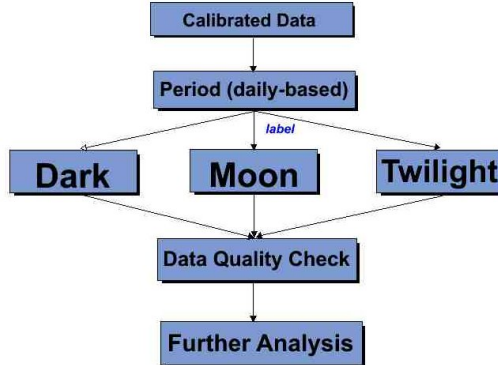


Figure 7.8: The data check procedures for the MAGIC dataset

## 7.7 Mrk421 Data Overview and Strategies Of Data Classification and Selection

From 2004 to 2008, MAGIC upgraded its hardware and software several times, see Table 7.5. Each time, the telescope performance changed. Different hardware configurations and different background light intensities make analysis complicated. In order to make the analyzed data more homogeneous and take care of the different hardware conditions, we divided the data into 6 different observational periods. Considering different background light conditions during the

observation, we further divided the data of each period into three different light conditions: dark night, moonlight and twilight, according to the MAGIC central control file, see Fig. 7.8. The data sets were further divided into several subsets while taking into account their different zenith angles. The reasons for this complicated data hierarchies are summarized as follows:

- The high DTs (Discriminator Thresholds) setting decreases the  $\gamma$  efficiency. Different DT levels need to be corrected by different factors. It is, therefore, better to classify the data by different light conditions.
- The light conditions during twilight observations are normally changing dramatically. Thus, those data sets are better treated separately.
- Data taken at large zenith angle have different properties. For example, at high zenith angles, the hadron rate decreases and SIZE-Energy distributions are different from those at low zenith angles. Therefore, data taken under different zenith angle bins are trained using different Random Forest matrices.

Mrk421 is visible at the MAGIC site from October to next June. Thus, its period of visibility fortunately overlaps with that of the Crab Nebula at the MAGIC site. All the data sets have to be investigated by a "data quality check", such as hadron rate, DT and cloudiness. The hadron rate depends on the zenith angle and weather conditions. In order to know how the rate changes with the zenith angle, studying the data taken under good weather and dark night conditions is necessary. Additionally, to know how the data quality affects the physics results, e.g. sensitivity, the same analysis methods are applied on crab data. Data runs which do not fulfill the data quality cuts will not be used in further analysis. In summary, the following data quality checks are performed before further analysis.

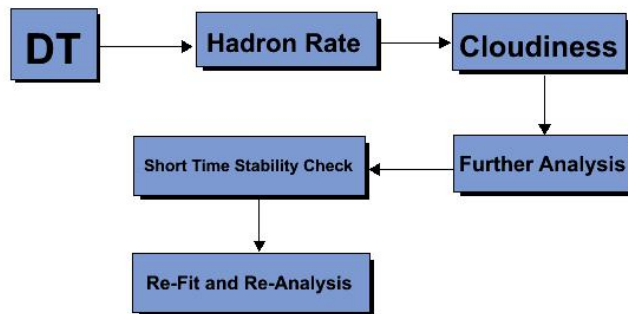


Figure 7.9: The data quality selection procedures.

- Discriminator threshold: DT.

Period	Time	Note
P0	Sep 2004-April 2006	Commissioning phase+Siegen FADC, published [152]
P1	Dec 2005-April 2006	Siegen FADC
P2	April 2006-June 2006	Siegen FADC, Siegen FADC+Splitter
P3	Oct 2006-Jan 2007	Siegen FADC + Splitter
P4	Feb 2007-June 2007	MUX FADC was installed.
P5	Dec 2007-June 2008	MUX FADC is installed.

Table 7.4: Classifies the Mrk421 Data taken in 2004-2008 into 6 different periods. Note that Mrk421 is visible from October to next June at the La Palma Site.

- Hadron Rate after a certain SIZE cut (taking into account the  $\theta$ ), spark cut and car-flash cut.
- Measurements from Pyrometer : cloudiness, humidity, etc.
- Shifter LogBook: as a reference.

All the cuts are fixed before analyzing data. Cut parameters are studied and optimized by analyzing the data from Crab. Cut parameters are chosen such that the significance of the signal from Crab is optimized.

## 7.8 Moon and Twilight Observation

As mentioned, the additional observations under moon and twilight conditions increase the duty cycle of IACTs. In order to optimize the performance of the telescope during such conditions, not only the hardware (see Chapter 5), but also the analysis methods should be tuned. As mentioned before, moon and twilight conditions have a higher NSB level, which increases the accidental trigger rate due to the afterpulses of the PMTs. To overcome this problem, increasing the DTs for each pixel in the trigger region is necessary. The price to be paid is a higher energy threshold and a lower of the  $\gamma$ -ray efficiency. This can be explained as follows:

- Increasing DTs in the trigger region decreases the detection efficiency for low energy  $\gamma$ -rays. In Fig. 7.11, shower B, which contains minor partial images inside the camera, will not be triggered anymore because of the increase of DTs in the trigger region. One may think that the loss could be recovered by increasing the analysis energy threshold. However, this is not the case, see Fig. 7.10. The number of  $\gamma$ s doesn't recover if we apply a higher SIZE cut. This indicates that even though we believe high energy  $\gamma$ s may trigger our telescope with higher DT, those  $\gamma$ s are "missing" or "mis-recognized" as hadrons during the  $\gamma$ -hadron separation. The reason will be explained in the next paragraph.
- Increase the number of islands after image cleaning. The accidental trigger increase with background light destroys the calculation of the Hillas parameters. This results in worse

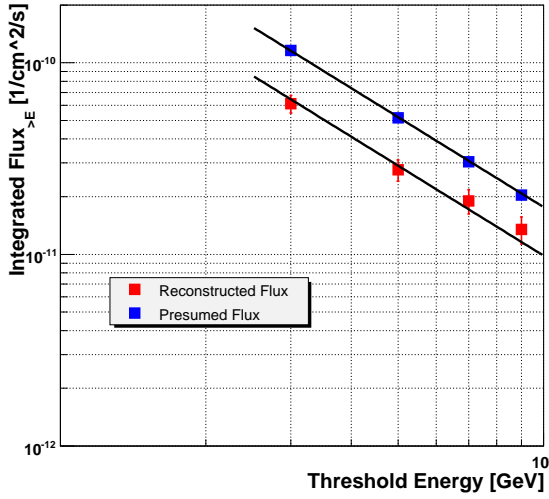


Figure 7.10: Reconstructed integrated flux with different energy thresholds by increasing the SIZE cut. The reconstructed integrated flux cannot be fully recovered by increasing the threshold. The Crab data was taken on 24 February 2007 with an average DT = 29.

recognition of the  $\gamma$ -ray. The remedy could be using a dedicated "moonlight" image cleaning level or a proper island cut. Further descriptions can be found in [156].

### 7.8.1 Moonlight Conditions

Moonlight Crab data taken in early 2007 when the MUX-FADC had just been installed shows a strong correlation of the hadron rate with the DTs after a 100 phe. SIZE cut, see Fig. 7.13. All the data used here are within  $15^\circ$  zenith angle. The zenith correction concerning the rate is small. Note that when the DT increases up to 20, the hadron rate drops by about 15% compared with the dark night data.

Normally, moonlight observation is defined by the moon shining above the horizon while the data is taken. From Fig 7.12, we see that the average DC current from the inner pixel of the camera is stable. Moreover, the hadron rate after a basic SIZE cut  $\geq 100$  phe. and spark cut is also quite stable.

We chose 3 different nights of Crab MUX-FADC data in period 3 (P3). These three different nights had three different background light levels and three different DTs were set. The width distribution of these three different nights after higher SIZE cut ( $\geq 400$  phe) were almost the same after normalization to the total number of the events.

The SIZE distribution of these three nights after normalization to the observation time are shown in Fig. 7.15. The number of events shows deficits in the smaller SIZE events in high DT nights, but remains the same in the larger SIZE events. Thus, smaller SIZE events are affected (will not survive) after the normal image cleaning procedure, even though they are triggering the

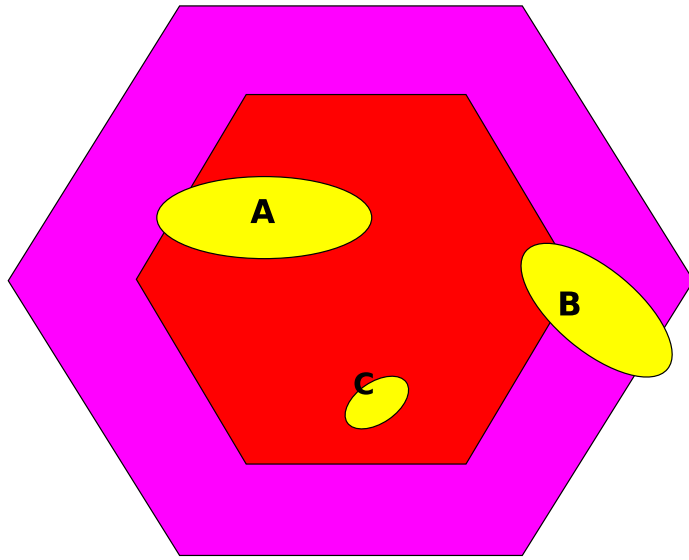


Figure 7.11: The red region is the trigger region, the pink region is the whole camera. When DT in the inner region (red) is increasing, shower B, which is partially contained in the inner trigger region, will not trigger anymore.

telescope anyhow.

An interesting effect on the trigger is the DIST distribution of the events in the whole camera. In Fig. 7.15, in a high DT night, the number of the events decreases with increasing the distance from the camera center. The effect is due to the fact that events which occur at some distance from the center of the camera are partially contained in the inner trigger region. While under a normal DT setup, these events are triggering. However, when the DT increases, the inner parts of the image cannot pass the trigger anymore. The same effect is shown in Fig. 7.11. Counting only the events which are fully contained in the inner camera, as in Fig. 7.15, we found that the distributions for the three individual nights were equal. We also tried to keep the events only in the inner camera and reconstruct the integrated flux from those events, but we failed to obtain the expected Crab flux. This shows that using the current 10-5 image cleaning method, the  $\gamma$ -hadron separation becomes worse under moon conditions because of the island effect mentioned above. Therefore, while during flux reconstruction, the  $\gamma$  events are lost because of bad recognition. Further studies of the moon data issue are beyond the scope of this thesis. More comprehensive studies are going on.

## 7.8.2 Twilight Conditions

Astronomically, twilight is defined as the time when the center of the Sun is between  $12^\circ$  and  $18^\circ$  below the horizon. There are two periods of twilight each day, one is dawn, the other is dusk. The duration of the twilight depends on the latitude and the seasons. At the La Palma site, twilight duration time is usually 10 - 15 mins. Within this short period of time, the ambient light

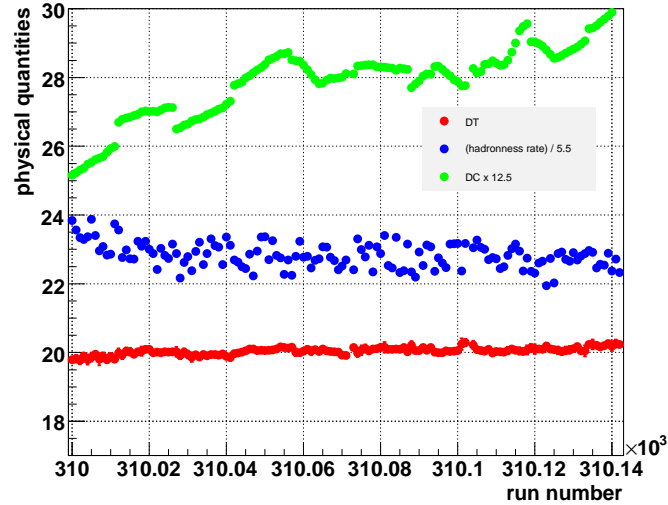


Figure 7.12: The plot shows the hadron rate (after spark cut and 100 phe. SIZE cut), inner pixel DC current and DT under moonlight conditions. Note that the hadron rate and DC current are multiplied by a constant factor separately. The DC value changes very little. All the three values are very stable during moonlight observation.

changes considerably. Fig. 7.16 shows the sharp decrease of the rate, which makes the analysis not trivial. In this thesis, twilight data is used only if the DT of that data run is below 20 (note that it is selected on a run-by-run basis).

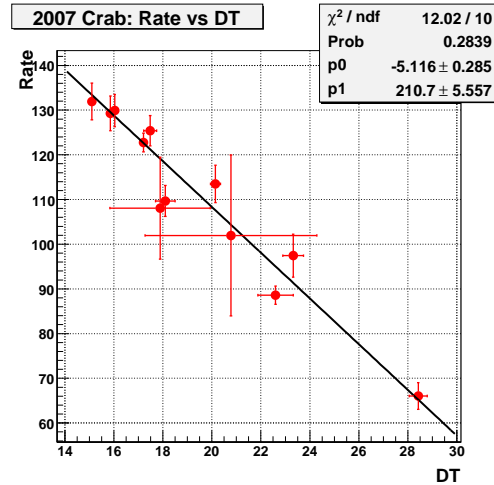


Figure 7.13: Hadron Rate vs DT from the early 2007 Crab data.

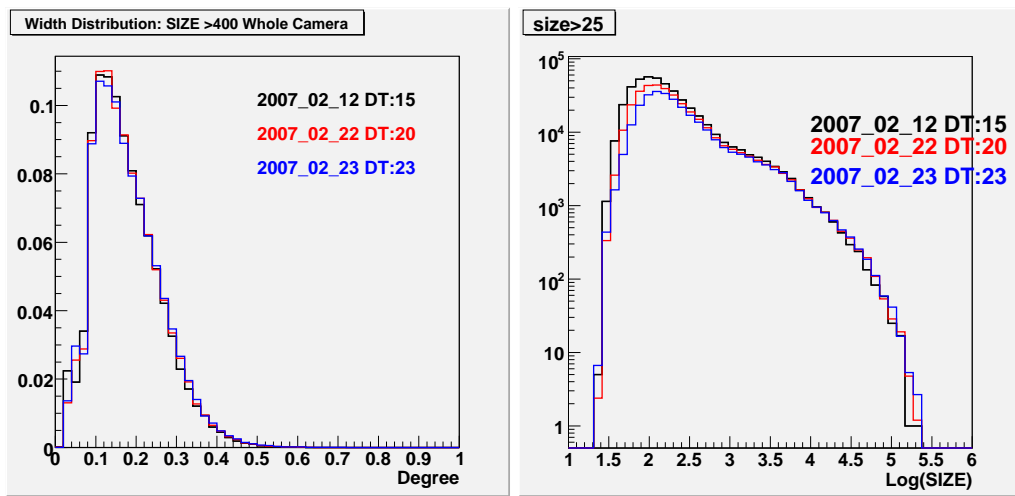


Figure 7.14: The left plot shows the Width distribution of all the events on the camera with the SIZE 400. The right plot shows the SIZE distribution of the events of three different DT nights.

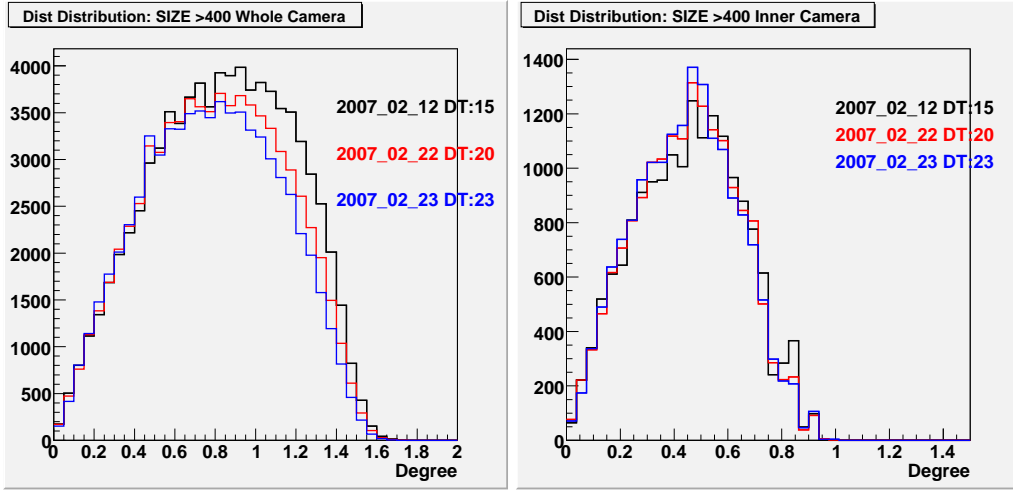


Figure 7.15: The DIST distribution of the events under three different background light conditions and three different DTs. The left plot shows the event DIST distribution in the whole Camera with a SIZE cut larger than 400 phe. The right plot shows only the events which are fully contained in the inner camera with the same SIZE cut of 400 phe. These two plots show that if we increase the analysis energy threshold (here 400 phe) and limit the events to only those that are fully contained in the inner camera, the triggered events will have the same DIST distribution irrespective of the light conditions. However, if we consider the full camera, events such as B in Fig. 7.11 will not trigger, and we will have a discrepancy in the DIST distribution.

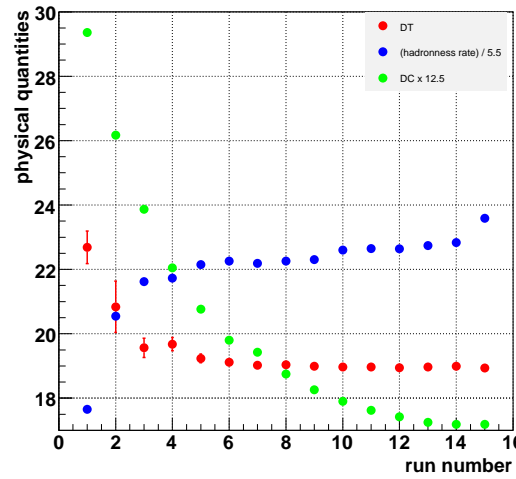


Figure 7.16: Example of a twilight observation. The plot shows DT, hadron rate and DC from consecutive 15 data runs. It is clear that the DC changes dramatically.

## 7.9 Multiwavelength Study on Blazars and Brief Review of Optical and X-ray Experiments

In the following, I will briefly introduce the Optical and X-ray observatories or satellites whose data were used for multiwavelength studies in this thesis.

### 7.9.1 Multiwavelength Data

#### Optical Observatory

KVA (Kungliga Vetenskapsakademien) [157], is a 60 cm robotic telescope operated by the University of Turku, Finland, under an agreement with the Royal Swedish Academy of Sciences. It is located at the Roque de Los Muchachos Observatory, La Palma, Canary Islands. The total field of view is  $5.3' \times 3.5'$  and the effective aperture ratio of the system is f/15. The telescope is equatorial mounted. The basic activities of the KVA telescope include long term photometric monitoring of blazars and support observations for MAGIC. KVA provides precise optical magnitudes in the R band data in the AGN monitoring program.

#### X-ray Data

The X-ray adopted in this thesis were mainly provided by two X-ray satellites. One is the Rossi X-ray Timing Explorer (RXTE) [158] and the other one is the Swift Gamma-Ray Burst Mission Satellite [159].

- RXTE was launched in 1995 from NASA's Kennedy Space Center. It features unprecedented time resolution in combination with moderate spectral resolution to explore the variability of X-ray sources. On board, there is an All-Sky Monitor (ASM) instrument which scans about 80% of the sky every orbit, allowing monitoring at time scales of 90 minutes or longer. Besides, there are two pointing instruments; the Proportional Counter Array (PCA) designed to cover the lower part of the energy range, and the High Energy X-ray Timing Experiment (HEXTE), covering the upper energy range.
- The Swift Gamma-Ray Burst Mission consists of a robotic spacecraft called Swift, which was launched in November 2004. It contains the Burst Alert Telescope (BAT), which covers a large fraction of the sky. It is a coded aperture imaging instrument with a 1.4 steradians field-of-view (half coded). The data from the BAT can also produce a sensitive hard X-ray all-sky survey. The energy range is 15 - 150 keV. There are two more instruments called X-ray Telescope (XRT) and Ultraviolet/Optical Telescope (UVOT).

The ASM, on board the RXTE, operates in the energy band from 1.5 to 12 keV. The BAT, also on Swift, is a large field of view (1.4 steradians) X-ray telescope with imaging capabilities in the energy range from 15 to 150 keV.

Waveband	Instrument	Energy Range (eV)	Note
Optical X-ray	KVA	2.1-2.5	Almost Simultaneous with MAGIC data-taking
	XRT	0.2-10 keV	public data
	ASM	2-10 keV	public data
	BAT	15-150 keV	public data
VHE- $\gamma$	MAGIC	50-10TeV	this thesis
	Whipple	200-10TeV	published paper and ONLINE analysis

Table 7.5: Summary of the different instruments from different energy bands whose data were used in this thesis.

## 7.10 The Analysis Tool

Besides the MAGIC standard analysis chain, additional analysis tools are used and developed for further analysis on specific topics.

### 7.10.1 Variability

To quantify the amplitudes of the source variability, we computed the so-called Normalized Variability Amplitudes (NVA). The NVA is defined as [160]

$$NVA = F_{var} = \sqrt{\frac{S^2 - \bar{\sigma}^2}{\bar{F}^2}} \quad (7.3)$$

Sometimes, NVA is called, the factional RMS variability amplitude  $F_{var}$ . The  $\bar{F}$  is the mean flux, S is the standard deviation, and  $\sigma$  is the mean measurement error.

$$\bar{\sigma}^2 = \frac{1}{N} \sum_{i=1}^N (\sigma_i^2) \quad (7.4)$$

$$S = \sqrt{\frac{1}{N-1} \sum_{i=1}^N (F_i - \bar{F})^2} \quad (7.5)$$

Another useful quantity is the point-to-point fraction RMS variability,  $F_{pp}$ .

$$F_{pp} = \sqrt{\frac{1}{2(N-1)} \sum_{i=1}^{N-1} (F_{i+1} - F_i)^2 - \bar{\sigma}^2} \quad (7.6)$$

Where each flux measurement  $F_i$  has a measurement error  $\sigma_i$ ,  $\bar{F}$  is the arithmetic mean of the flux.  $F_{var}$  quantifies the integrated level of variability present in a particular waveband while  $F_{pp}$  probes the short-timescale variabilities by measuring the variations between adjacent points in the lightcurves. The ratio between  $F_{var}$  and  $F_{pp}$  provides information about the power spectral density.

### 7.10.2 Temporal Analysis

There is only a small number of observables from  $\gamma$ -ray observations. A very crucial one is the photon arrival time. Temporal studies provide independent and complementary information for the spectral studies. However, usually the temporal analysis is not very trivial, especially for IACT data. The inevitable time gaps between observations due to natural limitations (such as day-night, moon effects) make the results of temporal analysis ambiguous. Special care must be taken if the data are not well sampled (biased samples) or the observation is relatively short compared to intrinsic time scales of the target sources (aliasing effect). Various temporal analysis methods are proposed in literature. The methods used in this thesis will be introduced here.

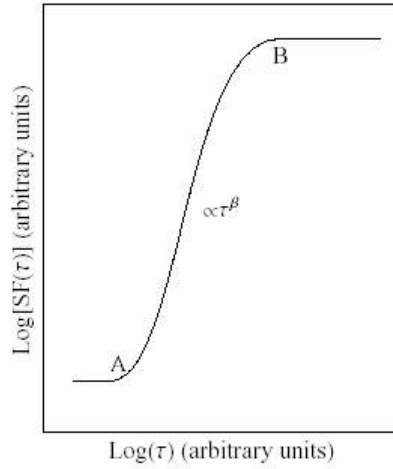


Figure 7.17: An example of the structure function.

#### Structure Function (SF)

The structure function (hereafter SF) provides information on the nature of the physical process causing observed variability. SF is better and easier to calculate than other methods like the Power Spectral Density (PSD) function. PSD cares about the time gaps between observations. However, the SF is not so sensitive to time gaps in sampling. The first order SF is defined as

$$SF(\tau) = \frac{1}{N} \sum [f(t) - f(t + \tau)]^2 \quad (7.7)$$

where  $f(t)$  is the flux point in the time series of lightcurves and the summation is performed over all the pairs separated in time by  $\tau$ .  $N$  is the number of the pairs. In [161], the authors imposed different weights on different pairs because of different significances. An example plot of SF against different time scales is shown in Fig. 7.17. The important parameters of the SF are the slopes  $\beta$ , and the characteristic time scale  $T_{char}$ . The SF is related to power spectrum density (PSD) distribution  $P(f) \propto f^{-\alpha}$ , where  $f$  is the frequency and  $\alpha \sim \beta + 1$ . This approximation is not valid if  $\alpha$  is smaller than 1. The SF will be further discussed in Chapters 9 and 10.

### 7.10.3 The Hardness Ratio

To have a better estimation of the differential spectrum, we need enough events in each energy bin. Thus it is sometimes more useful to use the "integrated effects". The Hardness Ratio (hereafter HR) could describe the steepness of a differential spectrum for a given source in any time bins and indicate whether the spectral index of the power law changes during different flux states. The HR is calculated as follows: For an assumed power law spectra,  $dF(t)/dE = F_0 E^{-\alpha}$ , the HR for a given time bin  $i$  and energy intervals  $[min_1, max_1]$  and  $[min_2, max_2]$ .

$$HR(t_i) = \frac{\int_{t_{min}}^{t_{max}} dt' \int_{min_2}^{max_2} dE \frac{dF(t')}{dE}}{\int_{t_{min}}^{t_{max}} dt' \int_{min_1}^{max_1} dE \frac{dF(t')}{dE}} \quad (7.8)$$

From the above, we calculate the integration.

$$HR(t_i) = \frac{max_2^{-\alpha+1} - min_2^{-\alpha+1}}{max_1^{-\alpha+1} - min_1^{-\alpha+1}} \quad (7.9)$$

From the equation, we know that the spectral index  $\alpha$  is a function of HR or can be estimated from HR.

### 7.10.4 Excess $\sigma$ -Flux Relations

The excess variance  $\sigma_{exc}^2$  is obtained by subtracting the contribution of experimental errors (including systematics and statistical errors) from the variance of the fluxes ( $f_k$ ,  $k=1\dots N$ ) measured at different times  $t_k$ .

$$\sigma_{exc}^2 = \sigma_{measured}^2 - \sigma_{err}^2 \quad (7.10)$$

where

$$\sigma_{err}^2 = \sigma_{sys}^2 + \sigma_{stat}^2 \quad (7.11)$$

It has been found that in X-ray binaries [162] and Seyfert galaxies [163] [164].  $\sigma_{exc}$  has a linear relationship with flux. In addition, it implies that a flux state which shows no variability at all exists. It will be discussed in Chapter 10.

### 7.10.5 Correlation Between Different Wavelengths

Information from different wavelengths such as cross correlations and time delays, give us important information about the photon emission. To find the correlation, one of the most common methods we use is the so-called Pearson's correlation coefficient.

$$\text{corr}(X, Y) = \frac{\sum_{i=1}^n (x_i - \bar{x})(y_i - \bar{y})}{\left[ \sum_{i=1}^n (x_i - \bar{x})^2 \sum_{i=1}^n (y_i - \bar{y})^2 \right]^{1/2}} \quad (7.12)$$

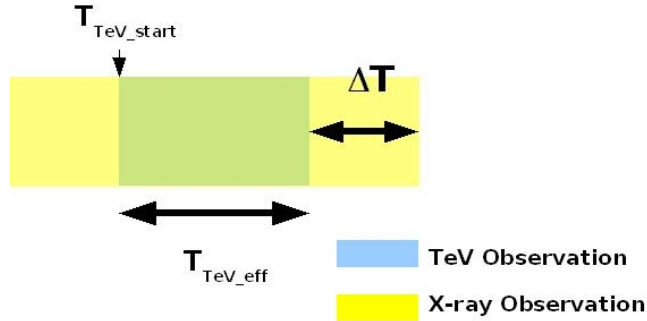


Figure 7.18: The plot shows the correlation time searching window between the TeV/X-ray or TeV/Optical observation.

Eq. 7.12 assumes, among other things, that the measurement errors are the same for each measured pair (X,Y). However, in reality, the error for each point is different from measurement to measurement. In order to estimate the significance of the correlation, a simulation is necessary. The errors of the correlation coefficient are calculated by the so-called Fisher's z transformation [105]. Besides, since in most cases, the measurements in optical, X-ray and TeV  $\gamma$ -ray bands may not be taken at the same time, the correlation is determined within systematic time shifts  $\Delta T$  between two data sets. Assuming the TeV observation starts at  $T_{Tev\_start}$  and having the effective observation time  $T_{Tev\_eff}$ , we are looking for multiwavelength data only at certain timing windows  $T_{window}$ :

$$T_{window} = T_{Tev\_eff} + 2\Delta T \quad (7.13)$$

$$(7.14)$$

In this thesis, we take  $\Delta T = 6$  hours, meaning that if the time difference between two lightcurves is within 6 hours, we treat them as simultaneous data. The whole concept is depicted on Fig. 7.18.

When two independent signals are compared, the procedure is known as cross-correlation. When the same signal is compared to phase shifted copies of itself, the procedure is known as auto-correlation. Auto-correlation is a method frequently used for the extraction of the fundamental frequency,  $F_0$ . If a copy of the signal is shifted in phase, the distance between correlation peaks is taken to be the fundamental period of the signal.

### 7.10.6 Intra-Night Short Time Variability

Given two sets of data, we would like to know whether these two data sets were drawn from the same distribution function or not. The two most commonly used testing functions are the  $\chi^2$  square test and the Kolmogorov-Smirnov test.

Mrk421 has been famous for its short time variability. We have systematically searched for

Mrk421 short time variability in about 4 years of MAGIC data. The  $\chi^2$  test method has been applied.

### 7.10.7 The EBL De-absorption

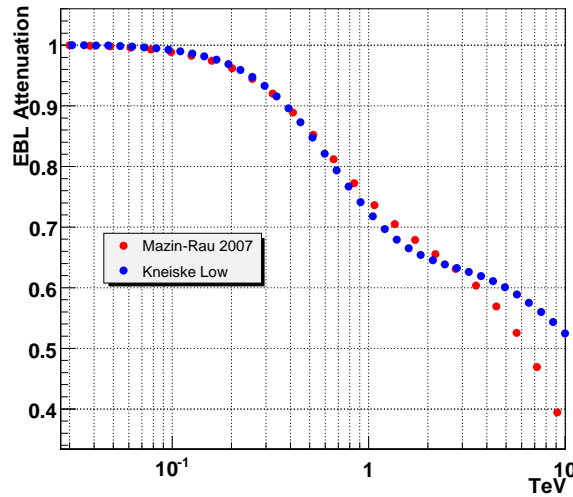


Figure 7.19: Compare the two different EBL absorption models. Red dots show the model of Mazin-Rau 2007, blue dots show the Kneiske low model. Assume the source is at  $z=0.03$ , where the Mrk421 is located. The x-axis is the  $\gamma$  energy in TeV, the y-axis is the surviving probability of the corresponding high energy of  $\gamma$  rays.

$\gamma$ -rays from the deep universe will interact with low energy background photons, which are part of the so-called extragalactic background light (EBL). As discussed in Chapter 1, the most common reaction channel between VHE  $\gamma$  and low energy photons of EBL is the  $e^+/e^-$  pair production. The intrinsic (de-absorbed) photon spectrum,  $dN/dE_{intrinsic}$ , of a blazar located at redshift  $z$  is given by

$$(dN/dE)_{obs} = (dN/dE)_{intrinsic} \times e^{(-\tau_{\gamma\gamma}(E,z))} \quad (7.15)$$

where the  $(dN/dE)_{obs}$  is the observed spectrum and  $\tau_{\gamma\gamma}$  is the optical depth which is a function of the  $\gamma$  photon energy and source distance. Mrk421 is not very far away ( $z = 0.03$ ), the attenuation will not be strong see, Fig. 7.19. Photons at energy 1 TeV will be attenuated down to 70 %. A correction for the EBL absorption is necessary to get the intrinsic spectra.

### 7.10.8 SED

Since Blazars show EM radiation in a wide energy range, combining radio, optical, X-ray  $\gamma$ -ray, and TeV  $\gamma$  photometry to create a broad band spectrum is necessary for understanding the emission mechanisms. However, there are at least three observational problems affecting the construction of SEDs.

- It is challenging to obtain real simultaneous multiwavelength data. In particular, TeV and optical observations are much affected by either natural or operational limitations.
- Different instruments probing different wavelengths may observe different positions of the sources. Because of the limitations of the angular resolutions, emissions may in reality come from different regions.
- The uncertainty of EBL absorption corrections for the TeV  $\gamma$ -ray data. The absorption inside the source or interstellar medium is not well understood.

## 7.11 Mrk421 P0, P1 Data

### 7.11.1 Data Samples and Selections from P1 Mrk421 Data.

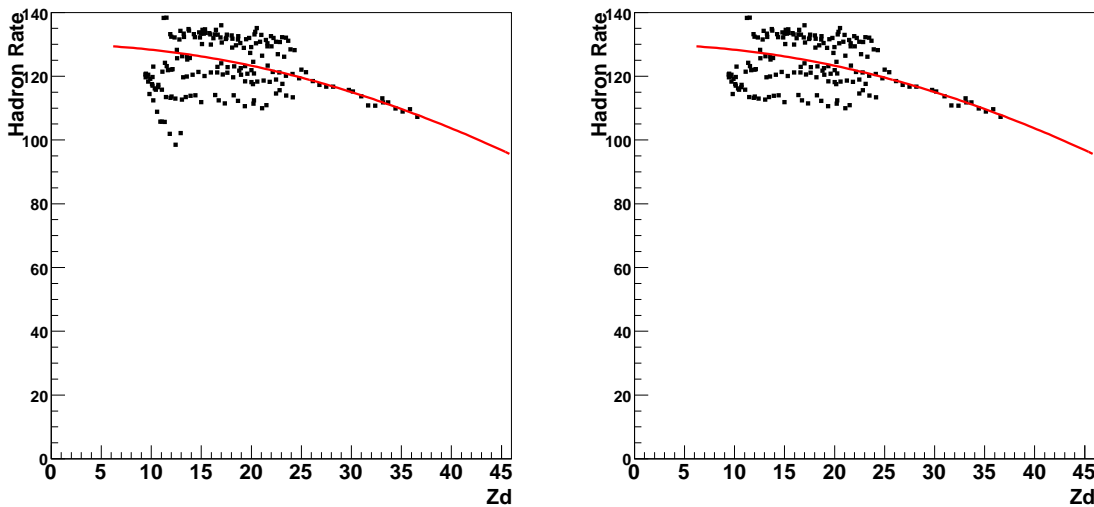


Figure 7.20: The hadron rate versus zenith angle from this period of Mrk421 data . The left plot shows the hadron rate before cut. From the plot, a deficit of the hadron rate at low zenith angle can be clearly seen. The bad data are from 27 December 2007. The plot on the right gives the distribution after the cut.

Date	MJD	$T_{eff}$ (mins)	zenith ( $^{\circ}$ ) (mean)	Rate (Hz)	Mode
2005_12_02	53706.3	36.6	16-24 (20.2)	119.08	W
2005_12_04	53708.3	46.5	15-25 (19.73)	132.7	W
2005_12_07	53711.2	55.4	9-21 (18.43)	132.3	W
2005_12_08	53712.2	75.3	11-25 (17.2)	130.8	W
2005_12_09	53713.3	35.7	11-17 (13.65)	127.1	W
2005_12_10	53714.2	75.1	10-25 (16.3)	113.8	W
2005_12_27	53731.2	98.4	12-24 (13.1)	117.03	W
2006_01_03	53738.1	38.6	18-37 (28.1)	116.40	W

Table 7.6: Mrk421 observed by MAGIC Telescope from December 2005 to January 2006, period P1.

The analysis results of Crab data from these two periods P0 and P1 can be found in Appendix A.1. Each data run was checked according to formula A.1. The rate  $R_0$  could be derived from the same period of the Crab data. The data runs, which was  $3\sigma$  away from formula A.1 will be excluded from the further analysis.

The data which were used for further analysis after data selection are listed in Table 7.6. The total amount of analyzed data is 8 hours in P1. In Fig. 7.20, the deficit of the hadron rate in the low zenith angle range can be clearly seen. Those data runs were completely ignored. We also found that for AGN intra-night variability studies the data quality check should not be performed on a night-by-night basis only but on a run-by-run basis. Sometimes, within one night, just part of the data runs are affected by bad sky conditions or suffer from hardware problems. These data sets should not be used for further analysis. Indeed, we found that careless treatment of the data quality selection may easily introduce an artificial intra-night variability. The INV will be described in more detail in the following section. The Random Forest matrix was trained by dim AGN data which were taken during the same period of time. All cuts are optimized with the Crab data to obtain the best sensitivity.

### 7.11.2 Analysis Results from the P1 Mrk421 Data.

#### The Lightcurve

The daily lightcurve from periods P0 and P1 are shown in Fig. 7.21 and Fig. 7.22. In order to have a complete picture, Whipple Mrk421 monitoring data were superimposed. The Whipple data were taken from their AGN monitoring website<sup>2</sup>.

In general, the flux of gamma rays from Mrk421 observed by MAGIC in the two periods ranged between 1.0 and 2.0 in Crab Units.

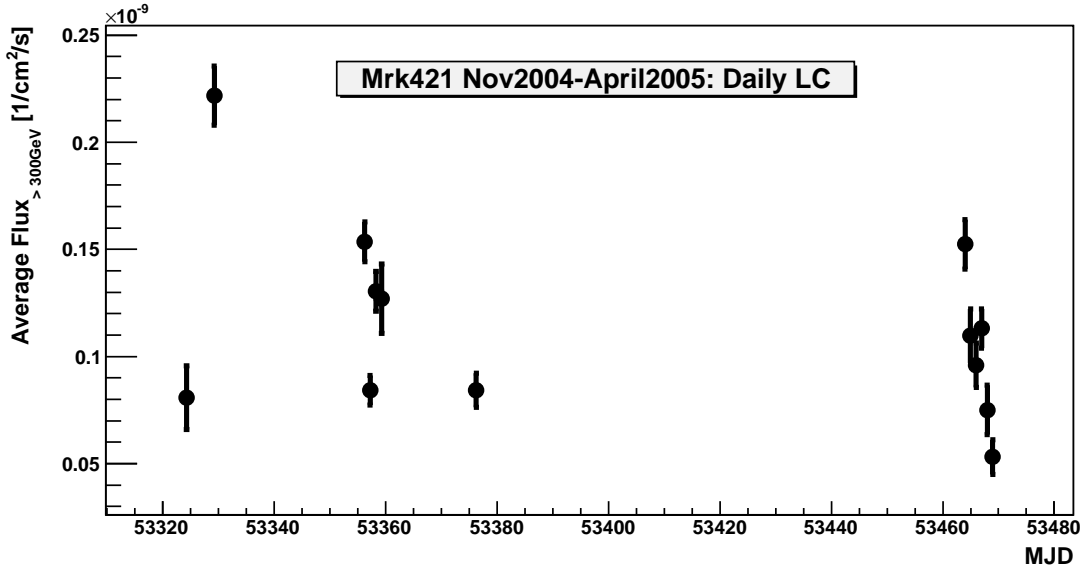


Figure 7.21: The daily flux ( $\geq 300\text{GeV}$ ) from Mrk421 in period P0.

### The Intra-Night Variability

In order to search for intra-night variability, the same procedure as described in the previous section was used. Fig. 7.23 gives the background fit  $\chi^2$  distribution per night in 10 minutes timing bins. The results show that after the cut, the background rates are stable. In Fig. 7.24, the distribution of the  $\chi^2$  per degree of freedom from the background and the signal is shown. No significant INV in these Mrk421 data sets can be seen in the plot.

### The Flux States

The frequency distribution of different states is another point of interest. The distribution of the different states may give us a clue about the emission mechanism. In Fig. 7.25, each entry is for about 10 minutes of effective observation time. In total, the plot contains 43 entries. The observation is biased toward high states, because we have a high state trigger at the end of 2005.

### 7.11.3 Multiwavelength Study

The multiwavelength study on this period is presented in Fig. 7.26. There is only one point from the KVA optical observatory in this period. The multiwavelength correlation study will be discussed in Chapter 10.

We calculated  $F_{var}$  and  $F_{pp}$  for different wavelengths. The BAT data was omitted because most points from the BAT data are less than  $3\sigma$ . The results of the variability values are listed in

<sup>2</sup><http://veritas.sao.arizona.edu/documents/summarymrk421.table>

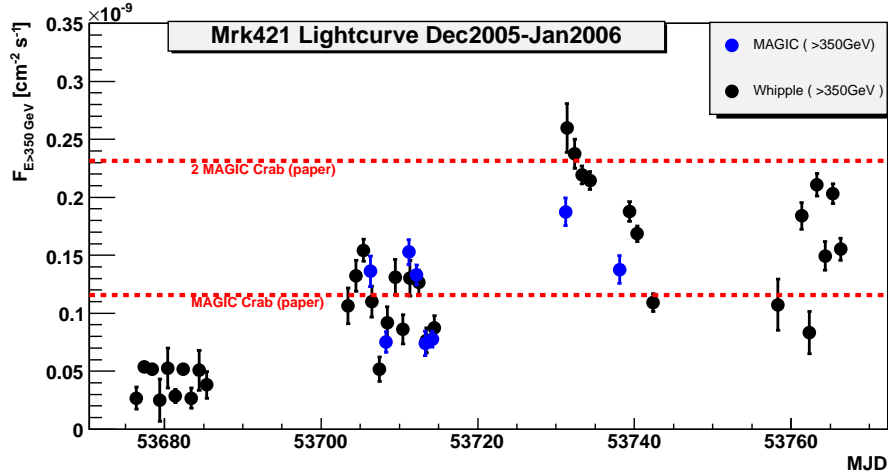


Figure 7.22: The Mrk421 lightcurve above 350 GeV in period P1. In order to have a complete picture, we display the data from the Whipple very preliminary public results in the same plot.

Wavelength	$F_{var}$	$F_{pp}$	$F_{var}/F_{pp}$
ASM	$0.42 \pm 0.03$	0.21	2
TeV	$0.29 \pm 0.04$	0.16	1.81

Table 7.7: Mrk421 observed by the MAGIC Telescope and ASM from December 2005 to January 2006 (i.e.:P1). The variability and point to point variability of the measurements are listed. Note that for calculating  $F_{var}$  and  $F_{pp}$ , a 10 minutes lightcurve is used instead of a daily lightcurve. Therefore, each data point has equal observation of about 10 minutes.

Table 7.7. Furthermore, calculation of  $F_{var}$  and  $F_{pp}$  was done using 10 minutes lightcurves.

#### 7.11.4 The Spectrum

The Mrk421 spectral distributions for different flux levels during this period are shown in Fig. 7.27. The spectra shown here are without EBL de-absorption. The curves are fitted with a simple power law (PL) and a simple power law plus exponential cutoff.

The spectra which are fitted with a power law plus a cut-off (PL+Cutoff) are shown in Fig. 7.27. Table 7.9 gives the fitting parameters.

Date	$f_0$	$\alpha$
2005_12_02	$0.78 \pm 0.11$	$-2.71 \pm 0.24$
2005_12_04	$0.57 \pm 0.08$	$-2.72 \pm 0.21$
2005_12_07	$0.88 \pm 0.09$	$-2.47 \pm 0.13$
2005_12_08	$0.72 \pm 0.06$	$-2.56 \pm 0.1$
2005_12_27	$1.03 \pm 0.083$	$-2.35 \pm 0.1$

Table 7.8: The fitting parameters for the spectrum of Mrk421 data in P1. All the spectra are fitted with a pure power law  $dF/dE = f_0 \cdot (E/E_0)^\alpha$  with  $E_0 = 300$  GeV. The normalization factor  $f_0$  is given in units of  $10^{-9} \text{ cm}^{-2} \text{s}^{-1}$

Date	$f_0$	$\alpha$	$E_c$
2005_12_02	$0.8 \pm 0.3$	$-2.69 \pm 0.86$	$27.36 \pm 900$
2005_12_04	$0.57 \pm 0.08$	$-2.72 \pm 0.21$	$99.60 \pm 400$
2005_12_07	$0.98 \pm 0.16$	$-1.95 \pm 0.54$	$1.56 \pm 1.62$
2005_12_08	$0.95 \pm 0.23$	$-1.76 \pm 0.57$	$0.89 \pm 0.69$
2005_12_27	$1.11 \pm 0.01$	$-1.87 \pm 0.35$	$1.83 \pm 1.36$

Table 7.9: The fitting parameters for the spectrum of Mrk421 data in P1. All the spectra are fitted with a simple power law plus exponential cutoff.  $dF/dE = f_0 \cdot (E/E_0)^\alpha e^{E/E_c}$  with  $E_0 = 300$  GeV. The normalization factor  $f_0$  is given in units of  $10^{-9} \text{ cm}^{-2} \text{s}^{-1}$ .  $E_c$  is the cutoff energy.

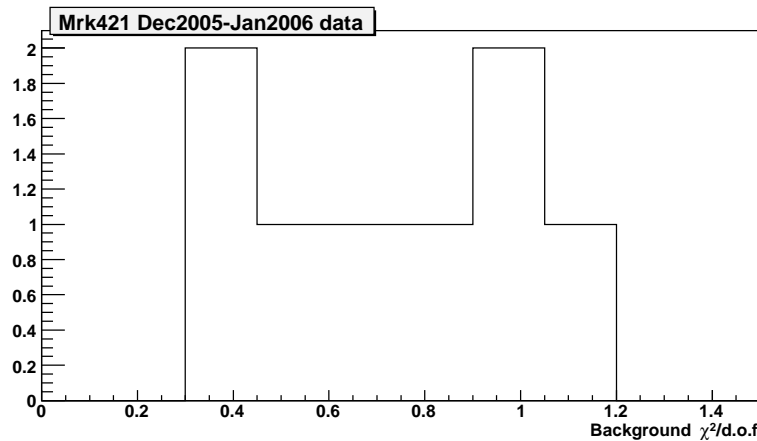


Figure 7.23: The 10 minutes' lightcurve background fit per night from Mrk421 data. 10 minutes' lightcurves were produced per night and the background was fitted with a constant value. Afterwards, bad points which were  $5\sigma$  away were excluded and the data points within one night re-fitted. The  $\chi^2$  distribution is shown.

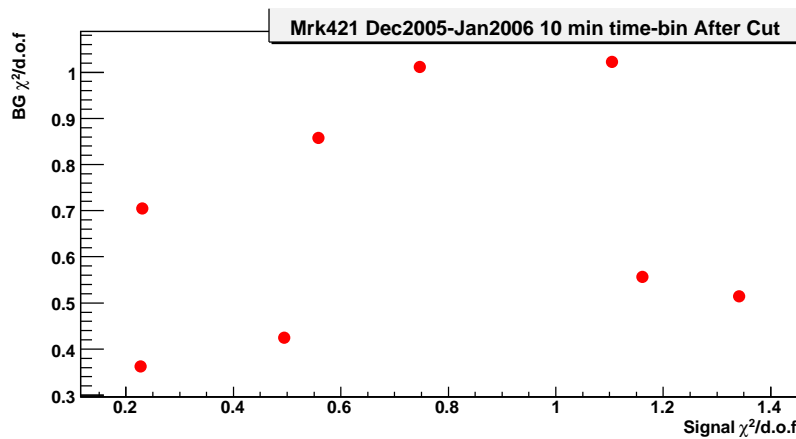


Figure 7.24: The background and signal  $\chi^2$  fit results from December 2005 to March 2006. Most of the fitting signals per night show a smaller  $\chi^2$  within 1.

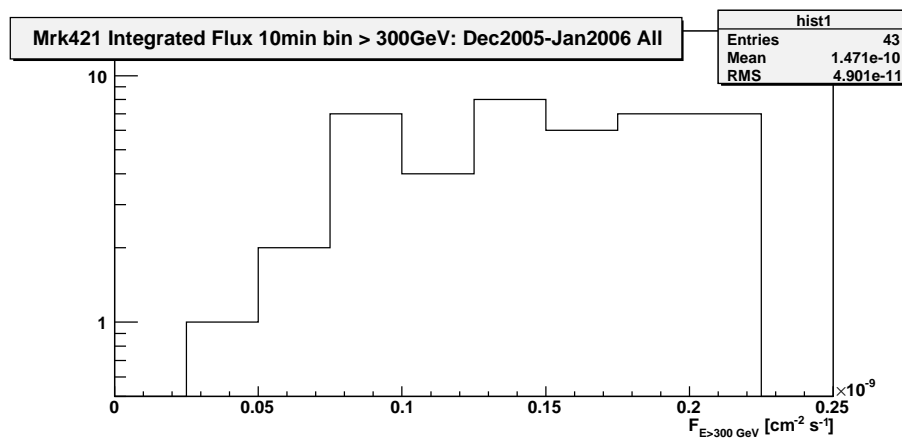


Figure 7.25: Mrk421 10 minutes' flux states histogram. The data are from December 2005 to January 2006 after data selection and stability cut. The histogram shows that the TeV observation is completely biased by high flux states.

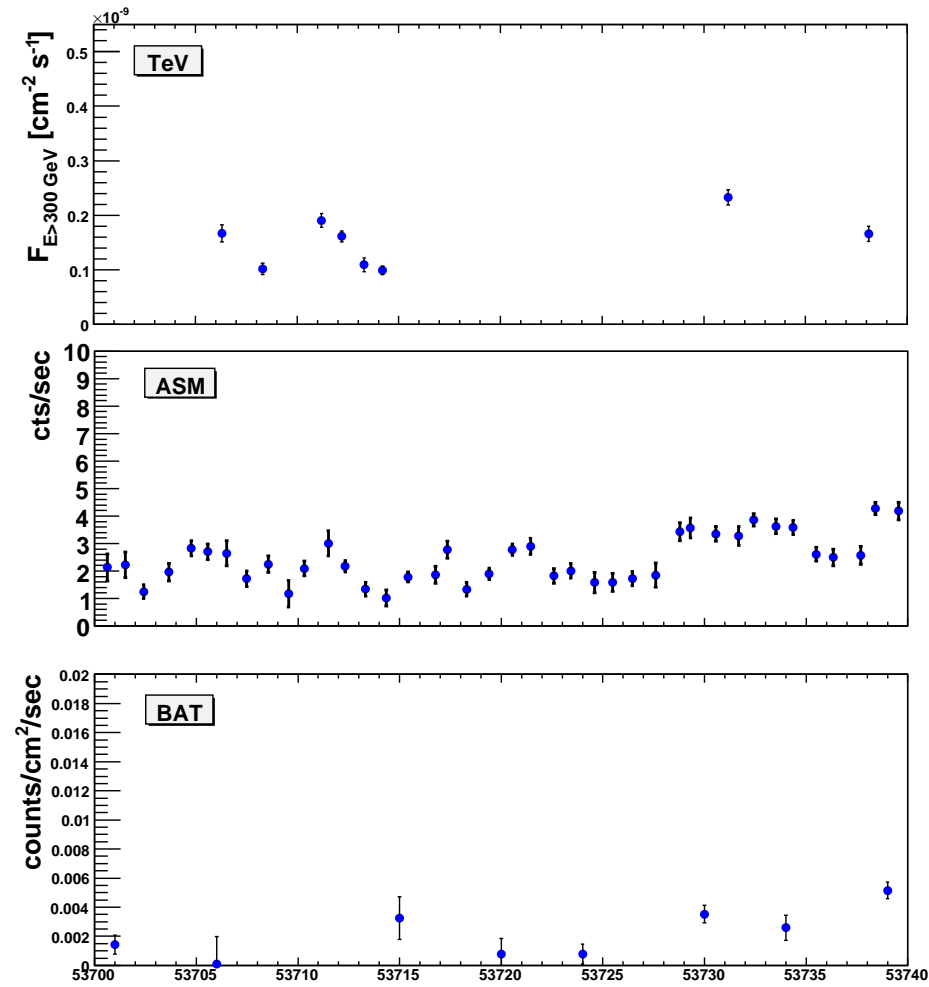


Figure 7.26: The three different wavelength lightcurves from Mrk421 data in this period.

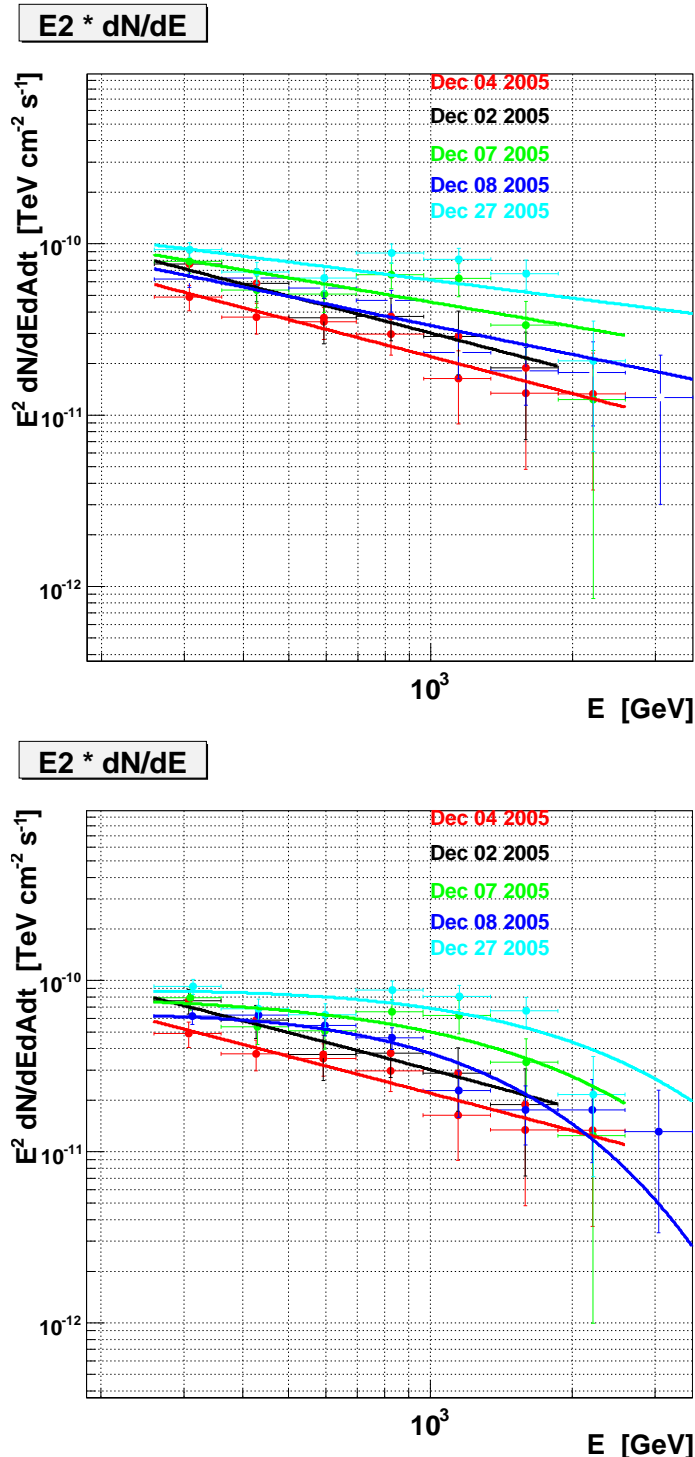


Figure 7.27: Mrk421 spectral energy densities for different flux levels. The solid curves are fitted by a simple power law (PL) (upper) and a PL plus exponential cutoff (bottom). The fitted parameters are shown in Table 7.8 and Table 7.9.

# Chapter 8

## The Mrk421 from April 2006 to June 2007

In April 2006, an electric splitter was installed which separates the signals into high gain and low gain routes. The main purpose is to increase the dynamical range of the telescope. One year later, in Feb. 2007, we upgraded our 300 MHz FADC into the new 2GHz MUX FADCs, which greatly improved the telescope's sensitivity and performance. In this chapter, analysis results from Mrk421 data which were taken in periods P2, P3 and P4 will be presented. The analysis results of P2, P3 and P4 Crab data are shown in Appendix A.2.

### 8.1 Mrk421 P2, P3 Data Summary and Analysis Results

28 nights of Mrk421 data were taken in period P2 and P3. Most of the observations were performed in Wobble mode. The hadron rate per run is shown in Fig. 8.1. We excluded the data runs which are more then  $3\sigma$  away from the fitting. After the data selection cut, 11 nights remained. The total observation time is 6.8 hours. The data were analyzed using the standard analysis and calibration software as described in Chapter 6. The  $\gamma$ -ray signals were extracted from the  $\theta^2$  approach. The final cut  $\theta^2 \leq 0.03$  was applied on the data. It was chosen from optimizing the significance of the Crab data. For the spectrum determination, the cut on  $\theta^2$  was chosen for each energy bin such that the  $\gamma$  efficiency was kept at 80%. The energy threshold (which is defined as the peak position in the differential energy distribution of the MC $\gamma$  events after cuts) was about 200 GeV.

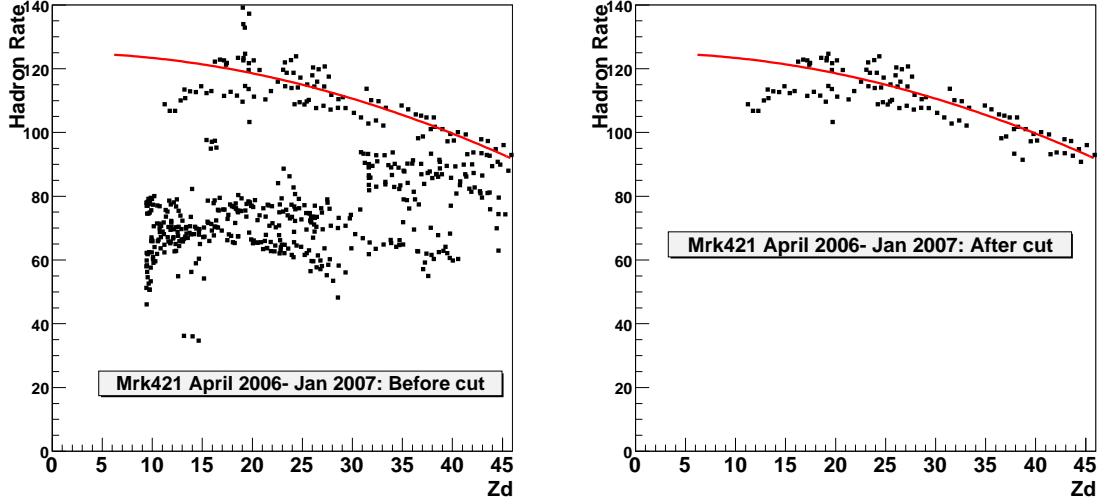


Figure 8.1: The hadron rate of Mrk421 data in period P2. Note that only the data within  $46^\circ$  are presented here. The left plot shows the hadron rate versus zenith angle before cuts. The plot on the right hand side shows the results after the data quality cut. The red curves on both plots are the best fit for the good data.

Date	MJD	$T_{eff}$ [min]	Zenith [ $(^\circ)$ ]	Rate	Mode
2006_05_22	53876.9	19.5787	15-21 (18.2)	122.35	W
2006_05_24	53878.9	17.9432	20-25 (22.65)	124.25	W
2006_05_26	53880.9	17.9747	18-28 (25.2)	131.279	W
2006_06_15	53900.9	18.6632	41-46 (43.2)	80.335	W
2006_11_23	54062.2	45.638	24-34 (28.4)	107	W
2006_11_27	54066.2	36.4573	23-30 (26.1)	115	W
2006_12_16	54085.1	67.5198	31-46 (38.8)	102.83	W
2006_12_24	54097.1	37.7762	36-45 (40.68)	94.58	W
2007_01_01	54111.1	51.697	11-21 (15.21)	111.5	W
2007_01_11	54115.1	38.0435	35-46 (41.18)	88	W
2007_01_15	54123	57.4172	30-40 (34.7)	93	W

Table 8.1: The Mrk421 data which were taken from April 2006 to January 2007, (periods P2 and P3), i.e. just before installation of the MUX FADCs.

## 8.2 Lightcurve from Mrk421.

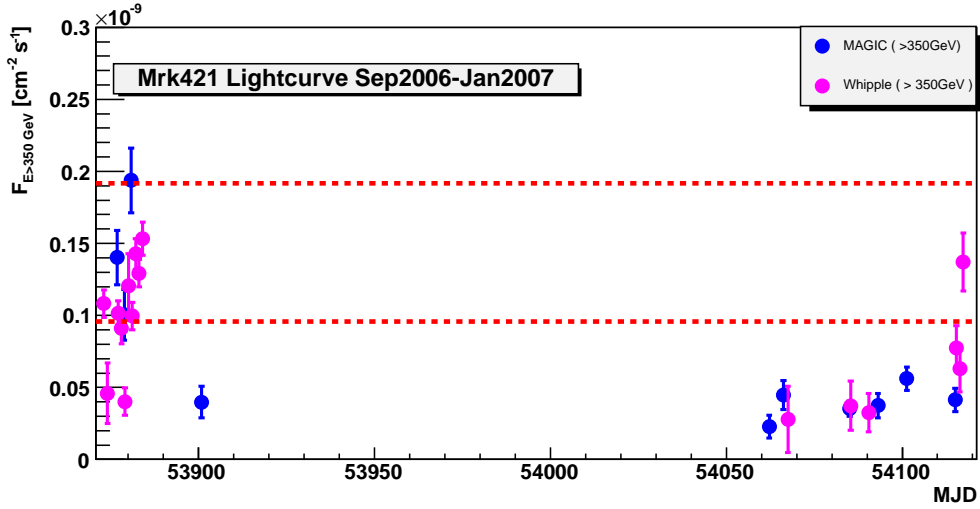


Figure 8.2: The daily lightcurve above 350 GeV from Mrk421 in periods P2 and P3.

The daily lightcurve from Mrk421 in period P2 is shown in Fig. 8.2. Daily variability is clearly evident. In Fig. 8.3, we enlarge the first part of the lightcurve. From the plot, Mrk421 was always detectable with a minimum flux level of  $\sim 0.5$  C.U. In 2007, Mrk421 was inactive and, in general, the flux level was below 1 C.U. during MAGIC observations. These low flux states increase the statistics in the flux states' study.

The daily lightcurve of Mrk421 in P4 is shown in Fig. 8.4. The analysis procedures are similar to those in the periods P2 and P3. The PSF of the Monte Carlo samples is 13.6 mm. All cuts were optimized by using P4 Crab data. We enlarge the first part of the lightcurve in Fig. 8.3. The very preliminary results from VERITAS AGN Monitoring ONLINE analysis are also added in the plot. Mrk421 does not show much activity in 2007 data.

### 8.2.1 Variability of the Short Time Scale

#### Mrk421: Period P2

We checked the short time variability of Mrk421 in this period of data. As we can see from Fig. 8.5, no significant intra-night variability was found. There was one day which gave about  $1.5 \chi^2/\text{d.o.f.}$  It shows about  $2\sigma$  effect of INV from the  $\chi^2$  fitting.

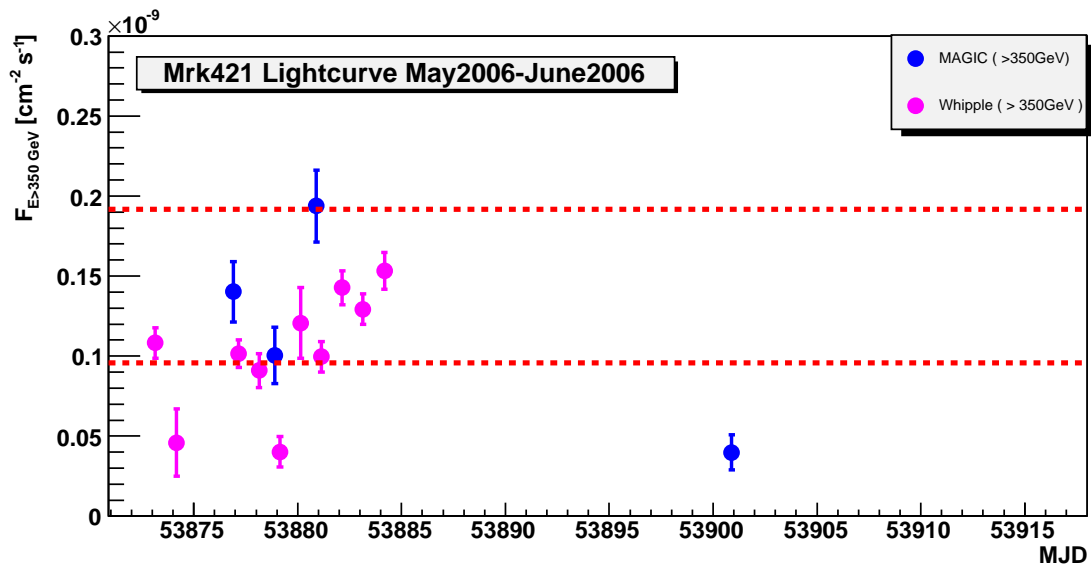


Figure 8.3: The daily lightcurve above 350 GeV from Mrk421 in period P2.

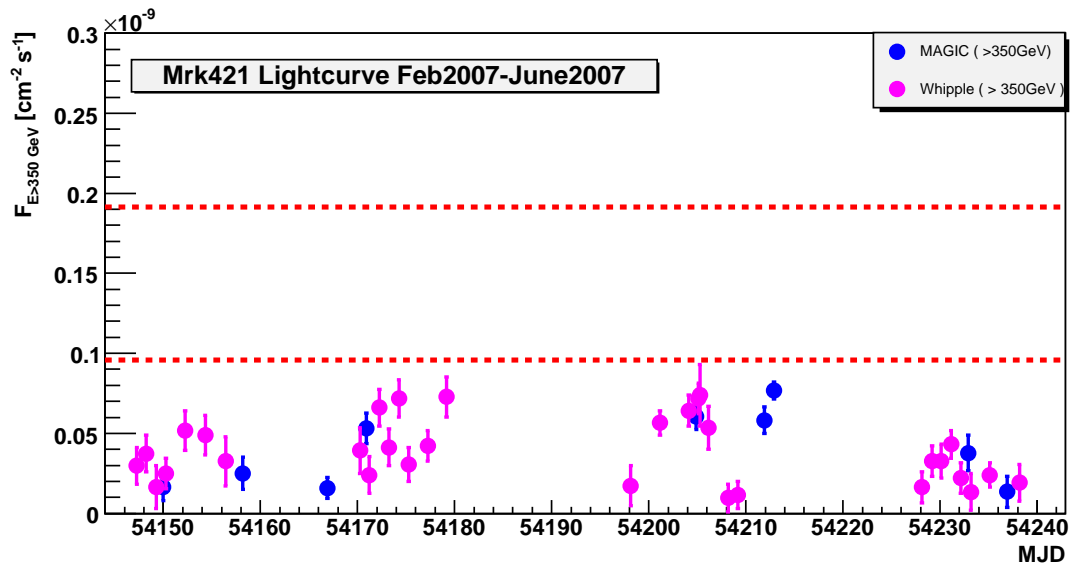


Figure 8.4: The daily lightcurve from Mrk421 from February 2007 to June 2007 (period P4)

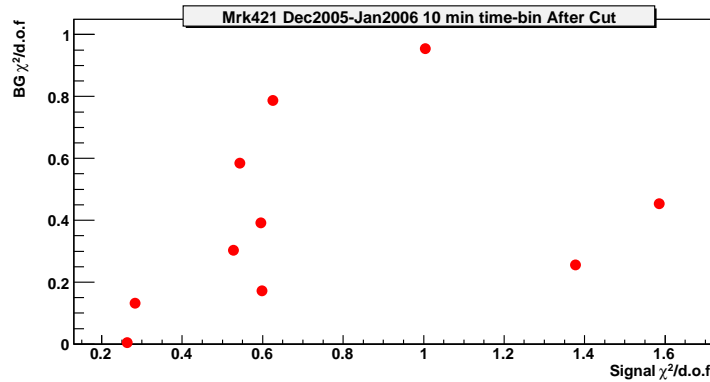


Figure 8.5: The  $\chi^2/\text{d.o.f.}$  for background and signal per night for Mrk421 data from December 2006-January 2007. Each point is the data per night and the  $\chi^2$  10 minutes' lightcurves per night are calculated

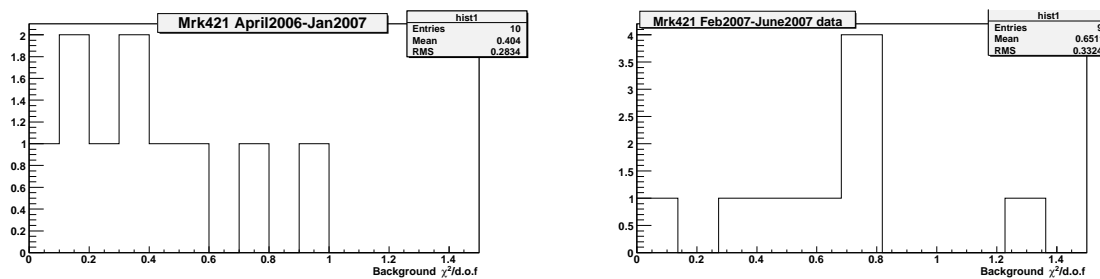


Figure 8.6: The  $\chi^2/\text{d.o.f.}$  for background from Mrk421 data from December 2006 to January 2007 (upper panel) and February 2007 to June 2007 (lower panel). Each entry in the histogram is a 10 minutes' timing bin.

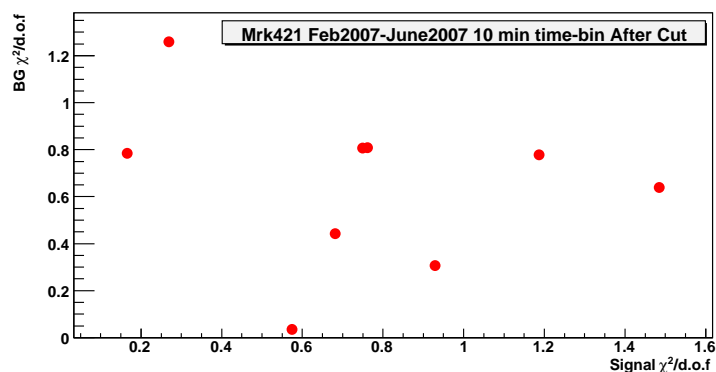


Figure 8.7: The  $\chi^2/\text{d.o.f.}$  for background and signal per night for Mrk421 data from February 2007 to June 2007. 10 minutes' timing bins per night are used.

### 8.3 The Spectrum

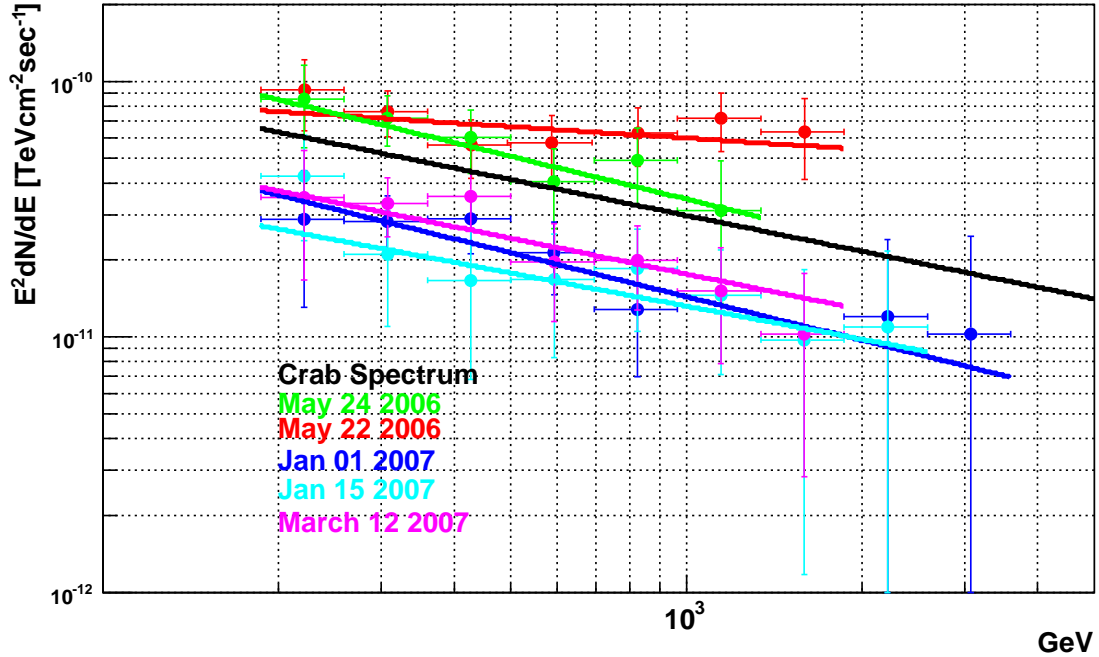


Figure 8.8: The spectrum of Mrk421 from P2, P3 and P4.

The Mrk421 spectra before EBL de-absorption during periods P2 and P3 are shown in Fig. 8.8. All spectra can be fitted with a simple power law. The final fitting parameters are shown in Table 8.2. The spectral index is correlated with the flux. The correlation could be explained by the shift of the IC peak to higher energies during the higher flux states. The correlation between spectral index and flux states is shown in Fig. 8.9. The correlation can be described by a linear function  $\alpha = \alpha_0 + p_0 \cdot F$  with  $\alpha_0 = p_1 = (2.65 \pm 0.29)$  and  $p_0 = (-3.10 \pm 3.24) \cdot 10^9 \text{ cm}^2 \text{s}^{-1}$ . The correlation coefficient  $r = -0.61^{+0.25}_{-0.27}$  is about  $1\sigma$  different from zero.

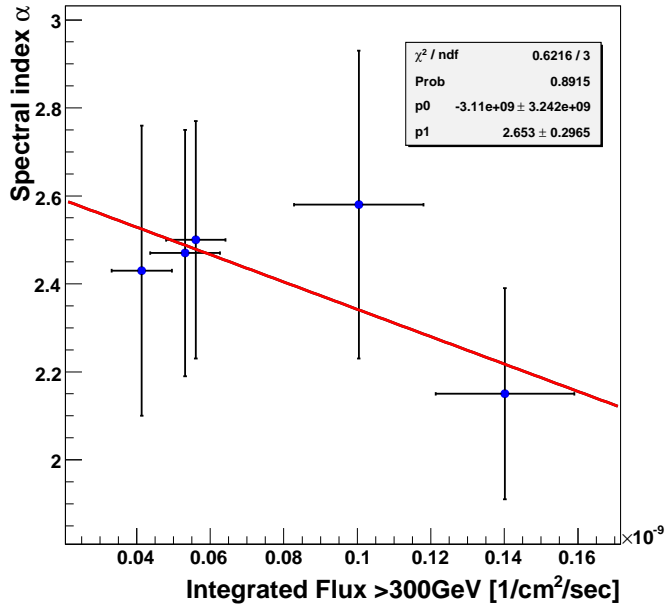


Figure 8.9: The correlation of flux level and slope. The figure shows the integral flux at energy  $E \geq 300\text{GeV}$ . The spectral index is obtained from a power law fit to the energy spectrum between 150 GeV and 5000 GeV. The correlation shows the spectra's tendency of hardening with an increasing flux level.

Date	$f_0$	$\alpha$	$\chi^2/\text{d.o.f.}$
2006_05_22	$0.79 \pm 0.15$	$-2.15 \pm 0.24$	2.42/5
2006_05_24	$0.77 \pm 0.13$	$-2.58 \pm 0.35$	3.18/4
2007_01_01	$0.31 \pm 0.07$	$-2.50 \pm 0.27$	1.73/5
2007_01_15	$0.24 \pm 0.1$	$-2.43 \pm 0.33$	2.32/6
2007_03_12	$0.32 \pm 0.07$	$-2.47 \pm 0.28$	5.35/5

Table 8.2: The spectrum fitting parameters of Mrk421 data in P2, P3 and P4. All the spectra are fitted with a pure power law  $dF/dE = f_0 \cdot (E/E_0)^\alpha$  with  $E_0 = 300\text{ GeV}$ . The normalization factor  $f_0$  is given in units of  $10^{-9} \text{ cm}^{-2}\text{s}^{-1}$

# Chapter 9

## Mrk421 data from December 2007 to June 2008

Mrk421 was observed very intensively by the MAGIC telescope in period P5. Due to a few occurrences of high flux triggers, extended observations were initiated by the monitoring and multiwavelength ToO proposals. Few times of fast and large flares were caught. Several joint observations among different IACTs and other telescopes in different wavelengths were carried out. The important physics results will be presented in this chapter. The corresponding Crab data in this period can be found in Appendix A.3. This chapter begins with the analysis results of six months of Mrk421 data. Particularly, several high flux nights with possible Intra-Night Variability (INV) will be shown. Flares are fitted based on a presumed flare model. I will discuss a published physics results on the joint observation of the June flare with several different telescopes in different wavelengths. Finally, this chapter closes with a discussion about the spectra measured at different flux states and their multiwavelength correlations.

### 9.1 The Data Selection and Quality Check.

### 9.2 Mrk421 Data Selections and Analysis

On Mrk421 the same data selection cuts were applied as on the crab data. A DT cut with 20 unit was selected and all the high DT runs were kept for further study. Note that since the twilight data are usually short in effective time, effective time cut was chosen to be 10 minutes. The data which pass through the data selection cut are listed in Table 9.1 and Table 9.2. In total, we have 53 nights of Mrk421 data in P5 and the total effective observation time is about 52 hours.

#### 9.2.1 Lightcurve

The overall Mrk421 daily lightcurve above 300 GeV in P5 is shown in Fig. 9.1. The 350 GeV lightcurve with Whipple observations is also shown in Fig. 9.2. We found that Mrk421 was very active during this period and never below 0.5 Crab Unit (C.U.) above 300GeV from MAGIC

Date	MJD	Hadron Rate	Zenith Angle (Mean)	$T_{eff}$ (min)
2007_12_04	54438.2	$120.26 \pm 6.82$	28-47 ( $36.60 \pm 5.30$ )	88.
2007_12_05	54439.2	$130.77 \pm 5.14$	23-41 ( $31.87 \pm 4.8$ )	82.
2007_12_06	54440.2	$132.11 \pm 4.5$	17-45 ( $32.18 \pm 7.98$ )	109.
2007_12_07	54441.2	$144.85 \pm 4.68$	8-34 ( $25.93 \pm 4.19$ )	70.3
2007_12_08	54442.2	$144.89 \pm 6.35$	10-28 ( $19.78 \pm 6.04$ )	54.9
2007_12_09	54443.2	$144.6 \pm 3.23$	9-28 ( $20.45 \pm 6.3$ )	53.4
2007_12_12	54446.3	$132.96 \pm 5.14$	9-11 ( $9.6 \pm 0.20$ )	10.3
2007_12_14	54448.3	$139.95 \pm 3.55$	9-10 ( $9.5 \pm 0.088$ )	13.6
2007_12_15	54449.3	$130.87 \pm 3.12$	9-10 ( $9.45 \pm 0.083$ )	11.54
2007_12_16	54450.3	$137.21 \pm 4.46$	9-11 ( $9.52 \pm 0.33$ )	12.86
2007_12_17	54451.3	$139.73 \pm 2.96$	9-11 ( $9.69 \pm 0.21$ )	12.6
2008_01_01	54466.2	$114.27 \pm 5.24$	9-45 ( $21.65 \pm 11.06$ )	263.
2008_01_02	54467.2	$124.75 \pm 4.2$	9-34 ( $17.46 \pm 6.86$ )	222.
2008_01_03	54468.1	$86.0 \pm 3.1$	36-40 ( $37.8 \pm 1.$ )	21.1
2008_01_04	54469.1	$140.56 \pm 7.40$	14-41 ( $25.74 \pm 7.38$ )	116.
2008_01_05	54470.1	$136.1 \pm 6.7$	20-40 ( $29.9 \pm 6.25$ )	76.
2008_01_06	54471.1	$125.47 \pm 3.88$	33-41 ( $36.92 \pm 2.38$ )	31.4
2008_01_07	54472.1	$129.06 \pm 2.06$	34-40 ( $37.26 \pm 1.4$ )	29.7
2008_01_08	54473.2	$148.17 \pm 10.55$	9-41 ( $18.53 \pm 10.94$ )	128.7
2008_01_09	54474.2	$143.69 \pm 9.23$	9-40 ( $17.13 \pm 8.68$ )	136.12
2008_01_10	54475.2	$139.96 \pm 11.49$	11-34 ( $21.22 \pm 7.89$ )	86.15
2008_01_11	54476.2	$148.34 \pm 2.24$	10-20 ( $15.28 \pm 3.06$ )	35.5
2008_01_12	54477.2	$150.55 \pm 5.31$	9-31 ( $16.63 \pm 7.04$ )	95.8
2008_01_13	54478.2	$151.34 \pm 2.25$	10-18 ( $13.93 \pm 2.09$ )	43.
2008_01_14	54479.2	$150.52 \pm 2.57$	9-14 ( $10.84 \pm 1.17$ )	35.
2008_01_15	54480.2	$138.34 \pm 7.18$	18-41 ( $28.45 \pm 6.47$ )	84.
2008_01_16	54481.2	$148.424 \pm 7.37$	9-33 ( $16.61 \pm 6.89$ )	167.
2008_01_17	54482.2	$147.58 \pm 5.07$	9-29 ( $14.97 \pm 5.72$ )	88.5
2008_01_18	54483.3	$130. \pm 3.2$	25-30 ( $27.53 \pm 1.06$ )	18.5
2008_01_20	54485.3	$133.029 \pm 2.0$	26-28 ( $27.06 \pm 0.54$ )	10.
2008_01_29	54494	$119.45 \pm 2.71$	28-41 ( $34.38 \pm 3.38$ )	9.5

Table 9.1: Mrk421 data used in the final analysis, from December 2007 to January 2008. The data shown here are already after the data selection and quality cuts.

MJD	Date	Hadron Rate	Zenith Angle (mean)	$T_{eff}$ (min)
2008_02_04	54500.1	$143.1 \pm 2.61$	23-31 (27.32 $\pm$ 1.86)	37.8
2008_02_05	54501	$132.88 \pm 4.62$	28-37 (32.21 $\pm$ 2.58)	38.0
2008_02_06	54502.1	$144.77 \pm 7.57$	9-36 (17.97 $\pm$ 7.92)	219.
2008_02_11	54507.1	$147.12 \pm 2.3$	12-21 (16.56 $\pm$ 2.64 )	48.0
2008_03_01	54526	$97.95 \pm 3.0$	33-6 (34.13 $\pm$ 0.78 )	12.3
2008_03_08	54533	$124.5 \pm 2.1$	18-26 (21.93 $\pm$ 1.68)	35.8
2008_03_11	54535.9	$118.45 \pm 6.2$	32-47 (39.1 $\pm$ 3.75)	57.9
2008_03_12	54536.9	$127.08 \pm 6.85$	28-46 (38.96 $\pm$ 3.66)	73.16
2008_03_30	54554.9	$96.31 \pm 2.$	38-40 (39.3 $\pm$ 0.3)	7.
2008_03_31	54555.9	$135.2 \pm 3.37$	14-38 (20.8 $\pm$ 3.96)	115.
2008_04_02	54558	$135.624 \pm 3.10$	17-20 (18.62 $\pm$ 0.76)	15.
2008_04_04	54560	$131.41 \pm 8.65$	10-34 (20.49 $\pm$ 7.25)	48.
2008_04_05	54561	$134.1 \pm 3.32$	10-25 (18.6 $\pm$ 5.84)	15.
2008_04_06	54562	$136.35 \pm 4.93$	10-22 (14.18 $\pm$ 4.37)	24.2
2008_05_04	54589.9	$126.83 \pm 1.71$	9-10 (12.24 $\pm$ 3.65)	16.4
2008_05_05	54590.9	$126.83 \pm 1.71$	9-36 (25.84 $\pm$ 6.73)	57.
2008_05_10	54595.9	$101.8 \pm 2.5$	10-28 (18.1 $\pm$ 5.5)	108.9
2008_06_03	54619.9	$137.79 \pm 1.2$	24-27 (25.47 $\pm$ 0.77)	13.77
2008_06_05	54622.9	$117.59 \pm 4.3$	31-42 (36.88 $\pm$ 2.96)	47.6
2008_06_06	54623.9	$110.84 \pm 1.47$	31-38 (34.86 $\pm$ 1.63)	32.83
2008_06_07	54624	$99.83 \pm 1.88$	44-46 (45.21 $\pm$ 0.46)	7.84
2008_06_08	54625.9	$95.26 \pm 4.61$	34-46 (39.61 $\pm$ 3.09)	52.7

Table 9.2: Mrk421 Data used in the final analysis, from February 2008 to June 2008. The data shown here are those after data selection and quality cuts.

Date	MJD	$\chi^2/\text{d.o.f}$	probability	Note
2008_01_15	54480.1	2.55	0.021	two time slots
2008_02_06	54502.	3.2	$1.07 \cdot 10^{-6}$	high flux
2008_02_11	54507.	2.41	0.045	two time slots
2008_03_31	54555.9	1.51	0.095	high flux

Table 9.3: The data from the nights which showed  $2\sigma$  away from constant flux values. The  $\chi^2$  fitting using an integrated flux above 300GeV 10 minutes lightcurve. These nights may give hints about intra-night variability.

data. Furthermore, several TeV flares ( $\geq 2$  C.U.) were detected. The TeV flux of Mrk421 was increasing from December 2007 and then became higher in January 2008. A nice "drop and up" V-shaped lightcurve could be clearly seen. On 6 February, the flux reached a local maximum of up to 3 C.U. and then decreased. At the beginning of March 2008, the flux decreased from the local maximum to about 1 C.U. until the middle of March. On 31 March 2008, another spectacular flare of about 4 C.U. was observed, which had an even higher flux than the flare in February. The high flux continued for a few days until 10 April. In May, another tremendous high flux peak occurred. The Whipple/VERITAS collaboration caught this giant flare. Unfortunately, due to the bad weather conditions in La Palma, MAGIC only detected part of the May flare. In early June, another flare was detected; both MAGIC and Whipple (VERITAS) were triggered at that moment. Thus, joint observations with telescopes in different wavelengths, such as AGILE, the optical telescopes WEBAT, were performed. It was a successful multi-wavelength campaign. The detailed physics analysis results of the June flare will be described in a later section. After June, Mrk421 is not visible at the MAGIC site.

The multiwavelength lightcurves of this period are shown in Fig. 9.3. The ASM, BAT, and KVA lightcurves were established with the daily-averaged data. The X/TeV correlation can be clearly seen. On the other hand, the Optical/TeV correlation is not very promising. I will quantify the cross bands correlations in a later section.

### 9.2.2 Short Time Variability

The same method was used in searching for INV in Mrk421 P5 data. The plots concerning signal  $\chi^2/\text{d.o.f}$  versus background  $\chi^2/\text{d.o.f.}$  are given in Fig. 9.4. Plots are produced by 10 minutes and 5 minutes short time lightcurves respectively. From the plot, few nights in P5 show a controllable background  $\chi^2/\text{d.o.f.}$  but large signal  $\chi^2/\text{d.o.f.}$ . They give hints of the intra-night variability. These few different nights are listed in Table 9.3. The analysis for these particular nights will be discussed in a later section.

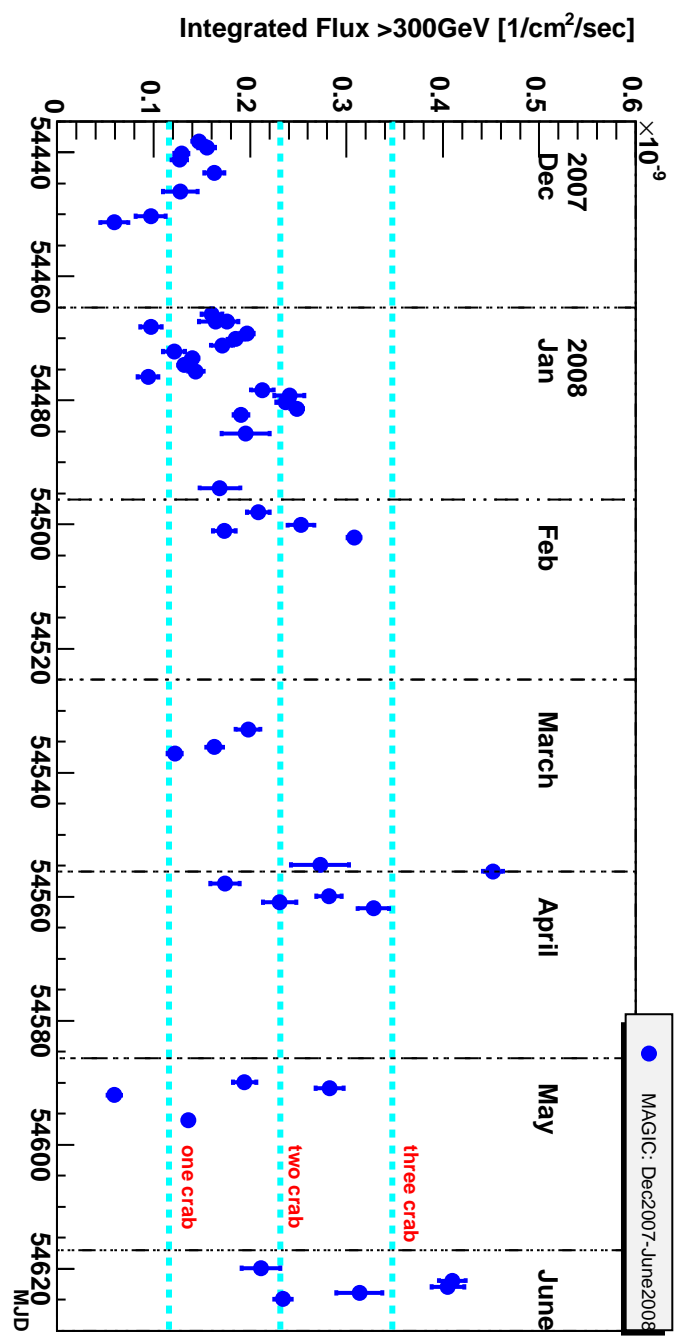


Figure 9.1: The total Mrk421 lightcurve from December 2007 to June 2008

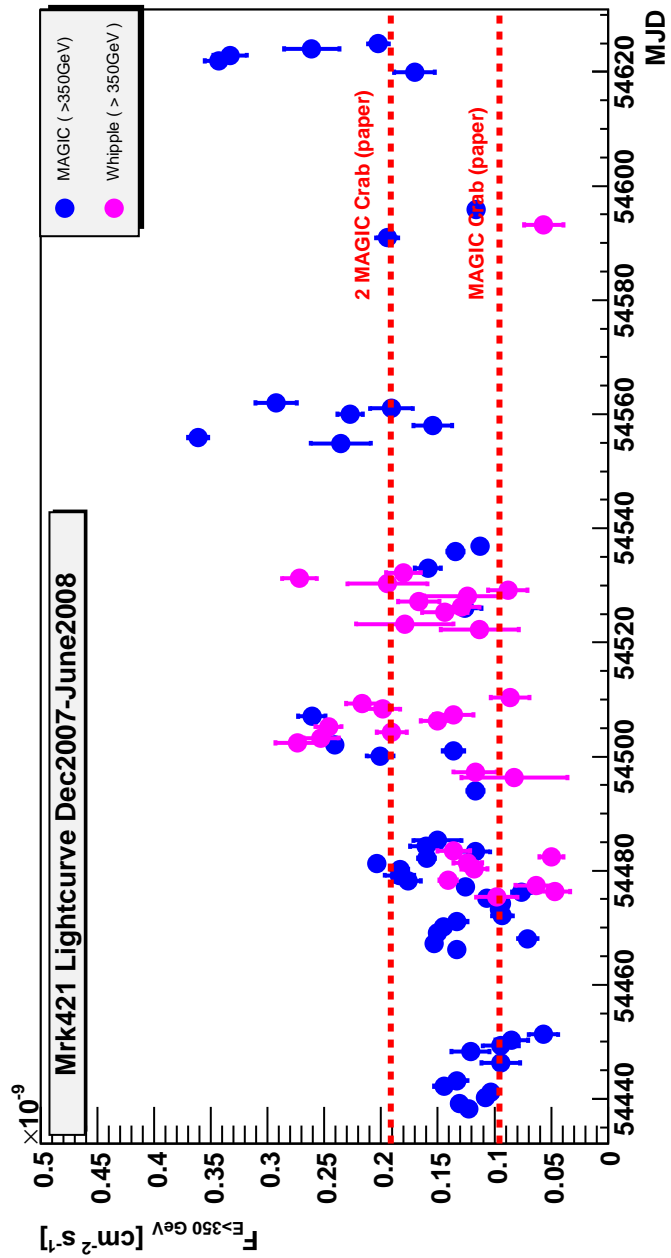


Figure 9.2: The total Mrk421 lightcurve from December 2007 to June 2008 above 350 GeV with VERITAS data.

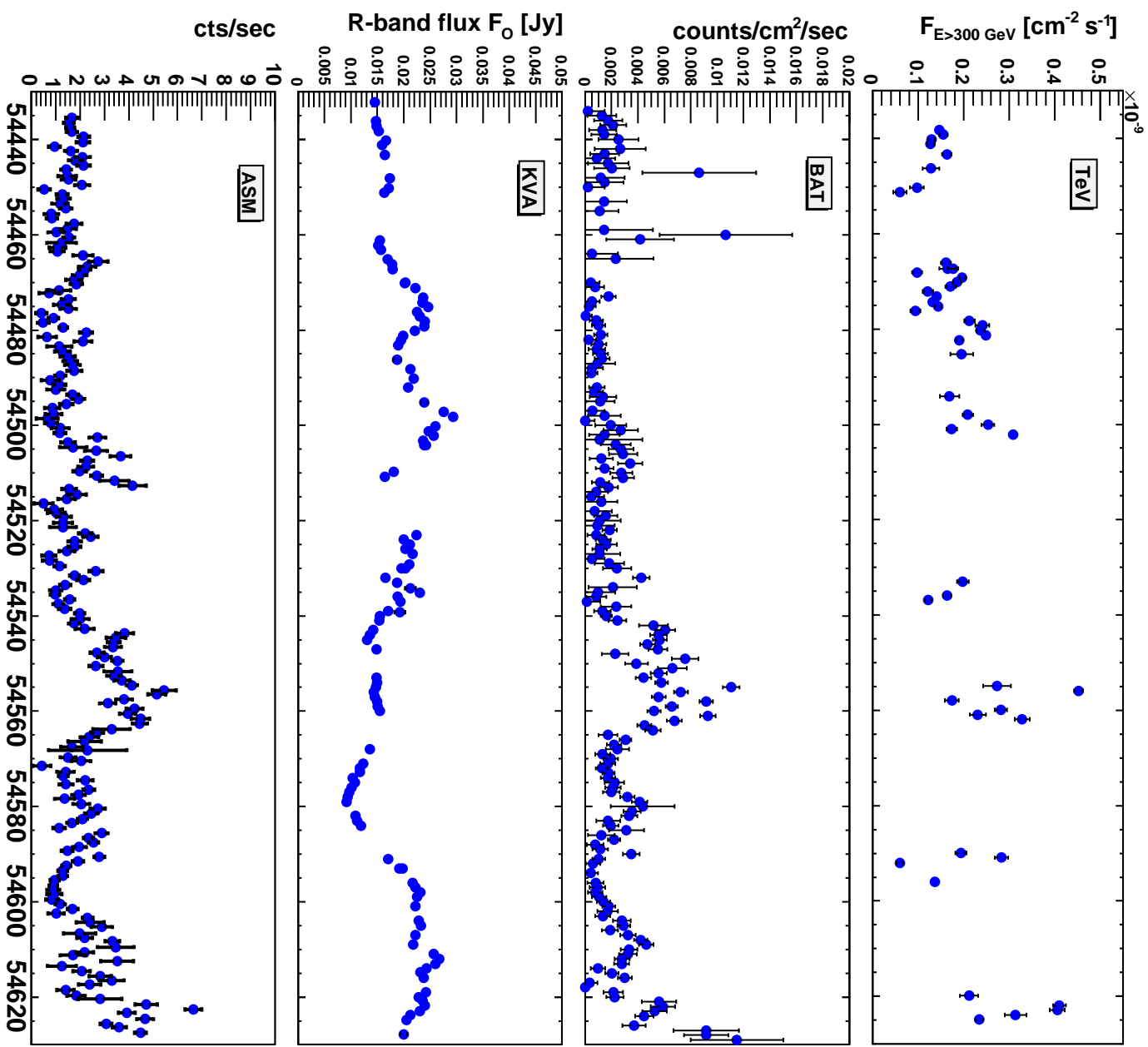


Figure 9.3: The total Mrk421 lightcurve from December 2007 to June 2008 multiwavelength

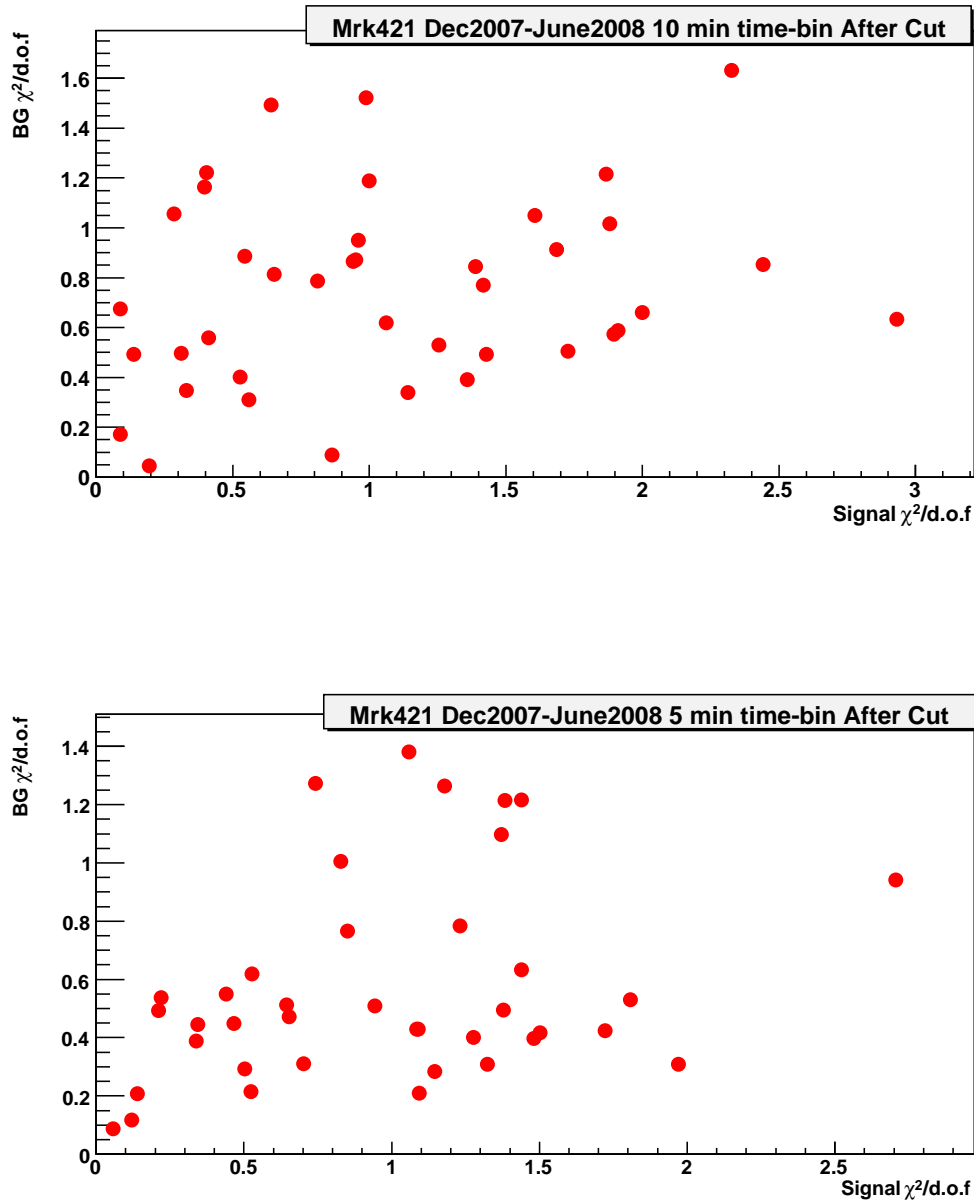


Figure 9.4: The Mrk421 P5 data,  $\chi^2$  fitting of the background and the signal using 10 minutes timing bins. From the plot, it is clear that there are few nights which show a stable background with controllable  $\chi^2/\text{d.o.f}$  but with large  $\chi^2/\text{d.o.f}$  in the signals. These nights give a hint of the intra-night variability.

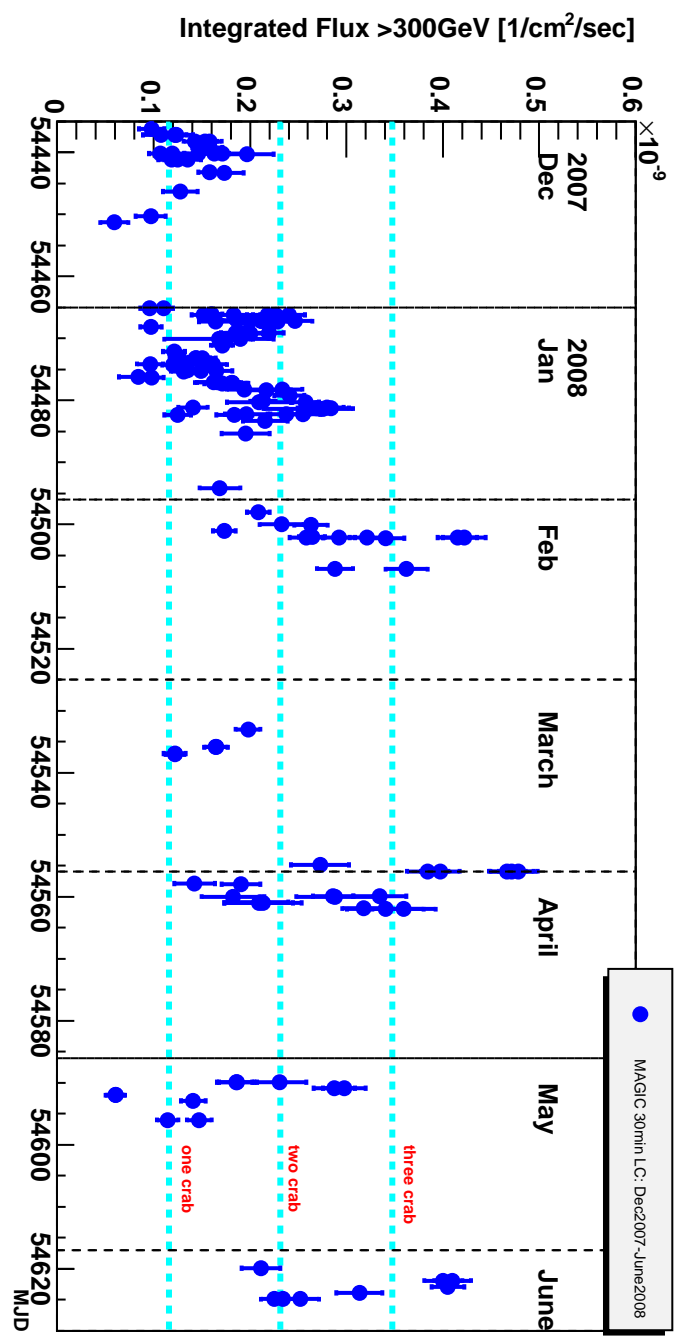


Figure 9.5: The total Mrk421 30min lightcurve from December 2007 to June 2008.

Value	$F_{var}$	$F_{pp}$	$S_{flux}$	$\overline{\sigma^2}$
Mrk421	$0.4 \pm 0.23$	0.13917	8.8299e-11	2.63018e-11

Table 9.4: Mrk421 data taken from December 2007 to June 2008. The data are calculated by using 10 minutes lightcurves.

### 9.2.3 Short Time Lightcurve

Current IACT observations are unfortunately limited in specific observational time and conditions. Unlike air shower arrays, long exposure time is not possible. However, current IACTs are sensitive enough to catch short time flares down to a few minutes which current long exposure shower arrays cannot achieve. The 30 minutes lightcurve is shown in Fig. 9.5 and the 10 minutes lightcurve in Fig. 9.6. In the 30 minutes lightcurve, each point has roughly 30 minutes effective observation time ( $T_{eff}$ ) and 10 minutes in 10 minutes lightcurve. The data points with  $T_{eff}$  smaller than 15 minutes were cut off, for 30 minutes lightcurves, and those with  $T_{eff}$  smaller than 5 minutes for 10 minutes one. All the background levels in 30 minutes and 10 minutes lightcurves were tested with a stability check. Therefore, the background level within the same day was stable.

Even though TeV data is limited due to moon period, darkness nights only, limited visibility of the sources, etc, we believe that with randomly un-biased choosing of the data, we will know the different probabilities of the source at different states. This may reveal the emission mechanism of the sources. In Fig. 9.7, the 10 minutes flux distribution of the Mrk421 in P5 data is displayed. The plot here is biased to high states because of many times of high state triggers. Some theories explain the relation between the flux states distribution and the emission mechanisms. For example, it has been suggested by Lyubarskii [165] that in changing the accretion rates introduced in the accretion disks of the AGNs, the X-ray flux states will follow the logarithm normal distribution and other features such as linear correlation between the RMS variability and the flux. This scenario will be discussed in this thesis.

### 9.2.4 Variability

The Mrk421 lightcurves in period P5 show strong variability in different time scales and different wavelengths. Different time scales of variability may be introduced by different emission mechanisms. We evaluated  $F_{var}$  in different time scales (e.g.: one day, one week, half a month, one month, and two months) and tried to see how the flux changed with different scales of time duration. From the previous old IACTs historical studies and P0 - P4 data of MAGIC observations described in this thesis, we know that Mrk421 rarely shows intra-night variabilities (INV). In addition, INV, if at all, mostly occurs during high flux states. However, there is still a possibility of INV happening during low states, too. It could be due to the limited sensitivity of current IACTs; thus, such variabilities have never been detected before. Though INV does not occur very often, from the long-term lightcurve, say a few months, flux variability can be clearly seen. Hence, it is believed that the AGN variability may be larger if the time scale is longer.

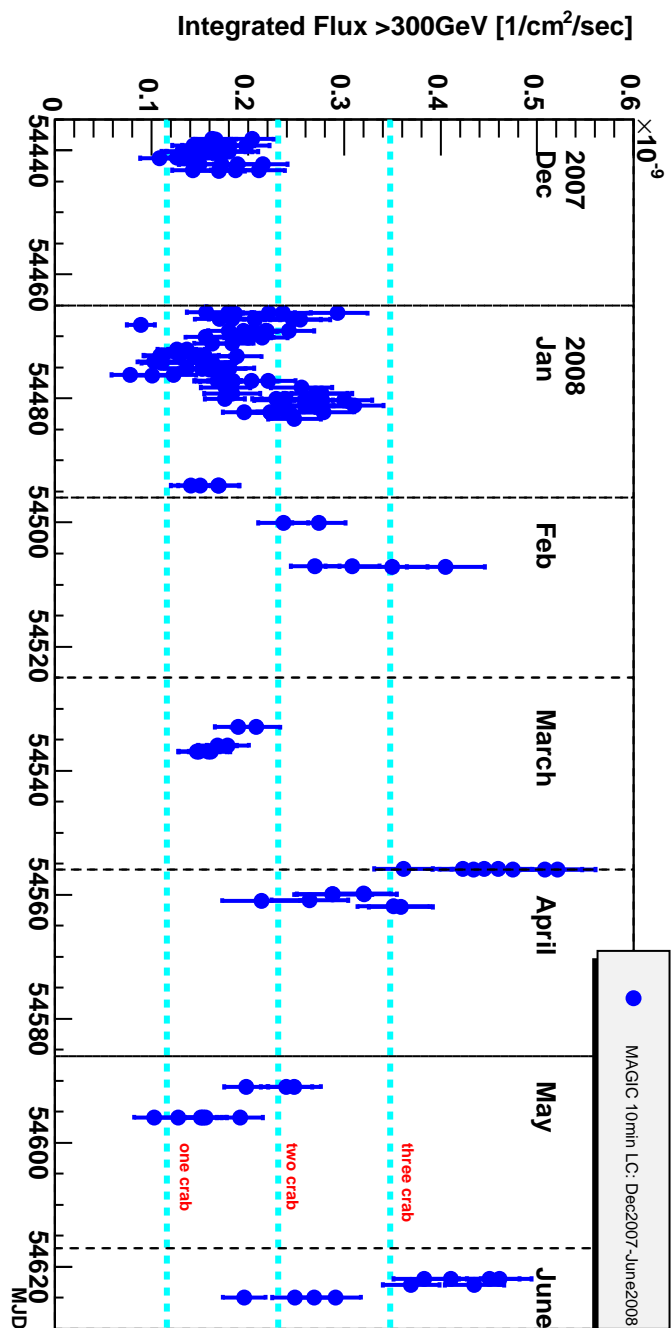


Figure 9.6: The Mrk421 10min total lightcurve from December 2007 to June 2008. integrated flux above 300 GeV.

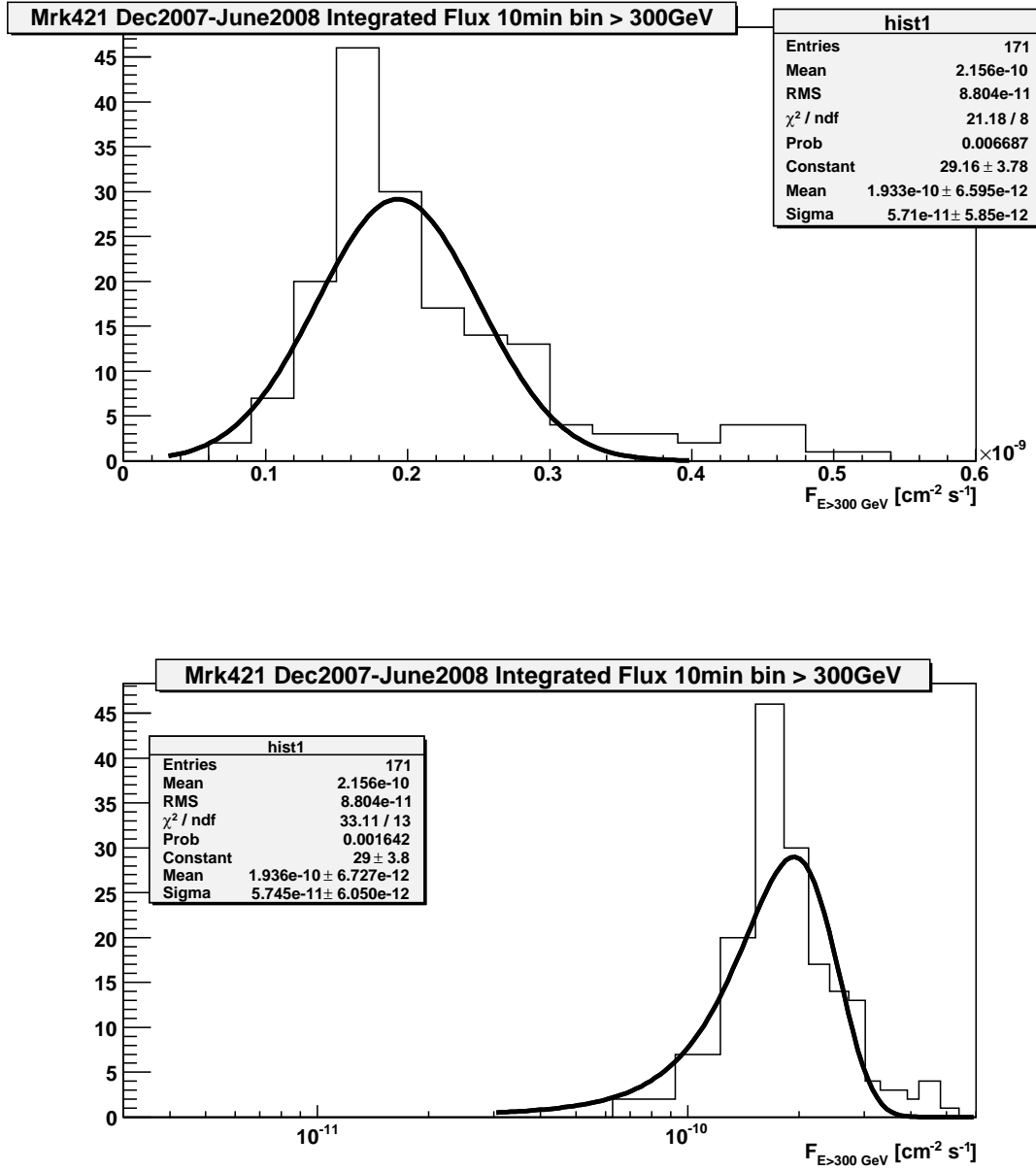


Figure 9.7: The Mrk421 flux states histogram in P5 data. The upper plot shows linear scale in horizontal axis, the bottom plot shows integrated flux distribution in log scale. Both are fitted with Gaussian.

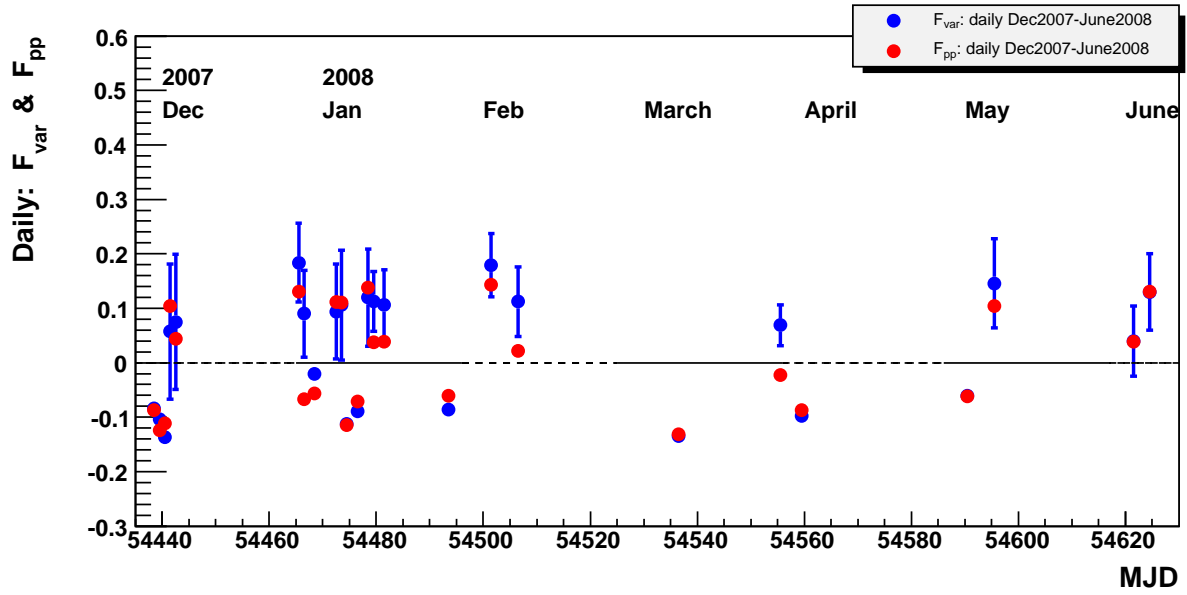


Figure 9.8: The  $F_{var}$  and  $F_{pp}$  in the daily scale. The plot indicates that most of the nights show very small or even negative  $F_{var}$  and  $F_{pp}$  in daily scale, except for the nights which show hints of daily variability.

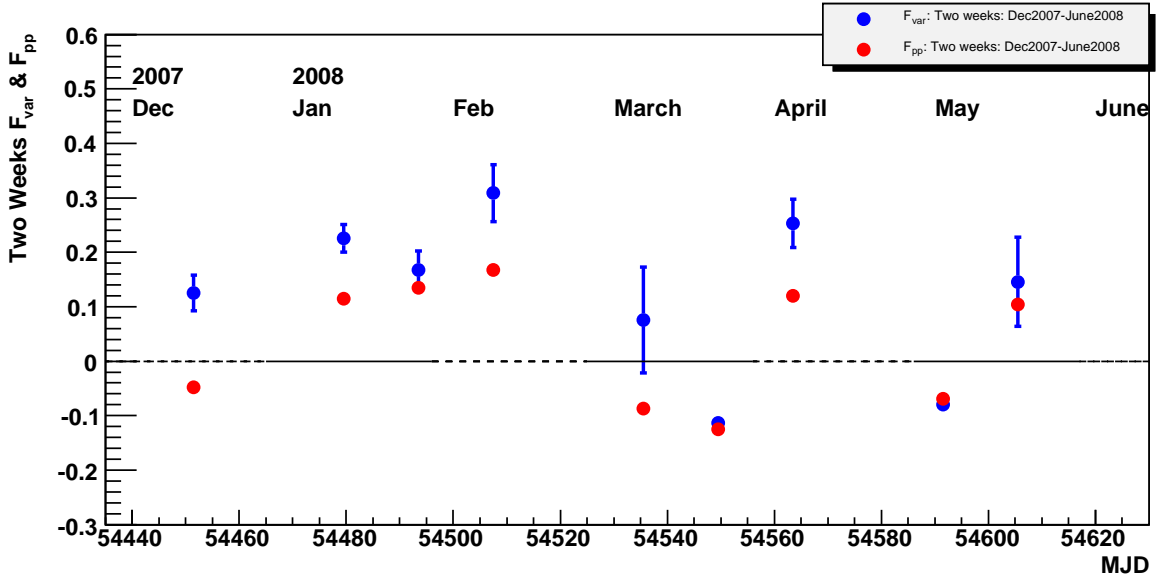


Figure 9.9: The  $F_{var}$  and  $F_{pp}$  in two weeks' scale. Note that the two weeks (14 days) are counted from the first observational day of this period.

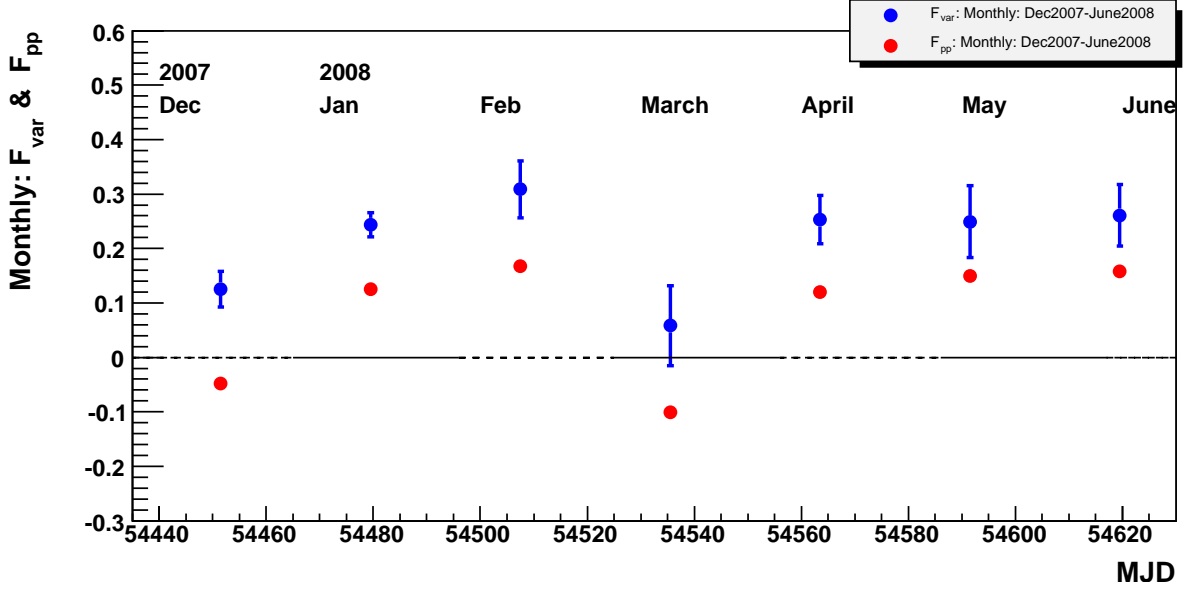


Figure 9.10:  $F_{var}$  and  $F_{pp}$  in a monthly (28 days) scale. Note that the 28 days are counted from the first observational day of this period; therefore, the monthly average is not counted as in our daily calendar.

From Fig. 9.8, we know that  $F_{var}$  is usually quite small, even negative, with big errors in daily scale. This is reasonable and to be expected, since INV occurs very scarcely. The daily  $F_{var}$  should have very small values. In longer time scales, say two weeks and one month,  $F_{var}$  and  $F_{pp}$  increase, see Fig. 9.9 and Fig. 9.10. If we exclude the data set of December 2007 and March 2008,  $F_{var}$  and  $F_{pp}$  remain almost constant in a 28 days' scale. We also found that the points of these excluded two months (December 2007 and March 2008) had the lowest integrated flux among all other points. If we use the whole period of data (7 months in total), the value of  $F_{var}$  is about 0.4, see Table 9.4. The ratio between  $F_{var}$  and  $F_{pp}$  is close to two, which shows characteristics of red noise [166]. The VERITAS/Whipple collaborations observed Mrk 421 during the 2006 multiwavelength campaigns. They observed the same behavior in their data set. This red noise behavior is not clear, if we calculate the ratio in shorter time scales. Fig. 9.14 shows the ratios between  $F_{var}$  and  $F_{pp}$  in two different time scales. Obviously, in longer time scales, the ratio is close to 2.

The value of  $F_{var}$  is related to the power spectrum. If the TeV emission coming from Mrk421 is really red noise, the variability should be larger in longer time scales. Usually, noise behavior could be recognized by Fourier transformation of the lightcurves into power spectrum. Due to the inevitable observational gaps in time series in observations, it is not easy to calculate the power spectrum from TeV data. Thus here, instead, we calculate  $F_{var}$  in different timescales. The results are shown in Fig. 9.11. We try to fit the plot with the formula  $F_{var} = P_1 f^{P_0}$ . The data points can be fitted with a line if we plot it in the Log-Log plane. We try to fit with a constant

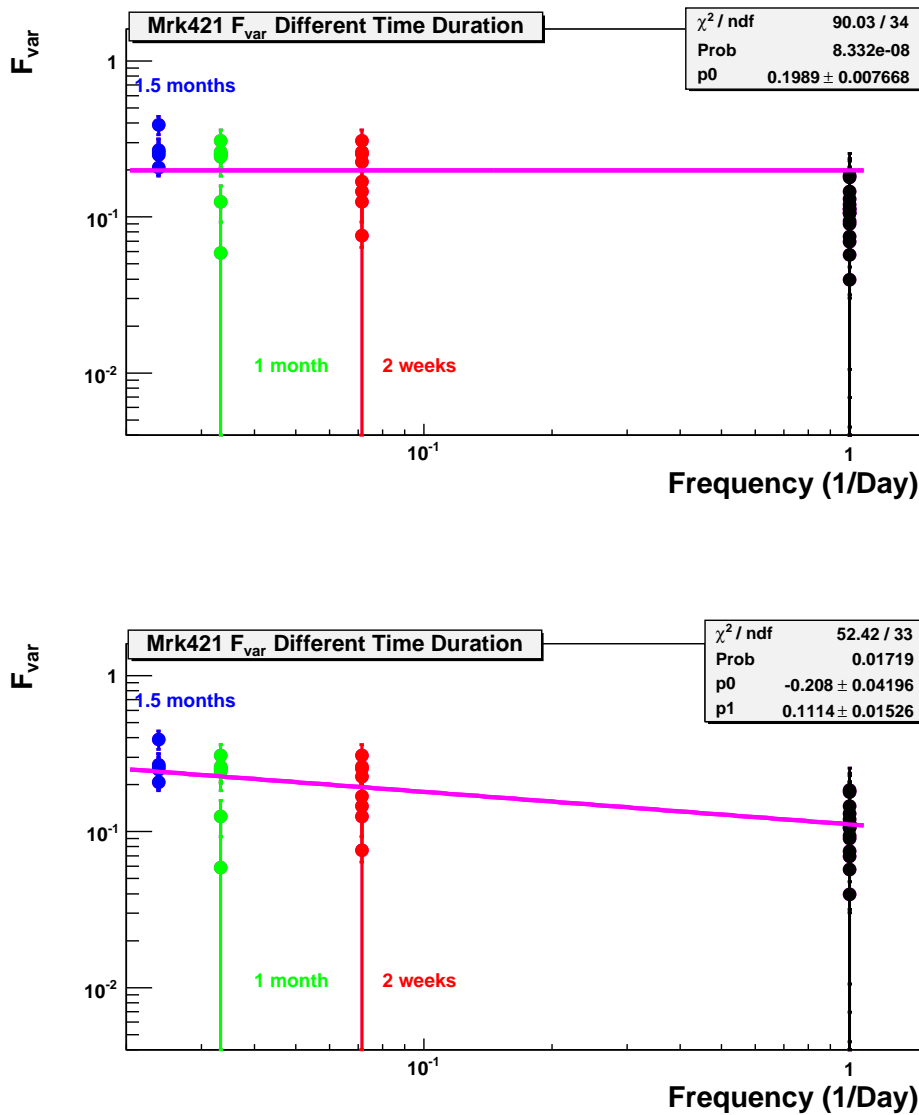


Figure 9.11:  $F_{var}$  in four different time scales in different periods of data.  $F_{var}$  is closer to the value 0.4, once the time scale is longer than one month, the errors are smaller if we consider longer time scales.

horizontal line, the value  $P_1 \sim 0.2$  with  $\chi^2/\text{dof} = 90/34$ . However, if we fit with a sliding line,  $P_0$  is about  $-0.21 \pm 0.04$  and  $P_1$  is about  $0.11 \pm 0.01$ , the  $\chi^2/\text{dof} = 52.42/33$ , which is better than the constant fit. Therefore, we claim that there is a weak correlation between flux variabilities and timescales. More data are necessary to prove the current hypothesis in the future.

### 9.2.5 Variability vs Flux States

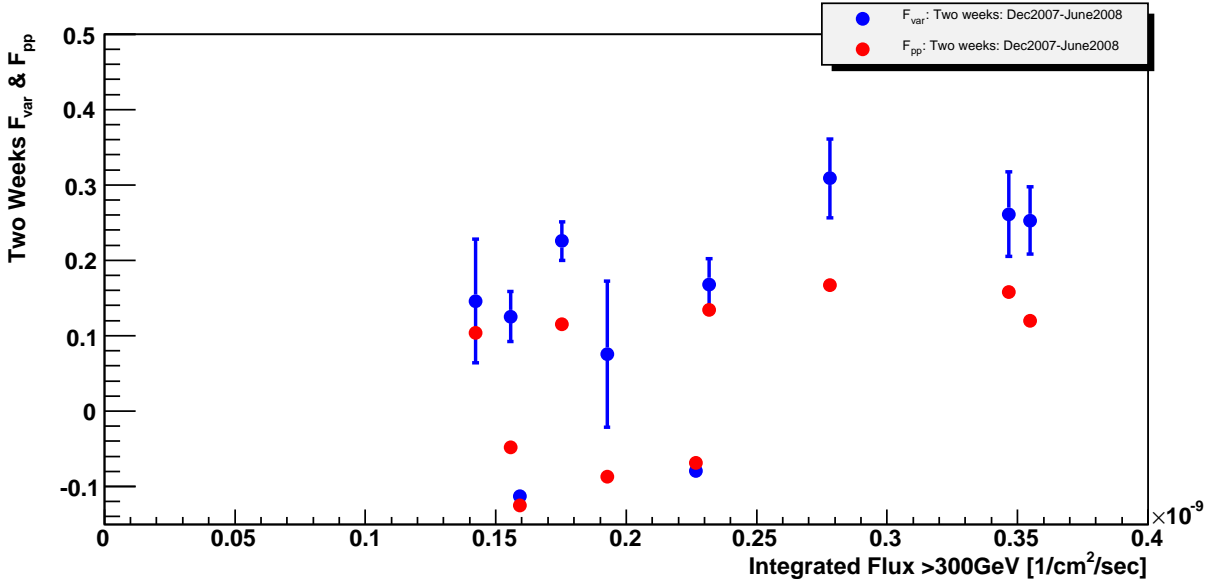


Figure 9.12:  $F_{var}$  and  $F_{pp}$  vs average integrated flux (above 300 GeV) in a two weeks, (14 days) scale. Note that the 14 days are counted from the first observational day of this period; therefore, the two weeks average is not necessarily counted from Monday.

The intrinsic variability of AGNs may depend on the flux states. One of the best examples is the fact that the intra-night variabilities were always seen in high states. In addition, as has been described in Chapter 7, in some Seyfert galaxies' cases, it was found that the intrinsic X-ray flux variations  $\sigma$  have a linear relationship with the integrated flux, the so-called  $\sigma$ -flux relation [167]. Thus a natural question about the variability of Mrk421 or other blazars is whether the degree of variability in the TeV band changes with the mean flux level. Fig. 9.12 and Fig. 9.13 show  $F_{var}$  and  $F_{pp}$  versus integrated flux in two different time scales. In general,  $F_{var}$  is larger and stays constant in higher flux levels.

### 9.2.6 $\sigma$ - Flux Relation

It has been found that in some non-beamed systems like Seyfert galaxies and X-ray binaries, their variability RMS has a linear correlation with flux states. Some models, for example,

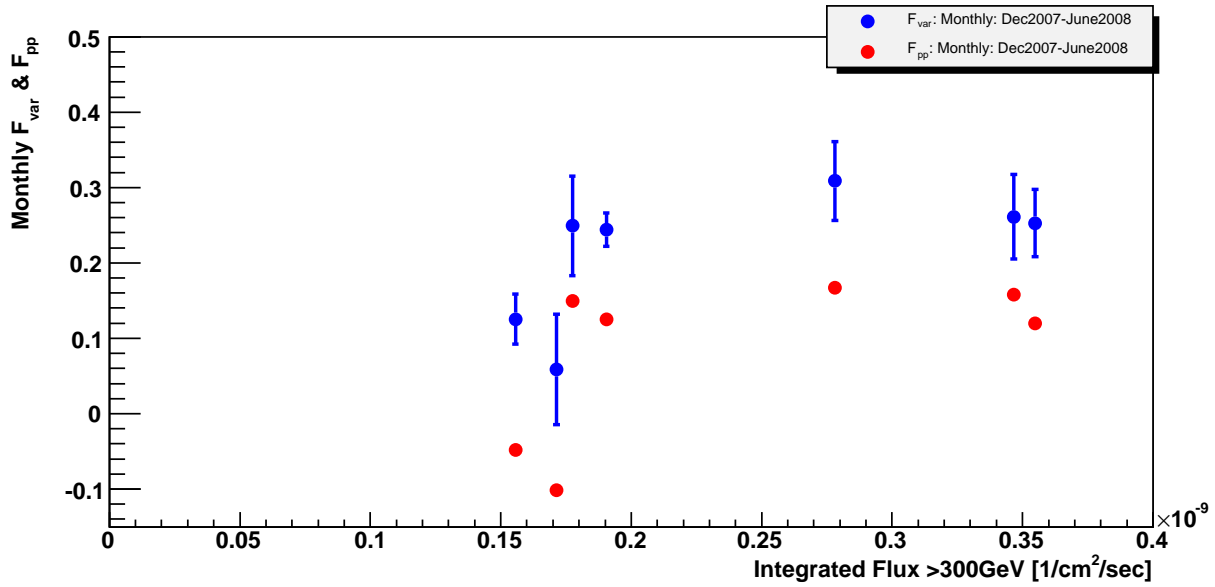


Figure 9.13:  $F_{var}$  and  $F_{pp}$  versus average integrated flux (above 300 GeV) in a monthly (28 days) scale. Note that the 28 days are counted from the first observational day of this period; therefore, the monthly average is not counted like in our daily calendar.

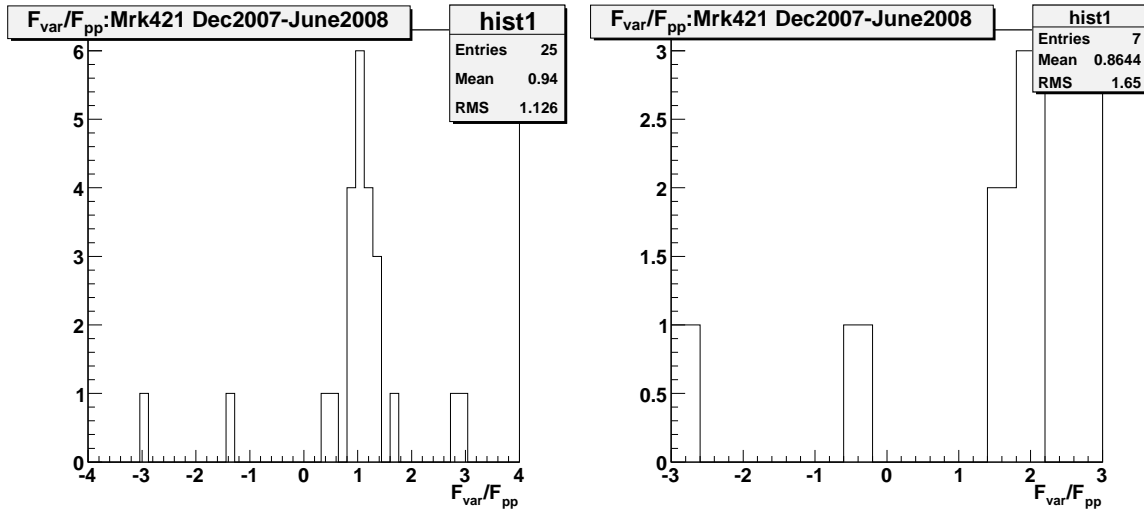


Figure 9.14: The ratio between  $F_{var}$  and  $F_{pp}$  in two different time scales, daily and monthly (28 days). Note that from the daily scale,  $F_{var}$  is similar to  $F_{pp}$ , however, in longer time scale,  $F_{var}$  is always larger than  $F_{pp}$ , which hints at Mrk421 showing bigger variabilities in the longer time scale during this period.

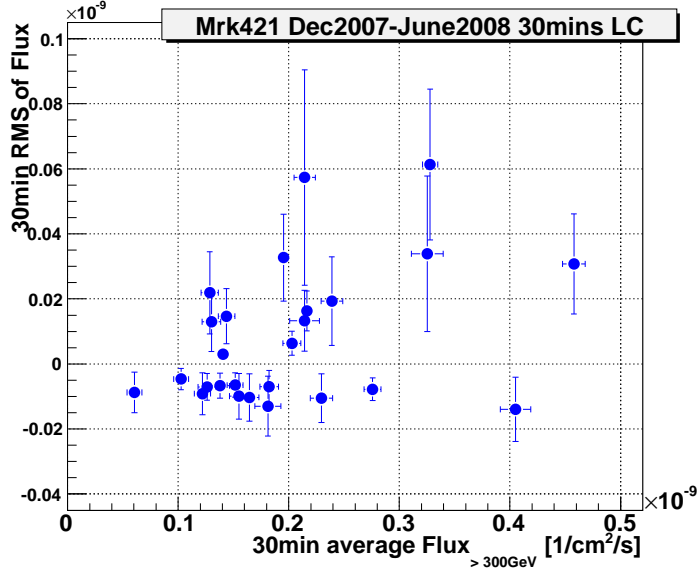


Figure 9.15: The figure shows the  $\sigma$ -flux relation in the TeV band using the MAGIC P5 data. Each point represents a measurement over one day. For each daily measurement, we use 30 minutes lightcurves to calculate the mean flux and  $\sigma$ . The correlation coefficient between  $\sigma$  and average flux is  $0.39 + 0.16 - 0.19$ , and the significance is  $2\sigma$  away from 0.

Lyubarskii [165], has explained that the behavior is resulted from instabilities of the annulus in the accretion disc and propagating inwards which they modulate the emission.

Fig. 9.15 shows the relation between average flux and RMS of flux using MAGIC P5 data. Each point in the plot stands for one day. For each day, the 30 minutes lightcurve was used for  $\sigma$  and mean flux calculation. This method has been explained in Chapter 7.

We assign the RMS to be negative if  $\sigma^2$  is negative, which means they have almost no intrinsic variability. They were included in the plot but with the negative value  $-\sqrt{|\sigma^2|}$ . The plot suggests that the high flux nights do not necessarily show high intrinsic variabilities. Superina et al. [16] and B. Degrange et al. [168] have used similar methods to investigate the PKS2155-304 flare in the 2006 H.E.S.S. data. The flare was 10-15 C.U. above 200GeV. In their papers, they claim that there is a linear relation between  $\sigma$  and flux, see Fig. 9.16. Note that in [16], they explicitly explain that only the points with a significant variability (i.e. positive excess variance) are taken into account in their data analysis. Note that in Fig. 9.16, the solid least-squares fitting lines always pass through the origin (0,0), which will not happen in our case even if we remove the negative points on the plot in Fig. 9.15. There will be an off-set in the flux axis with zero variability. This offset has been observed and explained in the X-ray data of other sources, such

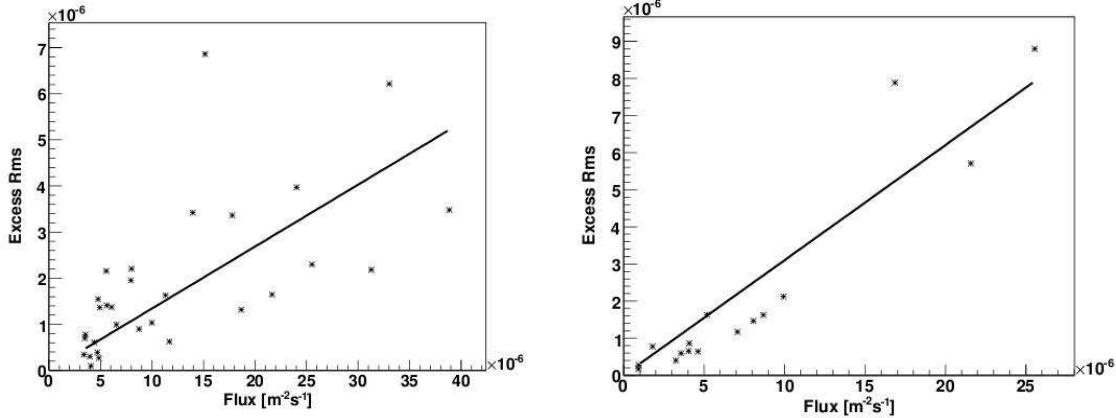


Figure 9.16: The excess r.m.s. versus average fluxes for the segments of lightcurve of different time durations. The data and plots are from AGN PKS2155 from H.E.S.S. observation [16]. The plot on the left-hand side has 20 minutes duration. The sampling rate is 1 minutes. The plot on the right-hand side shows the duration of 80 minutes and sampling rate of every 4 minutes.

as Cygnus X-1. In P. Uttley et al. [167], they explain that there are at least two components in the Cygnus X-1 X-ray lightcurves. One shows a striking linear dependence of RMS variability on the flux, while the other component may contribute a constant RMS to the lightcurve or, more simply, may not vary at all with the flux state. Moreover, they suspect that those two components may have different origins and emission mechanisms. The baseline could be produced by constant contribution from static (or long-time scale) changing components. On top of that, there is a quick variability components which varies with the different flux levels. It is interesting that if we take away all the negative points on Fig. 9.15 and try to fit with a linear line, the off set flux in TeV is about  $0.3 \sim 0.5$  C.U. above 300 GeV, which is equal to the lowest flux level we detected in this period of Mrk421. In the future, with more intensive data, we could resolve these two components if they exist.

## 9.2.7 Further Discussion on Lightcurves

### The Structure Function

In order to quantify the variability in different time frequencies, structure function (SF) was performed using P5 data. We have checked how  $F_{var}$  changes with different time scales in the previous section. The SF will give us further information. As explained earlier, the SF is correlated with PSD. It gives a crude but convenient estimation of the corresponding PSD distribution which characterizes the variability.

In general, the SF gradually changes its slope  $\beta$  with the time interval  $\tau$ . On shorter time scales, variability can be well approximated by a linear function of time;  $a(t) \propto t$ . In this region, it is usually the steepest portion of the SF curve. The SFs of the X-ray lightcurves and TeV lightcurves show a variety of features. We calculated SF by using Mrk421 TeV and X-ray P5

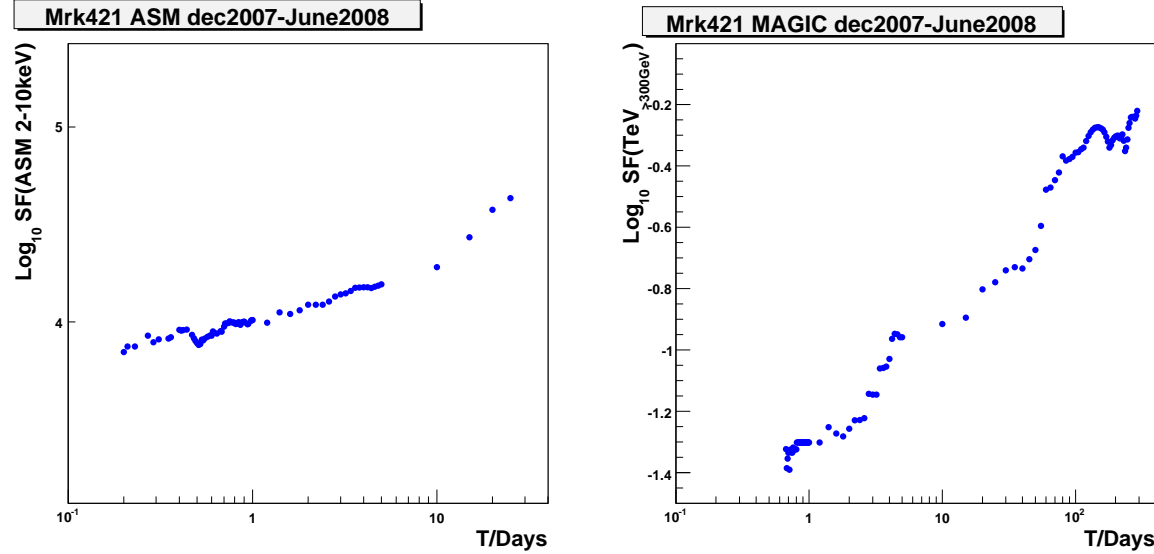


Figure 9.17: Left: The structure function of the ASM data from Mrk421. Right: The structure function of the TeV data from Mrk421.

data from MAGIC and ASM, respectively. The SF of Mrk421 from X-ray ASM and MAGIC data is shown in Fig. 9.17. Note that the number of pairs in the SF calculation decreases as the time difference increases and accordingly, the uncertainty becomes larger [169].

The TeV SF are calculated from MAGIC P5 data using 10 minutes lightcurves. We selected the data with at least 30 pairs. The X-ray SF are calculated from ASM data using per point per dwell lightcurves. We found that both TeV and X-ray SF cannot be described as a simple power-law. The wiggling features at the long time scales are due to the finite number of flares that exist in the observed lightcurves and thus, are not intrinsic to the sources. In Tanihata 2001 [161], the SF from 3 famous established TeV blazars, Mrk421, Mrk501 and PKS2155-304 are investigated by using ASCA monitoring data. The conclusion is that TeV blazars have a SF with a steep rise at shorter time scales and a break at a characteristic time scale  $\tau$ , see Fig. 9.18.  $\tau$  is about 1 day for Mrk501,  $\sim 2$ - $3$  days for PKS2155-304 and  $\sim 0.5$  day for Mrk421, indicating the time scales of individual flares.

The peak value of the clear turn-over in Mrk421 SF from Tanihata's paper is around  $40 \sim 50$  ksec, which is approximately a 0.5 day scale. In the ASM plot from P5, a small turn-over around  $0.4 \sim 0.5$  day is seen. In ASCA data, from 100 k to 1000 k sec, SF starts to wiggle. However, in P5 ASM data, the wiggling is not very clearly seen from time scales 1.5 days to 7 days. The MAGIC TeV SF curve shows more substructures. The curve rises sharply at around 5 days and then returns to a normal slope after 100 days. Above 100 days, the errors become larger since the number of pairs becomes smaller and smaller. The number of pairs is limited by the total observation time. The strong wiggling above 100 days could be explained by few strong flares. Furthermore, because of the limited numbers of pairs, the heavier double counting causes the wiggle structure.

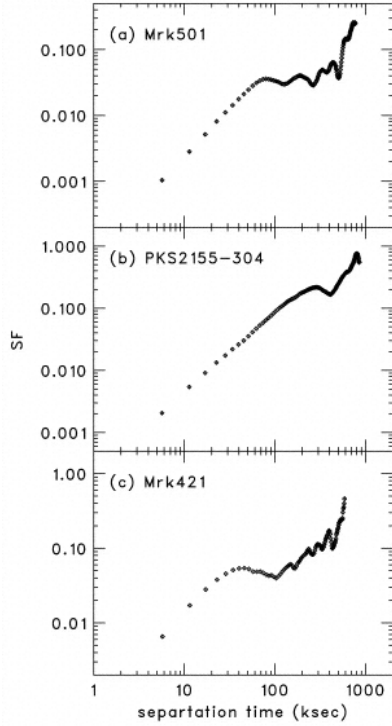


Figure 9.18: The structure function of the ASCA data from three bright blazars: Mrk501, PKS2155-304, Mrk421. All the data are from ASCA monitoring. Mrk501, PKS2155-304 were observed continuously for 10 days in 2000. Mrk421 was observed for 7 days in 1998.

### The Self Auto-correlated Function

Time periodicity of the lightcurves, once found, could give an important physics implication. We calculated the ACF on the lightcurves of Mrk421. If a copy of signals is shifted in phase, from the peak position of the correlation function, the fundamental periods of the signal will be revealed. In Fig. 9.19, we include two identical TeV lightcurves from MAGIC P5 observations, delayed one of the lightcurves on purpose and tried to find the correlation coefficients. Note that since the number of data points is limited, the number of pairs in the correlation coefficient calculation is becoming smaller if we have large time delays. In order to minimize the errors on the correlation coefficient calculation, we ignore the data points with fewer than 10 pairs. In consequence, we don't have any data points between 10-day and 20-day delays. From the plot, we see that the correlation peak is at zero, and there is no other peak which gives high and strong correlation coefficients. Therefore, we conclude that there is no hint of any significant TeV time periodicity structures from the MAGIC TeV observation in P5 data.

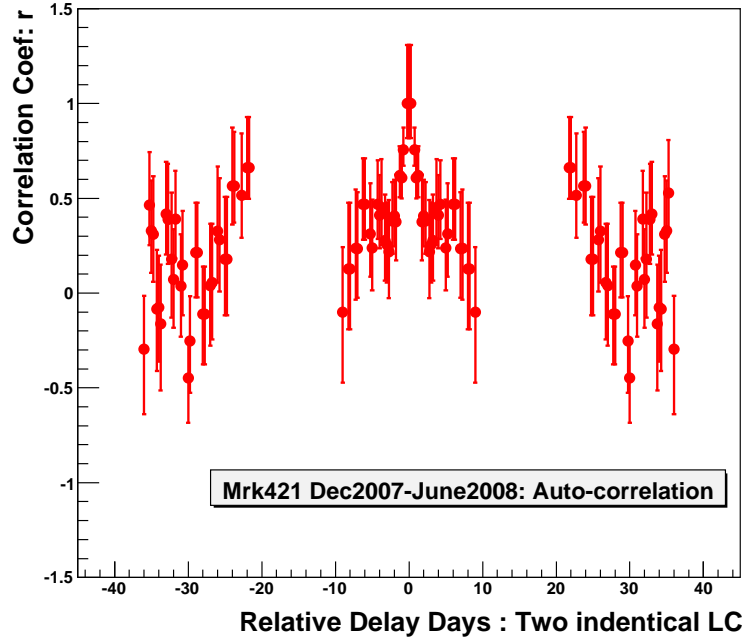


Figure 9.19: The correlation coefficient. against different time lags. The plot shows the results of auto-correlated function. The inputs are two identical Mrk421 30 minutes lightcurves from P5 data. We selected the data points with more than 10 data pairs after the time delay. Thus, after the selection cut, there is a neutrino data point between 10-day to 20-day delays. The time resolution for the correlation scan is 6 hours.

## 9.3 Multi-Wavelength Study

### 9.3.1 Multiwavelength Correlation.

The multi-wavelength lightcurves of Mrk421 in period P5 is shown in Fig. 9.3. In this plot, TeV and X-ray correlation is seen. The TeV/optical correlation is not very clear in the case of Mrk421. I will try to quantify the cross-band correlations between different wavelengths. At the same time, possible time lags in P5 data between the TeV and X-ray bands will be searched for. The physics results on the study of multiwavelength correlations using the data from P0 to P5 will be discussed in Chapter 10.

### 9.3.2 TeV/X-ray, TeV/Optical Time Lag search.

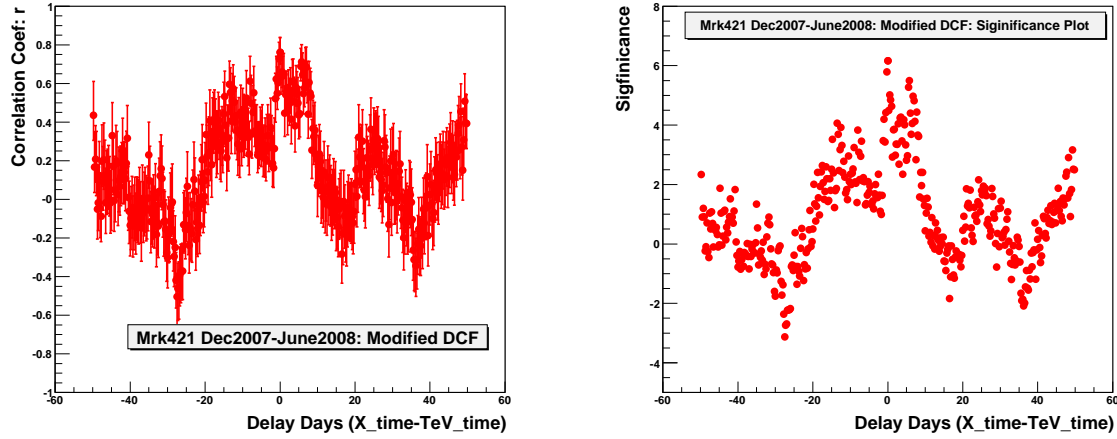


Figure 9.20: Left : The correlation between ASM X-ray flux and TeV  $\gamma$  flux with different time lags. The X-ray data are from ASM dwell based data. The time searching window is 6 hours every step. Right : The significance between ASM X-ray flux and TeV  $\gamma$  flux correlations with different time lags. The X-ray data are from ASM dwell based data. The time searching window is 6 hours every step.

Since true simultaneous multiwavelength data are difficult to obtain, we give two different observations a tolerance in time while performing a correlation study. The tolerance is 6 hours, i.e. any ASM X-ray data which is within  $\pm$  6 hours of TeV Magic data will be treated as "simultaneous" (no time lag). The time lag searching between TeV/X-ray lightcurves is shown in Fig. 9.20. From the plot, at time zero, we have a maximum correlation coefficient of about 0.76. Therefore, no clear time lag signal was observed unless the delay was within our time resolution of 6 hours. The number of pairs decreases while the time lag window becomes larger due to the limited number of samples. The corresponding significance plot is also shown in Fig. 9.20. The highest significance point is at time 0, which is about 6.2 sigma away from 0. It is known that searching for time lags is complicated and tricky. The uneven sampling of the data and indispensable observational time gaps in the lightcurves are the main problems. For example, Edelson et al.(2001) proposed that the lags on the time scales of hours in X-ray data could be an artifact of the periodic gaps in the lightcurves introduced by the Earth occultation of the satellites every  $\sim$  1.6 hours. In the TeV regime, the very uneven distribution of data makes the situation more complicated. The physics implications of the time lag between different wavelengths will be discussed in Chapter 10.

## 9.4 June Flare of Mrk421: Multiwavelength Observation.

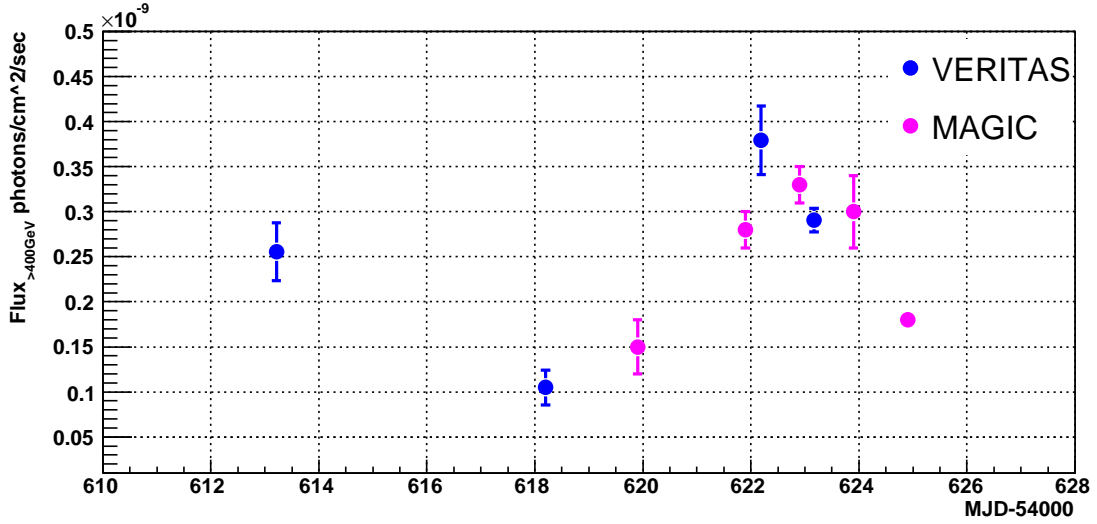


Figure 9.21: The joint lightcurve of MAGIC and VERITAS in June 2008. The combined lightcurve shows that Mrk421 was about 1 C.U. around MJD 54618 and then within 4-5 days, the flux went up to about 4 C.U. around MJD 54622. Afterwards, the flux started to decrease. It is unfortunate that AGILE did not observe during this period.

From 24 May to 23 June, an intensive multiwavelength observation of Mrk421 spanning several decades of wavelengths was planned and performed. A high state of Mrk421 was detected by different instruments in wide energy range. In the VHE regime, MAGIC and VERITAS observed the source and obtained interesting combined lightcurves. This extraordinary set of simultaneous data, covering a twelve decade spectral range, allowed for a deep analysis of the spectral energy distribution as well as of correlated lightcurves.

### 9.4.1 Observations in VHE $\gamma$ -Rays

MAGIC observed Mrk421 from 1 to 10 June 2008 in WOBBLE mode. The zenith angle was between  $28^\circ$  and  $48^\circ$ . After the data quality cut, the total amount of the data was 2.95 hours, and the data were taken from 3 to 8 June. They were analyzed by using the MAGIC standard calibration and analysis methods. The  $\gamma$ -ray excess was derived from the  $\theta^2$  distribution.  $\theta$  was estimated using the so-called DISP method. VERITAS data were taken in WOBBLE mode as well, but with  $0.5^\circ$  offset from the camera center instead of  $0.4^\circ$  in MAGIC. After the data quality cut, about 1.17 hours of data remained. The  $\gamma$ -ray direction and air shower impact parameters on the ground were reconstructed by using stereoscopic techniques. The TeV joint lightcurve of MAGIC and VERITAS is shown in Fig. 9.21. In total, a signal corresponding to a significance

level of  $44\sigma$  was derived from VERITAS and  $66\sigma$  from MAGIC. The significance calculation is based on formula 17 in Li & Ma [111].

We could roughly divide the whole observations into two different time periods. Period 1 is from 3 to 8 June 2008. X-ray (RXTE and BAT), MAGIC and VERITAS were included in the observation. The second period is from 9 to 15 June 2008, including optical, UV, X-rays (XRT and Super AGILE) and gamma-ray data (AGILE). The optical, soft and hard X-ray bands strongly constrain the SED around the synchrotron peak.

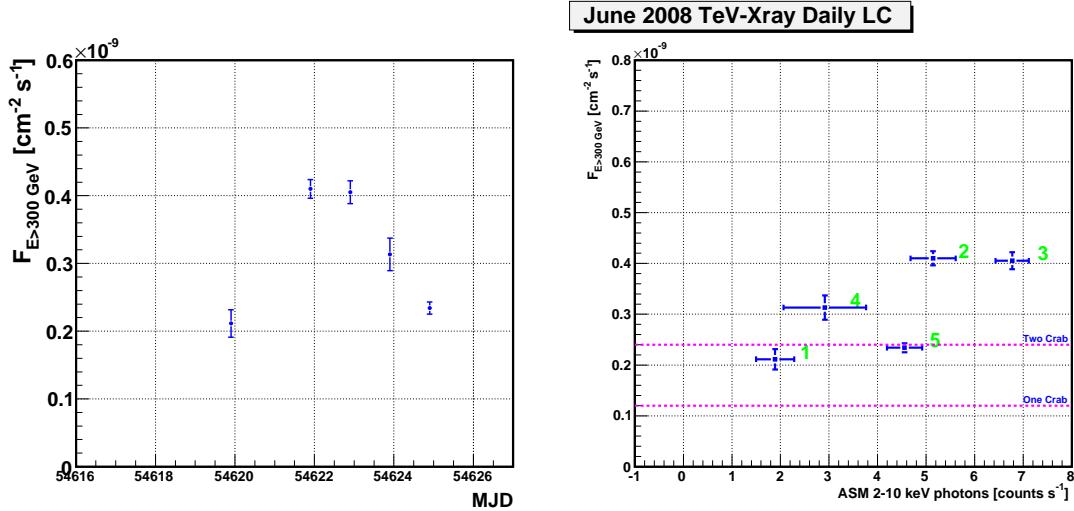


Figure 9.22: Left plot: Mrk421 June flare MAGIC daily lightcurves. The integrated flux is above 300 GeV. Right plot: X-ray and TeV flux diagram. The marker from 1 to 5 represents the time evolution of the source flux in this plane. The X-ray and TeV flux show a high correlation coefficient of  $r = 0.75+0.18-0.49$ .

In the multiwavelength plot, possible correlations of the optical, X-ray and TeV measurements are presented. The optical lightcurve shows variations of the order of 10% on the time scale of a few days, superimposed on a long decay during the entire period. Individual soft and hard X-ray peaks increased fluxes by a factor of  $\sim 2.5$  and  $\sim 5$ , respectively. The correlation between X-ray ASM and TeV MAGIC measurements are shown in Fig. 9.22 (right panel). The X-ray and TeV observation indicates a high correlation with a correlation coefficient of  $r = 0.75+0.18-0.49$ .

The TeV MAGIC lightcurve and the X-ray/TeV flux plane are shown in Fig. 9.22. In Fig. 9.23, we see how the TeV flux varies with the hardness ratio in time. This is the so-called (F,h) plane. The (F,h) pattern was first introduced for studying the synchrotron peak [170]. Later, [171] introduce the same method for TeV emission by assuming the internal shock model and SSC mechanism. The characteristic hysteresis patterns are explained with the interplay of the synchrotron (Inverse Compton) cooling time  $\tau_{cool}$ , the particle acceleration time  $\tau_{acc}$  and the intrinsic variability time  $\tau_{var}$  [172]. The time evolution of the loop reveals the differently dominated time scales. For example, if the evolution pattern is clockwise, the cooling controls the spectral slope. If it is

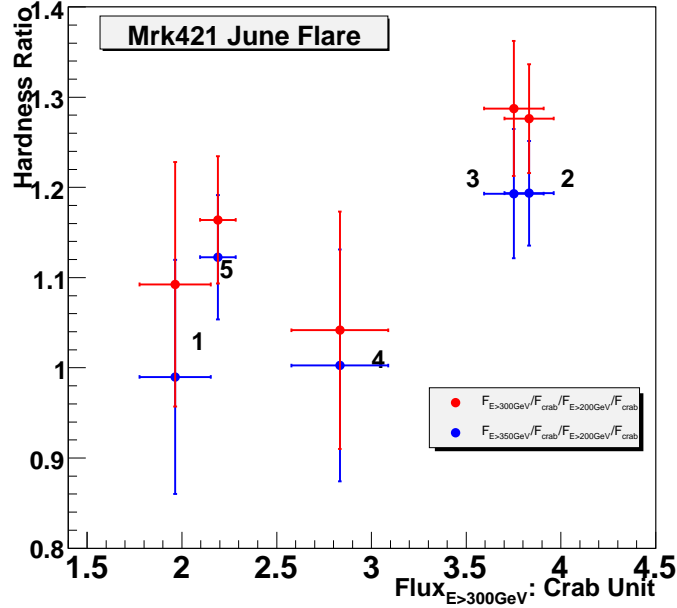


Figure 9.23: Time evolution of the Mrk421 June flare on the so-called (F,h) plane. Each point of the plot is the daily averaged lightcurve. Note that the time evolution of Mrk421 on the June flare is very likely following the counterwise rotation in the plane.

an anti-clockwise loop, cooling and acceleration times are equal. The MAGIC June data seems to tell that the time evolution is clockwise. A similar pattern from Mrk421 was observed by HEGRA in their 2000 and 2001 data [148] and Mrk501 data observed by MAGIC in 2005 [10]. In this scenario, the so-called "soft lag" is expected [172]. Because the cooling time decreases with energy, the highest energy particles cool quickest. Depending on  $t_{acc}$  and  $t_{var}$ , the time scales of the flare rising and falling are different [172].

The VERITAS energy spectrum from 6 June is shown in Fig. 9.24. A power law fit over the energy range 0.3 - 5 TeV resulted in a  $\chi^2/\text{d.o.f.} = 0.7$  with a photon index  $\Gamma = 2.78 \pm 0.09$ . The EBL de-absorption model is Raue & Mazin 2008 [173]. If we fit the intrinsic spectrum with a power law, it yields a photon index  $\Gamma = 2.59 \pm 0.08$ , which is not significantly harder than the observed spectrum due to the relatively low redshift. The SED modeling procedures are as follows: We first consider the modeling of the synchrotron peak using the optical, soft and hard X-ray data. The short time variability of the X-ray data constrains the size of the emitting region.  $R \leq cT\delta \sim 5 \times 10^{16}(\delta/20) \text{ cm}$ . If we consider the SSC model, assume that the Doppler factor is 20 and the co-moving size of the blob is  $R = 4 \times 10^{16} \text{ cm}$  [82], we can calculate the electron energy distribution function which is described by a double power-law

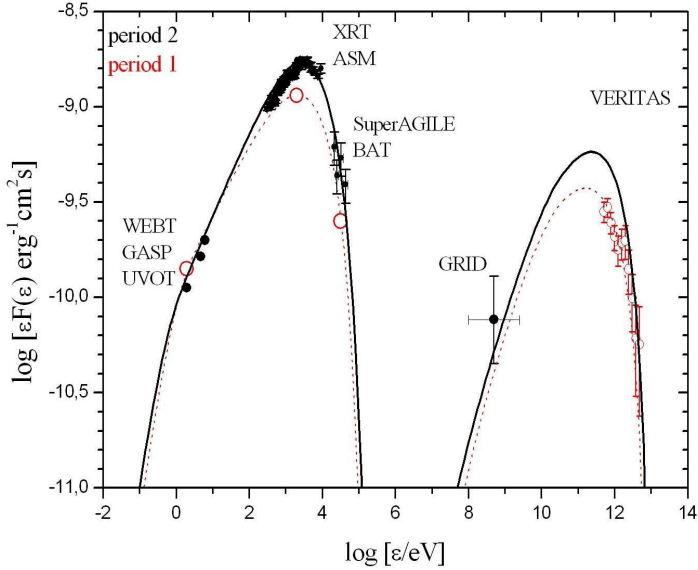


Figure 9.24: The SED of Mrk421 calculated by combining the data from GASP-WEBT, Swift/UVOT, RXTE/ASM,XRT, SuperAGILE, BAT,GRID and VERITAS data in the first period and the second period. Both of them could be fitted well with one zone SSC models [17].

$$n_e(\gamma) = \frac{K\gamma_b^{-1}}{(\gamma/\gamma_b)^{p_1} + (\gamma/\gamma_b)^{p_2}} \quad (9.1)$$

The co-moving Lorentz factor  $\gamma$  varies from the range  $\gamma_{min} = 4 \times 10^3 \leq \gamma \leq \gamma_{max} = 1.3 \times 10^6$ ; the other parameters could be also calculated [17]. With these values, we obtained the best fitted of the co-moving magnetic field  $B = 0.1$  G. Variability could be caused by several reasons. Here I consider two cases: (i) hardening/softening of the electron energy distribution function caused by particle acceleration processes. (ii) The particle number density changes, resulting in increasing or decreasing numbers of particle injection/loss by the shock process. We expect that the TeV variability to be comparable with the X-ray one if case (i) is applied, due to the emission in the Klein-Nishina regime in the TeV band. On the other hand, for case (ii), we expect the TeV relative variability to be a factor of 2 higher than that of the X-ray flux variability. From the multiwavelength data, case (i) is supported. The SED modeling is shown in Fig. 9.24. It is interesting that the model predicts an even higher TeV flux to appear in the second period. However, unfortunately no TeV data were available.

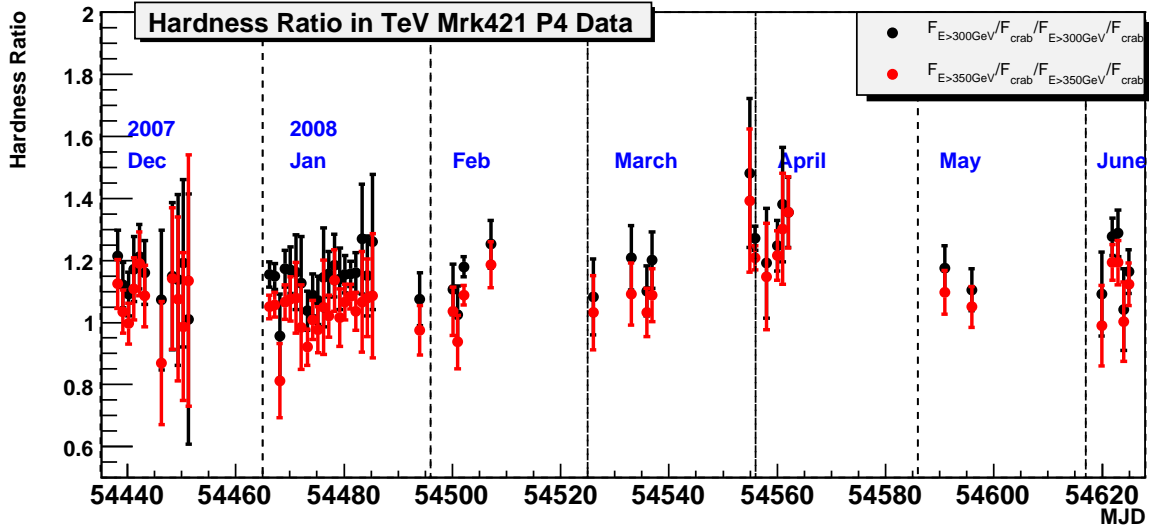


Figure 9.25: The hardness ratio calculated from three lightcurves with different threshold energies. The red points are the ratio between a daily integrated flux above 350 GeV and 200 GeV. The black points are the a daily integrated flux above 300 GeV and 200 GeV.

## 9.5 Spectral Distribution

### 9.5.1 Hardness Ratio

The definition and calculation of the hardness ratio have been shown in Chapter 7. For a daily overview of the spectral evolution, we calculated the hardness ratio using P5 data. The daily hardness ratio is shown in Fig. 9.25. Value 1 in the plot means the spectrum is Crab-like and has the same spectrum index as the Crab.

Fig. 9.26 shows the hardness ratio against the integrated flux (in Crab Unit). The two plots show the hardness ratios of two different energy thresholds. There is a tendency that the hardness ratio increases with an increasing flux. The changes of the HR could be considered as the changing of the IC peak position.

### 9.5.2 Spectral Study

The spectrum from the de-absorption of the EBL was also derived. The state-of-art EBL model was used [173]. Most of the derived Mrk421 spectra could be fitted either by a simple power law with the formulation  $f = f_0 \cdot (E/r)^\alpha$  or a power law with a cutoff  $f = f_0 \cdot (E/r)^\alpha \exp(-E/E_c)$ . Fig. 9.27 shows the Mrk421 fitting spectrum with and without de-absorption. The left plot is without EBL de-absorption. These two plots show the probability of the spectrum being fitted with two mentioned functions. One data point in the plot means data taken during

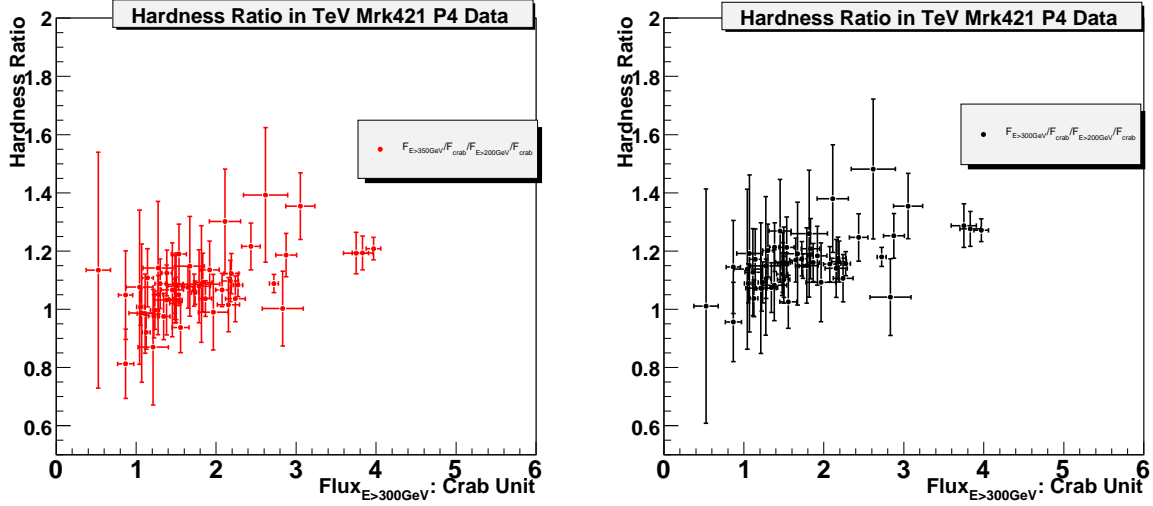


Figure 9.26: The hardness ratio of three different threshold energies versus different daily average flux. The left figure is the ratio between a daily integrated flux above 350 GeV and 200 GeV in C.U.. The right figure is the ratio between daily integrated flux above 300 GeV and 200 GeV, also both in C.U. A few nights show big error bars simply because of the short observation time.

one night. There are few points which show a small probability to be fitted by a simple power law (the points in the far lower right). These points are good candidates for being to be fitted by a power law with an exponential cut-off spectrum.

It has been mentioned that the spectral index may change with different flux states because of the IC peak shifting. We selected the nights whose spectra were well fitted with a simple power law. In Fig. 9.28, we see that the spectrum index seems to evolve with different flux states. The whole plot could be fitted by a linear function.  $\alpha = p_0 * F + p_1$ , where  $p_0 = 1.49 * 10^9 \pm 1.76 * 10^8$ ,  $p_1 = -2.78 \pm 0.04$ . Note that this best-fit line happens to pass the crab point. All the spectral indexes are without de-absorption. If we apply the Raue and Mazin [173] EBL model, the final de-absorbed spectrum index versus flux is shown in Fig. 9.28 in the lower panel. The spectrum index after de-absorption is roughly 0.2 harder than without de-absorption in the case of Mrk421.

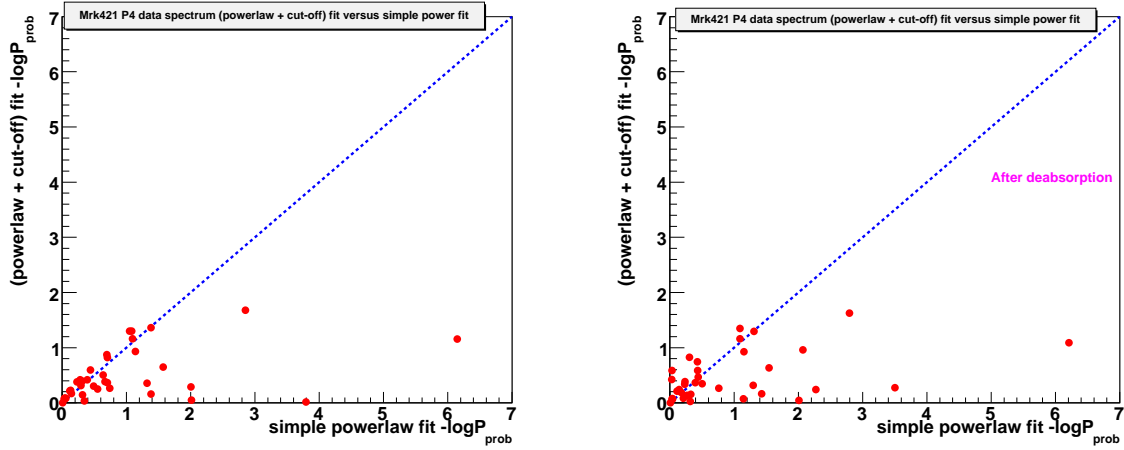


Figure 9.27: The probability of spectra fitted with a simple power law (PL) and a simple power law with an exponential cut-off (PL+CutOff). The left panel shows the spectra before EBL de-absorption and the right panel shows the spectra after EBL de-absorption. few nights spectra show much better fitting with PL+CutOff.

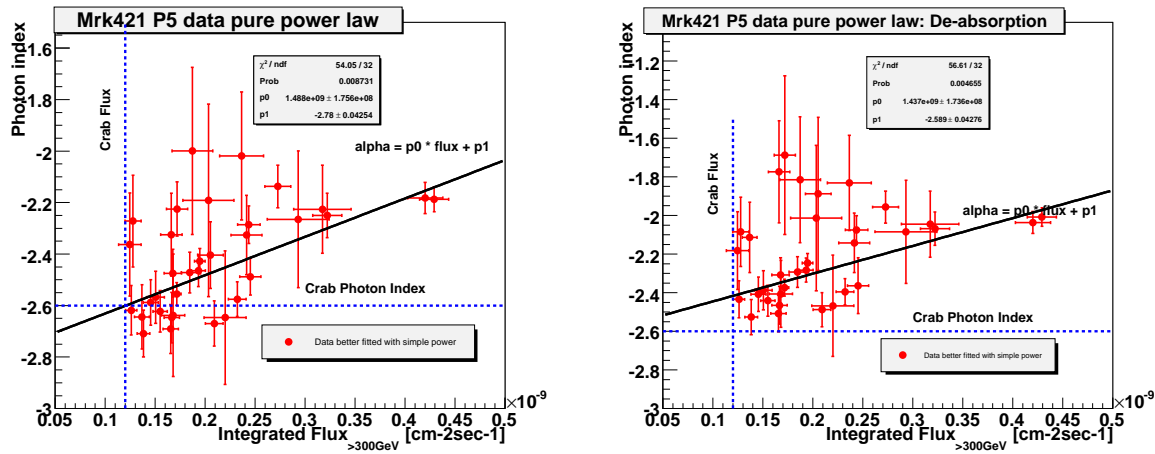


Figure 9.28: The fitted photon index of the spectra versus the integrated flux ( $>300\text{GeV}$ ) before and after EBL de-absorption and subsequent fitting with a simple power law.

## 9.6 Flare Analysis

Based on Fig. 9.4, we further looked into the nights which showed controllable background stabilities but large deviations from  $\chi^2/\text{d.o.f.}$  constant flux fitting. Table 9.3 shows the nights which gave indications of intra-night variability. We took the nights with an accidental probability smaller than 0.05 and 0.003, which is about 2 and 3  $\sigma$  significance, respectively. For higher accuracy, two different timing bins in the lightcurve were checked, namely 5 minutes and 10 minutes. In particular, the two highest states nights were selected, i.e. 6 February and 31 March.

### 9.6.1 6 February 2008

The night MJD = 54502 has an averaged flux ( $\geq 300$  GeV) of  $3.4 \times 10^{-10} \text{ cm}^{-2}\text{s}^{-1}$ . That night, MAGIC observed Mrk421 for about 3.8 hours. Fig. 9.29 shows the 8 minutes timing bins lightcurve with different energy thresholds. The plot shows the flux changes from a baseline of about  $2 \times 10^{-10} \text{ cm}^{-2}\text{s}^{-1}$  ( $\geq 400$  GeV) to  $3 \times 10^{-10} \text{ cm}^{-2}\text{s}^{-1}$  ( $\geq 400$  GeV) within half an hour.

The doubling time  $t_2$  could be calculated from the fluxes  $\phi_k$  as follows [174]:

$$t_2 = \tau_{kl} = \left| \frac{t_k - t_l}{\phi_k - \phi_l} \right| \frac{\phi_k + \phi_l}{2} \quad (9.2)$$

It defines each part of the flux measurements in the lightcurve. We could also define  $t_2$  to be the minimum value of  $\tau_{kl}$  or the average of the five smallest values of  $\tau_{kl}$ . In order to have more photon statistics, the flux values must fulfill the two following conditions: (i) Both fluxes  $\phi_k$  and  $\phi_l$  must be different from zero with a significance higher than  $3\sigma$ . (ii) The relative error on the flux difference  $|\phi_k - \phi_l|$  must be smaller than 30%. Timing properties from the flare could be derived.

We also applied a formula which was used in [10] for flare modeling.

$$F = F_{\text{baseline}} + \frac{a}{2^{\frac{t-t_0}{\tau_{\text{fall}}} + 2^{\frac{t-t_0}{\tau_{\text{rise}}}}}} \quad (9.3)$$

The parameters in this formula are: The flux baseline  $F_{\text{baseline}}$ , the rise and fall time  $\tau_{\text{fall}}$ ,  $\tau_{\text{rise}}$ . The flare maximum time  $t_0$  and the flare amplitude  $a$ . In formula 9.3, while the time  $t=t_0$ , the flux  $F$  has its maximum value  $F = F_{\text{baseline}} + a/2$ .  $\tau_{\text{fall}}$  and  $\tau_{\text{rise}}$  could be explained as doubling and half time respectively. The above flaring model is based on the assumption that the fast flares begin with a constant (or slowly increasing) flux.

In case of more than one flare occurring within one night, it is also possible to make a combined fit. A linear combination of the flares with the following formula is performed [10].

$$F = F_{\text{baseline}} + \frac{a_1}{2^{\frac{t-t_0}{\tau_{\text{fall}1}}} + 2^{\frac{t-t_0}{\tau_{\text{rise}1}}}} + \frac{a_2}{2^{\frac{t-t_2}{\tau_{\text{fall}2}}} + 2^{\frac{t-t_2}{\tau_{\text{rise}2}}}} \quad (9.4)$$

Fit	$t_0$	$\tau_{rise}$	$\tau_{fall}$	$\chi^2/\text{dof}$	Fit prob.
One flare	54502.108	$10.8 \pm 5.45$	$24.5 \pm 7.5$	28.05/22	0.1742
Two flares: 1	54502.09	$8.43 \pm 3$	$16 \pm 7$	5.95/12	0.9185
Two flares: 2	54502.125	$4.13 \pm 2$	$5.36 \pm 2$	5.01/7	0.6588

Table 9.5: Results on the fitting parameters in the night of 6 February 2008. The first row assumes that there was only one big flare in the plot. The second and third rows assume there were two flares in that particular night but with different rising and falling times.

If such consecutive flares occur in the same night, we fit the flares with different rising and falling times  $\tau_{rise_i}$  and  $\tau_{fall_i}$ . A combination fit of the flares occurring during the night of 6 February is shown in Fig. 9.30. The results of the different fitting parameters are written in Table 9.5. The doubling time from the fit is about 10 -15 minutes independent of being fitted with one or two flares.

Unfortunately, there was no simultaneous data available neither in X-ray (ASM or XRT) nor optical during these two high flux days. The short time variability and the exponential increase/decrease of the flux level from a blazar could be explained by the shock acceleration models. Short time variability and shock acceleration model will be discussed in more detail in the final chapter.

### Short Time Hardness Ratio

According to the shock model, the slope of the spectrum in the TeV regime depends on different stages of the flares. During the rising stage, the spectrum will be softer than during the decaying stage of the flare [175]. Therefore, the highest flux does not necessarily have the hardest spectrum. The hardness ratio versus time within the night 6 February is shown in Fig. 9.31. Historically, Whipple saw the delay between the peak of the flare and the hardness slope of the spectrum [176] within one day.

The flux versus hardness ratio is shown in Fig. 9.32. Since the error are big, it is difficult to tell whether the hardness changes with flux levels or not.

### 9.6.2 31 March 2008

The giant flare on 31 March has an integrated flux of appr. 4 C.U above 300 GeV. The total observation time during this night was about 2 hours. The integrated flux above 400 GeV, 300 GeV and 200 GeV with a control background plot are shown in Fig. 9.33. The mean flare flux is  $4.6 \times 10^{-10} \text{ cm}^{-2}\text{s}^{-1}$  ( $\geq 300 \text{ GeV}$ ) with about  $2\sigma$  away from fitting a constant value. The whole flare is fitted with the formula 9.3 and 9.4. The flare was fitted separately with two flares and a single one individually.

The plots in Fig. 9.34 show fitting with one big flare and two consecutive flares. All the fitting parameters are written in Table 9.6.

Fit	$t_0$	$\tau_{rise}$ (min)	$\tau_{fall}$ (min)	$\chi^2/\text{dof}$	Fit prob.
/One flare	54555.925	$24.72 \pm 14.4$	$60 \pm 215.$	8.56/10	0.5745
Two flare: 1	54555.89	$25.6 \pm 5.2$	$12.5 \pm 3.6$	2.23/5.	0.816
Two flare: 2	54555.925	$9.5 \pm 5.8$	$5.8 \pm 4.2$	1.837/4	0.767

Table 9.6: Results of the fitting parameters in the night of 31 March 2008. The first row assumes that there was only one big flare. The second and third rows assume that there were two flares in that particular night but with different rising and falling times.

### The Hardness Ratio

The hardness ratio as a function of time on this particular day can be seen from Fig. 9.35. The spectrum index looks almost static. The flux as a function of hardness ratio can be seen from Fig. 9.32. The spectrum index is also almost constant throughout the night.

### 9.6.3 15 January and 11 February 2008

The Mrk421 integrated flux above 300 GeV on 11 February was about  $3.2 \times 10^{-10} \text{ cm}^{-2} \text{s}^{-1}$ . There were two observational time slots in that night. The two time slots above 300 GeV show  $\chi^2/\text{d.o.f} \sim 2.4$ , slightly away from a constant value, see Fig. 9.36. From the MAGIC lightcurve, the flux seems to rise from the first observational slot to the second. But there was no observation between these slots and it is completely unknown what happened in between. However, there was an ASM observation between MJD=54506.99 and MJD=54507.21. The ASM data, though with big errors, shows a tendency of X-ray counts going up, the maximum X-ray count being located at MJD=54507.2047. If the good correlation between X/TeV flux also applied in this case, we have reasons to believe that the TeV flux was also rising. The situation on 15 January is the same as 11 February. There were two observation time slots and the duration between them was about 3.6 hours. The flux also shows a tendency of increasing with time, see Fig. 9.36. The average flux was lower than 11 February.

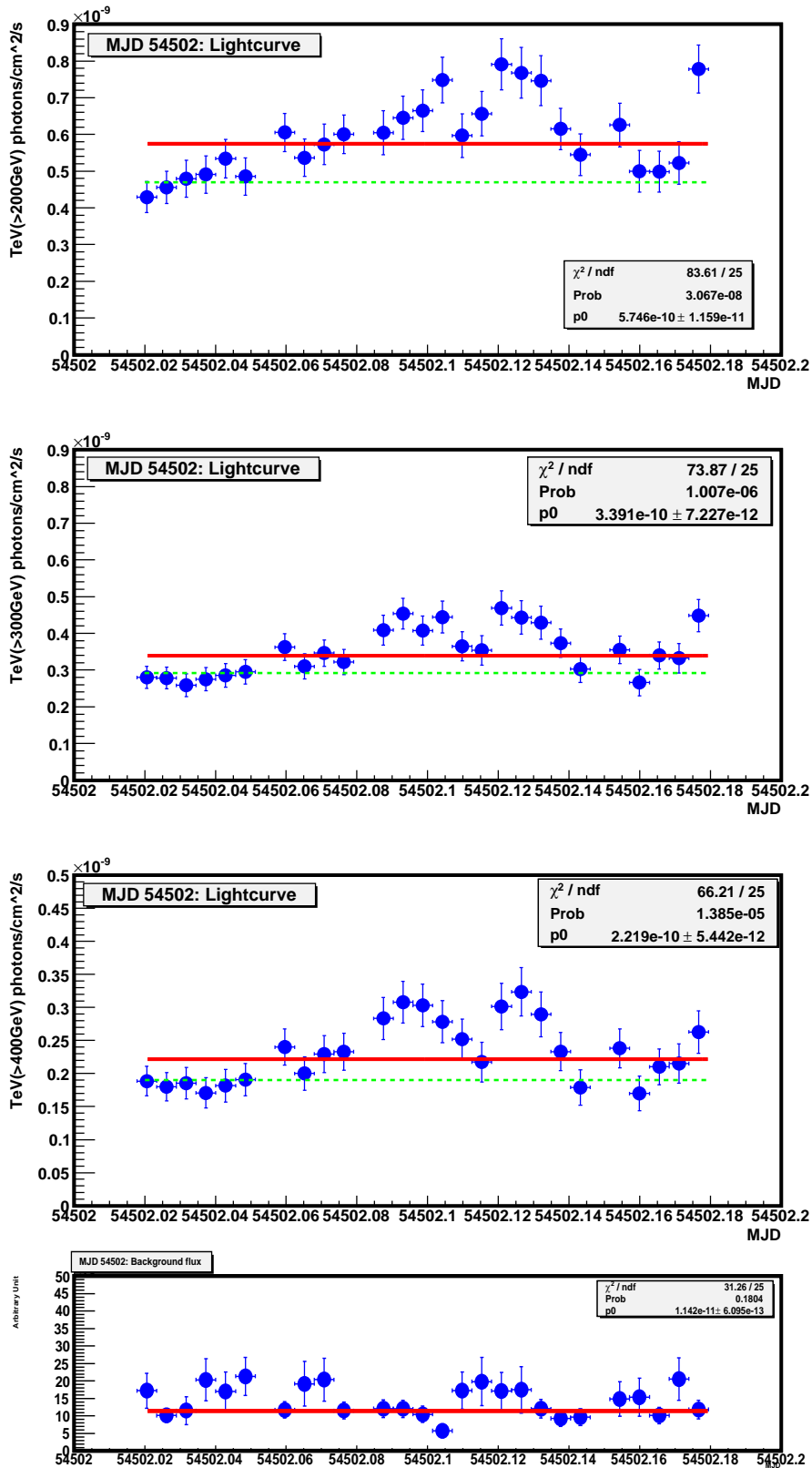


Figure 9.29: Mrk421 High Flux days in P5.

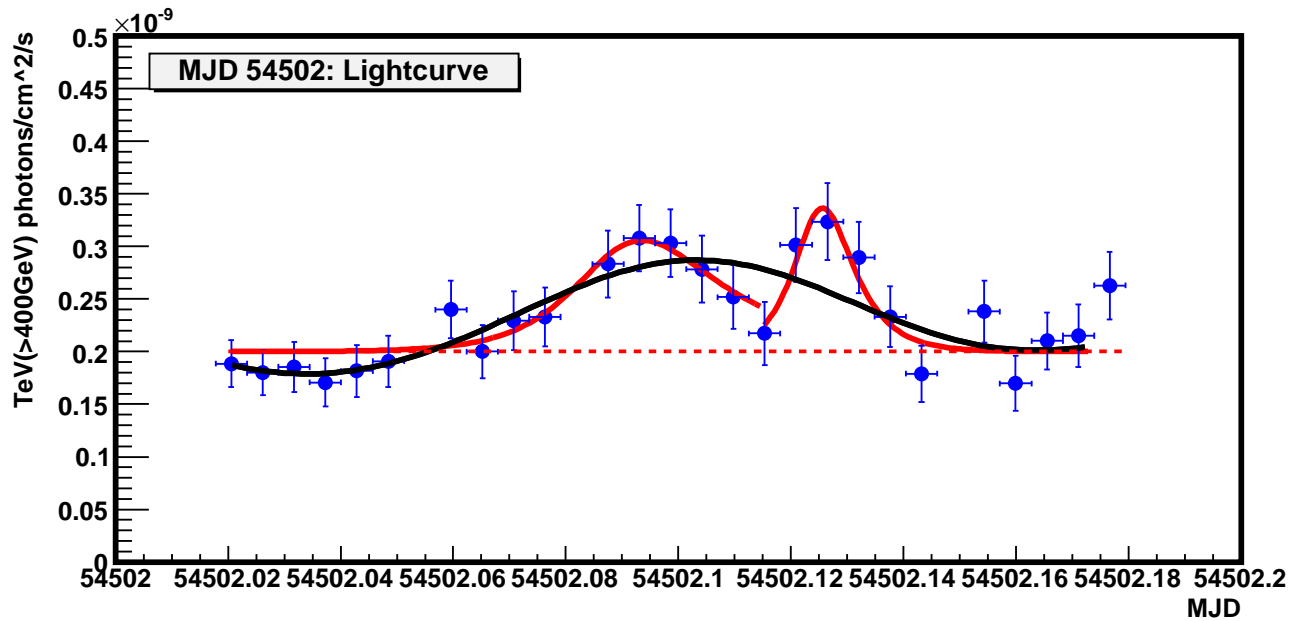


Figure 9.30: Flare fit in the night of 6 February. The lightcurve is above 400 GeV. The red curve shows the fitting with two flares, the black curve shows the fitting with only one giant flare.

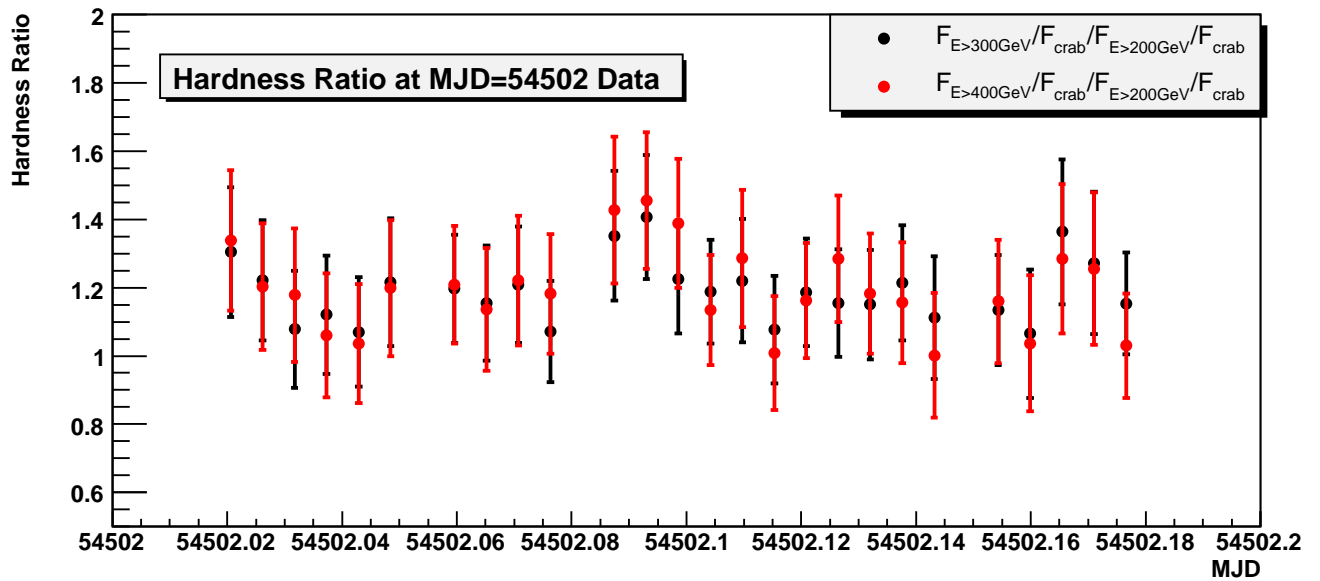


Figure 9.31: The hardness ratio of 2 different energy thresholds in the night of 6 February.

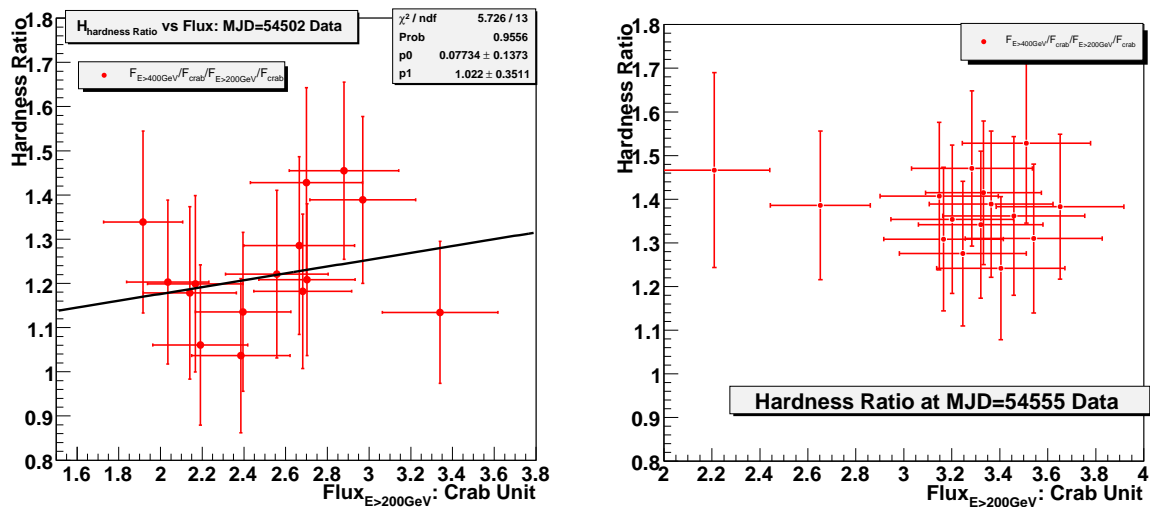


Figure 9.32: Left: The hardness ratio versus flux level in the 10 minutes timing bin in the night of 6 February. Right: The hardness versus flux level using 10 minutes timing bin on 31 March. The flux is above 200 GeV. From the plot, the hardness of the spectrum is almost constant throughout the night.

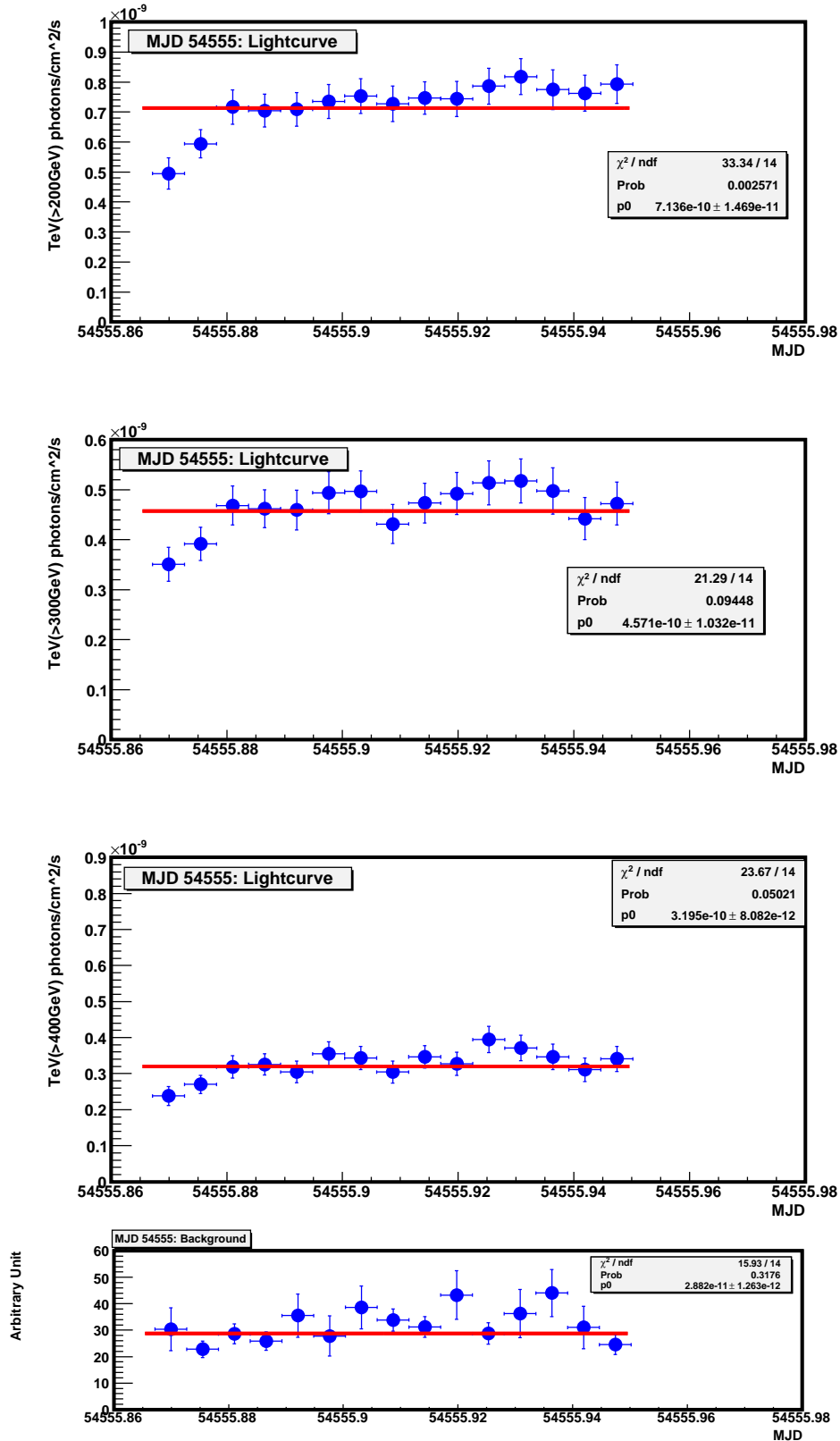


Figure 9.33: The 8 min lightcurve for Mrk421 on 31 March 2008. The lightcurves are above 200 GeV, 300GeV and 400 GeV.

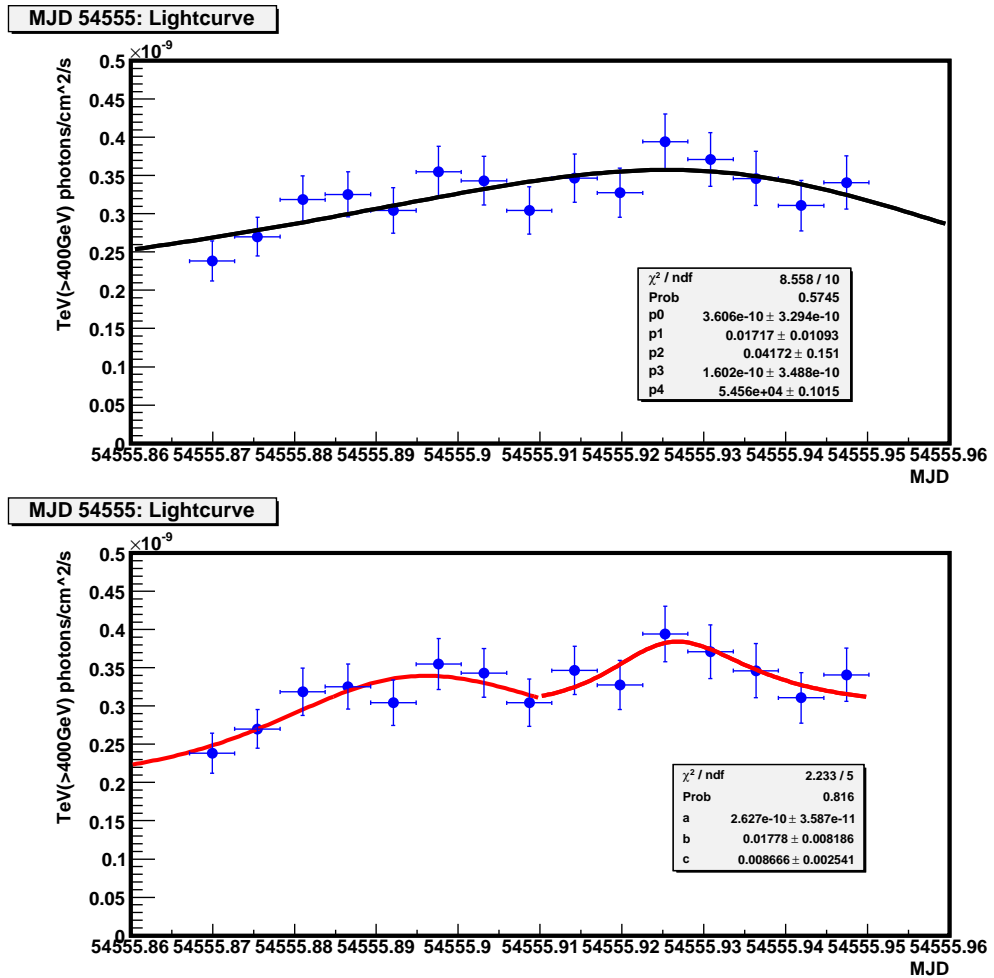


Figure 9.34: Lightcurve of 31 March fitted with different flare models. The upper one is fitted with a giant big flare. The bottom plot is fitted with two consecutive flares with different rising and falling times.

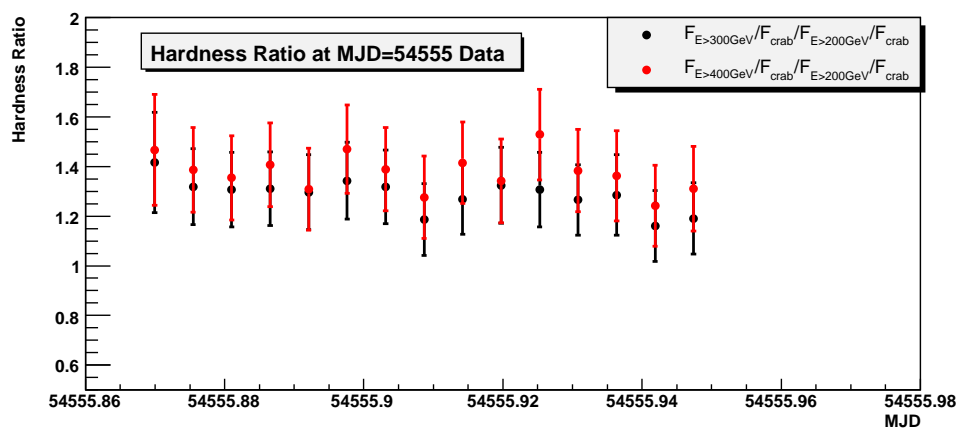


Figure 9.35: The flare analysis for Mrk421 on 31 March. The lightcurve is above 400 GeV.

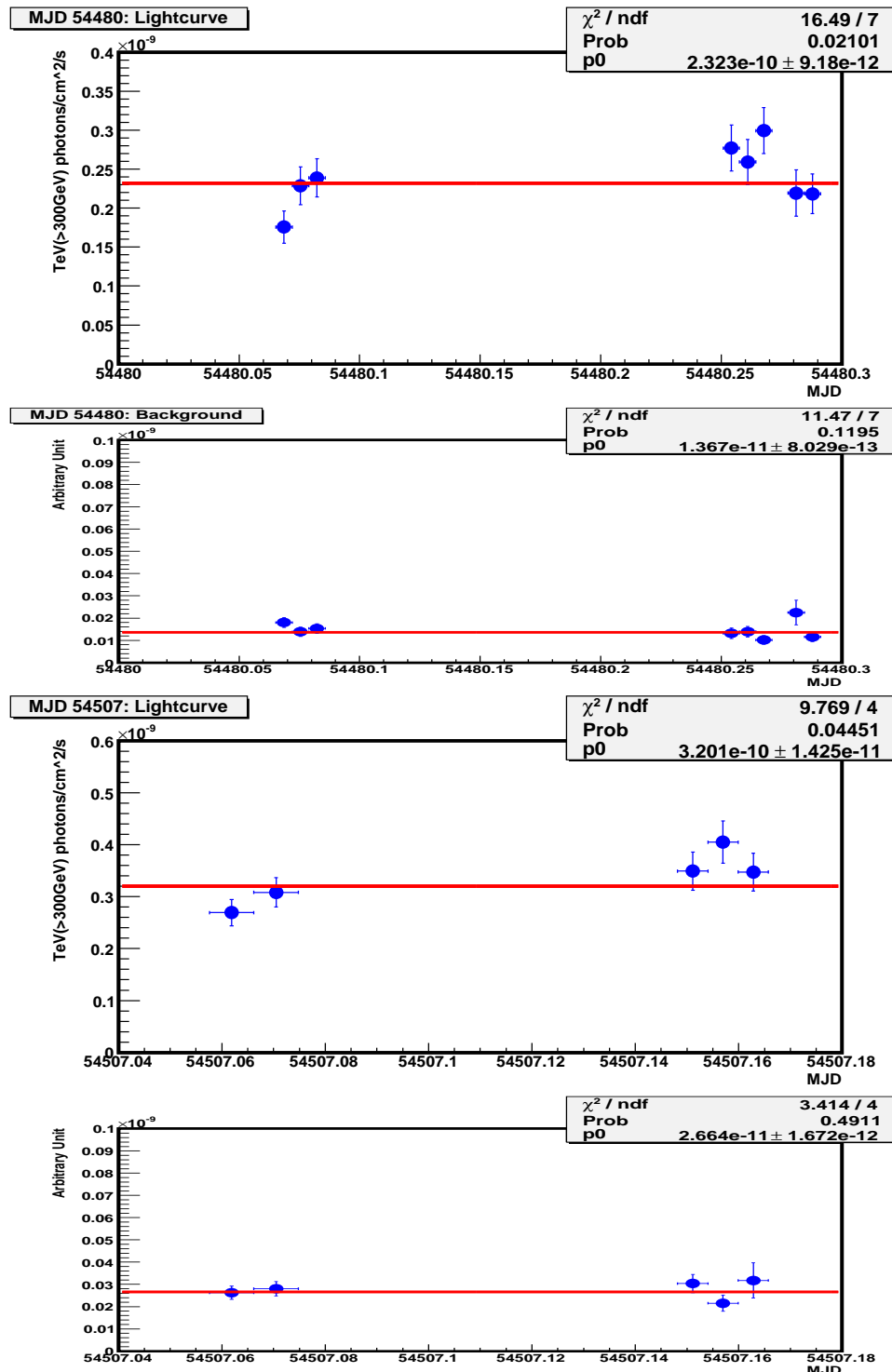


Figure 9.36: The upper two panels are the lightcurves of Mrk421 and the background control plot above 300 GeV on 15 January. The bottom two panels are the lightcurves and the background control plot above 300GeV on 11 February.

## 9.7 The Spectrum Study

### 9.7.1 Observed Spectrum Study

Mrk421 was very active in P5. In order to get higher photon statistics at higher energies, we grouped several different flux nights and unfolded the spectrum together. Before we combined the spectra, we checked different spectra in the same flux group making sure that they had similar spectra.

The spectra of Mrk421 at two highest flux nights with several other different flux nights are shown in Fig. 9.37. The plot is the measured spectrum without EBL de-absorption. The spectra from these nights are fitted with a pure exponential power law (PL) and a power law with an exponential cut-off (PL+Cutoff). The fitting results are listed in Table 9.7 and Table 9.8. We found that when the integrated flux is lower, the spectrum could be described either by PL or PL+Cutoff. However, when the integrated flux level is high, the spectrum is better described by PL+Cutoff. The flux levels which are higher than 2 Crab are already showing bad  $\chi^2/\text{dof}$  when fitted with PL. The cut-off energy of the high flux nights range from 1 - 6 TeV, consistent with historical values. For low flux nights, the cutoff energy has big errors, since in the high energy bins, the photon statistics are much lower than in the high flux nights.

Date	$f_0$	$\alpha$	r	$\chi^2/\text{dof}$
2008_02_06	$0.12 \pm 0.01$	$-2.51 \pm 0.04$	0.3	71.82/7
2008_03_31	$0.16 \pm 0.01$	$-2.16 \pm 0.03$	0.3	18.5/7
Very High State (3-4 C.U.)	$0.15 \pm 0.01$	$-2.18 \pm 0.04$	0.3	10.23/7
High B State (2.5-3 C.U.)	$0.12 \pm 0.01$	$-2.17 \pm 0.05$	0.3	11.52/7
High C State (2-2.5 C.U.)	$0.11 \pm 0.09$	$-2.39 \pm 0.04$	0.3	35.45/7
High State ( $\sim 2$ C.U.)	$0.89 \pm 0.03$	$-2.45 \pm 0.05$	0.3	64.31/6
Mid-High State (1.5-2 C.U.)	$0.80 \pm 0.23$	$-2.59 \pm 0.4$	0.3	3.04/7
Middle State (1-1.5 C.U.)	$0.63 \pm 0.06$	$-2.7 \pm 0.16$	0.3	6.25/6
Low State ( $\leq 1$ C.U.)	$0.45 \pm 0.09$	$-2.68 \pm 0.2$	0.3	4.12/5

Table 9.7: The spectra fitting for 9 different flux levels in period P5, using a pure power law. The fitting function has the formula :  $dF/dE = f_0 (E/r)^\alpha$ . r is chosen to be 0.3 TeV.  $f_0$  has the unit  $10^{-8} \text{ cm}^{-2} \text{s}^{-1} \text{TeV}^{-1}$ . Note that these spectra are the measured ones, i.e. before EBL de-absorption.

### 9.7.2 Intrinsic Energy Spectrum

The intrinsic spectra were obtained after EBL de-absorption. We used the Mazin and Raue 2007 model [173] for EBL de-absorption. Note that the effect of high energy photons turning reddish due to the expansion of the universe has been taken into account in the unfolding procedures. Since Mrk421 is a close-by source, the effect will not be very significant. The photon energy will be shifted towards the lower energy side by around 3% at the distance of Mrk421.

States	$f_0$	$\alpha$	r	$E_c$	$\chi^2/\text{dof}$
2008_02_06	$1.3 \pm 0.1$	$-1.51 \pm 0.16$	0.3	$1.26 \pm 0.29$	1.31/6
2008_03_31	$1.7 \pm 0.1$	$-1.92 \pm 0.1$	0.3	$4.24 \pm 1.62$	6.27/6
Very High State (3-4 C.U.)	$1.5 \pm 0.1$	$-2.08 \pm 0.12$	0.3	$11.18 \pm 12.85$	9.48/6
High B State (2.5-3 C.U.)	$1.2 \pm 0.1$	$-1.65 \pm 0.21$	0.3	$2.18 \pm 0.89$	3.69/6
High C State (2-2.5 C.U.)	$1.1 \pm 0.1$	$-2.01 \pm 0.11$	0.3	$2.65 \pm 0.72$	5.61/6
High State ( $\sim 2$ C.U.)	$0.96 \pm 0.03$	$-1.55 \pm 0.13$	0.3	$0.98 \pm 0.14$	6.97/6
Mid-High State (1.5-2 C.U.)	$0.80 \pm 0.03$	$-2.0 \pm 0.1$	0.3	$1.82 \pm 0.34$	8.27/6
Middle State (1-1.5 C.U.)	$0.69 \pm 0.06$	$-1.81 \pm 0.31$	0.3	$0.98 \pm 0.36$	8.79/5
Low State ( $\leq 1$ C.U.)	$0.75 \pm 0.63$	$-0.87 \pm 2.31$	0.3	$0.37 \pm 0.47$	4.23/3

Table 9.8: The spectra fitting for 9 different flux states in this period, using a power law plus exponential cutoff. The formula is  $dF/dE = f_0 (E/r)^\alpha \exp(-E/E_\alpha)$ . r is chosen to be fixed at 0.3 TeV.  $f_0$  has the unit  $10^{-8} \text{ cm}^{-2} \text{s}^{-1} \text{TeV}^{-1}$ . Note that this spectrum is the observed one, i.e. without EBL de-absorption.

The spectra with different states after EBL de-absorption are shown in Fig. 9.38. If we compare the cut-off energy between two nights, 6 February and 31 March, they have small differences. The difference in cut-off energy on different days could be due to the intrinsic effect, such as internal absorption. It is striking that the cut-off energy does not change if we consider the de-absorption of the EBL using Mazin and Raue 2007 [173] model, which strengthens, the cut-off behavior because of the intrinsic effect. In their model, approx. 50% of  $\gamma$ s are absorbed at 5 TeV at the distance of Mrk421. [144] has shown that both Mrk421 and Mrk501 have similar cut-off energy in their spectra, around 3 - 6 TeV.

State	$f_0$	$\alpha$	r	$\chi^2/\text{dof}$
2008_02_06	$1.2 \pm 0.01$	$-2.32 \pm 0.03$	0.3	72.7/7
2008_03_31	$1.6 \pm 0.01$	$-2.0 \pm 0.03$	0.3	14.75/7
Very High State (3-4 C.U.)	$1.6 \pm 0.1$	$-2.0 \pm 0.04$	0.3	12.08/7
High B State (2.5-3 C.U.)	$1.3 \pm 0.1$	$-1.99 \pm 0.05$	0.3	11.82/7
High C State (2-2.5 C.U.)	$1.1 \pm 0.09$	$-2.09 \pm 0.04$	0.3	19.32/6
High State ( $\sim 2$ C.U.)	$0.94 \pm 0.03$	$-2.30 \pm 0.03$	0.3	64.5/6
Mid-High State (1.5-2 C.U.)	$0.86 \pm 0.02$	$-2.4 \pm 0.03$	0.3	51.35/7
Middle State (1-1.5 C.U.)	$0.67 \pm 0.04$	$-2.52 \pm 0.06$	0.3	16.04/6
Low State ( $\leq 1$ C.U.)	$0.46 \pm 0.09$	$-2.43 \pm 0.23$	0.3	4.34/4

Table 9.9: The spectrum fitting for several different flux nights in this period, using a power law. The formula is  $dF/dE = f_0 (E/r)^\alpha$ . Note that this spectrum is after EBL de-absorption. The EBL de-absorption is adapted from Raue and Mazin 2007.

[h] States	$f_0$	$\alpha$	r	$E_c$	$\chi^2/\text{dof}$
2008_02_06	$1.4 \pm 0.1$	$-1.32 \pm 0.15$	0.3	$1.04 \pm 0.16$	1.39/6
2008_03_31	$1.8 \pm 0.1$	$-1.77 \pm 0.1$	0.3	$4.61 \pm 1.86$	7.28/6
Very High State (3-4 C.U.)	$1.6 \pm 0.1$	$-1.9 \pm 0.12$	0.3	$11.08 \pm 12.6$	9.17/6
High B State (2.5-3 C.U.)	$1.3 \pm 0.1$	$-1.65 \pm 0.18$	0.3	$2.94 \pm 1.41$	5.93/6
High C State (2-2.5 C.U.)	$1.1 \pm 0.1$	$-1.83 \pm 0.11$	0.3	$2.65 \pm 0.72$	5.71/6
High State ( $\sim 2$ C.U.)	$1.1 \pm 0.0$	$-1.67 \pm 0.1$	0.3	$1.31 \pm 0.2$	8.86/6
Mid-High State (1.5-2 C.U.)	$0.87 \pm 0.03$	$-1.88 \pm 0.09$	0.3	$1.99 \pm 0.38$	7.86/6
Middle State (1-1.5 C.U.)	$0.72 \pm 0.05$	$-1.88 \pm 0.23$	0.3	$1.4 \pm 0.52$	8.15/6
Low State ( $\leq 1$ C.U.)	$0.67 \pm 0.42$	$-1.34 \pm 1.56$	0.3	$0.6 \pm 0.88$	3.57/3

Table 9.10: The spectrum fitting for 9 different flux states in this period, using a power law plus exponential cutoff. The formula reads  $dF/dE = f_0 (E/r)^\alpha \exp(-E/E_\alpha)$ . Note that these spectra already contain the EBL de-absorption.

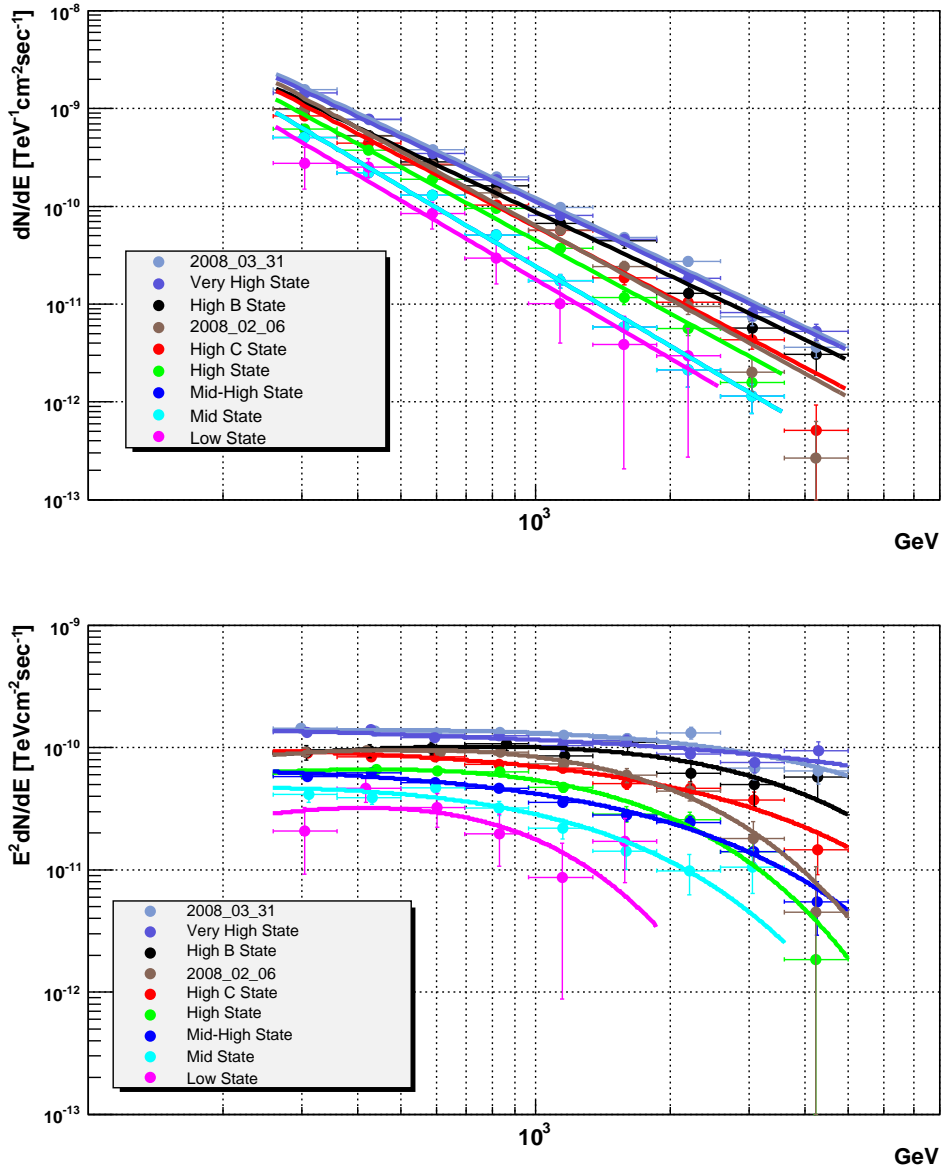


Figure 9.37: The spectra of Mrk421 at the two high flux nights with 7 other different flux states. The upper panel, the differential spectra are fitted with a pure power law, PL. In the lower panel, they are fitted with a power law plus exponential cutoff, PL+Cutoff. Note that the spectra here are without EBL de-absorption.

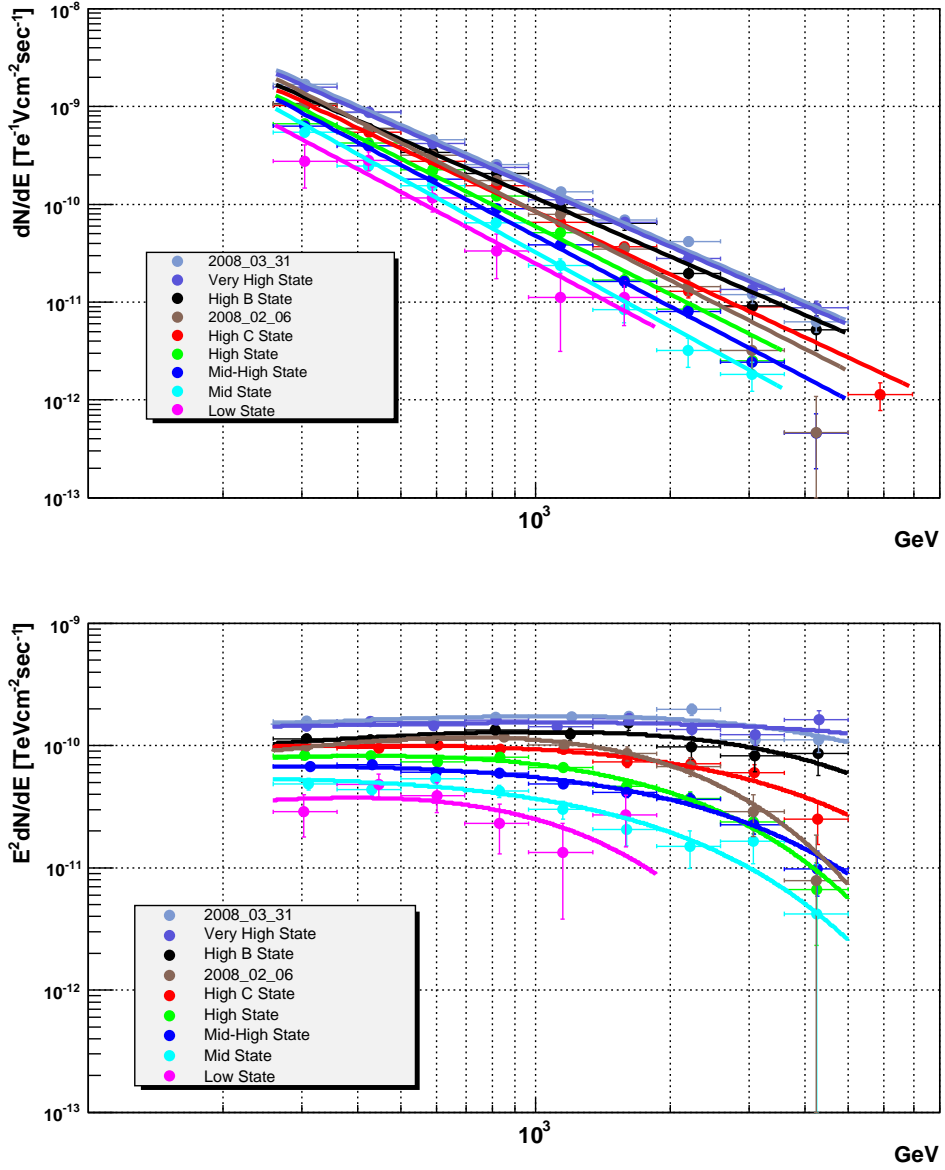


Figure 9.38: The spectrum of Mrk421 at two high flux nights with 7 other different flux states. In the upper panel, the differential spectra are fitted with a pure power law, PL. In the lower panel, they are fitted with a power law plus exponential cutoff (PL+Cutoff). Note that the spectra already contain the EBL de-absorption.

## 9.8 SED Modeling

Date	MAGIC Duration (min)	ZA	Swift-XRT Duration (min)	Overlap (min)
2008_01_08	44.6	31-41	34.	14.
2008_01_09	136.	6-20	34.	34.
2008_01_10	58.2	10-34	38.	19.
2008_01_16	109.	6-21	21.	20.
2008_01_17	57.3	6-20	14.	14.
2008_02_11	25.	10-18	33.	19.
2008_04_02	15.	17-22	15.	10.
2008_04_04	23	15-23	20.	19.

Table 9.11: The simultaneous data sets of MAGIC and Swift-XRT observations in P5 [21]. In total, there were 8 nights, 145 minutes of overlapping time slots.

Date	TeV Flux $cm^{-2}s^{-1}$ $[\times 10^{-10}]$ $E \geq 200 \text{ GeV}$	$f_0$ $cm^{-2}s^{-1}TeV^{-1}$ $[\times 10^{-10}]$ $E_0 = 0.3 \text{ TeV}$	a	b	$\chi^2/ndf$
2008_01_08	$2.13 \pm 0.2$	$5.9 \pm 0.7$	$-2.72 \pm 0.12$	-	2.5
2008_01_09	$2.61 \pm 0.11$	$6.3 \pm 0.3$	$-2.5 \pm 0.07$	$-0.44 \pm 0.15$	4.38/7
2008_01_10	$2.53 \pm 0.16$	$7.4 \pm 0.5$	$-2.42 \pm 0.08$	$-0.52 \pm 0.2$	7.55/6
2008_01_16	$4.42 \pm 0.14$	$10. \pm 1.$	$-2.25 \pm 0.07$	$-0.33 \pm 0.1$	2.01/6
2008_01_17	$3.8 \pm 0.19$	$9.8 \pm 1.2$	$-2.37 \pm 0.1$	$-0.57 \pm 0.18$	4.17/6
2008_02_11	$5.34 \pm 0.32$	$12 \pm 1.$	$-2.11 \pm 0.14$	$-0.44 \pm 0.24$	6.6/6
2008_04_02	$2.94 \pm 0.32$	$7.1 \pm 0.5$	$-2.44 \pm 0.16$	-	0.93/3
2008_04_04	$4.53 \pm 0.3$	$11 \pm 0.1$	$-2.35 \pm 0.1$	-	2.22/6

Table 9.12: The fitted spectra (without de-absorption) of the 8 overlapping days' observations. The spectra are all fitted with power law with variable power indexes, where power index  $\alpha = a + b * \log_{10}(E/r)$ . The table is from [21].

During P5, there were several multiwavelength campaigns performed by MAGIC together with other instruments. Since Mrk421 was very active at the beginning of 2008, Swift-XRT, Swift-UVOT and MAGIC scheduled joint observations in several time slots from January 2008 to April 2008. Each time slot was about 10 to 15 minutes. In total, there were 8 time slots, see Table 9.11. The TeV spectra for these 8 days are fitted by a power law with variable power indexes, where power index  $\alpha = a + b * \log_{10}(E/r)$  [177]. The parameters  $a, b$  are listed in

Table 9.12. According to the SSC model, the location of the IC peak of Mrk421 is expected to be in the VHE region. Therefore, the spectrum is estimated to be curved. A simple power law fit may not be appropriate. Usually functions like broken power laws or power laws with exponential cutoffs are applied for fitting. The spectra from MAGIC, XRT (0.2-10keV) together with RXTE ASM (2-12 keV) and KVA (R-band) provided physics inputs of SED modeling. If we tried to use a one zone homogeneous SSC model, the seven physics parameters described in Chapter 2 would be derived as listed in Table 9.13. Based on these multiwavelength data, the constraints on SSC physics parameters will be discussed in Chapter 10.

date	$\gamma_{min}$ [ $\times 10^3$ ]	$\gamma_b$ [ $\times 10^4$ ]	$\gamma_{max}$ [ $\times 10^6$ ]	$n_1$	$n_2$	B [ $\times 10^{-3}$ G]	K [ $\times 10^3 cm^{-3}$ ]	R [ $\times 10^{15} cm$ ]	$\delta$
2008_01_08	7.0	6.0	3.0	2.0	4.	50	1.7	9.	46
2008_01_09	10.	2.9	3.0	2.0	4.	43	3.7	5.	85
2008_01_10	6.0	5.7	3.0	2.0	4.	37	3.3	5.	70
2008_01_16	8.3	6.7	3.0	2.0	4.	25	4.0	5.	80
2008_01_17	10.0	6.0	0.7	2.0	4.2	37	2.6	7.2	60
2008_02_11	11.0	6.9	3.0	2.0	3.7	20	2.4	6.6	85
2008_04_02	8.0	3.2	1.0	2.0	3.5	50	5.9	3.9	70
2008_04_04	17.0	20.0	3.0	2.0	4.	40	2.0	8.5	40

Table 9.13: SED fit with a one zone SSC model in 8 nights of simultaneous observation performed by MAGIC and Swift-XRT in P5 [21]. The  $\gamma_{min}$ ,  $\gamma_{max}$  and  $\gamma_b$  are minimum, maximum and break energies of the electron spectrum.  $n_1$  and  $n_2$  are the two slopes of the electron energy spectrum. K is the electron density. B is the magnetic field, R is the size of the emission region and  $\delta$  is the Doppler factor. This table is from [21].

# Chapter 10

## Summary of Long Term Monitoring

The analysis results of MAGIC Mrk421 data taken from 2005 to 2008 have been described. The importance and success of the monitoring program have been demonstrated. In the final chapter, the physics interpretations and a summary of the results will be presented.

### 10.1 Long time Lightcurve

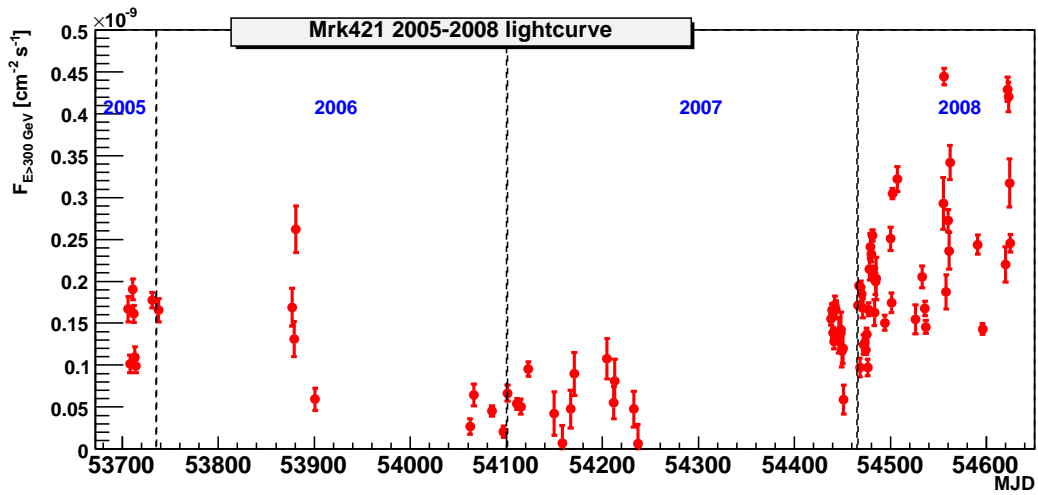


Figure 10.1: The MAGIC daily lightcurve of Mrk421 from 2005 to 2008. The threshold energy is above 300 GeV.

The MAGIC Mrk421 TeV daily lightcurve from 2005 to 2008, above 300GeV is shown in Fig. 10.1. In order to combine the MAGIC and Whipple/VERITAS preliminary ONLINE analysis results, the lightcurve with an energy threshold of 350 GeV is also shown in Fig. 10.2. The plots are crowded with data points at the beginning of 2008. Mrk421 was heavily sampled

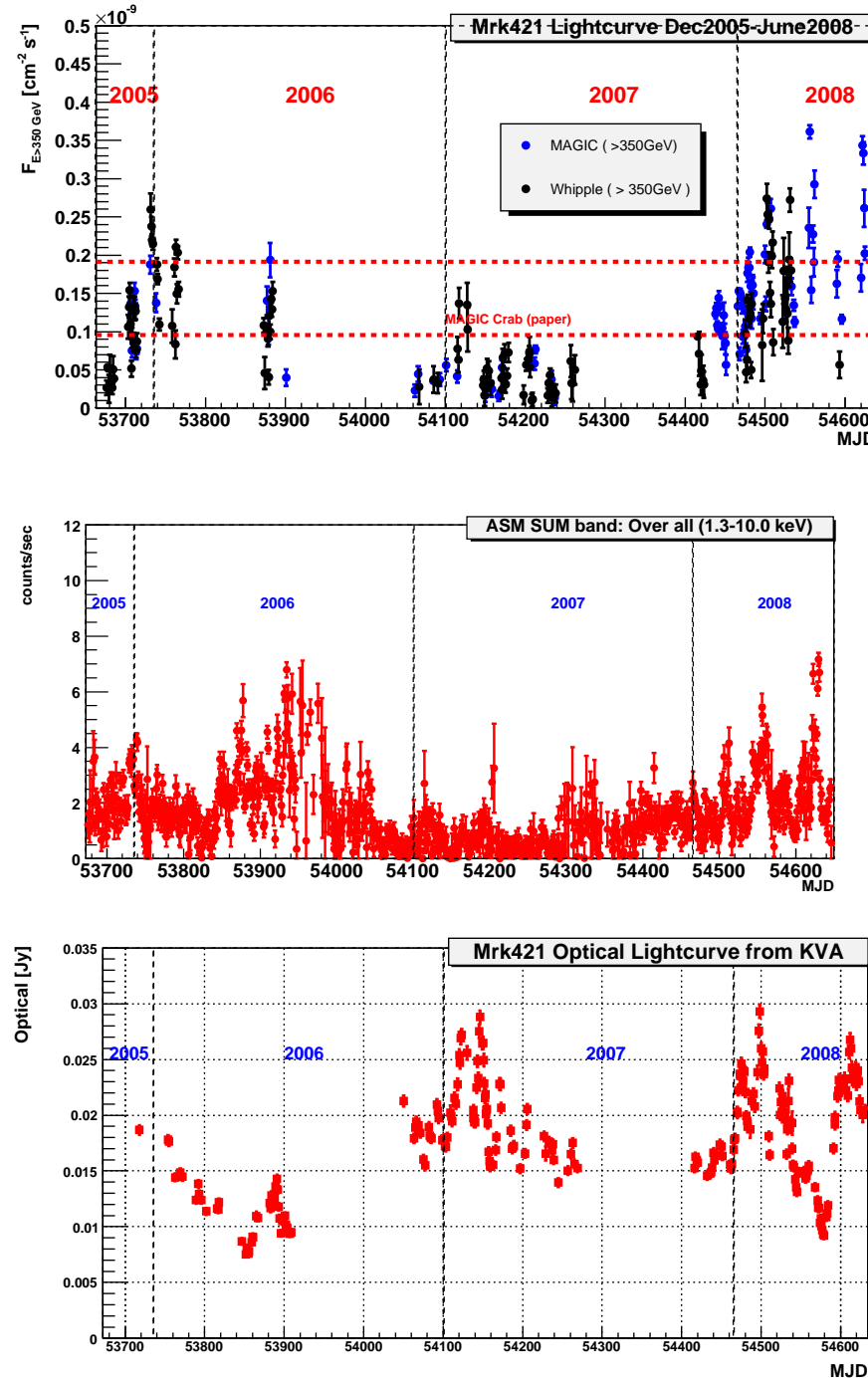


Figure 10.2: The Mrk421 daily lightcurves from 2005 to 2008 in different energy bands. The upper one : Daily integrated flux above 350 GeV. The black points are from the Whipple ON-LINE analysis and the blue points are from MAGIC. The middle: Daily average of ASM sum band data. The bottom: The KVA R band daily lightcurve. Note that the observations of the KVA telescope were almost overlapping with MAGIC.

by both telescopes. It was at high state  $\sim 2$  C.U. at the end of 2005, then faded away. The flux increased again around spring of 2006 and a multi-wavelength campaign was performed during the high state period [178]. In 2007, both MAGIC and VERITAS observed the source in rather low states. At the end of 2007, the  $\gamma$ -ray flux increased again and a few giant flares occurred in this period; the flux amounted to 4 C.U. The ASM X-ray data shows a similar behavior, see middle panel of Fig. 10.2. In 2006 and 2008, the X-ray lightcurves showed giant flares occasionally. However, throughout the year 2007, it was in relatively low states. The KVA R-band optical data in the bottom panel of Fig. 10.2 shows a quite different behavior compared with X-ray data in the middle of 2006 and beginning of 2007. Nevertheless, in 2008, a tendency of positive X-ray/optical correlation is seen. The multiwavelength correlations will be discussed further in later sections.

The long-time multiwavelength lightcurves from Mrk421 demonstrate variability, irregularity and unpredicted features. Several related questions are: What causes the variability ? Do all the variabilities in different energy bands have different origins ? Which part of the nuclei is emitting in various different energy bands ? One of the goals of this thesis is to identify and characterize the the observed variability and related physics processes. This will be discussed in the following section.

## 10.2 Variability

The origin of the blazar variability is not well understood. Usually, it has been described in terms of flares, each flare being thought of as a separate and independent event. It has been pointed out by [179] that there are two basic types of models which can explain intrinsic variability. The first assumes that the observed variations are related to changes in the geometry of emitting sources i.e. [180] [181]. The most common scenario explains the variability of the source as being due to blobs injected at the base of the jet. Such components move with finite angular momentum on a helical trajectory. The second kind of models assumes that variability is generated by changes of emission conditions inside the jet. Typical examples are the injection of fresh particles from the center of a source, or the acceleration of particles by a shock wave. The flares are attributed to shocks in the jet, and the shocked-jet models provide a good explanation of the main observational facts of large flux variations. They look for what is the source of the underlying variations driving the shock, which still remains as puzzle. Depending on the physical conditions, the variability could originate first from high energy bands (X-rays and gamma rays) and then spread out to the radio wavelengths. However, alternative cases are also observed, but only limited at low energies (optical to radio wavelengths) or at higher energies. The observed inter-bands time lags could give us hints. In Table 10.1, the established TeV AGNs show the variabilities in different time scales. The amplitudes of variability are also different. AGNs show their fastest variability in a regime down to a few minutes. However, some of them show variations in longer timescales of up to years. Note that AGNs which are not observed to be daily variable may not be intrinsically daily stable. The undetected variability could be due to the limited sensitivity of the current IACTs. Or it may be due to poor telescope samplings on these particular sources. In fact, the currently observed INV TeV AGNs are all strong sources

Source	Distance	TeV $\gamma$ Flux Var
Mrk421	0.031	Intra-night
M87	0.004	Intra-night
Mrk501	0.034	Intra-night
PKS2055-489	0.071	Year
RGB J0152+017	0.08	Month
PKS2155-304	0.116	Intra-night
H2356-309	0.165	Month
1ES1101-232	0.186	Year
1ES0347-121	0.188	Year
1ES2344-514	0.044	Month
H1426+428	0.129	Daily
PG 1553+113	$\geq 0.25$	Year
3C279	0.5	Day
1ES1959	0.04	Intra-night

Table 10.1: Different AGNs show different variabilities in different time scales.

and mostly the variabilities are observed during high states. This can be due to the observational biased.

The lightcurves of Mrk421 in different bands look completely random. They can be investigated further by their statistical properties. Spectral Power Density (power distribution in the frequency domain) is a useful tool. The spectral density could be classified by different power of the noises which are proportional to  $1/f^\alpha$ , where  $\alpha$  is an integer from -2 to 2.

- White noise:  $\alpha = 0$ . This signal produces a flat frequency spectrum. The signal has equal power in each frequency band.
- Pink (Flicker) noise:  $\alpha = 1$ . The frequency spectrum of pink noise is flat (equal power) in logarithmic space.
- Red (Brown noise):  $\alpha = 2$ . It can be generated by an algorithm which is similar to the Brownian motion or by integrating white noise.

Red noise usually refers to a power density which decreases by 6 dB per octave with increasing frequency (density proportional to  $1/f^2$ ). Compared with pink (flicker) noise, which has equal power in the logarithmic scale, the power drops faster at higher frequencies. This means that in a longer time scale (lower frequency), variability shows more strength. On the other hand, in shorter time scales (larger frequency), the variability remains smaller. The PSD of Mrk421 has been studied by ASCA X-ray observation, which has been mentioned in Chapter 9. In the TeV band, the poor sampling makes a direct PSD study difficult. However, the values of  $F_{ave}$ ,  $F_{pp}$  and Structure Function (SF) mentioned before give clues to PSD.

In general, we can classify AGN variabilities by three different time scales. Each variability could be introduced by the different physics mechanisms of the sources.

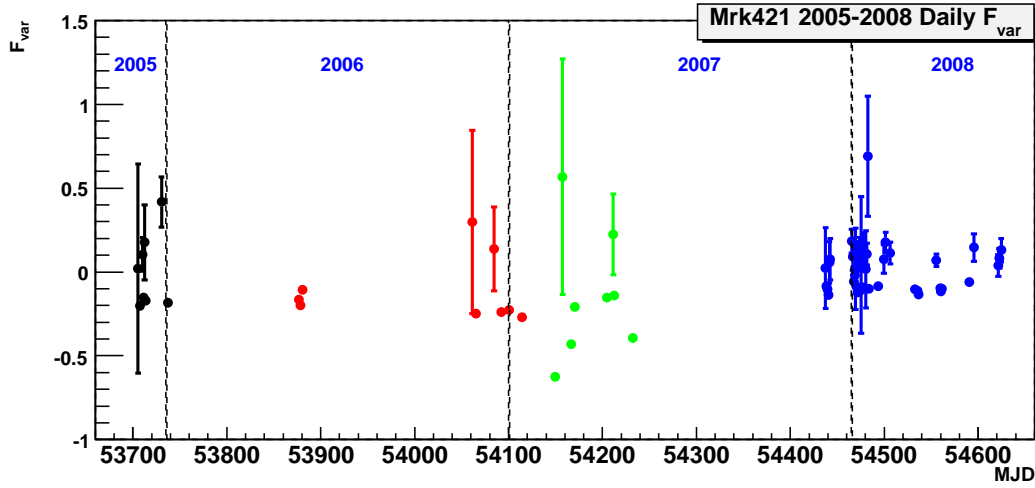


Figure 10.3: The daily variability  $F_{var}$  from 2005 to 2008, using 10 minutes flux bins.

- Intra-Night Variability (INV): From a few minutes to several hours within a day. INV is usually explained by the so-called "shock-in-jet model".
- Short term variability: From a few days to weeks. For example, Mrk501 was suspected to have a 23 days QPO behavior. The instabilities of the hot spots on the accretion disk can introduce such changes [182].
- Long term variability: From months to several years. One possibility could be attributed to the entire super massive binary black holes system, e.g., binary SMBHs.

The X-ray temporal analysis suggested that the X-ray emissions from TeV blazars indicate a strong red-noise, compared to a fractal, flickering-noise of Seyfert galaxies, see [161]. In [161], X-ray emissions from three TeV blazars, Mrk501, PKS2155-304 and Mrk421 were investigated. One striking feature in Fig. 9.18 is that all three TeV blazars show a slope  $\beta$  around 1.5 which is a bit steeper than pure red noise. [75] has pointed out that the TeV lightcurves from PKS 2155 have a power law Flourier spectrum  $P_\nu \propto \nu^{-2}$  which shows red noise behavior. Since normally TeV data are too sparse to be adequate for PSD analysis, it was suggested by [166] that the ratio between  $F_{var}$  and  $F_{pp}$  may imply the "color" of the noise. Fig. 10.5 shows the values of  $F_{var}$  and  $F_{pp}$  from MAGIC Mrk421 data in different time scales. Fig. 10.6 illustrates the ratio between these two values. We have found that the ratio is close to 2, if the time scale was longer than one to two months. If it is longer than 2 months, the ratio stays close to 2. In shorter time scales, say one day or one week,  $F_{var}$  fluctuates and  $F_{var}/F_{pp}$  ratios are usually smaller than 2. Sometimes,  $F_{var}$  is close to zero or even negative because of the flux being stable within such short periods.

The X-ray variabilities of some non-beamed systems like Seyfert galaxies and X-ray binaries were found to be remarkable. In those systems, few behaviors such as linear relation between

RMS variability and flux, the scaling of characteristic timescales with black hole mass and inversely with accretion rates have been found. All of these properties provide clues of the sources' variabilities. In addition, in these systems, we found that the variations in shorter timescales decrease in amplitude while the long timescale variations increase in amplitude. This could be a link between variations in different timescales. A model proposed by Lyubarskii [165] describes that the observed X-ray variations of a certain type of AGNs originate from the annulus in the accretion disc and propagate inwards, where they modulate the emission. The shorter wavelengths are damped as they travel inwards. Thus, we can easily associate smaller radii with shorter time scales of variabilities. The important aspect of this model is that the source of the variations is separated from the source of X-ray emission, because the variations of the flux are caused by the modulation of the variations in the disc traveling inwards and hitting the X-ray emission regions. In the TeV regime, if there is red-noise behavior, the origin of the associated underlying physics process is still unknown.

Another question is: Does the variability of the AGN depend on the flux states ? In other words, is Mrk421 more variable while at higher states ? So far, we have observed strong TeV flares from blazars only in their high states. To test this, Quinn et al [183] used Whipple Mrk501 data in 1997 when there was a short time flare as a testing sample. The purpose was to try to see if the daily scale Mrk501 variability observed during 1997 big flares would have been detected in 1996 and/or 1995 while the flux states were lower. Moreover, they wanted to test if the monthly scale variability seen in 1996 and 1997 would have been detected in 1995 while the source was in low state. They calculated the percentage deviations about the mean level from a period where significant variability was observed and then, using the mean signal and background level from another period. Subsequently, they calculated the signal and statistical error that would have been observed given the same percentage deviations of that mean. They found that neither the 1997 month-scale nor day-scale variability would have been detected at a significant level if it had been present in 1995, while the 1997 day-scale variability would have been detected if it had occurred in 1996. Hence, the conclusion is that there was a change in the flare characteristics, in addition to the change in the mean flux levels between the two different observation seasons [183].

Fig. 10.5 shows  $F_{var}$  values at different mean flux levels in different time periods. If the flux is high enough ( $\geq 1$  C.U.),  $F_{var}$  seems to be independent of the flux level, close to 0.4. We fit the plot 10.6 with Gaussian, excluding far isolated points and took the  $\sigma$  of the Gaussian from the fit. Defining the value  $r = F_{var}/F_{pp}$ , we found that  $r$  was very close to 2 (red noise-like) while the timescale is longer. Fig. 10.7 shows value  $r$  in four different timescales. We fit the plot with a constant function and a power law respectively. The power law fit gave us a power law index of  $-0.192 \pm 0.2$ . Obviously, it is not easy to draw any conclusion with the current dataset. However, hints of red noise behavior are not negligible. Hopefully, future high quality and dense sampling data will resolve this issue.

### 10.2.1 Short Time Variability

There are several models which explain the intra-night variability in blazars, such as shock-in-jet models, accretion-disk based models and plasma-process related models. They can explain INV over an extended range of wavelengths (Wagner & Witzel 1995 [184]; Urry & Padovani

1995 [19] and references therein). Very short time variabilities in the TeV regime, like the one of Mrk421 in 1996, which was shorter than 15 minutes, could be explained by varying dimensions of the emission regions of the jets and by different Doppler factors due to varying bulk jet Lorentz factors. From the causality argument, the size of the emission region  $R$  is calculated by  $R \leq ct_{var}\delta/(1+z)$ . The jet dimension is also strongly constrained by the transparency or the photon photon opacity condition. Because the size of the emission region cannot be infinitesimally small, the only possibility is to increase the Doppler factor. Furthermore, the TeV photons escaping the production regions implies that the emitting plasma moves with high bulk velocity. Therefore, these TeV photons could avoid pair creation through interacting with the soft radiation fields. However, it is important to point out that from VLBI radio observation, the jets of a few TeV blazars, like PKS 2155-304, Mrk501, Mrk421, have been resolved on sub-pc scales and show patterns with the Lorentz factor  $\Gamma$  about 10 or even smaller [185]. This contradictions can be removed if we consider the jet being efficiently decelerated on sub-pc scales [186] after the TeV emission has taken place. Another alternative is that we consider a structured jet with a faster core that could produce TeV  $\gamma$ -rays and slower outer parts that dominate the radio emission [187]. In order to explain the short time variability of the VHE  $\gamma$  emission, the so-called shock-in-jet models [188] [189] have provided natural explanations. The models introduce moving "laminar" shock fronts inside the jets instead of spherical emission regions. The typical laminar dimension is about  $10^{14}\text{m} \sim 0.01\text{pc}$  and the thickness  $\sim 5 \times 10^{-5}\text{pc}$ . Models for the production of non-thermal flares in blazars as well as GRBs often involve collisions between shells containing relatively cold matter, propagating down the jet with different velocities. The shell inhomogeneities can result from the modulation of the relativistic outflow by a central engine. Adopting this model, the non-thermal flares, produced by relativistic particles accelerated in the shocks excited by colliding shells, must be preceded by soft X-ray flares, which are produced by Comptonization of external radiation by the material in the cold shells before collision. This external radiation is, in fact, the same source which provides the "seed" photons for producing the  $\gamma$ -rays. We know that the SSC model originally was applied to the non-thermal emission of frequencies up to X-rays [190]. The short time variability is predicted in this model and it does not originate from a non-steady electron distribution but from changes of the parameters of the source when it moves through the jet [191]. While flaring, the hot electrons may not have enough time to reach a steady state because the scale of the cooling time is longer than the flare. Thus, the time evolution of the electron spectrum has to be considered.

Another issue is the place where these TeV  $\gamma$ -rays are produced. Conventionally, people assume that the variability is introduced by the center of the black hole, the crossing time of the event horizon is about the scale of  $GM/c^3$ , which is  $\sim 1.4m_9$  hours, where  $m_9 = M/10^9M_\odot$ . If a disturbance is created near the black hole, it could travel outward with a high Lorentz factor  $\Gamma$ , before radiating energy at a distance  $\geq \Gamma^2r_g$ . According to this picture, if we assume  $\Gamma \sim 10$ , the gamma rays are produced with about  $(10^2 - 10^4)r_g$ . This is exactly the region where the production of the radio emission is believed to take place. Furthermore, putting the gamma emission region far away from the center also avoids the problem of how the high energy  $\gamma$ s escape without producing pairs on the soft photon background [192].

However, the discovered short time variability of Mrk501, PKS2155 and Mrk421 challenged the above theory. The masses of the black holes of the mentioned AGNs are around  $10^8 - 10^9M_\odot$ .

Even if the disturbance is produced at the center of the BH, the shortest time scale is about 0.14 - 1.4 hour. The observed time scale is one or two orders of magnitude shorter than that. Thus, the TeV results indicate that the observed variability is imprinted either by a small fraction of the black hole's horizon or by a small-scale fluctuation intrinsic to the jet itself.

There is growing evidence from VLBA studies, for example [193] for Mrk501, [123] and [194] for Mrk421, of the jets, at parsec-scale, moving more slowly than expected. The largest superluminal velocity recorded for TeV blazars is about  $4c$ , measured in PKS2155-304. The small velocities could be interpreted as being due to the close alignment of the jet with the line of sight ( $\leq 1^\circ$ ). However, this assumption is in contrast to the typical angles needed by unification models. The reason is that the number of the parent FR I sources will become very large, if the orientation of each AGN is assumed to be random. But the short time variabilities from the TeV observations down to ten or a few minutes level, need rather large Doppler factors ( $\geq 50$ -100) such that the TeV photons could overcome the internal absorption. From the above observational evidences and considerations, we conclude that the jet must suffer deceleration from the sub parsec to the parsec scale. A large portion of the power transported by the jet should then be dissipated and probably radiated during the deceleration [195].

Georganopoulos and Kazanas (2003) [186] argued that the radiation from the outer slowing down part of the jet can provide a supplementary soft photon field for IC scattering by the electrons in the inner fast jet. Another scenario is proposed by [187]. The jets are constructed assuming that the slowing down portion of the jet is an external layer, because of deceleration caused by the interaction with the external medium. The radiation produced in the layer that can be a site for particle acceleration enters into a fast spine and is used to produce VHE photons through IC scattering. This idea originates from studying the the jet in low-power FR I radio-galaxies. There are indications that the jets are composed of a fast moving internal spine and a slow-moving outer layer. For example, the radio study of Mrk501 [193] shows such a structure, visible as a limb-brightened structure of the jet. Two nearby TeV radio-galaxies, Cen A and M87 provide a good environments for testing the model. The spine model has successfully explained M87 flare in February 2008 [187].

The discovery of VHE  $\gamma$ -ray emission from M87 established radio galaxies as a new class of TeV sources. The observation of the daily scale of the flux variability excludes the extended jet or kpc or Mpc scale radio lobes as the gamma ray emission region. It implies a compact emission region with a size comparable to the radius of the SMBH at the very center of M87, either the nucleus or the knot HST-1 in the inner jet. The joint observation of M87 in 2009 by H.E.S.S/MAGIC/VERITAS and VLBI has revealed [196] that a period of extremely strong VHE  $\gamma$ -ray flares was accompanied by a strong increase of the radio flux from its nucleus. These results indicate that charged particles are accelerated to very high energies in the immediate vicinity of the black hole.

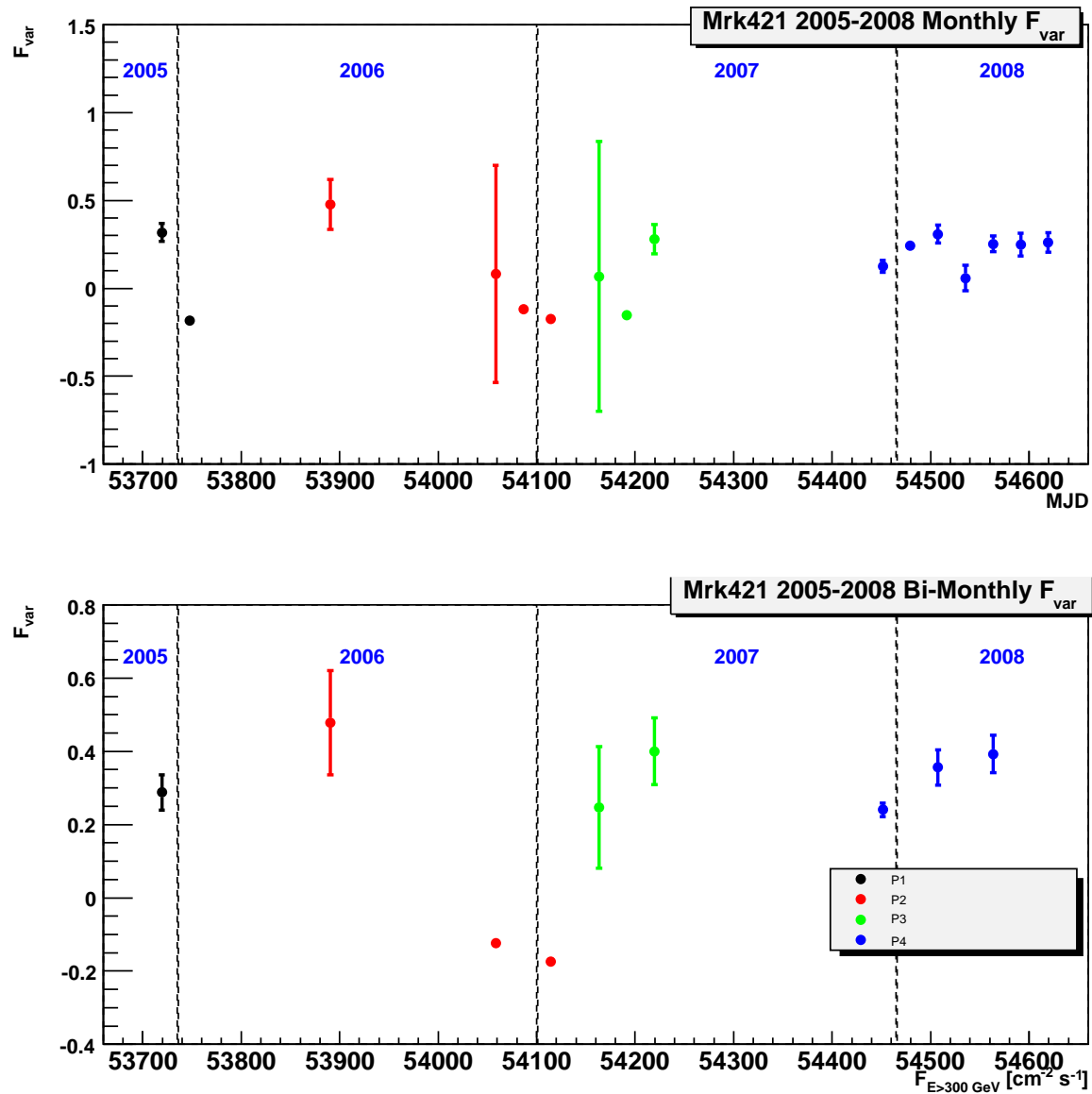


Figure 10.4: The monthly and bi-monthly variability  $F_{var}$  from 2005 to 2008, using 10 minutes flux bins.

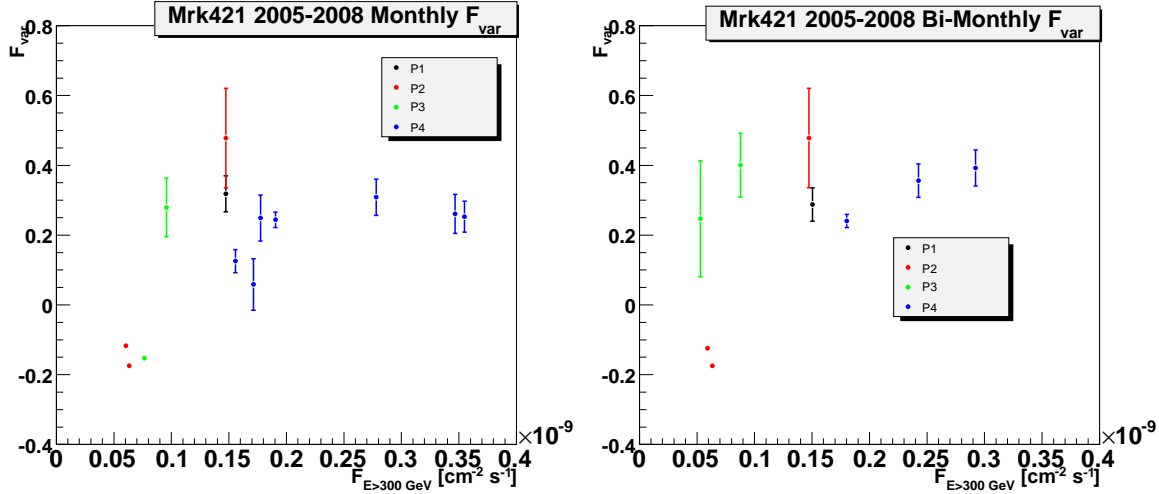


Figure 10.5: The monthly and bi-monthly variability  $F_{var}$  versus monthly and bi-monthly average integrated flux from 2005 to 2008, using 10 minutes flux bins.

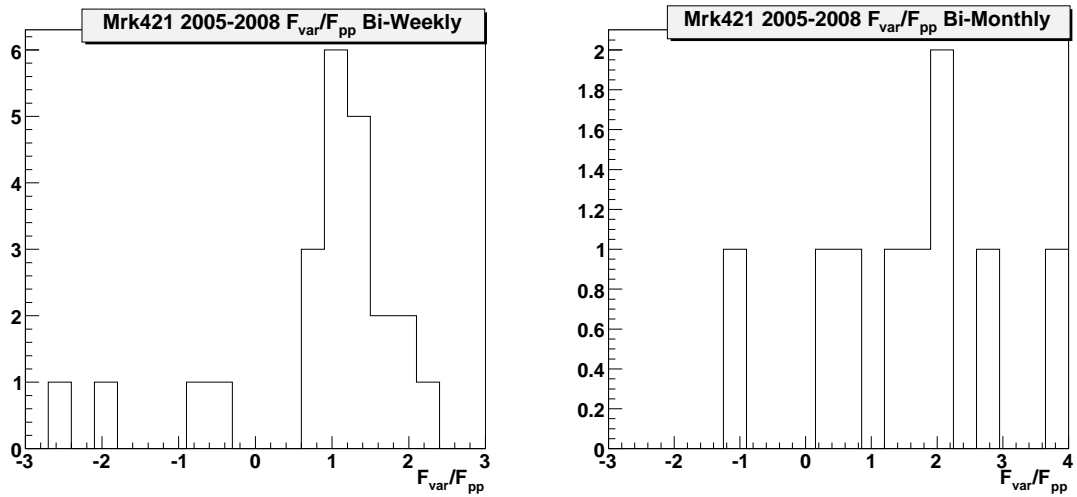


Figure 10.6: The bi-weekly and bi-monthly ratio of the values  $F_{var}$  and  $F_{pp}$ . If the timescale is longer, the ratio between these two values becomes larger. The emission is more red-noise like.

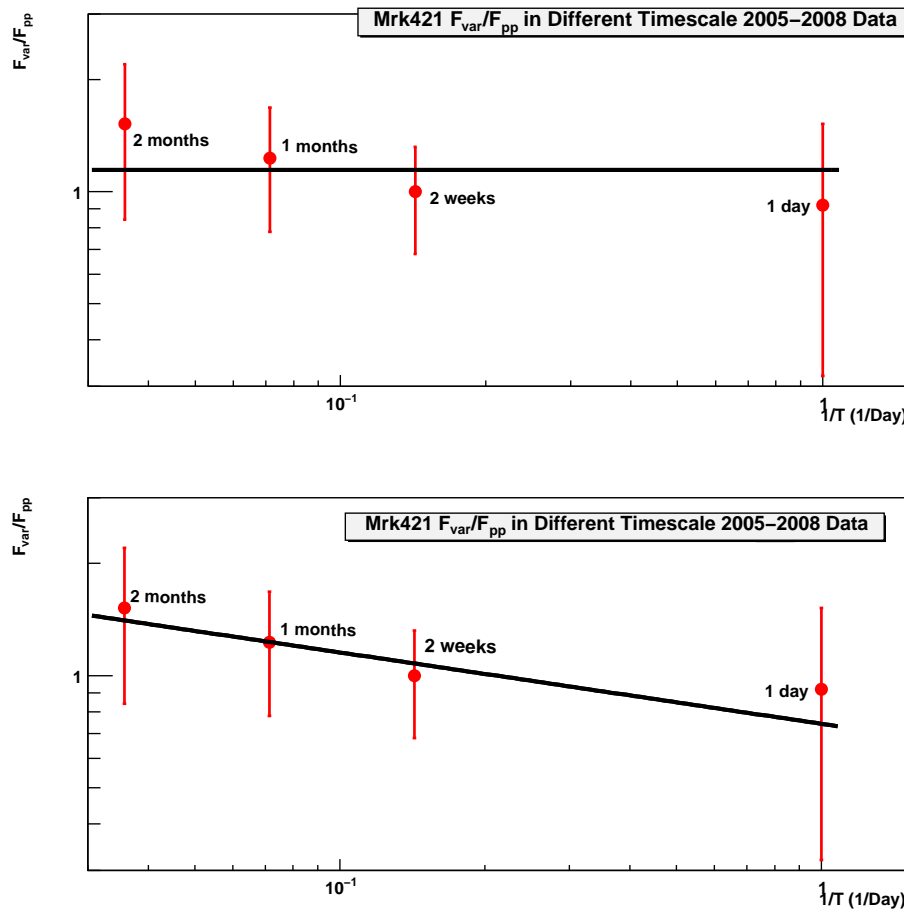


Figure 10.7: The values of the ratio  $r = F_{var}/F_{pp}$  in 4 different timescales, daily, weekly, monthly and bi-monthly. The value  $r$  in each timescale is derived from being fitted with a Gaussian distribution and  $\sigma$  is considered to be the error. If the timescale is longer, the ratio between these two values becomes close to 2, meaning it is more red-noise like.

## 10.3 Search for Time Lag

Time lags in different energy bands resolve the timescales of particle acceleration and cooling. Flares showing hard (higher energy photons lag) and soft (lower energy photons lag) lags have been observed in the X-ray regime [197] [198]. On the other hand, in the  $\gamma$ -ray regime, only a hard lag has been observed in the Mrk501 2005 flare [74]. Inter-band time lags between X-ray and TeV  $\gamma$  have been proposed, but not fully proved. [199].

In general, the soft lags could be interpreted as being caused by electron cooling. When electrons are accelerated rapidly to their maximum energy, because higher energy electrons cool faster than lower energy ones, they will produce variations in hard photons and then variations in softer ones. On the other hand, the explanation of the hard lags is related to particle acceleration or other exotic mechanisms, like the quantum gravity effect [74]. If the time scale for particle cooling is longer than the acceleration, then the radiation from the particle accelerating from low to high energies will show a hard lag. However, in this scenario, since the electrons do not have sufficient time to cool down before reaching their maximum energy, the total amount of produced radiation is small. Thus, hard lags will be more evident close to the spectral cutoff, where the radiative loss timescale is comparable with that of the acceleration timescale [200].

Generally speaking, three different timescales are considered to play important roles: the cooling timescale  $t_{cool}$ , the acceleration timescale  $t_{acc}$  in the observer frame as a function of the photon energy  $E$  and the last one, flare variability duration  $t_{var}$ . Below, We followed the discussion in [172]:

- $t_{var} \gg t_{cool} \gg t_{acc}$ : The observed spectra are expected to be stable during the flare. Only the flux changes during the flare.
- $t_{cool} \gg t_{var} \gg t_{acc}$ : In this case, the acceleration time could be considered as instantaneous. Since the cooling time decreases with energy, the highest energy particles cool faster, thus a "soft lag" is expected.
- $t_{cool} \gg t_{acc} \gg t_{var}$ : In this case, the flare may show as asymmetric in time. The reason is that a group of particles are picked up by the shock and then boosted to higher energies immediately. Then, high energy particles leak into the cooling region and the flux emitted at lower frequencies starts to fall.
- $t_{cool} \sim t_{acc} \sim t_{var}$ : The observed energy band is close to the synchrotron peak, where  $t_{cool}$  is comparable to  $t_{acc}$ . Usually, it happens when the occurrence of a flare propagating from lower to higher energy, like the particles are gradually accelerated into the radiation [170]. Such case is not very common, but have been observed with PKS 2155-034 in the X-ray band [201].

Following the treatment of Zhang et al. [166], the cooling timescale  $t_{cool}$  and the acceleration timescale  $t_{acc}$  in the observer frame could be written as a function of the photon energy  $E$ :

$$t_{cool}(E) \propto (1+z)^{1/2} B^{-3/2} \delta^{-1/2} E^{-1/2} \quad (10.1)$$

$$t_{acc}(E) \propto (1+z)^{3/2} B^{-3/2} \delta^{-3/2} E^{1/2} \xi \quad (10.2)$$

$$t_{cool}/t_{acc} \propto (1+z)^{-1} \delta E^{-1} \xi^{-1} \quad (10.3)$$

where the  $z$  is the red shift of the source,  $B$  is the magnetic field in Gauss,  $\delta$  is the Doppler factor of the emitting region and  $\xi$  is the parameter indicating the acceleration rate of the electrons [202]. It is known that the more energetic particles cool faster but accelerate slower than lower energy particles. If the acceleration process is short, such as with an instantaneous injection of electrons, the cooling will dominate the variability and a soft lag is expected. If the acceleration is slower and comparable with the cooling time scale, it takes longer for higher energy electrons to accelerate to high radiative energy, thus the acceleration dominates the process and a hard lag is expected. It should be noted that the ratio between  $t_{cool}$  and  $t_{acc}$  is independent of  $B$ . If we know the ratio of these two time scales at one particular energy (for example, at synchrotron peak energy, the ratio is close to 1), then the values of  $B$ ,  $\xi$  and  $\delta$  can be determined.

Another important timescale is the light crossing time of the emitting region  $t_{esc}$ . Ghisellini et al. [203] suggested that the synchrotron peak of HBL is produced by particles with a cooling time  $t_{cool} = t_{acc} \sim t_{esc}$ ;  $t_{acc}$  is the particle injection/acceleration timescale. In an internal shock scenario  $t_{acc}$  is similar to  $t_{esc}$ .

Takahashi [204] reported "hard" and "soft" lags from the X-ray lightcurves of some HBLs. A possible explanation of this effect in terms of competing acceleration, radiative cooling, and escape timescales of synchrotron emitting electrons [170], requires that all these timescales be comparable with the light crossing time. From this argument, the electrons must produce synchrotron photons in a weak magnetic field region ( $B \sim 0.1$  G). With this argument, the hypothesis of a proton-synchrotron origin of TeV radiation implies that the production region of TeV  $\gamma$ -rays ( $B \sim 100$  G) is different from the synchrotron X-rays ( $B \sim 0.1$  G).

Nevertheless, to associate a TeV flare with a X-ray flare with a certain time lag is not an easy task. It was mentioned in Chapter 7 that Whipple observed a TeV flare lags to X-ray flare in their Mrk421 2003 data. Whether it was a true time lag or an independent event (like a TeV orphan flare) is still being debated. We have checked the time lag between X-ray and TeV emissions of Mrk421 P5 data by using a correlation function described in Chapter 7. The correlation coefficient has a maximum significance around zero. We concluded that beyond 6 hours, no significant time lag between ASM and MAGIC P5 data is seen.

## 10.4 Multiwavelength Correlation

### 10.4.1 X/TeV correlation

The TeV flux  $F_\gamma$  and X-ray flux  $F_X$  could be modeled by the following relations

$$F_\gamma \propto F_X^\alpha \quad (10.4)$$

The power  $\alpha$  usually ranges from 0 to 3, depending on different physics conditions and models. If  $\alpha$  equals 2, it is SSC flare in the Thompson regime. In SSC, only synchrotron photons

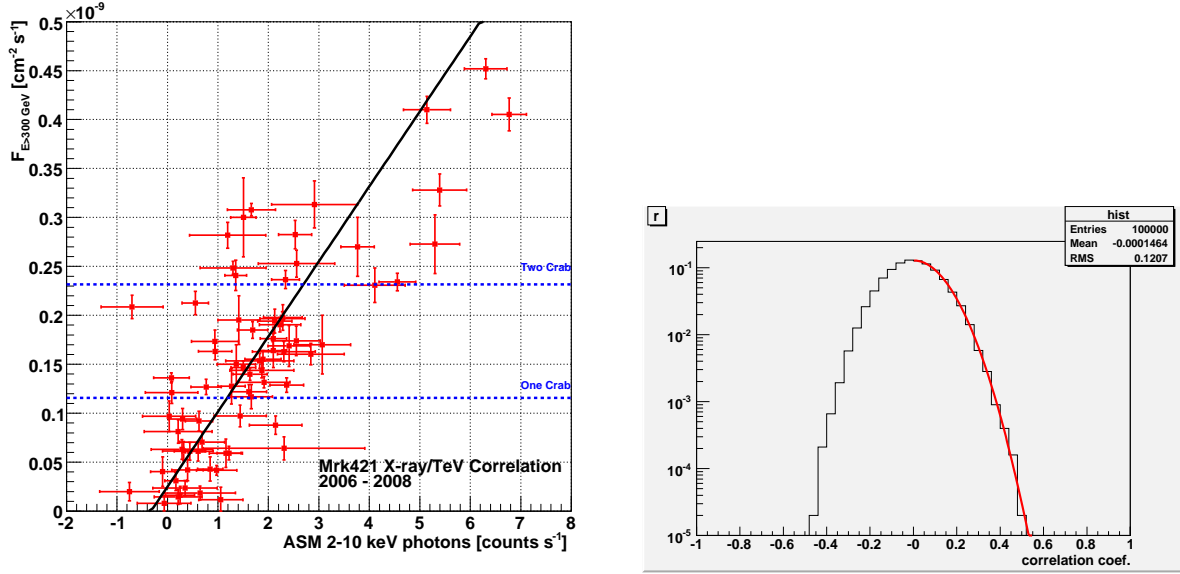


Figure 10.8: The X-ray (ASM) and TeV observations (MAGIC) correlations, from 2006 to 2008 data. In order to know how big the significance is, we randomize the pairs of X-ray/TeV observations and then calculate the Pearson's correlation coefficient. The randomized pairs have a significance distribution peak at zero, which is expected. The significance number 0.75 could be derived from the distribution and the number is about  $8\sigma$  effects.

contribute to the TeV  $\gamma$ -ray component, the synchrotron flux is proportional to the electron density  $F_X \propto N_e$ , but the IC TeV  $\gamma$ -ray flux is proportional to both the electron density and the synchrotron photon flux  $F_\gamma \propto N_e F_X$ . Thus the correlation  $F_\gamma \propto F_X^2$  is expected. On the other hand, if the seed photons of the IC scattering process are fed by external photons from the accretion disk [205] or from the central region of the AGN [206], then the TeV  $\gamma$ -ray/keV X-ray correlations may come down to linear a correlation, where  $\alpha$  is 1, i.e. the Compton effect dominates. Even more surprising was the PKS 2155-304 flaring in July-August in 2006. The  $\alpha$  value was about 3, which cannot be explained by current models [75].

In Fig. 10.8, the correlation of ASM X-ray and MAGIC TeV observations from 2006 to 2008 data is shown. Note that we give two data sets  $\pm 6$  hours of tolerance, i.e. data points from X-ray/TeV observations within 6 hours are treated as simultaneous. The final data pattern has a Pearson's correlation coefficient of about 0.76. The fitted straight line could be described by the simple formula  $y = p0*x + p1$ , where  $p0 = 7.67 * 10^{-11} \pm 3.1 * 10^{-12}$ ,  $p1 = 2.5 * 10^{-11} \pm 5.9 * 10^{-12}$ , if we assume the fitting line passing through the origin. The fitted line  $y = p0*x$ , where  $p0$  is  $8.75 * 10^{-11} \pm 2.16 * 10^{-12}$ .

The strong X-ray/TeV correlation supports the leptonic models. In order to estimate how good the correlation is, a simulation on the X-ray and TeV observational pairs was performed. The basic idea was to randomize the sequence of the X-ray data such that the pairing patterns between TeV and X-ray pairs were different. We calculated the Pearson's correlation coefficient

for different patterns. The MC results show that the correlation approximately has an  $8\sigma$  effect, see Fig. 10.8.

### 10.4.2 TeV Orphan Flares

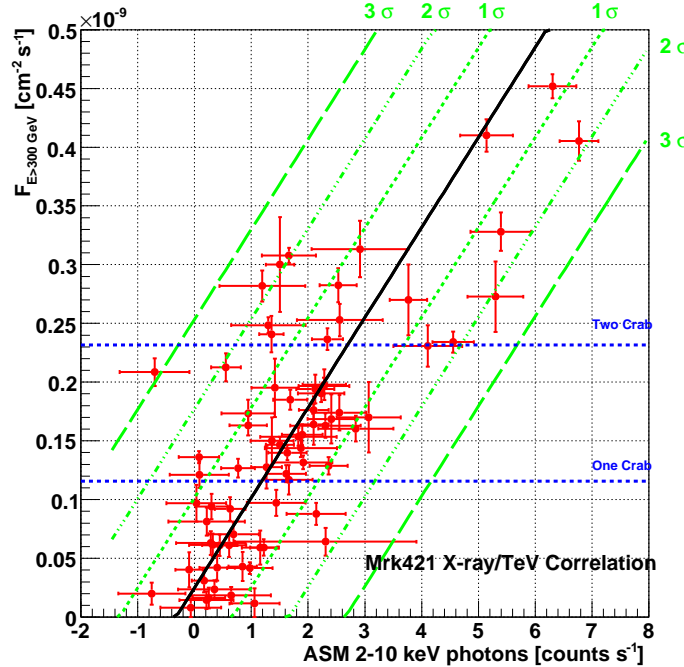


Figure 10.9: The X-ray TeV correlation with an estimation of statistical errors. Most of the points are within  $2\sigma$ , which means that they have good correlations. Note that it is not easy to estimate the systematic errors of this correlation calculation, because the time tolerance is 6 hours.

In the SSC model, a high TeV flux is always accompanied by X-ray flares. Usually the opposite is also true. However, exceptional cases have been observed, too. In 2002, a TeV flare was detected by the Whipple collaboration from nearby AGN 1ES1959 [175]. In addition [14] has pointed out that Whipple found an orphan TeV flare candidate during the 2003 multi-wavelength campaign on Mrk421. The latter case, suggested a hybrid flare. A hybrid flare is a common X-ray and TeV mixed flare followed by an orphan TeV flare about 1-2 days later. The physics explanation is that there is a typical electron dominated flare (with a certain proton content) and the photons are reflected by a nearby cloud and re-enter the flare region after a delay interacting with protons. Then pions are produced during this process and they decay into TeV  $\gamma$ s.

Another possible explanation is proposed by [207] within the framework of the SSC model. They assume that the TeV emission region is not homogeneous, which is different from the

conventional SSC model. In this model, the normal non-thermal electrons/positrons in the jet trigger the primary TeV  $\gamma$ s and X-rays flares. If the jets are not uniform and contain a few patchy regions, the X-rays which are produced by the primary flare will be injected on another dense region in the jet. This sudden increase of X-ray photons results in a strong TeV  $\gamma$ -ray flux by inverse Compton scattering, which is expected to be observed as an orphan flare.

If Compton scattering is happening in the Klein-Nishina (KN) regime, electrons scatter low energy photons and lose all their energies to the photons. Thus, the Compton cooling becomes very efficient compared to synchrotron cooling. As a result, the peaks of the synchrotron and Compton emission components are produced by the same electrons but with different energies. Furthermore, the  $\gamma$ -ray flux at the highest energies will tend to track the X-ray synchrotron flux linearly instead of quadratically as expected in the Thomson regime.

In the four years of MAGIC data, X-ray and TeV always show nice correlations. From Fig. 10.9, we estimated the orphan flare probability of X-ray/TeV pairs at certain particular states. We calculated how the X-ray or TeV flux deviated from the fitting red line. Most of the points are within  $2\sigma$  in a good correlation region. There is one point with an orphan flare effect of almost 3 sigma (only statistics). However, if we take a closer look, the X-ray and TeV observations had 5 hours of difference in time, thus the systematic error at this particular point is big.

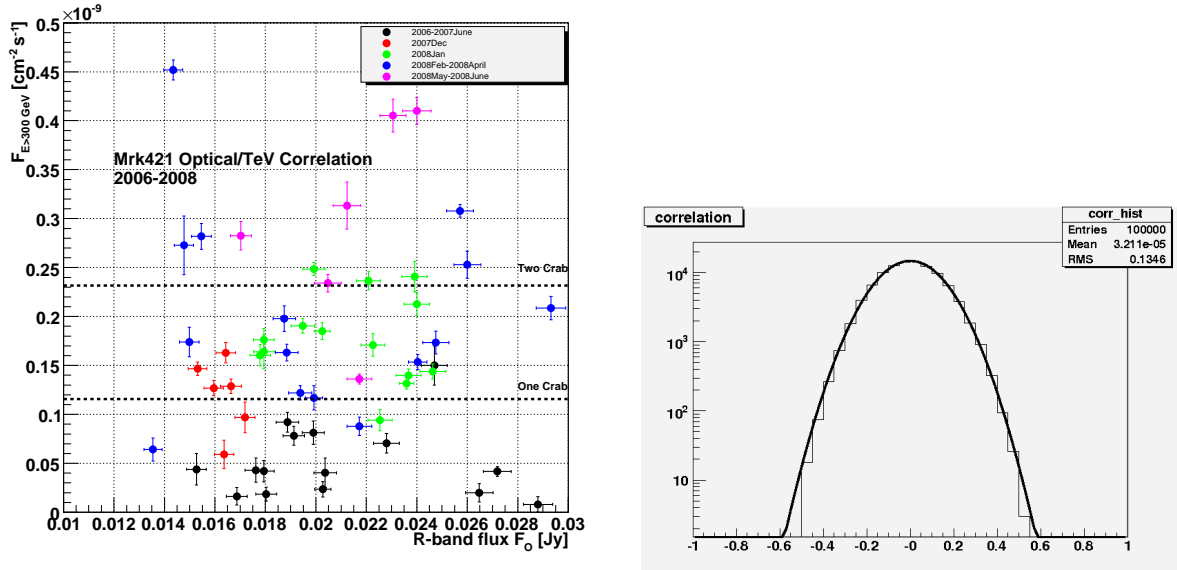


Figure 10.10: The optical R-band (KVA) and TeV observations (MAGIC) correlations, from 2006 to 2008 data. Different colors of the markers show data pairs in different time periods. The Pearson's correlation coefficient is about  $0.02 \pm 0.14$ . In order to know how big the significance is, we randomize the pairs of optical/TeV observations and then calculate the Pearson's correlation coefficient. The randomized pairs have a significance distribution peak at zero, which is expected. The significance can be estimated from the distribution, and the probability to obtain such number is about 10%, which is completely randomized.

### 10.4.3 Optical/TeV correlation

Unlike X-ray/TeV correlations in HBL, the relation between optical and TeV is not sure. So far, three extragalactic VHE  $\gamma$ -ray emitters have been found because of the high optical state trigger. They are Mrk180, 1ES1011+496 and S5 0716+714. Additionally, part of the BL Lac TeV data in 2005 and 3c279 TeV data in 2006, which resulted in a VHE  $\gamma$  discovery, were taken during the high optical states of the sources. However, none of them is a HBL. Nevertheless, some studies about the optical and TeV multiwavelength campaigns of the source PKS 2155-314 in August-September 2003 have been carried out. They showed a V-band time lag from the optical polarization flux about 2 days after the TeV emission, but the optical polarization fraction is almost synchronous with the TeV lightcurves. It is interesting that using VLBA observation, the radio and optical EVPAs (Electric Vector Position Angle) are almost orthogonal to each other. This relation suggests either a different spatial origin from the VLBA core and the optical (and later TeV) emission, or more probably, the emissions come from an unresolved compact region within the radio core.

The Mrk421 is categorized as a High peak BL lac object (HBL). The optical emission is at the regime on the left of the synchrotron peak, which does not change with the IC peak. In the observational history, it has been seen that strong optical variations are generally not seen during X-ray and  $\gamma$ -ray flaring events [208]. Investigation of the correlation between MAGIC TeV data and KVA optical R-band data in 2006 and 2008 provided the result which is shown in Fig. 10.10. In order to further explore the correlation in different time periods, different color markers are shown. The overall Pearson's correlation coefficient is about  $0.03 \pm 0.14$ . In addition, the optical/TeV pairs do not have any correlation either in different periods of data. Randomizing optical and TeV observations, the probability of obtaining 0.03 is high ( $\sim 10\%$ ), meaning that our true optical/TeV pairs are almost like random distributions. No correlation is found.

### 10.4.4 Radio/TeV correlation

Usually, the radio flux of Mrk421 is very stable. The radio emission is dominated by synchrotron radiation. The TeV and X-ray flares have no relation with radio outbursts. However, a correlated variability was seen in the radio region. Katarzy et al. (2003) [179] pointed out that the radio data taken from February to April 2001 show a well defined radio outburst which corresponds to an X-ray outburst observed by RXTE-ASM and a gamma-ray flare detected by HEGRA in the TeV range. This is the first direct observational evidence for a flare observed simultaneously in the radio range and at very high energies.

Through radio interferometry, we know that the non-thermal emission of blazars from radio to X-ray frequencies arises from jets of magnetized plasma that flow out from the core with relativistic velocities. However, since the jet becomes opaque to radio emission a little closer to the core, it is not so trivial to relate the blobs which introduce flares at optical, X-ray and  $\gamma$ -ray frequencies.

## 10.5 TeV Spectrum

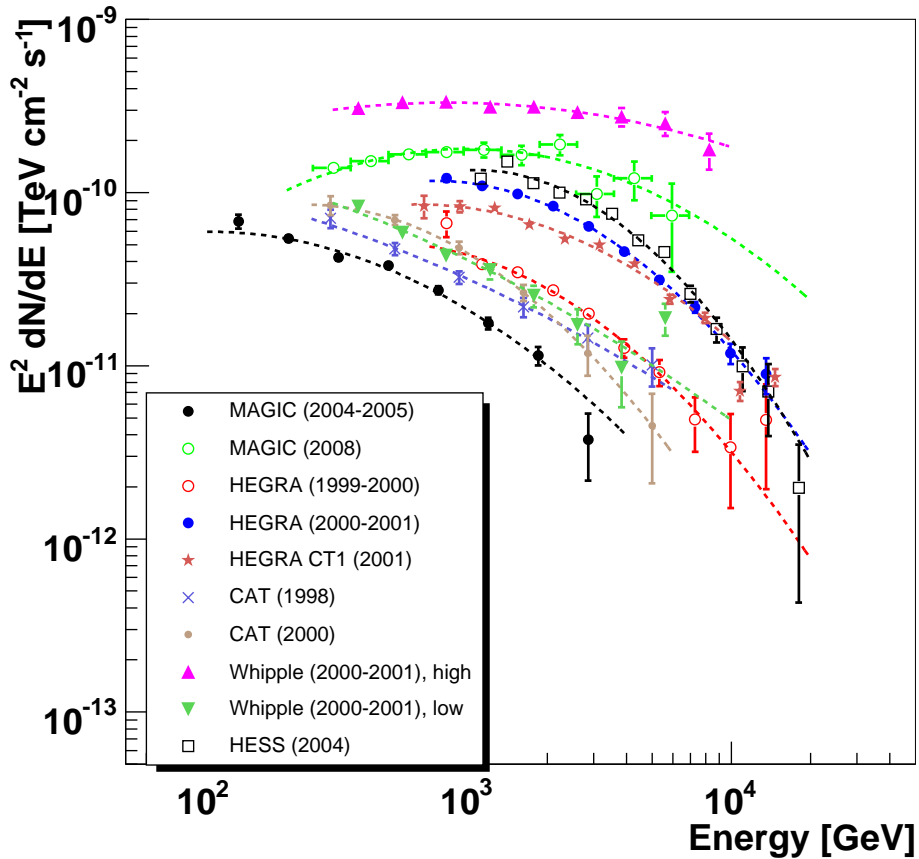


Figure 10.11: The Mrk421 spectrum in different states using different instruments.

The energy spectrum of Mrk421 at very high energy has been measured by several individual groups. Before 2001, due to the high energy thresholds and systematics uncertainties of the instruments, no solid claim of spectral variations in the TeV regime had been made. The first observational evidence of blazar spectral variation came from Mrk501. Its 1997 outburst showed hints of spectrum hardening [209]. Unfortunately the results cannot be proved and cross-checked by the other experiments [210]. Until 2001, HEGRA and Whipple both detected Mrk421 showing strong activities from January to May with spectral variations.

The spectra of Mrk421 have been measured in different flux levels. Fig. 10.11 shows Mrk421 historical spectra unfolded with the EBL absorption model by Mazin and Raue 2007. All the spectra are fitted with a curved spectrum [177]. A log parabolic (Log-P) model is physically well suited to describe the curved energy spectrum in the transition region close to the IC peak.

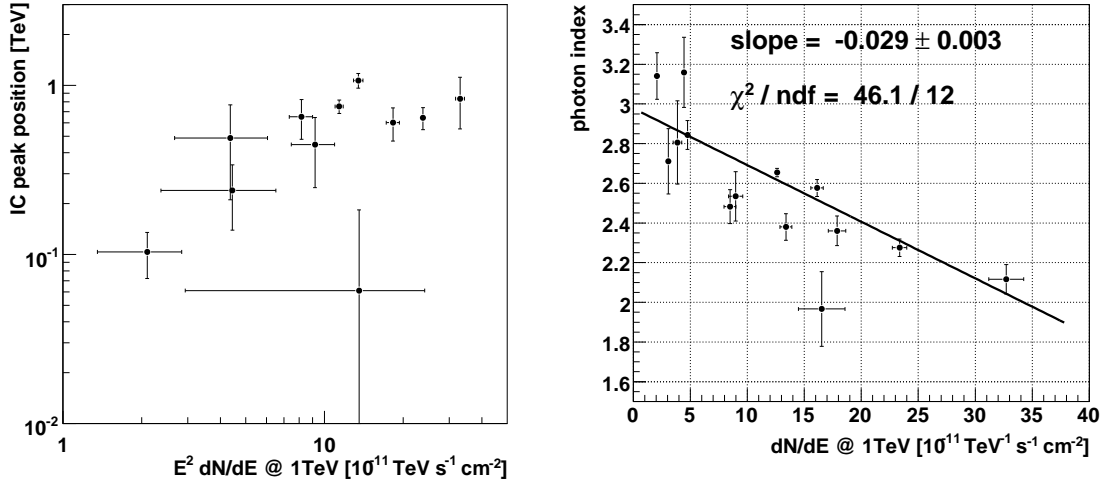


Figure 10.12: The inverse Compton peak of the Mrk421 spectrum from historical results. The peak energy  $E_p$  is calculated according to the text. Right plot: Relation between the flux state at 1 TeV (determined from a power law fitting of the spectra between 700 GeV and 4 TeV) and the fitted photon index. A correlation between the flux and photon index can be seen. Note that in the plot, we added MAGIC crab points and also other Whipple measurements inside.

The curvatures observed are an indication of a maximum in energy density and are usually interpreted as being due to inverse Compton scattering. The log-parabola fitting has the following parametrization:  $\log(\nu F_\nu) = A + B[\log(E) - \log(E_p)]$ , where  $\nu F_\nu = E^2 dN/dE$  and  $E_p$  is the energy of the peak position. In Fig. 10.12, we compare the peak positions for different instruments as a function of their flux at 1 TeV. Obviously, with an increase of the flux, the peak value shifts to higher energies. From the compiled de-absorbed historical Mrk421 spectra, it is evident that with an increasing flux state, the spectrum becomes harder. To verify this, we fitted the spectra by a simple power law ( $dN/dE \propto E^{-\alpha}$ ) in the overlapping energy region between 700 GeV and 4 TeV (the MAGIC 2008 data is fitted from 300 GeV). The resulting photon indices  $\alpha$  as a function of the fitted flux at 1 TeV are shown in Fig. 10.12.

HBLs always show a change in the positions of SED peaks. In reality, three different types of behavior have been observed among the TeV blazars [211]. (i) "Mrk421-like", the peak frequency changes very little despite large flux variations; (ii) "Mrk501-like", where during the flares, the peak shifts to higher energies by a few orders of magnitude (i.e. from 1 keV  $\sim$  100 keV.); (iii) "1ES 1426+428-like", which gives large peak variations (roughly the same order of magnitude as Mrk501) but during rather constant flux states. All three above differences and similarities suggest that there are common but intrinsically different mechanisms driving the variabilities [211].

## 10.6 SED Modeling

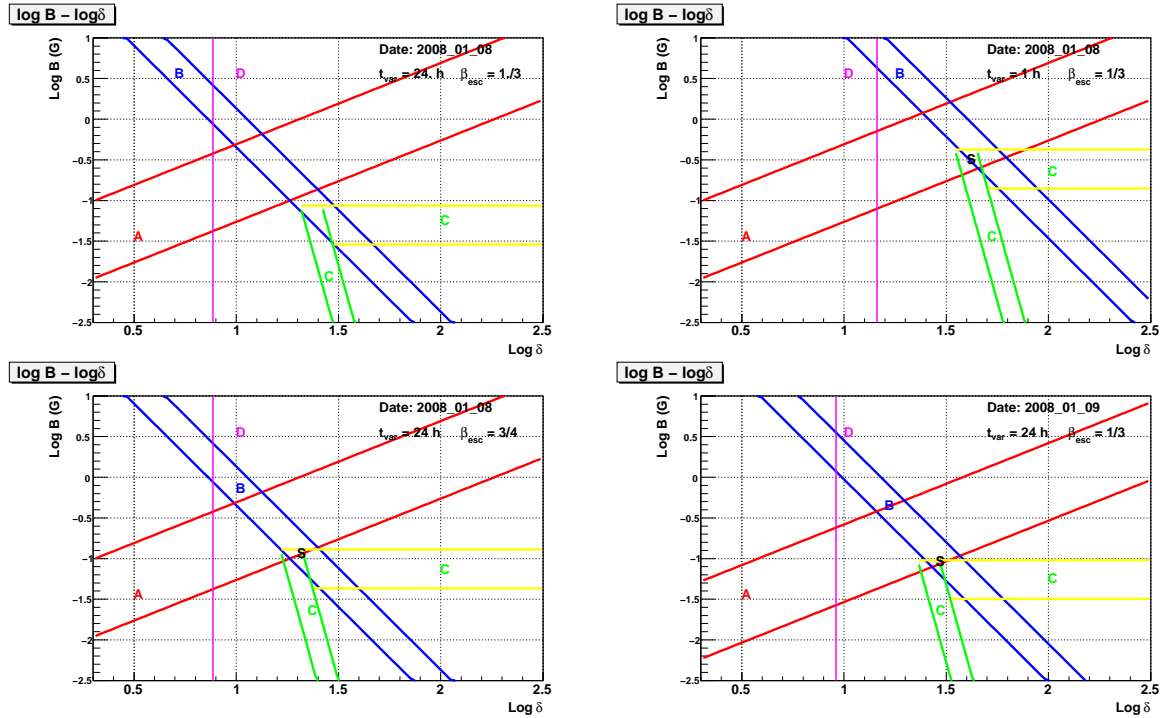


Figure 10.13: The  $(\log B, \log \delta)$  plane. The calculation is based on the multiwavelength observations assuming different time variation scales  $t_{var}$ . A, B, C, and D are estimated by the conditions in Eq.10.5, Eq.10.6, Eq.10.7 (Eq.10.8) and Eq.10.9, respectively. The region marked by S is the allowed region.

### 10.6.1 The Constraints on the SSC Parameters

In the SSC scenario, the maximum power of the inverse Compton emission occurs at an observed frequency of  $\nu_{IC} = (4/3) \gamma_b^2 \nu_{sync}$ . If the frequencies of these two peaks,  $\nu_{sync}$  and  $\nu_{IC}$  are determined from the observations, we can derive the break energy of the electrons  $\gamma_b m_e c^2$ . It is then possible to constrain the parameter space of the emission region and also the basic physics parameters, the Doppler factor D, and the rest-frame magnetic field, B, of the emitting plasma in the jets. We follow the calculation by Bednarek& Protheroe (1997) for the Mrk421 May 1994 flare [212], subsequently improved by e.g. Tavecchio, Maraschi and Ghisellini (1998) [82](hereafter TMD), Bednarek& Protheroe (1999) [213], Kataoka et al.(1999) [214]. Their modelings need precise simultaneous multiwavelength information. We apply the calculations on P5 multiwavelength campaign results and follow the calculations from [215]. There are four independent constraints in the  $(\log B, \log \delta)$  plane:

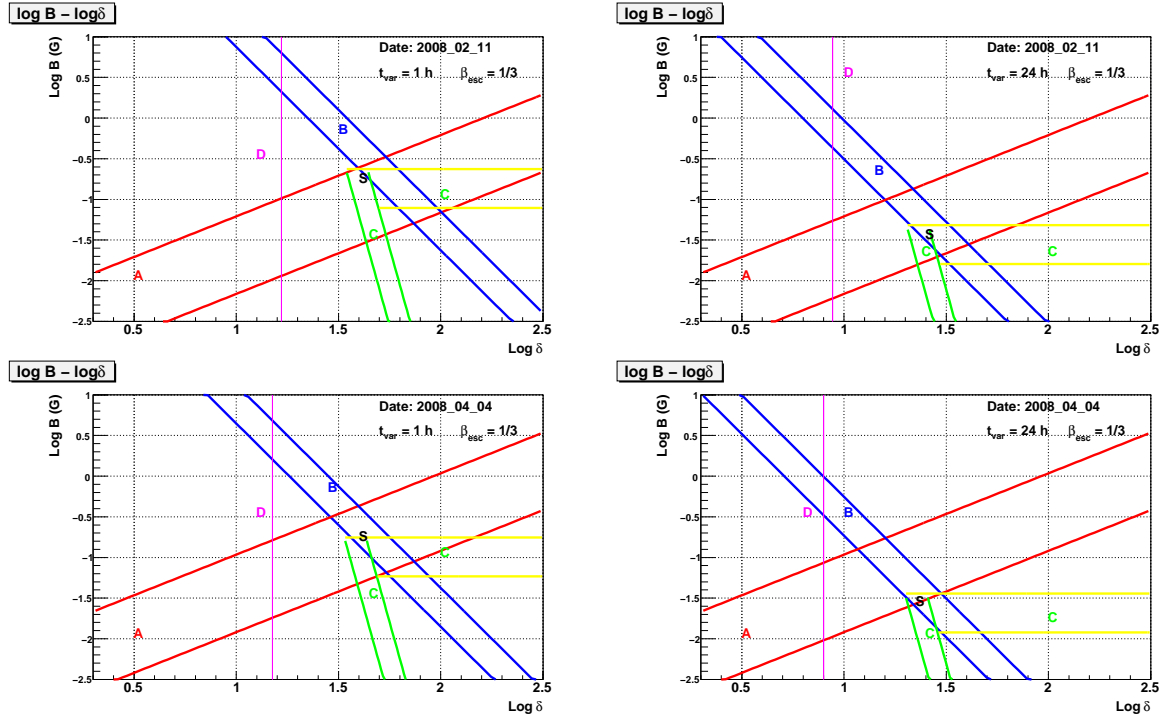


Figure 10.14: The  $(\log B, \log \delta)$  plane. The calculation is based on the multiwavelength observations assuming two different time variation scales  $t_{var}$ , 1 day and 1 hour. A, B, C, and D are estimated by the conditions in Eq.10.5, Eq.10.6, Eq.10.7 (Eq.10.8) and Eq.10.9, respectively. The region marked by S is the allowed region.

The first one is the position of the synchrotron and Compton peak frequency. The magnetic field and  $\delta$  have the following relations:

$$B\delta_{10}^{-1} \sim 1.5 \cdot \frac{\nu_{s,19}}{\nu_{IC,26}} \quad (10.5)$$

where the  $\delta_{10} = \delta / 10$ ,  $\nu_{s,19} = \nu_s / 10^{19}$ . Note that the positions of the peaks are very sensitive to EBL. In order to estimate the errors, we followed the discussion by TMD. An uncertainty of factor of 3 in the position of both the synchrotron and the IC peaks are taken into.

The second concern is the synchrotron and IC peak luminosities: From the ratio of the luminosities of the synchrotron and self-Compton peaks, we know the relative importance of the two processes. The ratio is directly related to the ratio between the magnetic energy density and the radiation energy density of the synchrotron photons. Therefore:

$$L_{sync}/L_{IC} = U'_B/U'_{sync}$$

We replace the total luminosity with peak luminosity, which is better accessible in observations.

$$B\delta_{10}^{2.5} \geq 0.5 \cdot (\nu_{s,19} \cdot \nu_{IC,26})^{-0.25} \cdot \frac{\nu_s L(\nu_s)_{45}}{\nu_{IC} L(\nu_{IC})_{45}^{0.5}} t_{var,h}^{-1} \quad (10.6)$$

where  $\nu_s L(\nu_s)_{45} = \nu_s L(\nu_s) / 10^{45} \text{ ergs}^{-1}$  and  $\nu_{IC} L(\nu_{IC})_{45} = \nu_{IC} L(\nu_{IC}) / 10^{45}$  are the observed luminosities of the synchrotron and the IC peaks.  $t_{var,h} = t_{var}/1h$  is the source variability time scale. We also consider a factor 3 of differences in the luminosity measurements.

The third concern is related to the equilibrium between the radiative cooling and the escape of electrons. Clearly, the cooling time is determined by the fastest of the two cooling processes - the synchrotron cooling or IC cooling. If it is Compton-cooling dominated:

$$B\delta_{10}^9 \geq 37 \cdot (\nu_s L(\nu_s)_{45})^2 t_{var,h}^{-2} \beta_{esc}^{-2} \nu_{IC,26}^{-1} \quad (10.7)$$

If it is in the synchrotron-cooling dominated regime:

$$B \geq 0.18 \beta_{esc}^{0.5} ((t_{var,h} \nu_{IC,26}))^{-0.5} \quad (10.8)$$

where  $\beta_{esc}$  is the electron escape velocity in units of speed of light. We still follow the arguments in the TMD paper. The value ranges from 1/3 to 1.

There are further conditions which give us better constraints for the models. To avoid strong absorption of TeV photons in the sources (blobs) due to pair production, a minimum value of  $\delta$  can be computed.

$$\delta \geq 6.6 \cdot \frac{(L(\nu_s)_{2.6})}{t_{var,h}} \sqrt{(\nu_{IC,26} \nu_{s,19})^{0.2} (t_{var,h})^{-0.2}} \quad (10.9)$$

In addition, the Doppler factor is related to the source dimension  $R$  and the time variability scale  $R \leq ct_{var}\delta(1+z)^{-1}$ . The relation only gives an upper limit on the dimension of the source. In order not to have a too large  $\delta$  value, TMD put a limit on the radius of the emission region in the range of  $ct_{var}\delta - ct_{var}\delta/3$ . [82]. With the above constraints, it is possible to check the Doppler factor and magnetic field in the  $\log B$ - $\log \delta$  plane. The  $(\log B, \log \delta)$  plots of 8 different nights in P5 data can be found in Fig. 10.14 and Fig. 10.13. We assume that the escape velocity of the electrons is 0.33 % of the speed of light. The summary results of the 8 nights are:

- If  $t_{var}$  is small, the Doppler factor must be larger in order to overcome the opacity, see line D (assuming the size of the emission region is fixed). However, region B shifts to lower values and region C moves upwards. This increases the allowed value of the magnetic strength. Constraint A is not affected by the variation time scale.
- Region A depends on the ratio of the synchrotron and IC peaks. In most cases, region A has negative slopes in the  $(\log B, \log \delta)$  plane. However, in some cases, for instance the Mrk501 1997 flare, the synchrotron peak shifted to a higher energy by at least a factor 100, which is much larger than the shift of the IC peak. Then the slope may change sign. The value of B increases with the value of  $\delta$ . A detailed investigation shows that during Mrk501 high states, not only  $\gamma_b$  increases but also magnetic field B [213]. In the case of Mrk421, both peaks do not change dramatically. Thus the allowed region shifts relatively little compared to Mrk501. Nevertheless, the allowed region moves downward (B is smaller) in high states.
- If we compare two different TeV flux nights, 8 January and 4 April, assuming identical time variation scales, say 1 hour, we found that the magnetic field and the Doppler factor were more or less static independent of the integrated flux level. However, the ratio between the positions of two peaks changes (which is the allowed region A), meaning that the break energy of the electron changes in different flares. This confirms previous observations that the different TeV flux states result from different groups of electron populations rather than from significant changes of the jet environment [152]. Nevertheless, if we consider different time scales of variabilities in two different nights, longer time variabilities loosen the constraints on the Doppler factor; also, the values of B and D are smaller in the allowed region. They may have different values in the different states.

## 10.6.2 Photons from the External Field

The phenomenon of Mrk421 having no emission lines contradicts the presence of a high radiation density photon field outside the jet [205]. For Mrk421, the detected TeV radiation can not be produced by the Compton scattering of UV photons simply because this would occur in the inefficient Klein Nishima regime. Therefore, the observed TeV photons are mostly caused by the scattering of the IR photons (seed photons) with highest energy electrons, then emitting synchrotron photons in the X-ray band.

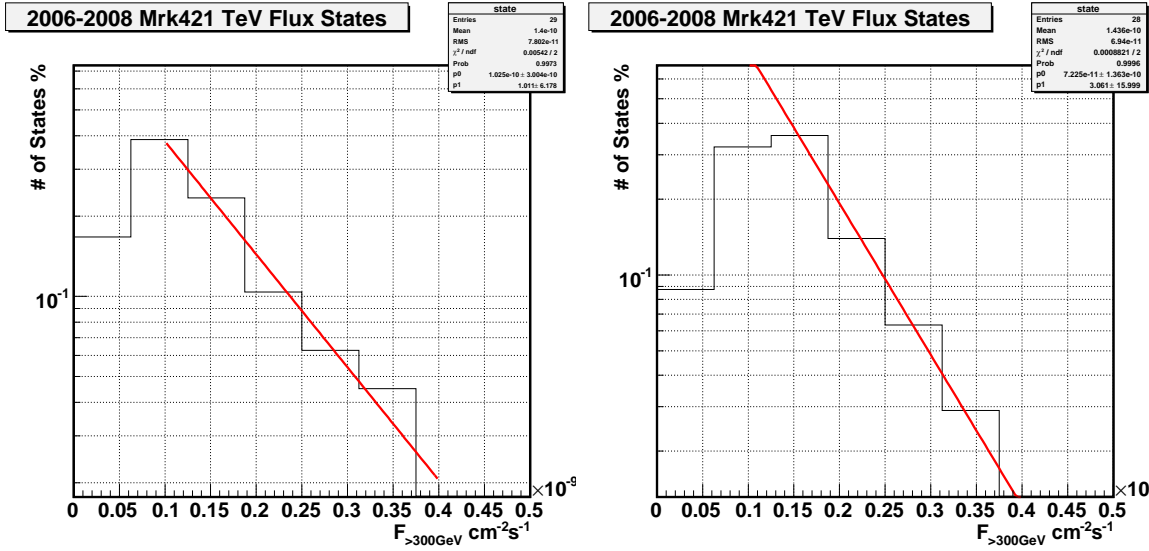


Figure 10.15: The TeV state probability. These two plots are fitted by the exponential formula described in the text. Note that the fitting starts from appr. 1 C.U.

## 10.7 Different State Probabilities

Due to the sensitivity of the MAGIC telescope, given 20 minutes of observation, a flux level above 30 % of the crab flux is detectable. From 2005 to 2008, Mrk421 was always visible to MAGIC. Mrk421 is always above 30 % flux of crab above 300 GeV and never below this value. To know what is the high state probability  $R_{HS}$  of the source is interesting and important. It was estimated by Tluczykont 2006 [216] using historical collected Mrk421 TeV and ASM historical data. Since TeV observation samples are limited and usually biased, random sampling is necessary for such kind of study. In order to have unbiased selections, I used two different methods for selecting MAGIC data randomly. The first method is to pick up every four days of MAGIC data blindly without knowing the flux before. The starting date is the first date we performed TeV observations (MJD = 53324). The second method is to pick up every 4 days of data from the last date (MJD = 54624) in the lightcurve. We also smeared the TeV flux according to its error. Also we weighted the flux according to effective observational time. Since the lower flux states are limited by the sensitivity of the instruments, we followed Tluczykont's method and fitted the differential state histograms from 1 C.U.. The state histogram derived from the two described methods are shown in Fig. 10.15.

The fitting assumes that the number  $N(E_{th})$  of flux states above a certain energy threshold  $E_{th}$  could be described by  $dN/dF = N_0 e^{-F(E_{th})/F_c}$ , where  $N_0$  is the normalization constant and  $F_c$  is the critical flux state which appears with the probability 1/e. In addition, it is also possible to assume that the number of states per flux follows  $dN/dF = N_0 F(E_{th})^{-\alpha}$ . The former assumption follows the exponential law; the latter one follows a simple power law with an index  $\alpha$ . The same distribution but fitted with a simple power law is shown in Fig. 10.16.

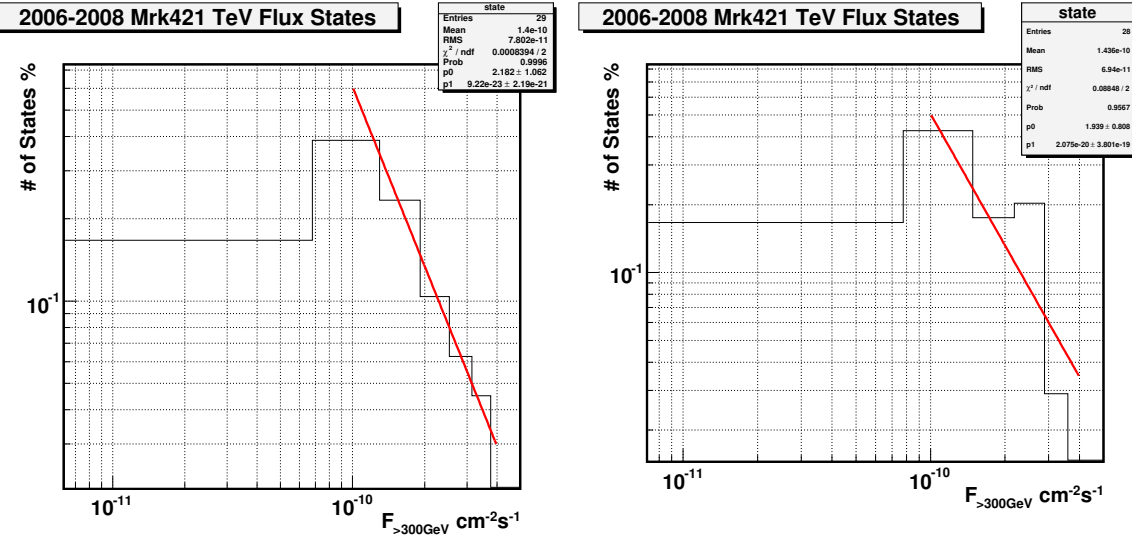


Figure 10.16: The TeV state probability. The distribution is fitted with a simple power law. Note that the fitting starts from appr. 1 C.U.

The fitting results give the value of  $\alpha \sim 2.18 \pm 1.2$ . The power law is very common in nature, like the relationship between the magnitude and the total number of earthquakes. The nature of a power law could be related to the self-similarity or self-organized criticality.

## 10.8 Comparison with Mrk501

Mrk501 is located at  $z=0.031$ ; it is well-known and also one of the most-studied objects. Surprisingly, it was not in the list of the EGRET source catalogs. The measurements taken by various TeV groups have shown that the energy spectrum of Mrk501 has a significance curvature. The curvature depends on the position of the IC peak. The observed rapid variabilities of TeV  $\gamma$  emission from Mrk501 were even shorter than Mrk421. A major difference between these two objects is that the emission from Mrk501 seems to have a base level, which changes on monthly and yearly timescales [183], whereas the VHE  $\gamma$  emission from Mrk421 has been described as consisting of a series of rapid flares with no underlying baseline [135]. Since Mrk421 and Mrk501 have almost the same redshift, they are particularly useful in separating the intrinsic spectral characteristics from the absorption effects of the EBL. The idea is to compare the cut-off energy between them. The cutoff energy of Mrk501 is a bit larger  $\sim \delta E = 3$  TeV. A difference in cutoff energies for two difference sources at similar distances excludes the possibility of the cut-off being only an absorption feature of the EBL. The spectrum cutoff could have several different origins. For example, the termination of the accelerated particle energy distribution (e.g. electrons), the sharp fall in the Klein-Nishina scattering of the cross section or absorption near or inside the  $\gamma$ -ray source itself. If the cutoff energy varied with time, it would most probably be due to the source itself and not the EBL absorption. During the flare, the synchrotron peak of

Mrk501 shifts to  $\sim 100$  keV, which is about 50-100 times larger than in low states. In the case of Mrk421, the X-ray spectral peak does shift to higher energies, but not as dramatically as for Mrk501. The peak of X-ray emission is never beyond  $\sim 2$  keV. Its peak is followed by a sharp cutoff which produces a deficit in the OSSE energy range. Therefore, there was no detection at all of Mrk421 by the OSSE instrument.

Another difference in the spectral energy distributions of these two objects is the power output in the VHE range and X-range. For Mrk421, it seems to maintain a similar output in the X-ray and TeV regimes. In contrast, the VHE range of output in Mrk501 is less than in X-rays in low state.

Kataoka et al. 2001 [169] argued that Mrk421 and Mrk501 were conspicuous concerning the synchrotron component of the photon spectrum. In the case of Mrk501, the position of the synchrotron peak shifts from low energies to high energies when the source becomes active, but for Mrk421, it remains mostly unchanged. [169] considers the time variation of the flux intensity to be caused by the increase in the number of high energy electrons in the case of Mrk421, while in the case of Mrk501, it is caused by the increase in the maximum acceleration energy of the electrons.

## 10.9 Future Prospects

The IACT observations were mostly biased to high states, thus constant and unbiased snapshots of known sources help unbiased sampling of different flux states and reveal possible different physics processes behind. Due to the limited sensitivity of the MAGIC telescope, a snapshot of 30 minutes could reach 0.3 C.U. flux level. If the flux is lower, only upper limits could be derived. With the second MAGIC telescope, stereo-observation is expected to improve the sensitivity and increase source low state statistics. In addition, when we have dedicated telescopes for monitoring or IACT networks widely distributed in different longitudes, we can have more and more observation time on one particular source.

Compared with TeV particle surface arrays, such as Tibet and Milagro, IACTs have relatively low duty cycles. However, they are more sensitive to detect short time flares down to a few minutes. With more monitoring time, we are able to gain a deeper knowledge of the intrinsic properties of the flares. The next generation of IACTs will have better sensitivity and explore the unprecedented energy regime. They will increase the photon statistics in the spectra, (e.g. at the cutoff energy), also energy cross calibration with space-based satellites (like FERMI) will allow us to reduce the systematics. With better photon statistics at the high energy end (e.g.  $\geq 15$  TeV), we can further constrain the effect of EBL absorption in the wavelength range above  $10 \mu\text{m}$ .

As we have seen, any studies of correlation of multiwavelength variability require simultaneous observations. FERMI, with about eight times the effective area of the EGRET detector, has been launched in June 2008. The design of FERMI allows monitoring simultaneously more than 2 steradians of the sky. Thus a large number of flares from multiple blazars will be detected and monitored at the same time. On the other hand, most current X-ray detectors feature a relatively narrow field of view, typically less than  $1 \times 1$  degree. It is important to know the history of X-

ray flux prior to a flare. thus, the monitoring of the entire sky in the X-ray band is necessary. MAXI, the all-sky X-ray monitor has been launched in 2009 and accomplished its first all sky image [217]. Simultaneous monitoring observations with these two instruments with optical and radio telescopes will be very important for AGN studies. With the next generation of more sensitive instruments and more multi-wavelengths co-observations, we are looking forward to resolving the jets of Mrk421 much better and hopefully we know furthermore general in AGN physics.

# Summary and Conclusion

This thesis has described the results of the Mrk421 data taken from 2005 to 2008 by the MAGIC telescope. Thanks to the high sensitivity and the low energy threshold of the instrument, we achieved progress in the understanding of this particular and richly-studied source.

In order to minimize the inhomogeneity of the data within three years taken under different hardware and software conditions, all the data sets discussed in this thesis work were selected in accordance with severe data selection criteria. Differential energy spectra down to about 150 GeV were reconstructed especially for nights with high photon fluxes. It is particularly helpful for HBL, like Mrk421, that their IC peaks are supposed to lie within the energy range covered by the MAGIC telescope. The determination of the IC peak gives valuable inputs for modeling the VHE  $\gamma$ -ray emission, in the framework of the SSC model. In the past, most of the Mrk421 VHE  $\gamma$ -ray data were taken during high flux nights or pre-scheduled MWL campaigns. This thesis, for the first time, deals with the regular long-term monitoring data of MAGIC since 2005. Within this time period, MWL observations and high state triggers occurred several times. SED modeling for these data has been discussed within this thesis. In this section, the main conclusions of the presented work are summarized and prospects of related topics in the future will be discussed.

Briefly, in this thesis, I have presented the following:

- Almost three years of Mrk 421 lightcurves in daily and 30 minutes time scales have been presented.
- Systematic search for short time variability (down to 5 minutes time scale) for three years of data. One night shows high significance of intra-night variability, the variability time scale is about 20 minutes.
- Confirmation of strong X-ray/TeV correlations in 2006 to 2008 data. The significance is about  $8\sigma$ . No X-ray/TeV time lag or orphan TeV, X-ray flare has been found.
- No significant optical/TeV correlation in any period has been verified.
- IC peak at TeV high state has been observed.
- Hints of strength of variability gets stronger in longer time scales. The TeV variability shows red noise-like behavior if the time scale is longer.
- Confirmation of correlations between spectral hardness and flux intensity.

- Confirmation of a source-inherent effects resulting in the curved spectrum after EBL de-absorption. Hints of different cut-off energies in different states which implies source intrinsic absorption effect in different states.
- Periodicity search in P5 data has been performed, no hint of any periodicity in TeV signals.
- No significant  $\sigma$ -Flux correlation has been found (using 30 minutes lightcurves in P5). However, if we drop off negative RMS points, a slightly positive correlation is found. Mrk421 shows no variability with a TeV flux state about 0.5 C.U.. Then, the variabilities increase linearly with the flux states. Note that the lowest variability occurring at 0.5 C.U. may be due to the sensitivity limit of the instrument.
- A three years unbiased TeV state probability is derived. The probability of a state with a flux larger than 2 C.U. is about 15-20 %. However, it is not sure that the state probability follows an exponential formula or a simple power law.
- Hints have been found that different flux states result from different electron populations (electron spectra) rather than from significant changes of the blob's Doppler factor and magnetic field inside the jets, if we assume that the variability timescales are the same for different states. If the variability timescales are different, the value of the Doppler factor and magnetic field may change.

From the important conclusions outlined above, the following are highlighted and described in more detail:

- No observation of TeV orphan flares: We have searched for orphan flares by applying the temporal analysis on 2005-2008 MAGIC Mrk421 data and RXTE ASM data, however, no significant evidence of an orphan TeV flare has been found. Nevertheless, since current simultaneous TeV data and X-ray data are rare, we do not exclude the possibility that there is a time lag between X-rays and Gamma rays of less than  $\pm$  6 hours. Nevertheless, within  $\pm$  6 hours, from ASM and MAGIC data, X-ray and TeV always show synchronized behaviors.
- Strong X-ray and TeV  $\gamma$  correlation: The time correlations (within 6 hours) between MAGIC TeV data and RXTE ASM X-ray data which were taken in the 2006 - 2008 period strongly support the SSC model. On the other hand, the optical/TeV correlation is very weak and of no significance. We have also checked if there is any hidden optical/TeV correlation in different time periods and different flux states. The result was negative and no significant correlation was found. It should again be noted that, as mentioned above, despite the lack of real simultaneous data, the possibility of a time lag between two energy bands cannot be excluded. Careful investigation of the correlation should be further done with more sensitive X-ray instruments such as RXTE/PCA.
- Intra-night variability: Intra-night variability of integrated flux above 400 GeV has been observed within this data set. The doubling time was estimated to be  $18 \pm 2$  minutes, which

constrains the size of the emission region down to the size of our solar system, if we assume the Lorentz factor is 10. The Mrk421 historical flare in 1996 gave us roughly the same doubling time scale. The unpredicted short time variability of the flares again strongly supports the leptonic origin of the VHE emission.

- The differences between flux states are due to different electron energy spectra in the framework of the SSC model. This might suggest that the electron population inside the jet is responsible for the TeV emission of the blazars. In this scenario, the flare activity could be caused by increasing the Lorentz factor of the electrons at the break energy  $E_b$ . However, the above scenario assumes that the time variability scale is more or less constant in different states. If the time variability scale changes, the Doppler factor and magnetic field have to be changed.

# Appendix A

## Crab Analysis

### A.1 Crab December 2005 to March 2006

Date	MJD	$T_{eff}$ (mins)	zenith ( $\circ$ )	Rate	mode
2005_12_02	53706.1	54.1828	10-24 (16.6)	103	W
2005_12_05	53709	51.726	11-46 (25.5)	86.	W
2006_01_21	53755.9	11.683	7-13 (8.5)	116	W

Table A.1: Crab data observed by the MAGIC Telescope from December 2005 to April 2006. Only Wobble data were selected. All the data have zenith angles lower than 30deg.

Crab data with a zenith angle lower than  $30^\circ$  were used for optimization of the analysis, since most of the Mrk421 data in this period were under  $30^\circ$ . Afterwards, the quality cuts mentioned in Fig. 7.9 were applied. Source independent  $\theta^2$  analyses were performed. The analysed Crab data are listed in the Table A.1. Because the Crab is the standard candle in the TeV energy regime, any reconstructed flux deviating from expected values is due to problems of hardware, anyalysis or simply bad weather or sky conditons.

Among all the data quality checks, the best index is the hadron rate. The hadron rate should only depend on the zenith angle if the weather condition is good. The hadron rate and zenith angle has the following relations:

$$R = R_0 * \cos^\alpha(\theta) \quad (\text{A.1})$$

The value of  $\alpha$  depends on the SIZE cut. Intuitively, if the shower's incident angle increases, the effective area (the size of the light pool) on the ground becomes bigger (with a  $1/\cos^2\theta$  factor). On the other hand, the path from the shower maximum to the observer becomes longer (with a  $\cos\theta$  factor). The attenuation of the shower due to the increased path length and the reducing light intensity due to the increasing light pool size of the inclined shower make the Cherenkov light intensity dimmer. However, we found that rate R decreases slower than expected. The

reason is that more  $\mu$  are produced in the inclined showers because of the longer path. A more detailed study on this effect will be shown in Appendix A.3.

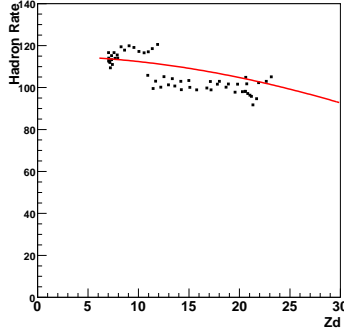


Figure A.1: The plot shows the hadron rate against  $z_d$  from per Crab data run. The red line is fitted with the formula  $R = R_0 * (\cos\theta)^{0.85}$ . The SIZE cut with 100 ph.e. was applied.

### A.1.1 Results from the Crab Analysis.

#### The Lightcurve

The daily lightcurve of the Crab data in this period is shown in Fig. A.2. The red line is the published MAGIC Crab integrated flux above 300 GeV. The pink line is the published H.E.S.S. Crab flux. The black line is the  $\chi^2$  best fitted flux from three data points.

#### The Short Time Stability Check

In order to check the stability of the telescope during the data taking and also exclude bad data points from intra-night variability analysis, we systematically calculated the integrated flux with finer timing bins down to the minute scale, 10 minutes and 30 minutes for each night. To exclude the bad data points due to bad weather or hardware instabilities, we fitted the background curves with a  $\chi^2$  test and excluded the points which were  $5\sigma$  away from the mean fitting value. At the same time, the corresponding signal data point in that timing bin was removed. After excluding these bad points, we re-fit the signal and background lightcurves with a constant value. If the  $\chi^2/\text{d.o.f}$  is far away from 1, then a hint of intra-night variability (INV) is shown. The same method could be applied on the Crab data to see stabilities of the hardware systems and analysis. Fig. A.3 shows the  $\chi^2$  fitting distribution of the background and signal per night after excluding the unstable background points. No hint of INV has been found.

#### The Spectrum

The Crab spectrum at high energy has been studied by many different instruments. In Table A.2, the Crab spectrum derived from different experiments is shown. At energies below a

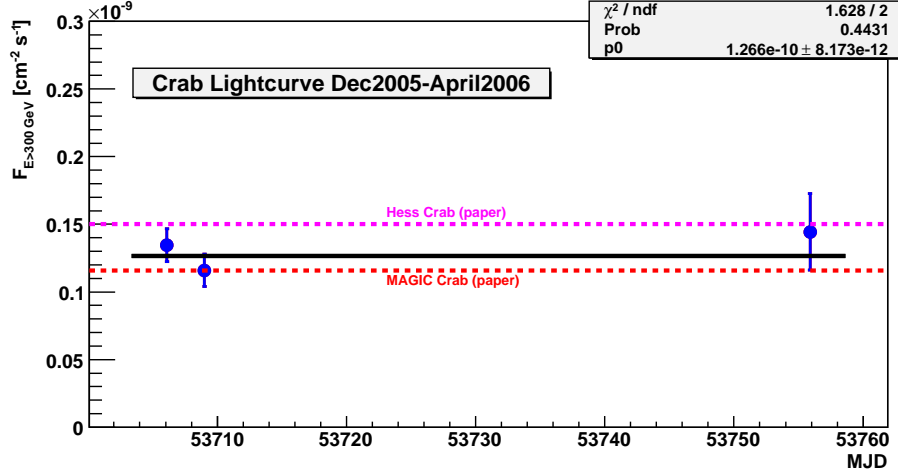


Figure A.2: The plot shows the Crab lightcurve from December 2005 to April 2006. Only the data taken in Wobble mode and with low zenith angles ( $\leq 30^\circ$ ) are shown here.

few hundred GeV, the Crab nebula spectrum is expected to deviate from the pure power law behavior due to the impact of the inverse Compton peak, which is modeled to lie at a few of 10 GeV [221]. At energies above 400 GeV, no curvature of the spectrum is expected. It can be fitted with a simple power law. Fig. A.4 compiles the spectral energy distribution (SED) measurements from different instruments. The EGRET data shows the high energy end of the synchrotron peak and the up-going part of the IC peak. In the VHE energy regime, data from IACTs, like MAGIC, Whipple, CANGRAOO, and HEGRA, cover the energy windows from 80 GeV to 80 TeV.

Group	The Spectrum [ $\text{cm}^{-2} \text{s}^{-1} \text{TeV}^{-1} (E/\text{TeV})$ ]	Reference
HEGRA CTS	$(2.83 \pm 0.04_{\text{stat}} \pm 0.6_{\text{sys}}) \cdot E^{(-2.62 \pm 0.02_{\text{stat}} \pm 0.05_{\text{sys}})} \cdot 10^{-11}$	[18]
H.E.S.S.	$(3.45 \pm 0.05) \cdot E^{(-2.63 \pm 0.01)} \cdot 10^{-11}$	[115]
HEGRA	$2.79 \pm 0.02 \pm 0.5 \cdot 10^{-11} E^{-2.59 \pm 0.03 \pm 0.05}$	[218]
Whipple	$2.73 \cdot 10^{-11} E^{-2.58}$	[219]
MAGIC	$(6.0 \pm 0.2) \cdot 10^{-10} E^{-2.31 - 0.26 \cdot \log_{10}(E/\text{TeV})}$	[220]

Table A.2: The Crab Spectrum observed by different IACT groups. The data are from DESY, multi-messenger webpage [22].

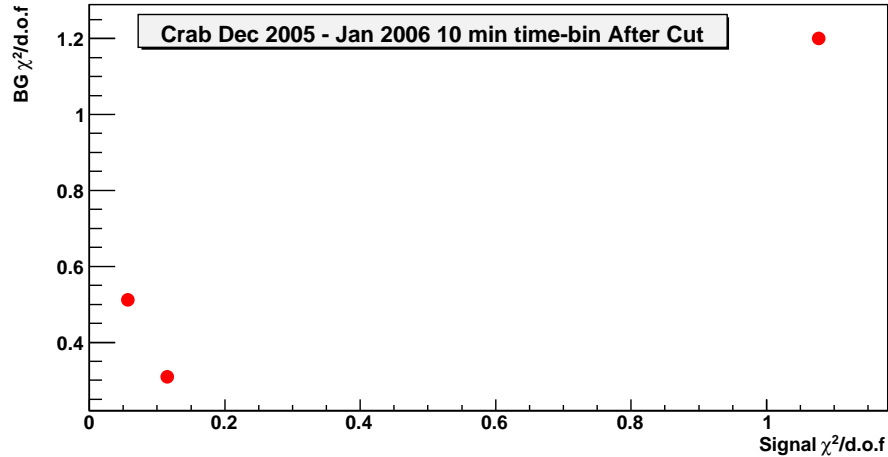


Figure A.3: The plot shows the re-fitting results after excluding the bad points from the first fitting.  $\chi^2$  per degree of freedom both on the background and signal from three Crab nights in the P1 period are shown.

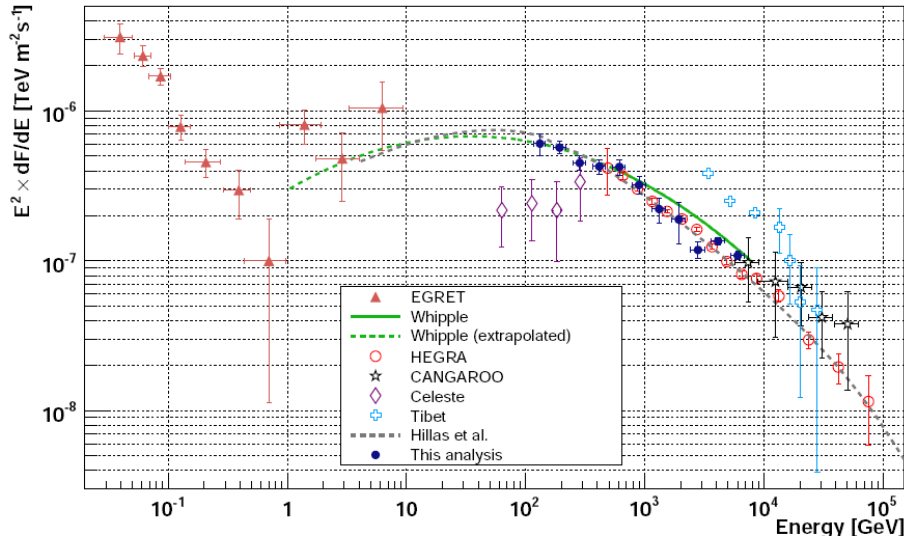


Figure A.4: The SED of the  $\gamma$ -ray emission from the Crab Nebula. The lower energy part ( $\leq 10$  GeV) is from EGRET. At energies above 400 GeV, all measurements are fitted quite well with a simple power law. The dashed curve is a model predicted by [18].

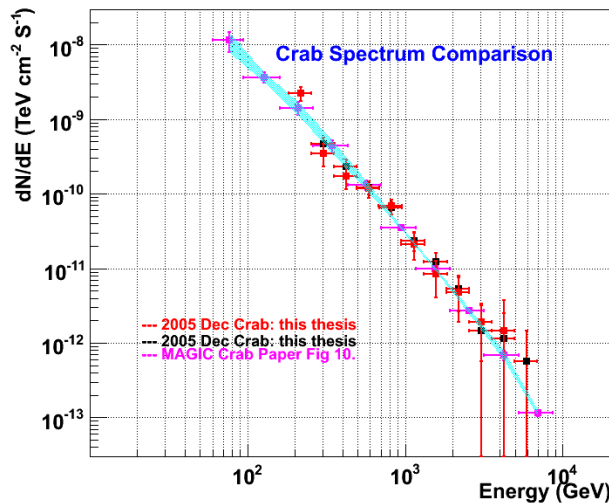


Figure A.5: The figures show the Crab spectrum from period P1. Two days of Crab data are shown. The results are superimposed with the MAGIC published spectrum.

## A.2 Crab Results from P2 and P3

### A.2.1 Crab Data from December 2006 to January 2007

Since Crab is visible at the MAGIC site only from September to March, no corresponding Crab data in period P2 (from April 2006 to June 2006) could be studied. We analyzed the data taken from September 2006 to January 2007. In total, 6 days of Crab Wobble data were analyzed; the total effective time is about 10.5 hours after data quality cuts. The data were calibrated with the standard analysis software which has been described in Chapter 6. The image cleaning level was 10p.e. and 5p.e. for core pixels and boundary pixels without using timing information from the showers. For the  $\gamma$ /hadron separation, the Random Forest method was used. The AGN 1ES0229+200 data taken during this period were treated as hadron samples. MC samples were provided by the MAGIC PIC data center. We fixed the SIZE cut at 200 phe. The hadronness and  $\theta^2$  cuts were optimized such that the significance of the signal was maximized. The  $\gamma$ -ray signals were extracted from the  $\theta^2$  approach. The energy of the  $\gamma$  events was estimated also using the Random Forest method.

#### The Lightcurve

The lightcurve from this period of crab data is shown in Fig. A.7. The fitted constant flux is  $1.181 \times 10^{-10} \pm 3.277 \times 10^{-12} \text{ [cm}^{-2}\text{s}^{-1}\text{]}$  above 300 GeV, which agrees well with the MAGIC publication [220]. The fitted  $\chi^2/\text{d.o.f} = 3.056/5$ , which is consistent with a constant.

#### The Crab Stability Check

To check the stability of the analysis in small timing bins, we applied the procedure which has been described in Chapter 7. We got a  $\chi^2/\text{d.o.f}$  distribution of the intra-night signal lightcurves versus the background lightcurves, see Fig. A.8. Both of them have an energy threshold of 300 GeV.

Fig. A.9 describes the flux distributions of these good 10 minutes' bins. The mean flux of those 10 minutes timing bin is  $1.244 \pm 0.1736 \times 10^{-10} \text{ [cm}^{-2}\text{s}^{-1}\text{]}$ , and is consistent with the

Date	MJD	$T_{eff}$ [min]	Zenith [ $^\circ$ ] (mean)	Mode
2006_09_24	54002.2	87.8	13-34 (23.7)	W
2006_09_25	54003.2	134.9	12-45 (27.9)	W
2006_10_23	54031.2	83.4	6-19 (10.4)	W
2007_01_16	54116	56.6	6-36 (21.2)	W
2007_01_22	54121.9	65.8	20-38 (29.1)	W
2007_01_23	54122.9	201.4	6-36 (17.5)	W

Table A.3: The Crab data taken from September 2006 to January 2007. Here, only the data with zenith angles of less than  $46^\circ$  are counted.

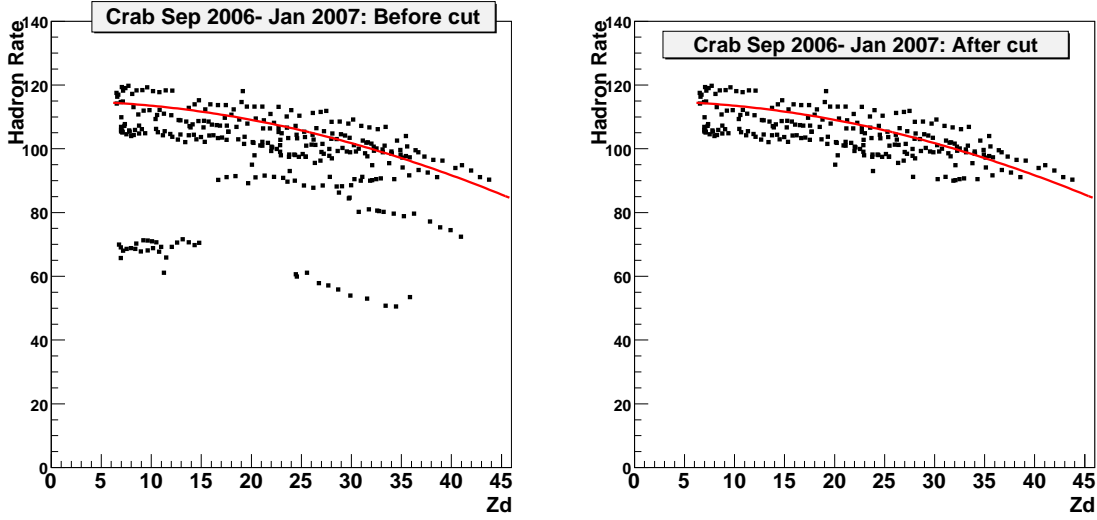


Figure A.6: The plots show the hadron rate of individual runs as a function of zenith angle after the SIZE cut 200 ph.e.. Left and right pictures are before and after the cut, respectively. The red line is the curve with the formula  $R = R_0 * \cos(\theta)^{0.85}$ . The data are from September 2006 to January 2007, i.e. period P3.

expected Crab flux above 300GeV.

### The Crab Spectrum

A pure power law fit was performed on the Crab spectrum in the region between 250 GeV and 5 TeV where no curvature of the spectrum is expected. It yields

$$\frac{dF}{dE} = (7.8 \pm 0.4) \cdot 10^{-10} \cdot \left(\frac{E}{250\text{GeV}}\right)^{-2.58} \text{TeV}^{-1} \text{cm}^{-2} \text{s}^{-1} \quad (\text{A.2})$$

At lower energies, say below 100 GeV, the Crab nebula spectrum is expected to deviate from the pure power law due to the inverse Compton peak. The crab spectrum in this period is shown in Fig. A.10

### A.2.2 Crab Data from February 2007 to June 2007

The Crab data were taken right after the MUX FADC installation. The data set after the data selection cut are summarized in Table A.4. After the data quality cut, the total amount of observation time is about 11.7 hours.

We fitted the hadron rate as a function of zenith angle and selected the data which were  $3\sigma$  within the fitting curves. The hadron rate plot is shown in Fig. A.11.

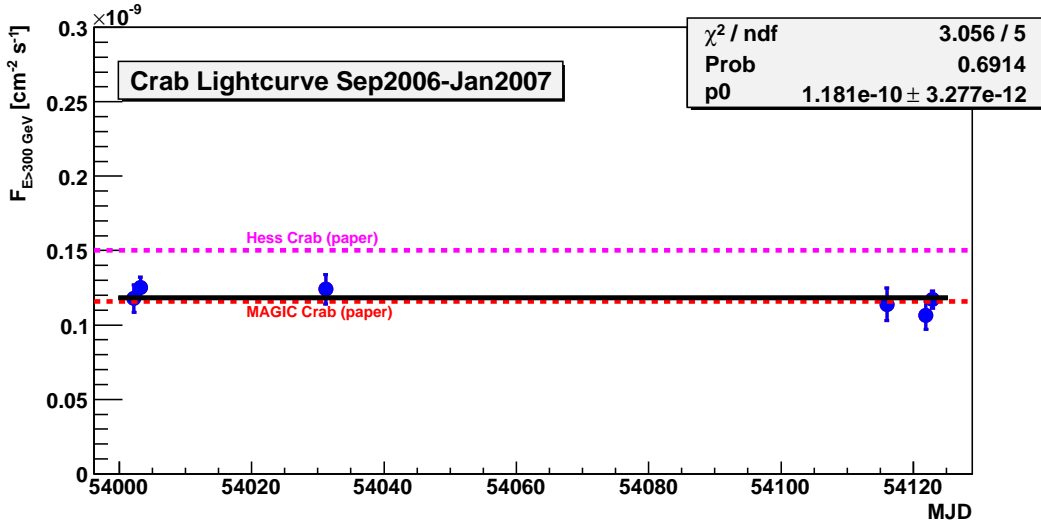


Figure A.7: The daily lightcurve of the Crab above 300 GeV in period P3.

### Crab Lightcurves

The daily lightcurve above 300 GeV of Crab data in period P4 is shown in Fig. A.12. The fitted flux is consistent with a constant value.

### A.2.3 Stability Check

We also checked the short time stability of our analysis and hardware using Crab data, following the same procedures as explained in Chapter 7. Fig. A.13 shows the fitting results after exclusion of the bad data points.

### Crab Spectrum

The crab spectra in P4 are shown in Fig. A.14. The spectrum was fitted by a power law.

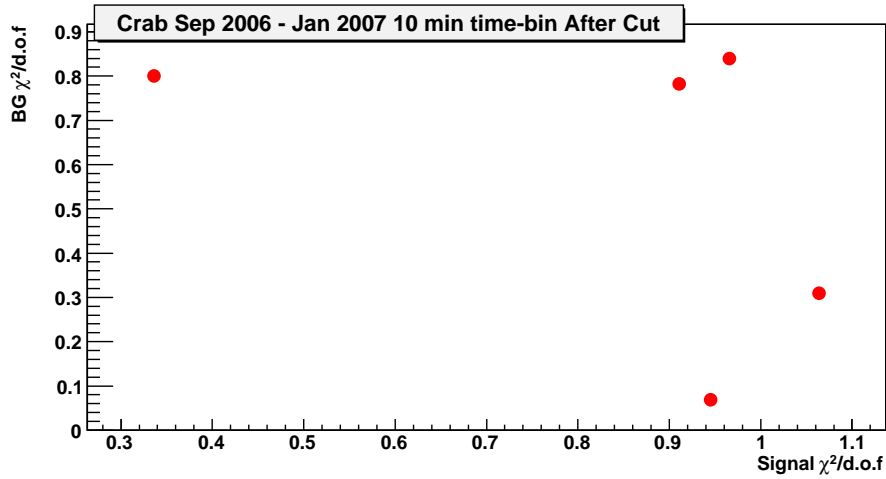


Figure A.8: The figure shows the  $\chi^2$  values for background and signal light curves of period P3 Crab data, assuming constant fluxes in both cases. The  $\chi^2$  is calculated after binning data in 10 minutes' bins. The  $\chi^2/\text{d.o.f}$  are the results from excluding the bad points (background fluctuates more than  $5\sigma$  away from the average) and subsequent refitting.

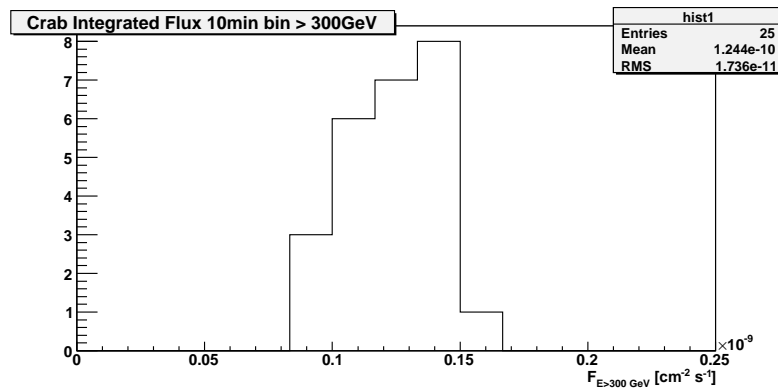


Figure A.9: The figure shows the gamma ray flux distribution of Crab for every 10 minutes-bin. Data were taken from September 2006 to January 2007 in period P3. Bad data showing large deviations in the background event rate are excluded.

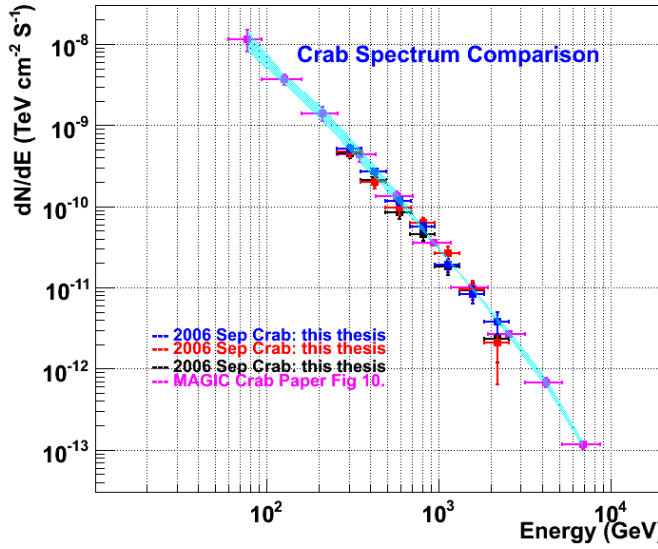


Figure A.10: The Crab spectrum from P4 data. Spectra of three different days are superimposed with the MAGIC published spectrum.

Date	MJD	$T_{eff}$ [min]	Zenith [ $(^{\circ})$ ] (mean)	Rate (Hz)	Mode
2007_02_10	54141	72	28-46 (32.7)	110.13	W
2006_02_12	54142.9	107	7-31 (18.2)	126.5	W
2006_02_14	54144.9	108	8-30 (18.2)	127.3	W
2007_02_16	54146.9	90	8-29 (18.2)	127.85	W
2007_02_18	54148.9	100	8-29 (17.5)	129.4	W
2007_02_21	54151.9	126.	6-28 (13.6)	126.9	W
2007_03_07	54165.9	79	9-28 (17.7)	117.5	W
2007_03_08	54166.9	18	19-46 (28.2)	109.5	W

Table A.4: Crab data taken in period P4 (February 2007 to March 2007). We selected eight days' data with low zenith angles ( $\leq 46^{\circ}$ ) and excluded the data which did not pass the quality check. In the end, 11.7 hours of good data were left.

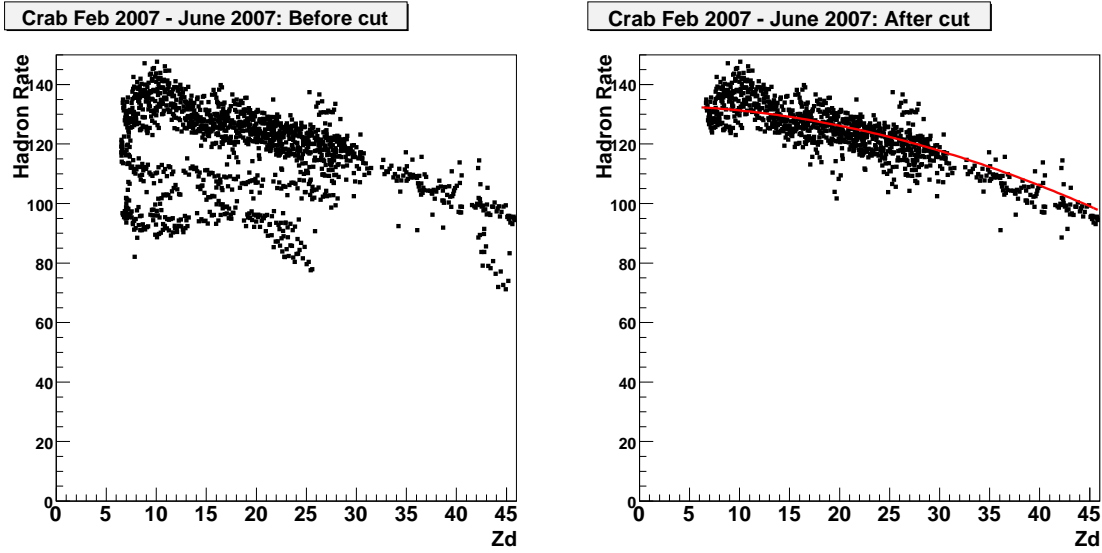


Figure A.11: The plots show the Crab data from February 2007 to June 2007 (period P4), hadron rate vs zd per data run before and after the hadron rate cut. The red line is based on the formula  $R = R_0 * \cos(\theta)^{0.85}$ .

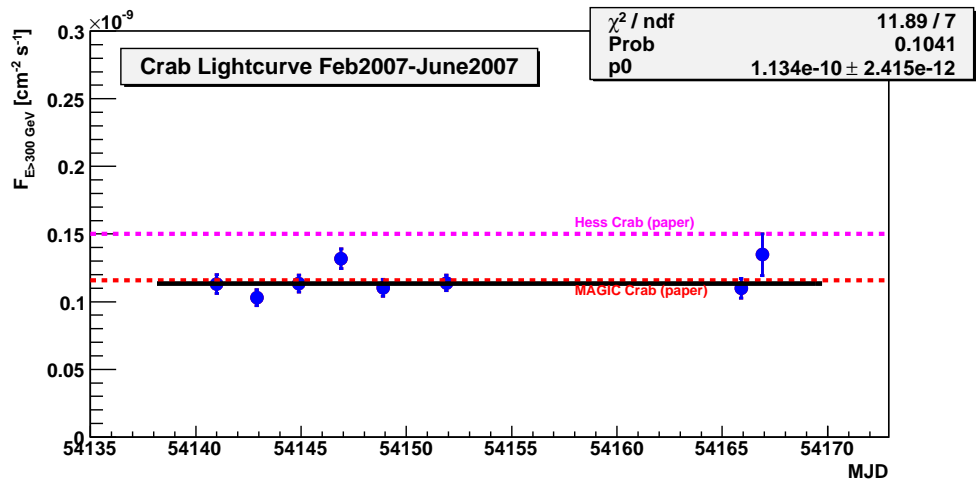


Figure A.12: The plot shows the daily lightcurve of Crab data from February 2007 to June 2007.

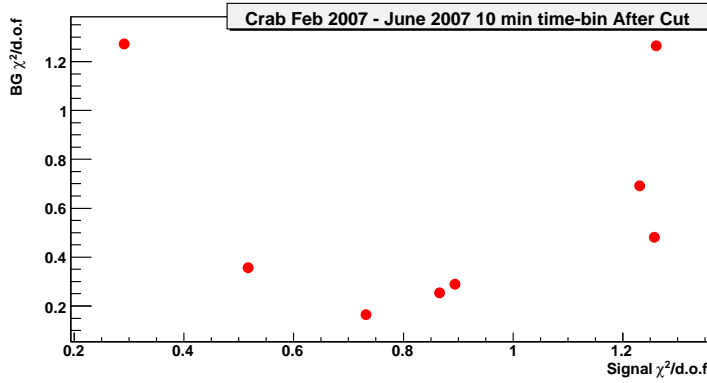


Figure A.13: The Crab data from February 2007 to June 2007 (period P4). The  $\chi^2/\text{d.o.f.}$  distribution of the signal and background.

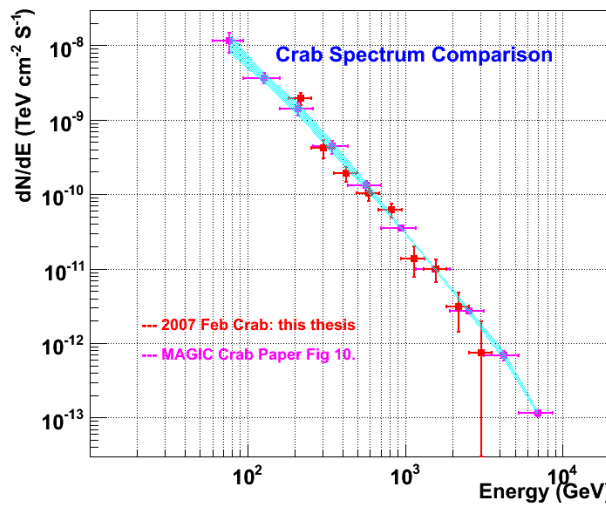


Figure A.14: The Crab spectrum from P3 data. Crab spectra from three different days are superimposed with the MAGIC published one.

## A.3 The Data Selection and Quality Check.

### A.3.1 Crab Data from December 2007 to March 2008

In October 2007, the MAGIC SUM trigger was installed. Since then, SUM trigger data were taken in parallel with normal trigger data. Mrk421 data were taken since December 2007 with a normal trigger. Hence, we analyzed the Crab data from December 2007 to March 2008 which covers the period of the time when the Mrk421 data were taken. In total, about 17 hours of Crab data were analyzed. 55% of them are lower zenith angle (below 30°) and 40 % of them are in the middle zenith angle range (between 30° to 45°), The rest are high zenith angle ( $\geq 46^\circ$ ) data.

The files were calibrated with the program Callisto, the image cleaning level is 6-3 and time cleaning is 4.5 -1.5. The data checking procedures described in previous chapters were applied. In period P5, we had additional information from the MAGIC weather station, which provides us with the local weather information such as humidity and cloudiness while the data was taken. In order to optimize the data quality, we performed a study on the dependence of the hadron rate on cloudiness using the Crab data.

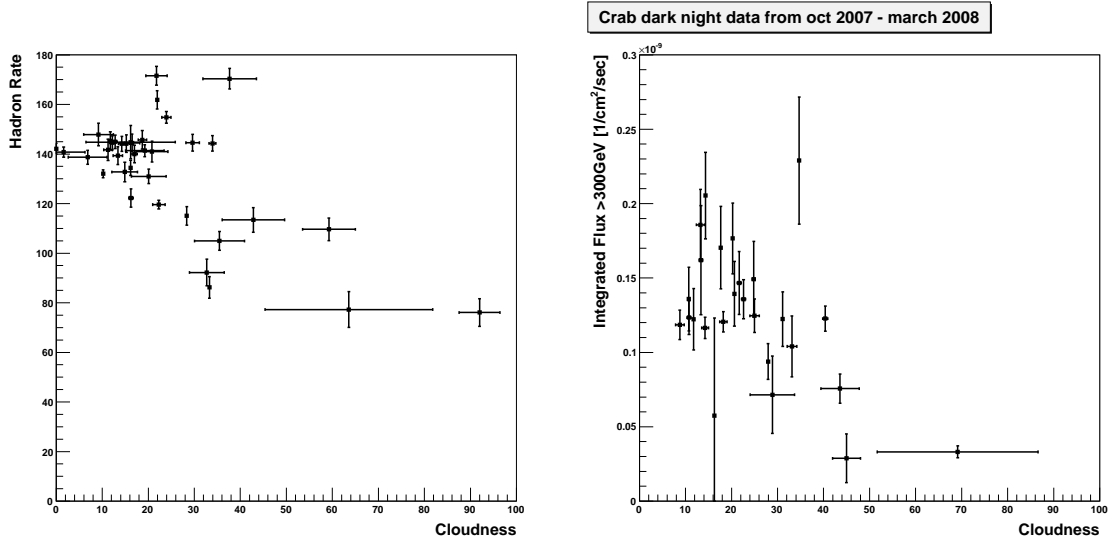


Figure A.15: Crab dark night data (zenith angle less than 28 degrees). The left figure shows the hadron rate as a function of cloudiness. The right figure shows the gamma ray reconstructed integral flux above 300GeV as a function of cloudiness. Both hadron rate and integrated flux decrease with higher cloudiness. We decided to cut out the data with a cloudiness larger than 25.

An example is shown in Fig. A.15. The hadron rate shows strong anti-correlation with cloudiness. If the cloudiness is high, the hadron rate is low. However, note that the pyrometer can only detect clouds of low altitude (high temperature). The high clouds (with low temperature) may not be detected by the pyrometer. Thus, it is possible to have a low hadron rate but a normal cloudiness value from the pyrometer. In order to keep the data as clean as possible, we apply not

Date	MJD	Hadron Rate	zenith range (mean)	$T_{eff}$ (min)
2007_12_15	54449	$127.92 \pm 1.3$	$27.07 \pm 2.1$	60.6
2007_12_29	54462.9	$144.3 \pm 2.1$	$22.7 \pm 2.0$	60.6
2007_12_31	54464.9	$142.52 \pm 1.3$	$23.38 \pm 1.14$	57.9
2008_01_01	54465.9	$144.19 \pm 3.53$	$22.58 \pm 3.33$	50.89
2008_01_02	54466.9	$144.94 \pm 2.71$	$22.02 \pm 3.45$	53.21
2008_01_03	54467.9	$141.34 \pm 2.39$	$20.48 \pm 2.81$	41.73
2008_01_04	54468.9	$144.47 \pm 3.35$	$21.56 \pm 3.59$	55.81
2008_01_05	54469.9	$140.97 \pm 4.17$	$21.43 \pm 3.92$	60.39
2008_01_06	54470.9	$144.12 \pm 2.99$	$21.62 \pm 3.64$	56.46
2008_01_08	54472.9	$144.72 \pm 3.75$	$23.5 \pm 3.27$	50.62
2008_01_10	54474.9	$144.79 \pm 6.68$	$20.73 \pm 3.99$	62.08
2008_01_11	54475.9	$147.88 \pm 4.52$	$18.68 \pm 6.46$	76.08
2008_01_12	54476.9	$132.04 \pm 1.61$	$20.16 \pm 2.74$	42.69
2008_01_26	54490.9	$120.1 \pm 1.71$	$23.40 \pm 3.54$	62.6
2008_01_29	54493.9	$140.01 \pm 3.53$	$22.27 \pm 3.46$	59.71
2008_02_02	54497.9	$139.34 \pm 3.57$	$20.32 \pm 3.02$	47.94
2008_02_03	54498.9	$138.72 \pm 2.82$	$19.90 \pm 2.90$	43.59
2008_02_05	54500.9	$142.13 \pm 2.20$	$19.64 \pm 1.55$	26.41
2008_02_06	54501.9	$140.75 \pm 2.04$	$19.19 \pm 1.20$	19.47
2008_02_07	54502.8	$122.27 \pm 3.68$	$18.93 \pm 1.09$	17.60
2008_02_08	54503.8	$134.46 \pm 3.06$	$18.06 \pm 0.78$	12.68

Table A.5: Crab data in P5 which were used in the final analysis after all quality cuts.

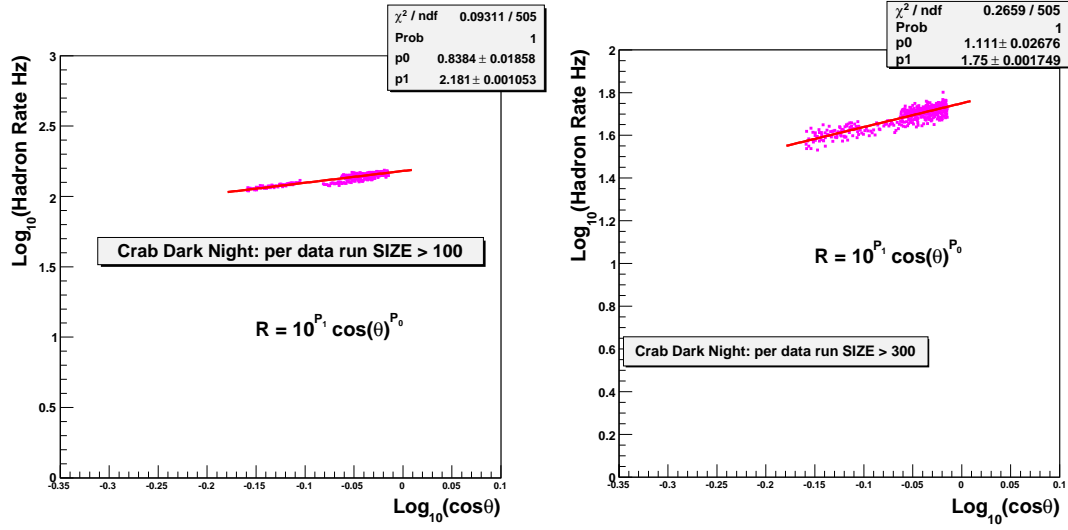


Figure A.16: Crab data taken from December 2007 to January 2008. Only the Crab data taken during dark nights are shown. The zenith angle is up to 45 degrees. Depending on the SIZE cut (energy threshold), the hadron rate changes with different powers of zenith angle. The larger the SIZE cut, the larger the power of the cosine dependent.

Size Cut	slope
100 phe.	0.83
200 phe.	1.01
300 phe.	1.1
800 phe.	1.4

Table A.6: The hadron rate vs different zenith angles. With a higher SIZE cut, the fitting slope changes. The data were taken during December 2007 and January 2008.

only the cloudiness cut but also the hadron rate cut.

The cloudiness could also be defined with more advanced devices, such as the lidar system. The idea has been carried out by HiRes and Auger experiments. In MAGIC, it is in the testing stage. The hadron rate changes with different zenith angles due to the change of the path length of cosmic showers in the atmosphere. The effective area increases with increasing ZA of observation. The longer the path in the atmosphere the lower the capability of the low energy showers to trigger the telescope. Instead, higher energy showers are expected to be seen with higher zenith angles. Unfortunately, the cosmic ray flux decreases with  $E^{-2.7}$ . Combine all of the above effects, the trigger rate follows the ZA with the following formula:

$$R = R_0 \cos^{0.5}(ZA) \quad (A.3)$$

When different SIZE cuts are applied, the hadron rate changes with ZA by different factors.

The power in formula A.3 becomes larger if we apply a higher SIZE cut. In Fig. A.17, the slopes of the hadron rates against zenith angles differ with different SIZE cuts. If we apply a stronger SIZE cut, the threshold of the higher zenith angle data increases not linearly but much faster. The curve becomes steeper because only the higher energy events survive. The hadron rate can be better fitted with  $R = 10^{P_1} \cos(\theta)^{P_0}$ , where  $P_0$  is related to the rate changing with ZA and  $P_1$  is the normalization constant. The results of the fitting parameters  $P_0$  can be found in Table A.6. The good data runs are supposed to follow the fitting function. We excluded bad data runs which were  $5\sigma$  away from the fitting function.

In addition, we applied the cloudiness cut on each data run and excluded data with a cloudiness larger than 25. The value 25 is based on Fig. A.16. If the cloudiness is larger than 25, the reconstructed Crab flux drops. At cloudiness 40, the reconstructed flux drops to about 60% of the presumed value. We also studied the hadron rate under different light and DT conditions which will be explained in the next subsection. In order to avoid high light background data, we cut away data with a DT higher than 20 units. For studying short time flare variability, the small timing bin stability of the data is also checked, like other periods of data.

## Short Summary

Summarizing the above, our data selection is based on the following criteria:

- Cloudiness smaller than 25%.
- Hadron rates in the range of 120-170 Hz after SIZE cut 100 photoelectrons.
- DTs smaller than 20 unit.
- Effective observation time longer than 10 minutes. Note that twilight light data is treated separately and not subjected to this rule.

The data are checked on a run-by-run basis. If any one of the above condition is not fulfilled, the respective data run will be discarded.

### A.3.2 Moon and Twilight Observations

#### Moon Observation

Moon night data are usually contaminated by high night-sky background light. The different levels of moonlight may introduce different levels of background light, thus the reconstructed  $\gamma$ -ray flux is suppressed. This phenomenon has been explained in Chapter 7. The level of the background light depends on the angle between the telescope and the moon, the moon phase, the atmospheric conditions, and geographical site dependent issues. The study of how these different parameters influence on the reconstructed flux is still going on. The main goal is to find an algorithm for reconstructing the deficit of integrated flux caused by these factors. In Table A.7, Crab data taken under different moonlight conditions are listed.

Date	MJD	Hadron Rate	Mean Zd	$T_{eff}$ (min)
2007_12_02	54436.1	$122.42 \pm 6.40$	$12.33 \pm 4.87$	59.26
2007_12_03	54437.1	$130.11 \pm 4.00$	$16.72 \pm 4.20$	70.17
2007_12_04	54438.1	$132.56 \pm 2.19$	$21.50 \pm 1.77$	23.58
2007_12_17	54451.0	$118.30 \pm 3.75$	$18.24 \pm 2.93$	45.31
2007_12_31	54465.1	$141.04 \pm 3.05$	$18.64 \pm 2.29$	31.65
2008_01_12	54477.9	$125.48 \pm 3.65$	$20.25 \pm 4.56$	71.84
2008_01_13	54478.9	$126.66 \pm 3.29$	$14.54 \pm 5.29$	91.12
2008_01_15	54480.0	$118.77 \pm 6.01$	$10.14 \pm 3.30$	105.31
2008_02_11	54507.9	$123.30 \pm 2.40$	$8.51 \pm 2.05$	34.61

Table A.7: P5 Crab data taken under the moon conditions.

Date	MJD	Hadron Rate	Mean Zd	$T_{eff}$ (min)
2008_01_29	54494.8	$89.07 \pm 2.10$	$30.85 \pm 0.95$	15.03
2008_02_06	54501.8	$120.98 \pm 7.57$	$24.09 \pm 1.15$	18.33
2008_02_07	54502.8	$101.54 \pm 5.41$	$22.66 \pm 1.10$	17.79
2008_02_08	54503.8	$112.62 \pm 7.16$	$22.14 \pm 1.13$	18.32

Table A.8: Crab Data from twilight conditions within this period.

The analysis is based on the following strategies: The cuts applied to the dark night data were equally used for these moonlight data sets. Only the hadron rate cut and DT cut were loosened. A plot which shows the gamma event rates from Crab as a function of DT is shown in Fig. A.18. From the plot, while the DT is above 19, the reconstructed integrated flux has been deviated from the mean P5 dark night Crab flux. The degrading of the reconstructed flux could be fitted by a straight line. However, there are data points deviated  $1\sigma$  away from the line for unknown reasons. This may imply that there are other parameters, besides DT which affect the reconstructed integrated flux. It is not yet very conclusive how the gamma ray efficiency drops with different moon/twilight conditions. In this thesis work, I did not use any strong moon/twilight data with DTs larger than 20 units.

### Twilight Observation

#### A.3.3 The results from the Crab Data

##### Lightcurve

The data were analyzed using the standard analysis and calibration softwares described in Chapter 6. The Random Forest method was used for the  $\gamma$ /hadron separation. AGN W-Comae and HB89-1553+11 wobble data were employed as the Random Forest hadron training samples. Several parameters were used for RF training, logSIZE, WIDTH, LENGTH, DIST,

Value	$F_{var}$	$F_{pp}$	$S_{flux}$	$\overline{\sigma^2}$
Crab	-0.021	0.059	$2.22 \times 10^{-11}$	$2.25 \times 10^{-11}$

Table A.9: Crab data was taken from December 2007 to January 2008. The  $F_{var}$  variability and  $F_{pp}$  are calculated. The negative value of  $F_{var}$  shows that the average intrinsic variability is much smaller than the measurement errors. The results are expected since Crab is a steady source. The  $F_{pp}$  is calculated by using the daily timing bins.

CONC, TIME RMS and Time Gradient. The files were calibrated using 6-3 image cleaning and 4.5-1.5 time cleaning. The MC samples were taken from the MAGIC data center (PIC) with PSF 10.6 mm, the data selection cuts as described in the above section were applied. Camera inhomogeneity was also checked and finally three wobble positions were used to get a better background estimation. The background was estimated by fitting a second order polynomial (without the linear term) to the  $\theta^2$  distribution of the normalized OFF data. The  $\gamma$ -ray signals were extracted from the  $\theta^2$  approach. In order to optimize the significance of the results, we varied the  $\theta^2$  cuts and tried to get the best value.

The results from the Crab data daily lightcurve is shown in the upper panel of Fig. A.19. The daily flux histogram is given in the lower panel showing the stability of the Crab flux observed by the MAGIC telescope. The mean daily flux above 300 GeV is about  $1.44 \times 10^{10} \text{ cm}^{-2} \text{s}^{-1}$ , with small RMS equal to  $1.15 \times 10^{11} \text{ cm}^{-2} \text{s}^{-1}$  for 21 data sets. The mean value of the Crab flux is about 15 % higher than the flux in the published MAGIC Crab paper, but still within systematics.

### Short Time Stability

Studying the Crab data is important for demonstrating the stability of the analysis, instrumentation and the whole telescope system. In order to search for the short time variability of the TeV AGNs, it is very important to exclude any possible artificial instabilities. Different timescales of lightcurves in 5, 10 and 30 minutes, respectively, are produced. In Fig. A.20, we see histograms of Crab integrated flux above 300 GeV in 5 and 10 minutes timing bins. Their mean flux values are better fitted with a constant line as expected. When the timing bin becomes shorter, the errors become bigger due to the poor photon statistics. The stability check of the Crab integrated flux was performed in 5 minute timing bins as shown in Fig. A.21. The  $\chi^2$  distributions of the background and signal are under control.

For testing the variability of the Crab integrated flux, we calculated  $F_{pp}$  and  $F_{var}$  by using the formula 7.6 defined in Chapter 7. The results are shown in Table A.9. The values of  $F_{var}$  and  $F_{pp}$  are pretty small, which means that the Crab TeV  $\gamma$  emission is quite stable. The same calculation was applied on Mrk421 data.

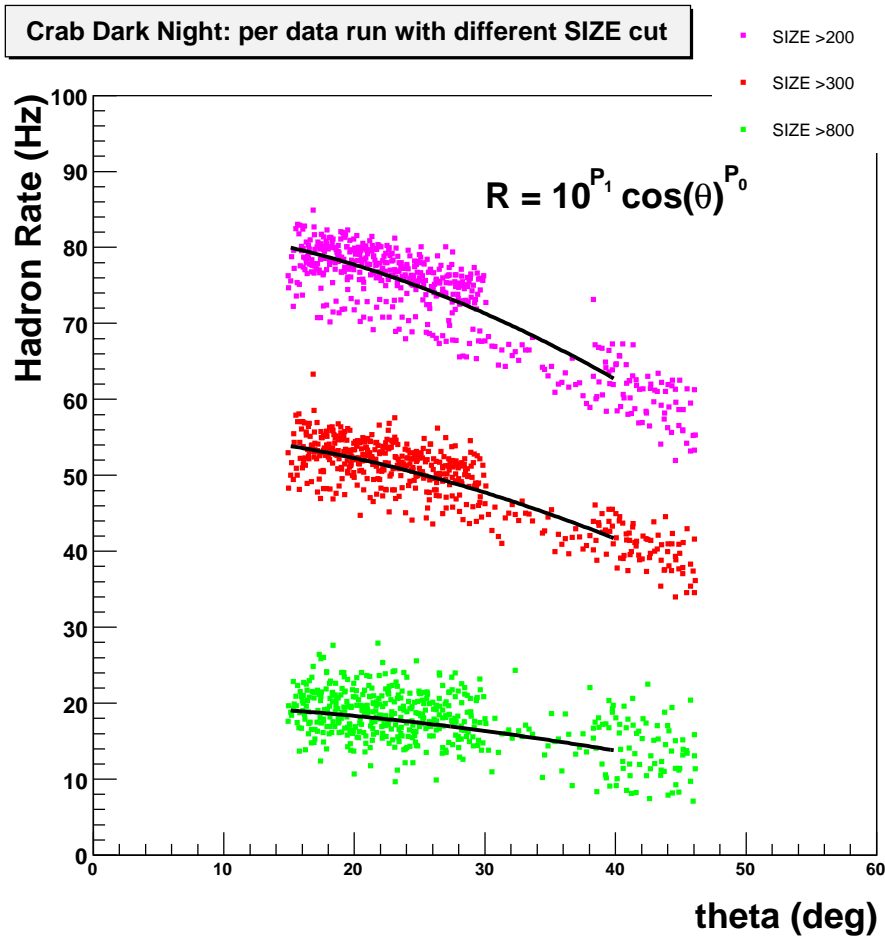


Figure A.17: From December 2007 to January 2008, the hadron rate of the Crab dark night data for different zenith angles up to 45 degrees. The hadron rate could be formulated with  $R=R_0 * \cos^{p_0}(\theta)$ , the power  $p_0$  depends on different SIZE cuts (energy threshold). The fitting parameters  $p_0$  are shown in Table A.6

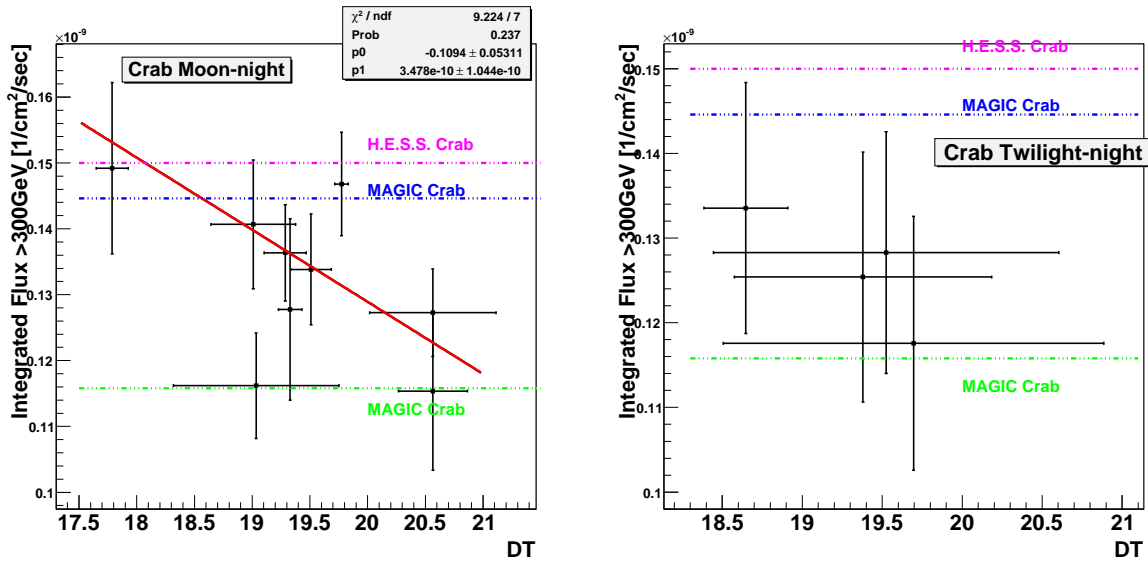


Figure A.18: The left plot: Crab moon night data from October 2007 to March 2008. Note that the upper MAGIC line is from the Crab data in period P5, which has been analyzed in this thesis. The lower MAGIC line is from the MAGIC published Crab paper. The right plot: From December 2007 to March 2008 Crab twilight observation for lower zenith angles ( $\leq 28\text{deg}$ ). The expected Crab integrated flux is given by measurements from two different groups. Note that the upper MAGIC line is from the Crab data in the period P5, which I has been analyzed in this thesis. The lower MAGIC line is from the MAGIC published Crab paper.

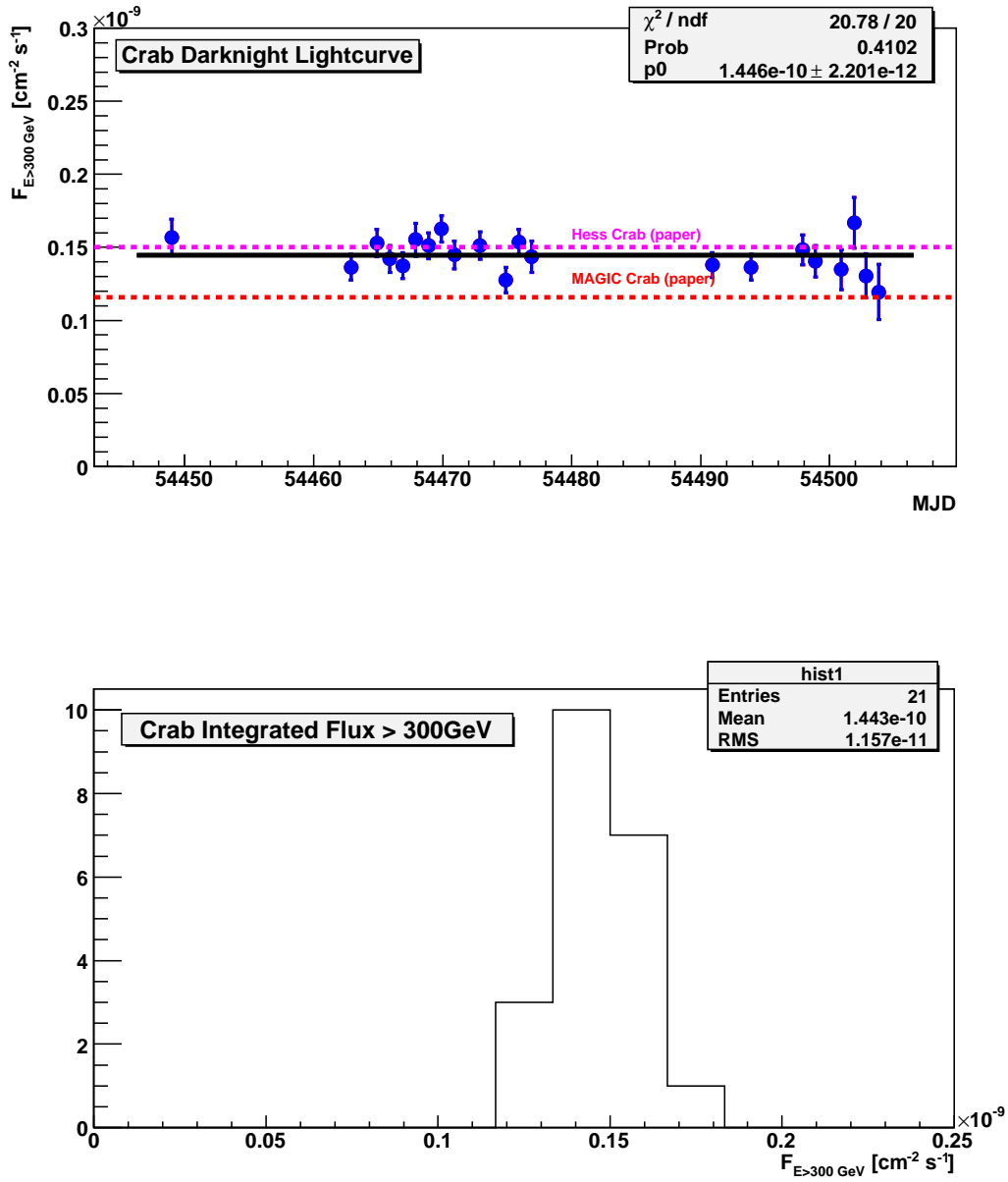


Figure A.19: The upper panel: Crab dark night data from December 2007 to March 2008: The black line is the fitted flux from the observed data. Crab fluxes from two independent groups are presented. Note all the data shown here are after the selection cuts. The bottom panel: Crab dark night daily flux from December 2007 to March 2008. The mean flux above 300 GeV is about  $1.44 \times 10^{-10} \text{ cm}^{-2} \text{s}^{-1}$ , with small RMS  $1.15 \times 10^{-11} \text{ cm}^{-2} \text{s}^{-1}$  for 21 data sets in total. The RMS value is less than 10% of the mean value.

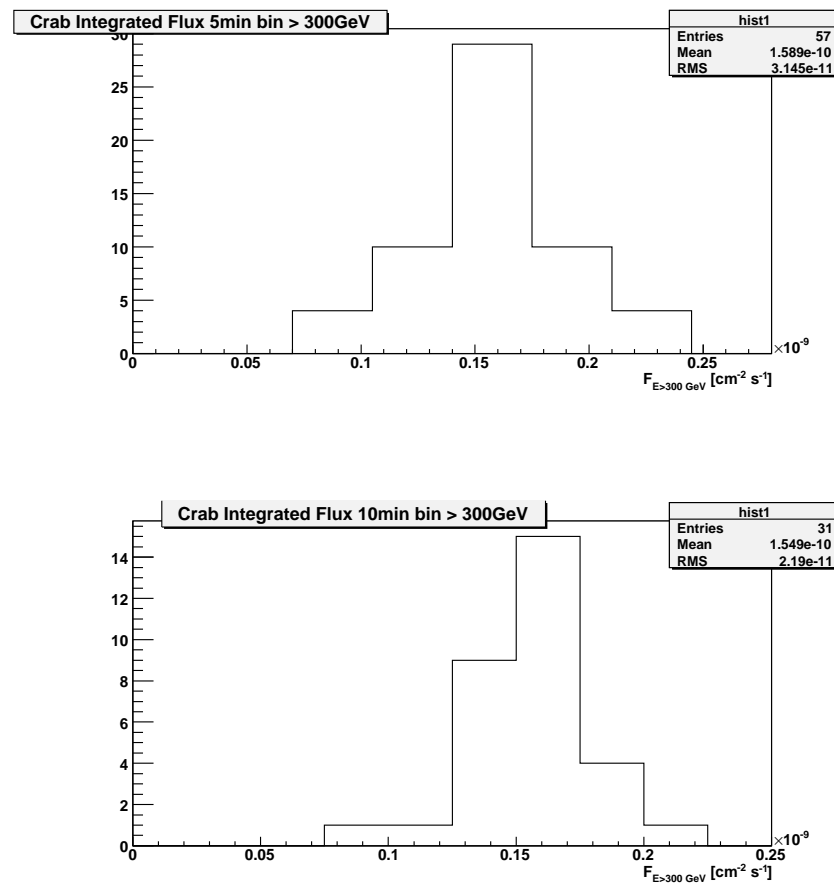


Figure A.20: Histograms of Crab flux in P5, with 5 minutes (the upper) and 10 minutes (the bottom) timing bins are shown.

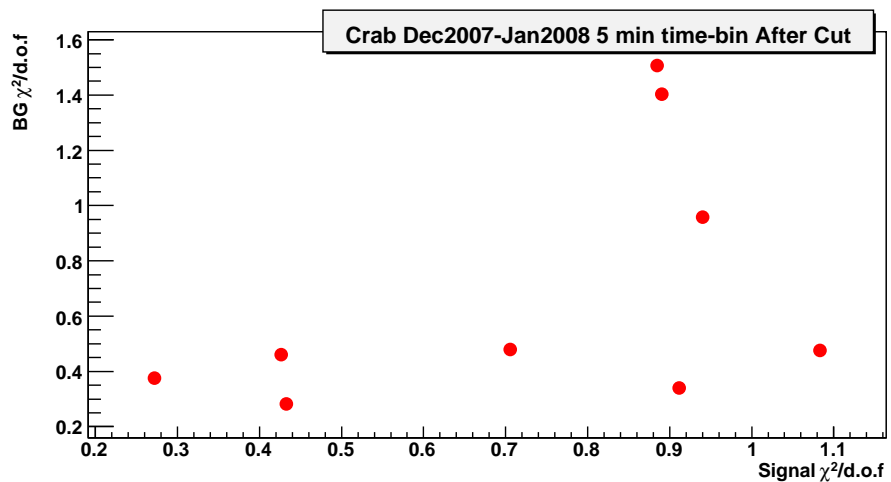


Figure A.21: The scatter plot of the  $\chi^2$  distributions of the background and the signal lightcurves using 5 minutes timing bins.

# Bibliography

- [1] M. Punch *et al.*, *Detection of TeV photons from the active galaxy Markarian 421*, *Nature* **358** (1992) 477–478.
- [2] F. Halzen, *Talk at taup 2007* , .
- [3] A. M. Hillas, *Cosmic rays: Recent progress and some current questions*, astro-ph/0607109.
- [4] *FERMI Official Website*. <http://fermi.gsfc.nasa.gov/>.
- [5] R. M. Wagner, *TeV Source Catalog*. <http://www.mppmu.mpg.de/~rwagner/sources/>.
- [6] M. Boettcher, *Physics Input from Multiwavelength Observations of AGNs*, astro-ph/0105554.
- [7] **STACEE** Collaboration, S. Oser *et al.*, *High Energy Gamma-Ray Observations of the Crab Nebula and Pulsar with the Solar Tower Atmospheric Cherenkov Effect Experiment*, astro-ph/0006304.
- [8] H. Bartko, *Observation of Galactic Sources of Very-High-Energy Gamma-rays with the MAGIC Telescope*. PhD Thesis, MPI fuer Physik, Muenchen, 2006.
- [9] D. Mazin, *A study of very high energy gamma-ray emission from AGNs and constraints on the extragalactic background light*. PhD Thesis, MPI fuer Physik, Muenchen, 2007.
- [10] R. M. Wagner, *Measurement of VHE  $\gamma$ -ray emission from four blazars using the MAGIC telescope and a comparative blazar study*. PhD Theis MPI fuer Physik, Muenchen, 2005.
- [11] D. Paneque, *The MAGIC Telescope: development of new technologies and first observations*. PhD Thesis, MPI fuer Physik, Muenchen, 2004.
- [12] A. De Angelis, O. Mansutti, and M. Persic, *Very-High Energy Gamma Astrophysics*, *Riv. Nuovo Cim.* **31** (2008) 187, [astro-ph/0712.0315].
- [13] P. Charlot, D. C. Gabuzda, H. Sol, B. Degrange, and F. Piron, *Simultaneous radio-interferometric and high-energy TeV observations of the gamma-ray blazar Mkn 421*, astro-ph/0607258.

- [14] M. Blazejowski *et al.*, *A Multi-wavelength View of the TeV Blazar Markarian 421: Correlated Variability, Flaring, and Spectral Evolution*, *Astrophys. J.* **630** (2005) 130–141, [[astro-ph/0505325](#)].
- [15] F. Aharonian, J. Buckley, T. Kifune, and G. Sinnis, *High energy astrophysics with ground-based gamma ray detectors*, *Rept. Prog. Phys.* **71** (2008) 096901.
- [16] G. Superina, B. DeGrange, and H.E.S.S. Collaboration, *Lognormal  $\gamma$ -ray flux variations in the extreme BL Lac object PKS 2155-304*, in *Blazar Variability across the Electromagnetic Spectrum*, 2008.
- [17] **VERITAS** Collaboration, V. Vittorini *et al.*, *The June 2008 flare of Markarian 421 from optical to TeV energies*, *Astrophys. J.* **691** (2009) L13–L19, [[astro-ph/0812.1500](#)].
- [18] **The HEGRA** Collaboration, F. Aharonian *et al.*, *The Crab nebula and pulsar between 500-GeV and 80-TeV: Observations with the HEGRA stereoscopic air Cherenkov telescopes*, *Astrophys. J.* **614** (2004) 897–913, [[astro-ph/0407118](#)].
- [19] C. M. Urry and P. Padovani, *Unified Schemes for Radio-Loud Active Galactic Nuclei*, *Publ. Astron. Soc. Pac.* **107** (1995) 803, [[astro-ph/9506063](#)].
- [20] J. Hinton, *Gamma-ray Astronomy*, [astro-ph/0712.3352](#).
- [21] G. Bonomini, *PhD Thesis : In preparation*.
- [22] *DESY Multi-messenger Group Website*.  
<http://www-zeuthen.desy.de/multi-messenger/GammaRayData/index.html>.
- [23] J. Blümner, R. Engel, and J. R. Hörandel, *Cosmic rays from the knee to the highest energies*, *Progress in Particle and Nuclear Physics* **63** (Oct., 2009) 293–338, [[astro-ph/0904.0725](#)].
- [24] R. Aloisio *et al.*, *A dip in the UHECR spectrum and the transition from galactic to extragalactic cosmic rays*, *Astropart. Phys.* **27** (2007) 76–91, [[astro-ph/0608219](#)].
- [25] *Connecting quarks with the cosmos: Eleven science questions for the new century*, . Washington, USA: Nat. Acad. Pr. (2003) 206 p.
- [26] M. S. Longair, *High-energy astrophysics. Vol. 2: Stars, the galaxy and the interstellar medium*, . Cambridge, UK: Univ. Pr. (1994) 393 p.
- [27] E. Fermi, *On the Origin of the Cosmic Radiation*, *Phys. Rev.* **75** (1949) 1169–1174.
- [28] L. O. Drury, *An introduction to the theory of diffusive shock acceleration of energetic particles in tenuous plasmas*, *Rept. Prog. Phys.* **46** (1983) 973–1027.
- [29] C. A. Norman, D. B. Melrose, and A. Achterberg, *The Origin of Cosmic Rays above  $10^{18.5}$  eV*, *454* (Nov., 1995) 60.

- [30] H. Kang, D. Ryu, and T. W. Jones, *Cluster Accretion Shocks as Possible Acceleration Sites for Ultra-High-Energy Protons below the Greisen Cutoff*, **456** (Jan., 1996) 422, [[arXiv:astro-ph/9507113](https://arxiv.org/abs/astro-ph/9507113)].
- [31] P. L. Biermann and P. A. Strittmatter, *Synchrotron emission from shock waves in active galactic nuclei*, **322** (Nov., 1987) 643–649.
- [32] **COMPTEL** Collaboration, V. Schoenfelder, *The first COMPTEL Source Catalogue*, [astro-ph/0002366](https://arxiv.org/abs/astro-ph/0002366).
- [33] **EGRET** Collaboration, P. Sreekumar *et al.*, *EGRET observations of the extragalactic gamma ray emission*, *Astrophys. J.* **494** (1998) 523–534, [[astro-ph/9709257](https://arxiv.org/abs/astro-ph/9709257)].
- [34] **HESS** Collaboration, . F. Aharonian, *Discovery of very high energy gamma-ray emission from Centaurus A with H.E.S.S*, *Astrophys. J. Lett.* **695** (2009) L40–L44, [[0903.1582](https://arxiv.org/abs/0903.1582)].
- [35] **HEGRA** Collaboration, F. Aharonian, A. Akhperjanian, and M. Beilicke, *Observations of 54 active galactic nuclei with the HEGRA system of Cherenkov telescopes*, *Astron. Astrophys.* **421** (2004) 529–537, [[astro-ph/0401301](https://arxiv.org/abs/astro-ph/0401301)].
- [36] M. Catanese *et al.*, *Detection of gamma rays with  $E \geq 300$ -GeV from Markarian 501*, .
- [37] M. Catanese *et al.*, *Discovery of  $\geq 350$ -GeV gamma rays from the BL Lacertae object 1ES 2344+514*, [astro-ph/9712325](https://arxiv.org/abs/astro-ph/9712325).
- [38] **MAGIC** Collaboration, J. Albert *et al.*, *Discovery of very high energy gamma-rays from Markarian 180 triggered by an optical outburst*, *Astrophys. J.* **648** (2006) 105–109, [[astro-ph/0606630](https://arxiv.org/abs/0606630)].
- [39] T. Nishiyama, *Detection of a new TeV gamma-ray source of BL Lac object 1ES 1959+650*, in *International Cosmic Ray Conference*, vol. 3 of *International Cosmic Ray Conference*, p. 370, Aug., 1999.
- [40] **H.E.S.S.** Collaboration, *H.E.S.S. ICRC 2007 contributions*, [astro-ph/0710.4057](https://arxiv.org/abs/astro-ph/0710.4057).
- [41] **MAGIC** Collaboration, J. Albert *et al.*, *Discovery of very high energy gamma-ray emission from the low-frequency peaked BL Lacertae object BL Lacertae*, *Astrophys. J.* **666** (2007) L17–L20, [[astro-ph/0703084](https://arxiv.org/abs/0703084)].
- [42] **The H.E.S.S. Collaboration**, F. Aharonian *et al.*, *Discovery of VHE gamma rays from PKS 2005-489*, *Astron. Astrophys.* **436** (2005) L17–L20, [[astro-ph/0504520](https://arxiv.org/abs/astro-ph/0504520)].
- [43] **HESS** Collaboration, . F. Aharonian, *Discovery of VHE gamma-rays from the high-frequency-peaked BL Lac object RGB J0152+017*, [astro-ph/0802.4021](https://arxiv.org/abs/0802.4021).
- [44] **VERITAS** Collaboration, . V. A. Acciari *et al.*, *VERITAS Discovery of  $\geq 200$ GeV Gamma-ray Emission from the Intermediate-frequency-peaked BL Lac Object W Comae*, [astro-ph/0808.0889](https://arxiv.org/abs/0808.0889).

- [45] P. M. Chadwick *et al.*, *PKS 2155-304 - a source of VHE gamma-rays*, astro-ph/9812122.
- [46] R. Ong, *VERITAS Discovery of VHE Gamma-Ray Emission from BL Lac object RGB J0710+591*, *The Astronomer's Telegram* **1941** (Feb., 2009).
- [47] D. Horan *et al.*, *Detection of the BL Lacertae object H1426+428 at TeV gamma-ray energies*, *Astrophys. J.* **571** (2002) 753–762, [astro-ph/0202185].
- [48] **VERITAS** Collaboration, . V. Acciari *et al.*, *Discovery of Very High-Energy Gamma-Ray Radiation from the BL Lac 1ES 0806+524*, astro-ph/0812.0978.
- [49] **H.E.S.S.** Collaboration, F. Aharonian *et al.*, *New constraints on the Mid-IR EBL from the HESS discovery of VHE gamma rays from 1ES 0229+200*, astro-ph/0709.4584.
- [50] **H.E.S.S.** Collaboration, F. Aharonian *et al.*, *A Low level of extragalactic background light as revealed by gamma-rays from blazars*, *Nature* **440** (2006) 1018–1021, [astro-ph/0508073].
- [51] **MAGIC** Collaboration, J. Albert *et al.*, *Discovery of VHE gamma-ray emission from 1ES 1218+30.4*, *Astrophys. J.* **642** (2006) L119–L122, [astro-ph/0603529].
- [52] **HESS** Collaboration, F. Aharonian *et al.*, *Discovery of VHE gamma-rays from the distant BL Lac 1ES 0347-121*, astro-ph/0708.3021.
- [53] **MAGIC** Collaboration, J. Albert *et al.*, *Discovery of Very High Energy gamma-rays from 1ES1011+496 at z=0.212*, *Astrophys. J.* **667** (2007) L21–L23, [astro-ph/0706.4435].
- [54] **H.E.S.S.** Collaboration, F. Aharonian *et al.*, *Evidence for VHE gamma-ray emission from the distant BL Lac PG 1553+113*, *Astron. Astrophys.* **448** (2006) L19–L23, [astro-ph/0601545].
- [55] **MAGIC** Collaboration, J. Albert *et al.*, *Detection of VHE radiation from the BL Lac PG 1553+113 with the MAGIC telescope*, *Astrophys. J.* **654** (2007) L119–L122, [astro-ph/0606161].
- [56] **VERITAS** Collaboration, . V. A. Acciari *et al.*, *VERITAS Observations of a Very High Energy Gamma-ray Flare from the Blazar 3C 66A*, *Astrophys. J. Lett.* **693** (2009) L104–L108, [astro-ph/0901.4527].
- [57] **MAGIC** Collaboration, E. Aliu *et al.*, *Discovery of a very high energy gamma-ray signal from the 3C 66A/B region*, *Astrophys. J. Lett.* **692** (2009) 29–33, [astro-ph/0810.4712].
- [58] **MAGIC** Collaboration, E. Aliu *et al.*, *Very-High-Energy Gamma Rays from a Distant Quasar: How Transparent Is the Universe?*, *Science* **320** (2008) 1752, [astro-ph/0807.2822].

- [59] M. Teshima and The MAGIC Collaboration, *MAGIC discovers VHE gamma ray emission from the blazar S50716+714*, *The Astronomer's Telegram* **1500** (Apr., 2008).
- [60] R. A. Ong, *Discovery of VHE Gamma-Ray Emission from the Fermi-LAT Source PKS 1424+240*, *The Astronomer's Telegram* **2084** (June, 2009).
- [61] HESS Collaboration, . F. Acero, *Detection of Gamma Rays From a Starburst Galaxy*, 0909.4651.
- [62] R. A. Ong, *VERITAS discovery of a new VHE Gamma-ray Source, VER J0521+211*, *The Astronomer's Telegram* **2260** (Oct., 2009).
- [63] R. A. Ong and P. Fortin, *Discovery of High-Energy Gamma-Ray Emission from the BL Lac Object RBS 0413*, *The Astronomer's Telegram* **2272** (Oct., 2009).
- [64] W. Hofmann and S. Fegan, *H.E.S.S. and Fermi-LAT discovery of VHE and HE emission from blazar 1ES 0414+009*, *The Astronomer's Telegram* **2293** (Nov., 2009).
- [65] R. A. Ong, *Discovery of VHE Gamma-Ray Emission from the Fermi-LAT Source 1ES 0502+675*, *The Astronomer's Telegram* **2301** (Nov., 2009).
- [66] M. Raue, B. Behera, A. Charbonnier, B. Giebels, M. Hauser, K. Kosack, M. Punch, and H. Zechlin, *H.E.S.S. discovers VHE emission from the Fermi LAT source PKS 0447-439*, *The Astronomer's Telegram* **2350** (Dec., 2009).
- [67] R. A. Ong, VERITAS Collaboration, D. Panque, and Fermi Large Area Telescope, *VERITAS Discovery of Very High-Energy Gamma-Ray Emission from 1FGL J0648.8+1516*, *The Astronomer's Telegram* **2486** (Mar., 2010).
- [68] A. Neronov, D. V. Semikoz, and I. Vovk, *Very high-energy gamma-ray emission from head-tail radio galaxy IC 310*, astro-ph/1003.4615.
- [69] A. D. Kerrick *et al.*, *Outburst of TeV photons from Markarian-421*, *Astrophys. J.* **438** (1995) L59–L62.
- [70] E. E. Salpeter, *Accretion of Interstellar Matter by Massive Objects.*, **140** (Aug., 1964) 796–800.
- [71] Y. B. Zel'Dovich and I. D. Novikov, *Mass of Quasi-Stellar Objects*, *Soviet Physics Doklady* **9** (Apr., 1965) 834.
- [72] R. D. Blandford and R. L. Znajek, *Electromagnetic extraction of energy from Kerr black holes*, **179** (May, 1977) 433–456.
- [73] M.-H. Ulrich, L. Maraschi, and C. M. Urry, *Variability of active galactic nuclei*, *Ann. Rev. Astron. Astrophys.* **35** (1997) 445–502.

- [74] J. Albert *et al.*, *Variable VHE gamma-ray emission from Markarian 501*, *Astrophys. J.* **669** (2007) 862, [[astro-ph/0702008](#)].
- [75] F. Aharonian *et al.*, *An Exceptional VHE Gamma-Ray Flare of PKS 2155-304*, *Astrophys. J.* **664** (2007) L71–L78, [[astro-ph/0706.0797](#)].
- [76] J. A. Gaidos, C. W. Akerlof, S. D. Biller, P. J. Boyle, A. C. Breslin, J. H. Buckley, D. A. Carter-Lewis, M. Catanese, M. F. Cawley, D. J. Fegan, J. P. Finley, A. M. Hillas, F. Krennrich, R. C. Lamb, R. Lessard, J. McEnery, G. Mohanty, P. Moriarty, J. Quinn, A. Rodgers, H. J. Rose, F. Samuelson, M. S. Schubnell, G. Sembroski, R. Srinivasan, T. C. Weekes, C. L. Wilson, and J. Zweerink, *Very Rapid and Energetic Bursts of TeV Photons from the Active Galaxy Markarian 421.*, **383** (1996) 319.
- [77] C. Tanihata, T. Takahashi, J. Kataoka, and G. M. Madejski, *Implications of variability patterns observed in TeV blazars on the structure of the inner jet*, *Astrophys. J.* **584** (2003) 153–163, [[astro-ph/0210214](#)].
- [78] D. Guetta, G. Ghisellini, D. Lazzati, and A. Celotti, *Internal shocks and the blazar sequence. Low and intermediate power BL Lac objects*, *Astron. Astrophys.* **421** (2004) 877–886, [[astro-ph/0402164](#)].
- [79] M. C. Begelman, R. D. Blandford, and M. J. Rees, *Theory of extragalactic radio sources*, *Reviews of Modern Physics* **56** (Apr., 1984) 255–351.
- [80] F. A. Aharonian, *Very high energy cosmic gamma radiation: A crucial window on the extreme universe*, . River Edge, USA: World Scientific (2004) 495 p.
- [81] G. Ghisellini, L. Maraschi, and L. Dondi, *Diagnostics of Inverse-Compton models for the  $\gamma$ -ray emission of 3C 279 and MKN 421.*, **120** (Dec., 1996) C503.
- [82] F. Tavecchio, L. Maraschi, and G. Ghisellini, *Constraints on the physical parameters of TeV blazars*, [astro-ph/9809051](#).
- [83] M. Pohl and R. Schlickeiser, *On the conversion of blast wave energy into radiation in active galactic nuclei and gamma-ray bursts*, [astro-ph/9911452](#).
- [84] K. Mannheim, *The proton blazar*, **269** (Mar., 1993) 67–76, [[arXiv:astro-ph/9302006](#)].
- [85] F. A. Aharonian and A. M. Atoyan, *Broad-band diffuse gamma ray emission of the Galactic Disk*, [astro-ph/0009009](#).
- [86] A. Mucke and R. J. Protheroe, *A proton synchrotron blazar model for flaring in Markarian 501*, *Astropart. Phys.* **15** (2001) 121–136, [[astro-ph/0004052](#)].
- [87] M. Bottcher, *A hadronic synchrotron mirror model for the 'orphan' TeV flare in 1ES 1959+650*, *Astrophys. J.* **621** (2005) 176–180, [[astro-ph/0411248](#)].

- [88] A. Neronov and F. A. Aharonian, *Production of TeV Gamma Radiation in the Vicinity of the Supermassive Black Hole in the Giant Radio Galaxy M87*, **671** (Dec., 2007) 85–96, [0704.3282].
- [89] F. M. Rieger and F. A. Aharonian, *Variable VHE gamma-ray emission from non-blazar AGNs*, **479** (Feb., 2008) L5–L8, [0712.2902].
- [90] J.-P. Lenain, C. Boisson, and H. Sol, *SSC scenario for VHE emission from 2 radiogalaxies: M 87 and Cen A*, astro-ph/0807.2733.
- [91] L. Stawarz, F. Aharonian, S. Wagner, and M. Ostrowski, *Absorption of Nuclear Gamma-rays on the Starlight Radiation in FR I Sources: the Case of Centaurus A*, *Mon. Not. Roy. Astron. Soc.* **371** (2006) 1705–1716, [astro-ph/0605721].
- [92] A. Levinson, *High-energy aspects of astrophysical jets*, *Int. J. Mod. Phys. A* **21** (2006) 6015–6054, [astro-ph/0611521].
- [93] M. G. Hauser and E. Dwek, *The Cosmic Infrared Background: Measurements and Implications*, *Ann. Rev. Astron. Astrophys.* **39** (2001) 249–307, [astro-ph/0105539].
- [94] A. M. Hillas, *Cerenkov light images of EAS produced by primary gamma*, in *International Cosmic Ray Conference* (F. C. Jones, ed.), vol. 3 of *International Cosmic Ray Conference*, pp. 445–448, Aug., 1985.
- [95] M. Garczarczyk, *First Observations of the GRB Prompt and Early Afterglow Emission Phase at 100 GeV Energy Regime with the 17 m Diameter MAGIC Imaging Atmospheric Cherenkov Telescope*. PhD Thesis, Universität Rostock, Rostock Germany, 2006.
- [96] H. Bartko, F. Goebel, R. Mirzoyan, W. Pimpl, and M. Teshima, *Tests of a prototype multiplexed fiber-optic ultra-fast FADC data acquisition system for the MAGIC telescope*, *Nucl. Instrum. Meth. A* **548** (2005) 464–486, [astro-ph/0505204].
- [97] M. Gaug, *PhD Thesis*. Universitat Autonoma de Barcelona, Barcelona, 2008.
- [98] D. Paneque et al, *A method to enhance the sensitivity of photomultipliers for air Cherenkov telescope*, *Nucl. Instr. and Meth. Phys. Rev. A* **504** (2003) 109–115.
- [99] R. Winston, *Light Collection within the Framework of Geometrical Optics*, *Journal of the Optical Society of America (1917-1983)* **60** (Feb., 1970) 245.
- [100] C. Leinert, S. Bowyer, L. K. Haikala, M. S. Hanner, M. G. Hauser, A.-C. Levasseur-Regourd, I. Mann, K. Mattila, W. T. Reach, W. Schlosser, H. J. Staude, G. N. Toller, J. L. Weiland, J. L. Weinberg, and A. N. Witt, *The 1997 reference of diffuse night sky brightness*, **127** (Jan., 1998) 1–99.
- [101] C. R. Benn and S. L. Ellison, *LA Palma Night-Sky Brightness*, astro-ph/9909153.

- [102] H. M. Badran, T. C. Weekes, and M. Urban, *Development of a filter for operation of atmospheric Cherenkov telescopes close to the moon*, *Nucl. Instrum. Meth.* **A385** (1997) 258–264.
- [103] A. Moralejo *et al.*, *MARS, the MAGIC Analysis and Reconstruction Software*, [astro-ph/0907.0943](#).
- [104] J. Albert *et al.*, *Implementation of the Random Forest Method for the Imaging Atmospheric Cherenkov Telescope MAGIC*, *Nucl. Instrum. Meth.* **A588** (2008) 424–432, [0709.3719].
- [105] W. T. V. William H. Press, Saul A. Teukolsky and B. P. Flannery, *Numerical Recipes*. Cambridge University Press, UK, 2007.
- [106] **MAGIC** Collaboration, H. Bartko, M. Gaug, A. Moralejo, and N. Sidro, *FADC pulse reconstruction using a digital filter for the MAGIC telescope*, [astro-ph/0506459](#).
- [107] R. Mirzoyan and Lorenz, *The F-factor Method*, *MAGIC Internal Note* (1997).
- [108] **MAGIC** Collaboration, E. Domingo-Santamaría, J. Flix, V. Scalzotto, W. Wittek, and J. Rico, *The DISP analysis method for point-like or extended gamma source searches / studies with the MAGIC telescope*, . Prepared for 29th International Cosmic Ray Conference (ICRC 2005), Pune, India, 3-11 Aug 2005.
- [109] D. Tescaro, *Timing analysis of the MAGIC telescope data after the installation of the unltra-fast 2 GSsample/s FADC readout*. IFAE Barcelona, Barcelona, 2007.
- [110] V. P. Fomin *et al.*, *New methods of atmospheric Cherenkov imaging for gamma-ray astronomy. 1: The False source method*, *Astropart. Phys.* **2** (1994) 137–150.
- [111] T. P. Li and Y. Q. Ma, *Analysis methods for results in gamma-ray astronomy*, *Astrophys. J.* **272** (1983) 317–324.
- [112] **MAGIC** Collaboration, E. Aliu *et al.*, *Improving the performance of the single-dish Cherenkov telescope MAGIC through the use of signal timing*, *Astropart. Phys.* **30** (2009) 293–305, [astro-ph/0810.3568].
- [113] T. C. Weekes *et al.*, *Observation of TeV gamma rays from the Crab nebula using the atmospheric Cerenkov imaging technique*, *Astrophys. J.* **342** (1989) 379–395.
- [114] **MAGIC** Collaboration, J. Albert *et al.*, *VHE Gamma-Ray Observation of the Crab Nebula and its Pulsar with the MAGIC telescope*, *Astrophys. J.* **674** (2008) 1037–1055, [0705.3244].
- [115] **H.E.S.S.** Collaboration, F. Aharonian *et al.*, *Observations of the Crab Nebula with H.E.S.S.*, *Astron. Astrophys.* **457** (2006) 899–915, [astro-ph/0607333].

- [116] R. D. Blandford, *Probing the Physics of AGN: A Summary*, *Publ. Astron. Soc. Pac.* **113** (2001) 1309, [[astro-ph/0110397](#)].
- [117] A. Sillanpää, L. O. Takalo, T. Pursimo, K. Nilsson, P. Heinämäki, S. Katajainen, H. Pietilä, M. Hanski, R. Rekola, P. Boltwood, G. W. Turner, J. W. Robertson, R. K. Honeycut, Y. S. Efimov, N. Shakhovskoy, M. Fiorucci, G. Tosti, G. Ghisellini, C. M. Raiteri, M. Villata, G. De Francesco, S. Bosio, G. Latini, and J. Heidt, *Optical Variations of OJ 287*, vol. 110 of *Astronomical Society of the Pacific Conference Series*, p. 74, 1996.
- [118] M.-H. Ulrich, T. D. Kinman, C. R. Lynds, G. H. Rieke, and R. D. Ekers, *Nonthermal continuum radiation in three elliptical galaxies*, **198** (June, 1975) 261–266.
- [119] M. J. Ricketts, B. A. Cooke, and K. A. Pounds, *X-ray transient source at high galactic latitude and suggested extragalactic identification*, **259** (Feb., 1976) 546.
- [120] C. von Montigny, D. L. Bertsch, J. Chiang, B. L. Dingus, J. A. Esposito, C. E. Fichtel, J. M. Fierro, R. C. Hartman, S. D. Hunter, G. Kanbach, D. A. Kniffen, Y. C. Lin, J. R. Mattox, H. A. Mayer-Hasselwander, P. F. Michelson, P. L. Nolan, H. D. Radecke, E. Schneid, P. Sreekumar, D. J. Thompson, and T. Willis, *High-Energy Gamma-Ray Emission from Active Galaxies: EGRET Observations and Their Implications*, **440** (Feb., 1995) 525.
- [121] Y. C. Lin, D. L. Bertsch, J. Chiang, C. E. Fichtel, R. C. Hartman, S. D. Hunter, G. Kanbach, D. A. Kniffen, P. W. Kwok, J. R. Mattox, H. A. Mayer-Hasselwander, P. F. Michelson, C. von Montigny, P. L. Nolan, K. Pinkau, E. Schneid, P. Sreekumar, and D. J. Thompson, *Detection of high-energy gamma-ray emission from the BL Lacertae object Markarian 421 by the EGRET telescope on the Compton Observatory*, **401** (Dec., 1992) L61–L64.
- [122] W. Collmar, *COMPTEL Observations of the TeV Sources Markarian 421 and Markarian 501*, in *International Cosmic Ray Conference*, vol. 3 of *International Cosmic Ray Conference*, p. 374, Aug., 1999.
- [123] B. G. Piner *et al.*, *VSOP and ground-based VLBI imaging of the TeV blazar Markarian 421 at multiple epochs*, [astro-ph/9906202](#).
- [124] P. G. Edwards and B. G. Piner, *The Subluminal Parsec-Scale Jet of Markarian 501*, **579** (Nov., 2002) L67–L70, [[arXiv:astro-ph/0210482](#)].
- [125] A. C. Gupta, D. P. K. Banerjee, N. M. Ashok, and U. C. Joshi, *Near Infrared Intraday Variability of Mrk 421*, *Astron. Astrophys.* **422** (2004) 505–508, [[astro-ph/0405186](#)].
- [126] F. K. Liu, B. F. Liu, and G. Z. Xie, *The long-term optical behavior of MRK421*, [astro-ph/9610208](#).
- [127] P. W. Gorham, L. van Zee, S. C. Unwin, and C. Jacobs, *Markarian 421'S Unusual Satellite Galaxy*, **119** (Apr., 2000) 1677–1686, [[arXiv:astro-ph/9908077](#)].

- [128] B. E. Markarian and V. A. Lipovetskij, *Galaxies with ultraviolet continuum. V.*, *Astrofizika* **8** (1972) 155–164.
- [129] W. H. Warren, Jr., *The HEAO A-1 X ray source catalog (Wood et al. 1984): Documentation for the machine-readable version, NASA STI/Recon Technical Report N 91* (July, 1990) 31069.
- [130] S. L. Mufson, D. J. Hutter, and Y. Kondo, *Relativistic Jet Models for the Bl-Lacertae Object MARKARIAN:421 during Three Epochs of Observation*, in *BL Lac Objects* (L. Maraschi, T. Maccacaro, and M.-H. Ulrich, eds.), vol. 334 of *Lecture Notes in Physics, Berlin Springer Verlag*, p. 341, 1989.
- [131] S. A. Laurent-Muehleisen, R. I. Kollgaard, G. A. Moellenbrock, and E. D. Feigelson, *Radio morphology and parent population of X-ray selected BL Lacertae objects*, **106** (Sept., 1993) 875–898.
- [132] P. Nilson, *Uppsala General Catalogue of Galaxies, 1973, Acta Universitatis Upsaliensis, Nova Regiae Societatis Upsaliensis, Series v: a Vol., Nova Acta Regiae Soc. Sci. Upsaliensis Ser. V* (1973).
- [133] **HEGRA** Collaboration, D. Petry *et al.*, *Detection of VHE gamma-radiation from Mkn 421 with the first two imaging Cherenkov telescopes of the HEGRA collaboration*, .
- [134] M. S. Schubnell *et al.*, *Very High Energy Gamma-Ray Emission from the Blazar Markarian 421*, *astro-ph/9602068*.
- [135] J. H. Buckley, C. W. Akerlof, S. Biller, D. A. Carter-Lewis, M. Catanese, M. F. Cawley, V. Connaughton, D. J. Fegan, J. P. Finley, J. Gaidos, A. M. Hillas, J. F. Kartje, A. Koenigl, F. Krennrich, R. C. Lamb, R. Lessard, D. J. Macomb, J. R. Mattox, J. E. McEnery, G. Mohanty, J. Quinn, A. J. Rodgers, H. J. Rose, M. S. Schubnel, G. Sembroski, P. S. Smith, T. C. Weekes, C. Wilson, and J. Zweerink, *Gamma-Ray Variability of the BL Lacertae Object Markarian 421*, **472** (Nov., 1996) L9+.
- [136] K. Okumura *et al.*, *Observation of gamma-rays greater than 10-TeV from Markarian 421*, *Astrophys. J.* **579** (2002) L9–L12, [*astro-ph/0209487*].
- [137] R. A. Ong, *Very high-energy gamma-ray astronomy*, *Phys. Rept.* **305** (1998) 93–202.
- [138] F. Krennrich *et al.*, *Measurement of the multi-TeV gamma-ray flare-spectra of Markarian 421 and Markarian 501*, *astro-ph/9808333*.
- [139] **HEGRA** Collaboration, F. A. Aharonian, *Observations of Mkn 421 during 1997 and 1998 in the energy range above 500-GeV with the HEGRA stereoscopic Cherenkov telescope system*, *astro-ph/9905032*.

- [140] L. Maraschi, G. Fossati, F. Tavecchio, L. Chiappetti, A. Celotti, G. Ghisellini, P. Grandi, E. Pian, G. Tagliaferri, A. Treves, A. C. Breslin, J. H. Buckley, D. A. Carter-Lewis, M. Catanese, M. F. Cawley, D. J. Fegan, S. Fegan, J. Finley, J. Gaidos, T. Hall, A. M. Hillas, F. Krennrich, R. W. Lessard, C. Masterson, P. Moriarty, J. Quinn, J. Rose, F. Samuelson, T. C. Weekes, C. M. Urry, and T. Takahashi, *Simultaneous X-Ray and TeV Observations of a Rapid Flare from Markarian 421*, **526** (Dec., 1999) L81–L84.
- [141] T. Takahashi, K. Maegami, F. Makino, H. Ozawa, and H. Kubo, *Markarian 421*, **6888** (Apr., 1998).
- [142] **HEGRA** Collaboration, H. Krawczynski *et al.*, *Simultaneous X-ray and TeV gamma-ray observations of the TeV blazar Markarian 421 during February and May 2000*, *Astrophys. J.* **559** (2001) 187–195, [[astro-ph/0105331](#)].
- [143] D. Horan *et al.*, *Multiwavelength Observations of Markarian 421 in 2005 - 2006*, *Astrophys. J.* **695** (2009) 596–618, [[astro-ph/0901.1225](#)].
- [144] F. Krennrich *et al.*, *Cutoff in the TeV energy spectrum of Markarian 421 during strong flares in 2001*, *Astrophys. J.* **560** (2001) L45–L48, [[astro-ph/0107113](#)].
- [145] F. Krennrich *et al.*, *Discovery of Spectral Variability of Markarian 421 at TeV Energies*, *Astrophys. J.* **575** (2002) L9–L14, [[astro-ph/0207184](#)].
- [146] **HEGRA** Collaboration, F. Aharonian *et al.*, *Variations of the TeV energy spectrum at different flux levels of Mkn 421 observed with the HEGRA system of Cherenkov telescopes*, *Astron. Astrophys.* **393** (2002) 89–100, [[astro-ph/0205499](#)].
- [147] **HEGRA** Collaboration, F. Aharonian, *The time averaged TeV energy spectrum of Mkn 501 of the extraordinary 1997 outburst as measured with the stereoscopic Cherenkov telescope system of HEGRA*, *Astron. Astrophys.* **349** (1999) 11–28, [[astro-ph/9903386](#)].
- [148] **the HEGRA** Collaboration, D. Horns, *Multi-wavelength observations of the TeV blazars Mkn-421, 1ES1959+650, and H1426+428 with the HEGRA Cherenkov telescopes and the RXTE X-ray satellite*, [astro-ph/0209454](#).
- [149] G. Fossati *et al.*, *Multiwavelength Observations of Markarian 421 in March 2001: an Unprecedented View on the X-ray/TeV Correlated Variability*, [0710.4138](#).
- [150] **The H.E.S.S.** Collaboration, F. Aharonian *et al.*, *Observations of Mkn 421 in 2004 with HESS at large zenith angles*, *Astron. Astrophys.* **95** (2005) 437, [[astro-ph/0506319](#)].
- [151] J. E. Carson *et al.*, *The spectrum of Markarian 421 above 100 GeV with STACEE*, . To appear in the proceedings of 29th International Cosmic Ray Conference (ICRC 2005), Pune, India, 3-11 Aug 2005, pp. 415-418.

- [152] **MAGIC** Collaboration, J. Albert *et al.*, *Observations of Mkn 421 with the MAGIC Telescope*, *Astrophys. J.* **663** (2007) 125–138, [[astro-ph/0603478](#)].
- [153] **MAGIC and HESS** Collaboration, D. Mazin *et al.*, *Concept of a global network of Cherenkov telescopes (GNCT) and first joint observations with HESS and MAGIC*, . Prepared for 29th International Cosmic Ray Conference (ICRC 2005), Pune, India, 3-11 Aug 2005.
- [154] B. Giebels, G. Dubus, and B. Khelifi, *Unveiling the X-ray/TeV engine in Mkn 421*, *Astron. Astrophys.* **462** (2007) 29–41, [[astro-ph/0610270](#)].
- [155] A. K. Konopelko, A. Mastichiadis, J. G. Kirk, O. C. de Jager, and F. W. Stecker, *Modelling the TeV gamma-ray spectra of two low redshift AGNs: Mkn 501 and Mkn 421*, *Astrophys. J.* **597** (2003) 851–859, [[astro-ph/0302049](#)].
- [156] D. Britzger, *Studies of the Influence of Moonlight on Observations with the MAGIC Telescope*. Universität München, Muenchen, 2009.
- [157] *KVA Telescope Website*. <http://www.astro.utu.fi/telescopes/60lapalma.htm>.
- [158] *Official RXTE Website*. <http://heasarc.gsfc.nasa.gov/docs/xte/xtegof.html>.
- [159] *Official Swift Website*. <http://heasarc.gsfc.nasa.gov/docs/swift/swiftsc.html>.
- [160] R. A. Edelson, T. Alexander, D. M. Crenshaw, S. Kaspi, M. A. Malkan, B. M. Peterson, R. S. Warwick, J. Clavel, A. V. Filippenko, K. Horne, K. T. Korista, G. A. Kriss, J. H. Krolik, D. Maoz, K. Nandra, P. T. O'Brien, S. V. Penton, T. Yaqoob, P. Albrecht, D. Alloin, T. R. Ayres, T. J. Balonek, P. Barr, A. J. Barth, R. Bertram, G. E. Bromage, M. Carini, T. E. Carone, F. Cheng, K. K. Chuvaev, M. Dietrich, D. Dultzin-Hacyan, C. M. Gaskell, I. S. Glass, M. R. Goad, S. Hemar, L. C. Ho, J. P. Huchra, J. Hutchings, W. N. Johnson, D. Kazanas, W. Kollatschny, A. P. Koratkar, O. Kovo, A. Laor, G. M. MacAlpine, P. Magdziarz, P. G. Martin, T. Matheson, B. McCollum, H. R. Miller, S. L. Morris, V. L. Oknyanskij, J. Penfold, E. Perez, G. C. Perola, G. Pike, R. W. Pogge, R. L. Ptak, B. Qian, M. C. Recondo-Gonzalez, G. A. Reichert, J. M. Rodriguez-Espinoza, P. M. Rodriguez-Pascual, E. L. Rokaki, J. Roland, A. C. Sadun, I. Salamanca, M. Santos-Lleo, J. C. Shields, J. M. Shull, D. A. Smith, S. M. Smith, M. A. J. Snijders, G. M. Stirpe, R. E. Stoner, W. Sun, M. Ulrich, E. van Groningen, R. M. Wagner, S. Wagner, I. Wanders, W. F. Welsh, R. J. Weymann, B. J. Wilkes, H. Wu, J. Wurster, S. Xue, A. A. Zdziarski, W. Zheng, and Z. Zou, *Multiwavelength Observations of Short-Timescale Variability in NGC 4151. IV. Analysis of Multiwavelength Continuum Variability*, **470** (Oct., 1996) 364, [[arXiv:astro-ph/9605082](#)].
- [161] C. Tanihata *et al.*, *Variability Time Scales of TeV Blazars Observed in the ASCA Continuous Long-Look X-ray Monitoring*, *Astrophys. J.* **563** (2001) 569–581, [[astro-ph/0108310](#)].

- [162] P. Uttley, I. M. McHardy, and S. Vaughan, *Non-linear X-ray variability in X-ray binaries and active galaxies*, *Mon. Not. Roy. Astron. Soc.* **359** (2005) 345–362, [[astro-ph/0502112](#)].
- [163] I. M. McHardy, K. F. Gunn, P. Uttley, and M. R. Goad, *MCG-6-30-15: long time-scale X-ray variability, black hole mass and active galactic nuclei high states*, **359** (June, 2005) 1469–1480, [[arXiv:astro-ph/0503100](#)].
- [164] I. M. McHardy, I. E. Papadakis, P. Uttley, M. J. Page, and K. O. Mason, *Combined long and short time-scale X-ray variability of NGC 4051 with RXTE and XMM-Newton*, **348** (Mar., 2004) 783–801, [[arXiv:astro-ph/0311220](#)].
- [165] Y. E. Lyubarskii, *Flicker noise in accretion discs*, **292** (Dec., 1997) 679.
- [166] Y. H. Zhang, *Cross-spectral analysis of the X-ray variability of Markarian 421*, **337** (Dec., 2002) 609–618, [[arXiv:astro-ph/0209063](#)].
- [167] P. Uttley and I. M. McHardy, *The flux-dependent amplitude of broadband noise variability in X-ray binaries and active galaxies*, *Mon. Not. Roy. Astron. Soc.* **323** (2001) L26, [[astro-ph/0103367](#)].
- [168] B. Degrange, G. Superina, B. Giebels, and F. Volpe, *The emission of blazars in VHE gamma-rays viewed as a random stationary process: the case of PKS 2155-304*, in *Blazar Variability across the Electromagnetic Spectrum*, 2008.
- [169] J. Kataoka *et al.*, *Five-year Monitorings of TeV Blazars with ASCA and RXTE*, [astro-ph/0105029](#).
- [170] J. G. Kirk, F. M. Rieger, and A. Mastichiadis, *Particle acceleration and synchrotron emission in blazar jets*, *Astron. Astrophys.* **333** (1998) 452–458, [[astro-ph/9801265](#)].
- [171] M. Georganopoulos, J. G. Kirk, and A. Mastichiadis, *The beaming pattern and spectrum of inverse Compton radiation in blazars*, *Astrophys. J.* **561** (2001) 111–117, [[astro-ph/0107152](#)].
- [172] J. G. Kirk and A. Mastichiadis, *Variability patterns of synchrotron and inverse Compton emission in blazars*, *Astroparticle Physics* **11** (June, 1999) 45–48.
- [173] D. Mazin and M. Raue, *New limits on the density of the extragalactic background light in the optical to the far-infrared from the spectra of all known TeV blazars*, *Astron. Astrophys.* **471** (2007) 439–452, [[astro-ph/0701694](#)].
- [174] B. Degrange, G. Superina, and V. F. Giebels, Berrie, *The emission of blazars in VHE gamma-rays viewed as a random stationary process: The case of PKS 2155-304*, *Pos BLAZARS* (2008) 016.

- [175] H. Krawczynski *et al.*, *Multiwavelength observations of strong flares from the TeV-blazar IES 1959+650*, *Astrophys. J.* **601** (2004) 151–164, [[astro-ph/0310158](#)].
- [176] F. Krennrich, I. H. Bond, P. J. Boyle, S. M. Bradbury, and J. H. Buckley, *Hourly spectral variability of Mrk 421*, [astro-ph/0305419](#).
- [177] E. Massaro, M. Perri, P. Giommi, and R. Nesci, *Log-parabolic spectra and particle acceleration in the BL Lac object Mkn 421: spectral analysis of the complete BeppoSAX wide band X-ray data set*, *Astron. Astrophys.* **413** (2004) 489–503, [[astro-ph/0312260](#)].
- [178] T. V. Collaboration, I. d. I. C. Perez, A. Ibarra, P. Rodriguez, and T. M. Collaboration, *Simultaneous Multiwavelength Observations of Markarian 421 During Outburst*, *Astrophys. J.* **703** (2009) 169–178, [[astro-ph/0907.3923](#)].
- [179] K. Katarzyński, H. Sol, and A. Kus, *The multifrequency variability of Mrk 421*, **410** (Oct., 2003) 101–115.
- [180] M. Camenzind and M. Krockenberger, *The lighthouse effect of relativistic jets in blazars - A geometric origin of intraday variability*, **255** (Feb., 1992) 59–62.
- [181] Gopal-Krishna and P. J. Wiita, *Swinging jets and the variability of active galactic nuclei*, **259** (June, 1992) 109–117.
- [182] W. Bednarek and R. J. Protheroe, *Modulation of AGN gamma-rays by interaction with X-rays from an accretion disc hotspot*, **290** (Sept., 1997) 139–144, [[arXiv:astro-ph/9612211](#)].
- [183] J. Quinn *et al.*, *The Flux Variability of Markarian 501 in Very High Energy Gamma Rays*, [astro-ph/9903088](#).
- [184] S. J. Wagner and A. Witzel, *Intraday variability in quasars and bl lac objects*, *Ann. Rev. Astron. Astrophys.* **33** (1995) 163–197.
- [185] B. G. Piner and P. G. Edwards, *The Parsec-Scale Structure and Jet Motions of the TeV Blazars IES 1959+650, PKS 2155-304, and IES 2344+514*, **600** (Jan., 2004) 115–126, [[arXiv:astro-ph/0309547](#)].
- [186] M. Georganopoulos and D. Kazanas, *Relativistic and slowing down: the flow in the hotspots of powerful radio galaxies and quasars*, *Astrophys. J.* **589** (2003) L5–L8, [[astro-ph/0304256](#)].
- [187] F. Tavecchio and G. Ghisellini, *Spine-sheath layer radiative interplay in subparsec-scale jets and the TeV emission from M87*, [0801.0593](#).
- [188] A. Mastichiadis and J. G. Kirk, *Models of variability in blazar jets*, [astro-ph/9903280](#).
- [189] M. Salvati, M. Spada, and F. Pacini, *Rapid Variability of Gamma-Ray Blazars: A Model for MKN 421*, [astro-ph/9801049](#).

- [190] T. W. Jones, S. L. O'dell, and W. A. Stein, *Physics of Compact Nonthermal Sources. H. Determination of Physical Parameters*, **192** (Sept., 1974) 261–278.
- [191] A. Celotti, L. Maraschi, and A. Treves, *A model for the spectral variability of BL Lacertae objects at high frequencies*, **377** (Aug., 1991) 403–416.
- [192] M. C. Begelman, A. C. Fabian, and M. J. Rees, *Implications of very rapid TeV variability in blazars*, [astro-ph/0709.0540](#).
- [193] M. Giroletti *et al.*, *Parsec Scale Properties of Markarian 501*, *Astrophys. J.* **600** (2004) 127–140, [[astro-ph/0309285](#)].
- [194] B. G. Piner and P. G. Edwards, *VLBA Polarization Observations of Markarian 421 After a Gamma-Ray High State*, *Astrophys. J.* **622** (2005) 168–177, [[astro-ph/0412383](#)].
- [195] F. Tavecchio, *Extragalactic jets: The high energy view*, [astro-ph/0401590](#).
- [196] T. V. Collaboration, t. V. . G. M. . M. Team, t. H. E. S. S. Collaboration, and t. M. Collaboration, *Radio Imaging of the Very-High-Energy Gamma-Ray Emission Region in the Central Engine of a Radio Galaxy*, *Science* **325** (2009) 444–448, [[astro-ph/0908.0511](#)].
- [197] T. Takahashi *et al.*, *ASCA Observation of an X-Ray/TeV Flare from the BL Lacertae Object Markarian 421*, *Astrophys. J.* **470** (1996) L89.
- [198] W. Brinkmann, I. E. Papadakis, C. Raeth, P. Mimica, and F. Haberl, *XMM-Newton timing mode observations of Mrk 421*, [astro-ph/0508433](#).
- [199] F. A. Aharonian and P. S. Coppi, *Simultaneous X-Ray and Gamma-Ray Observations of TeV Blazars: Testing Synchro-Compton Emission Models and Probing the Infrared Extragalactic Background*, *Astrophys. J.* **521** (1999) L33, [[astro-ph/9903159](#)].
- [200] A. Mastichiadis and K. Moraitis, *On the rapid TeV flaring activity of Markarian 501*, [astro-ph/0810.2420](#).
- [201] S. Sembay, R. S. Warwick, C. M. Urry, J. Sokoloski, I. M. George, F. Makino, T. Ohashi, and M. Tashiro, *The X-ray spectral variability of the BL Lacertae type object PKS 2155-304*, **404** (Feb., 1993) 112–123.
- [202] Y. H. Zhang, A. Treves, A. Celotti, L. Chiappetti, G. Fossati, G. Ghisellini, L. Maraschi, E. Pian, G. Tagliaferri, and F. Tavecchio, *Four Years of Monitoring Blazar PKS 2155-304 with BeppoSAX: Probing the Dynamics of the Jet*, **572** (June, 2002) 762–785, [[arXiv:astro-ph/0202378](#)].
- [203] G. Ghisellini, A. Celotti, and L. Costamante, *Low power BL Lacertae objects and the blazar sequence. Clues on the particle acceleration process*, **386** (May, 2002) 833–842, [[arXiv:astro-ph/0202367](#)].

- [204] T. Takahashi, G. Madejski, and H. Kubo, *X-ray observations of TeV blazars and multi-frequency analysis*, *Astropart. Phys.* **11** (1999) 177–187, [[astro-ph/9903099](#)].
- [205] C. D. Dermer and R. Schlickeiser, *Model for the high-energy emission from blazars*, *Astrophys. J.* **416** (1993) 458.
- [206] M. Sikora, M. C. Begelman, and M. J. Rees, *Comptonization of diffuse ambient radiation by a relativistic jet: The source of gamma rays from blazars?*, *Astrophys. J.* **421** (1994) 153.
- [207] M. Kusunose and F. Takahara, *A Structured Leptonic Jet Model of the “Orphan” TeV Gamma-Ray Flares in TeV Blazars*, *651* (Nov., 2006) 113–119, [[arXiv:astro-ph/0607063](#)].
- [208] G. Tosti, M. Fiorucci, M. Luciani, Y. S. Efimov, N. M. Shakhovskoy, E. Valtaoja, H. Teraesranta, A. Sillanpaeae, L. O. Takalo, M. Villata, C. M. Raiteri, G. de Francesco, and G. Sobrito, *Radio, optical and photopolarimetric observations of Markarian 421 around the great 1996-97 outburst*, *339* (Nov., 1998) 41–51.
- [209] J. P. Tavernet, *VHE Spectral Properties of Mrk 501 with the CAT telescope*, in *International Cosmic Ray Conference*, vol. 3 of *International Cosmic Ray Conference*, p. 322, Aug., 1999.
- [210] F. Aharonian, A. Akhperjanian, J. Barrio, K. Bernlöhr, H. Börst, H. Bojahr, O. Bolz, J. Contreras, J. Cortina, S. Denninghoff, V. Fonseca, J. Gonzalez, N. Götting, G. Heinzelmann, G. Hermann, A. Heusler, W. Hofmann, D. Horns, C. Iserlohe, A. Ibarra, I. Jung, R. Kankanyan, M. Kestel, J. Kettler, A. Kohnle, A. Konopelko, H. Kornmeyer, D. Kranich, H. Krawczynski, H. Lampeitl, E. Lorenz, F. Lucarelli, N. Magnussen, O. Mang, H. Meyer, R. Mirzoyan, A. Moralejo, L. Padilla, M. Panter, R. Plaga, A. Plyasheshnikov, J. Prahl, G. Pühlhofer, A. Röhring, W. Rhode, G. P. Rowell, V. Sahakian, M. Samorski, M. Schilling, F. Schröder, M. Siems, W. Stamm, M. Tluczykont, H. Völk, C. Wiedner, and W. Wittek, *The TEV Energy Spectrum of Markarian 501 Measured with the Stereoscopic Telescope System of HEGRA during 1998 and 1999*, *546* (Jan., 2001) 898–902.
- [211] L. Costamante, *A brief (blazar oriented) overview on topics for multi- wavelength observations with TeV photons*, *New Astron. Rev.* **48** (2004) 497–503, [[astro-ph/0308026](#)].
- [212] W. Bednarek and R. J. Protheroe, *Testing the homogeneous synchrotron self-Compton model for gamma-ray production in MRK 421*, *292* (Dec., 1997) 646, [[arXiv:astro-ph/9704185](#)].
- [213] W. Bednarek and R. J. Protheroe, *The physical parameters of Markarian 501 during flaring activity*, *310* (Dec., 1999) 577–584, [[arXiv:astro-ph/9902050](#)].

- [214] J. Kataoka, J. R. Mattox, J. Quinn, H. Kubo, F. Makino, T. Takahashi, S. Inoue, R. C. Hartman, G. M. Madejski, P. Sreekumar, and S. J. Wagner, *High-Energy Emission from the TEV Blazar Markarian 501 during Multiwavelength Observations in 1996*, **514** (Mar., 1999) 138–147, [[arXiv:astro-ph/9811014](https://arxiv.org/abs/astro-ph/9811014)].
- [215] J. Guy, C. Renault, F. A. Aharonian, M. Rivoal, and J. Tavernet, *Constraints on the cosmic infra-red background based on BeppoSAX and CAT spectra of Markarian 501*, **359** (July, 2000) 419–428, [[arXiv:astro-ph/0004355](https://arxiv.org/abs/astro-ph/0004355)].
- [216] M. Tluczykont, *Estimation of high-state rates from collected VHE and achived ASM data*, .
- [217] *MAXI Website at RIKEN*. <http://maxi.riken.jp/news/en/>.
- [218] **HEGRA** Collaboration, F. A. Aharonian *et al.*, *The energy spectrum of TeV gamma-rays from the Crab Nebula as measured by the HEGRA system of imaging air Cerenkov telescopes*, *Astrophys. J.* **539** (2000) 317–324, [[astro-ph/0003182](https://arxiv.org/abs/astro-ph/0003182)].
- [219] T. C. Weekes, M. F. Cawley, D. J. Fegan, K. G. Gibbs, A. M. Hillas, P. W. Kowk, R. C. Lamb, D. A. Lewis, D. Macomb, N. A. Porter, P. T. Reynolds, and G. Vacanti, *Observation of TeV gamma rays from the Crab nebula using the atmospheric Cerenkov imaging technique*, **342** (July, 1989) 379–395.
- [220] A. N. Otte *et al.*, *Observation of the Crab Nebula with the MAGIC telescope*, 0712.1386.
- [221] O. C. de Jager and A. K. Harding, *The expected high-energy to ultra-high-energy gamma-ray spectrum of the Crab Nebula*, **396** (Sept., 1992) 161–172.